

Hard X-Ray to Radio Multiwavelength SED Analysis of Local U/LIRGs in GOALS Sample with Self-consistent AGN Model Including Polar-dust Component

SATOSHI YAMADA ^{1,2} YOSHIHIRO UEDA ² MARTÍN HERRERA-ENDOQUI ³ YOSHIKI TOBA ^{4,2,5,6,7}
 TAKAMITSU MIYAJI ³ SHOJI OGAWA ² RYOSUKE UEMATSU ² ATSUSHI TANIMOTO ⁸ MASATOSHI IMANISHI ^{4,9} AND
 CLAUDIO RICCI ^{10,11}

¹RIKEN Cluster for Pioneering Research, 2-1 Hirosawa, Wako, Saitama 351-0198, Japan

²Department of Astronomy, Kyoto University, Kitashirakawa-Oiwake-cho, Sakyo-ku, Kyoto 606-8502, Japan

³Instituto de Astronomía sede Ensenada, Universidad Nacional Autónoma de México, Km 107, Carret. Tij.-Ens., Ensenada, 22060, BC, México

⁴National Astronomical Observatory of Japan, 2-21-1 Osawa, Mitaka, Tokyo 181-8588, Japan

⁵Department of Physics, Nara Women's University, Kitauoyanishi-machi, Nara, Nara 630-8506, Japan

⁶Academia Sinica Institute of Astronomy and Astrophysics, 11F of Astronomy-Mathematics Building, AS/NTU, No.1, Section 4, Roosevelt Road, Taipei 10617, Taiwan

⁷Research Center for Space and Cosmic Evolution, Ehime University, 2-5 Bunkyo-cho, Matsuyama, Ehime 790-8577, Japan

⁸Graduate School of Science and Engineering, Kagoshima University, Kagoshima 890-0065, Japan

⁹Department of Astronomical Science, Graduate University for Advanced Studies (SOKENDAI), 2-21-1 Osawa, Mitaka, Tokyo 181-8588, Japan

¹⁰Núcleo de Astronomía de la Facultad de Ingeniería, Universidad Diego Portales, Av. Ejército Libertador 441, Santiago, Chile

¹¹Kavli Institute for Astronomy and Astrophysics, Peking University, Beijing 100871, People's Republic of China

(Received October 14, 2022; Revised December 6, 2022; Accepted January 6, 2023)

ABSTRACT

We conduct a hard X-ray to radio multiwavelength spectral energy distribution (SED) decomposition for 57 local luminous and ultraluminous infrared galaxies (U/LIRGs) observed with Nuclear Spectroscopic Telescope Array and/or Swift/Burst Alert Telescope in GOALS (Armus et al. 2009) sample. We modify the latest SED-fitting code X-CIGALE by implementing the infrared (IR) CLUMPY model, allowing the multiwavelength study with the X-ray torus model (XCLUMPY) self-consistently. Adopting the torus parameters obtained by the X-ray fitting (Yamada et al. 2021), we estimate the properties of host galaxies, active galactic nucleus (AGN) tori, and polar dust. The star formation rates (SFRs) become larger with merger stage and most of them are above the main sequence. The SFRs are correlated with radio luminosity, indicating starburst emission is dominant in the radio band. Although polar-dust extinction is much smaller than torus extinction, the UV-to-IR (mainly IR) polar dust luminosities are ~ 2 times larger than the torus ones. The polar-dust temperature decreases while the physical size, estimated by the temperature and dust sublimation radius, increases with AGN luminosity from a few tens of parsec (early mergers) to kiloparsec scales (late mergers), where the polar dust is likely the expanding (i.e., evolving) dusty outflows. The comparison between SFRs and intrinsic AGN luminosities suggests that the starbursts occur first and AGNs arise later, and overall their growth rates follow the simultaneous coevolution relation that can establish the local galaxy–SMBH mass relation. We confirm the coexistence of intense starbursts, AGNs, and large-scale outflows in late mergers, supporting a standard AGN feedback scenario.

Corresponding author: Satoshi Yamada
 satoshi.yamada@riken.jp

Keywords: Infrared galaxies (790); Active galactic nuclei (16); X-ray active galactic nuclei (2035); Optical observation (1169); Infrared photometry (792); Radio continuum emission (1340)

1. INTRODUCTION

Galaxies and supermassive black holes (SMBHs) at their centers show a tight correlation between the masses of bulges (M_{bulge}) and SMBHs (M_{BH}), indicating that they have coevolved by regulating each other's growth (see e.g., Marconi & Hunt 2003; Kormendy & Ho 2013). Due to a huge scale gap between galaxies (~ 1 kpc) and SMBHs ($\ll 1$ pc), the mechanism of their physical connection has been controversial (e.g., Hopkins et al. 2008; Madau & Dickinson 2014). For understanding the mechanism of coevolution, the merging galaxies have received attention since the merger can extract the angular momentum of the gas and trigger obscuration and rapid accretion onto SMBHs (e.g., Koss et al. 2010, 2012, 2018; Kocevski et al. 2015; Lansbury et al. 2017; Ricci et al. 2017a, 2021; Yamada et al. 2018, 2021).

According to the major merger scenario, galaxies in the most active phase of mergers become luminous infrared galaxies (LIRGs; $L_{8-1000\mu\text{m}} \geq 10^{11} L_{\odot}$) and ultraluminous infrared galaxies (ULIRGs; $L_{8-1000\mu\text{m}} \geq 10^{12} L_{\odot}$), combined as U/LIRGs (Sanders & Mirabel 1996). Their large bolometric luminosities are derived from the starbursts and/or active galactic nuclei (AGNs) surrounded by gas and dust, most of which are radiated in the infrared (IR) band. After quenching the star-forming activities, U/LIRGs are thought to transit to unobscured quasars or elliptical galaxies (e.g., Hopkins et al. 2008).

The AGNs in U/LIRGs are well studied in the X-ray to radio multiwavelength bands (e.g., U 2022 for a review). When AGNs are heavily obscured, they radiate dimmed UV-to-near-IR emission compared to the AGN luminosity identified in the mid-IR and X-ray bands (see e.g., Hickox & Alexander 2018). The mid-IR studies reveal that the AGNs in U/LIRGs are deeply buried by a large amount of gas and dust, where even the direction of the lowest dust column-density can be opaque to the ionizing UV photons (e.g., Imanishi et al. 2006, 2008; Lee et al. 2012; Yamada et al. 2019). Hard X-ray observations, which are less affected by the contamination of starburst emission, can identify the AGNs with large hydrogen column densities (N_{H}). For local U/LIRGs observed with Nuclear Spectroscopic Telescope Array (NuSTAR; Harrison et al. 2013), Ricci et al. (2017a, 2021) analyze the broadband X-ray spectra and find the large fraction of Compton-thick (CT; $N_{\text{H}} > 10^{24} \text{ cm}^{-2}$) AGNs in late mergers. By conducting the X-ray spectroscopy with the X-ray clumpy

torus model (XCLUMPY; Tanimoto et al. 2019), Yamada et al. (2021) present the individual torus covering fractions, supporting the buried AGN structure in the late mergers.

Yamada et al. (2021) report that the AGNs in the final phase of mergers show high Eddington ratios (λ_{Edd}) and the signatures of multiphase outflows at subparsec to kiloparsec scales: that is, ultrafast outflows (UFOs), ionized outflows, and molecular outflows. The UFOs are extremely fast ($\sim 0.1\text{--}0.3c$) and highly ionized winds at ~ 0.01 pc (e.g., Tombesi et al. 2015; Mizumoto et al. 2019; Smith et al. 2019). The ionized outflows are the fast ($\sim 1000 \text{ km s}^{-1}$) winds with a size of kiloparsecs detected by optical and near-IR spectroscopy (e.g., Rich et al. 2015; Cortijo-Ferrero et al. 2017; Kakkad et al. 2018; Boettcher et al. 2020; Fluetsch et al. 2021). Molecular outflows are cold gas winds on ~ 400 pc with a velocity of $\sim 500 \text{ km s}^{-1}$ discovered at far-IR and submillimeter wavelengths (e.g., Spoon et al. 2013; Veilleux et al. 2013; Cicone et al. 2014; González-Alfonso et al. 2017; Laha et al. 2018). However, the properties of outflows in many U/LIRGs are still unclear because these methods using the blue-shifted emission/absorption lines have difficulty detecting weak outflows. Therefore, the new methods to systematically reveal the outflow properties are necessary to present the schematic picture of the merger-driven coevolution.

The observations of outflowing dust (e.g., Hönig 2019; Venanzi et al. 2020) may be an ideal means for the systematic studies on the outflows in U/LIRGs. Recent mid-IR observations with high spatial resolutions detect the extended dust emission along the polar direction, called polar dust (e.g., Asmus et al. 2016; Stalevski et al. 2017). An issue at this point is that, due to the poor understanding of the polar dust structure, it is not even clear whether the polar dust is (1) the galactic ISM or dust in a narrow line region (NLR) only being illuminated by the AGN or (2) the “outflowing” dusty winds launched from the inner edge of the torus. Asmus (2019) finds a positive correlation between their physical sizes and the Eddington ratios, supporting that the polar dust structure may be related to the AGN activities. The analytical model of polar dust emission has been implemented into the latest multiwavelength spectral energy distribution (SED) models (e.g., X-CIGALE; Boquien et al. 2019; Yang et al. 2020a). These models help us to estimate the properties of polar dust (e.g., Toba et al.

2021a; Buat et al. 2021), even though the degeneracy of torus and polar dust emission will provide uncertainties.

The combination of X-ray and IR observations will become the best way to constrain the properties of polar dust. The broadband X-ray study with XCLUMPY for several tens of Swift/Burst Alert Telescope (BAT)-selected AGNs by Ogawa et al. (2021) successfully constrains the torus covering fractions (C_T). These estimates are well consistent with the typical $\lambda_{\text{Edd}} - C_T$ relation (Ricci et al. 2017a), while are much smaller than those estimated with the IR CLUMPY model (Nenkova et al. 2008a,b). They indicate that the difference can be explained by the presence of the polar dust, which should have small effects on the obscuration in the X-ray band but re-radiate the large IR luminosities. Thus, the updated CLUMPY model consisting of the clumpy torus and polar dust components will provide rich information on polar dust by applying the torus parameters obtained by the X-ray fitting with XCLUMPY (Yamada et al. 2021).

In this study, we generate the updated CLUMPY model that can reproduce the IR emission from the clumpy torus and polar dust, and perform the multiwavelength (hard X-ray to radio) SED decomposition for the sample of 57 local U/LIRGs in Yamada et al. (2021). We first investigate the features of multiwavelength radiation, which are helpful to understand the environments from the nucleus to galactic scales. This will be incidentally useful for future works to explore buried AGNs in U/LIRGs in the distant universe. Taking into account these results, we examine the polar dust structures and their relation to the AGN activities, and finally discuss the coevolution process of the galaxies, SMBHs, and outflows in the merger phase.

This paper is organized as follows. In Section 2 and Section 3, we show the sample and their photometric data of multiwavelength observations, respectively. Section 4 describes the implementation of the updated CLUMPY model we create and the best-fit parameters of the multiwavelength SED decomposition. Section 5 illustrates the features of multiwavelength emission to understand the characteristics of the host galaxies and AGNs in U/LIRGs. In Section 6, we discuss the structure of the polar dust in U/LIRGs based on the results of the multiwavelength SED analysis. Section 7 provides the discussion on the coevolution process of galaxies, SMBHs, and outflows in U/LIRGs. The main results are summarized in Section 8. In this paper, we adopt the cosmology of a flat universe with $H_0 = 70 \text{ km s}^{-1} \text{ Mpc}^{-1}$, $\Omega_M = 0.3$, and $\Omega_\Lambda = 0.7$. Throughout this paper, the uncertainties are at the 1σ level unless otherwise stated, and the initial mass func-

tion (IMF) of Chabrier (2003) is assumed.¹

2. SAMPLE

The sample selection of 57 local U/LIRGs observed with the hard X-ray observations is described as follows. We focus on the Great Observatories All-sky LIRG Survey (GOALS; Armus et al. 2009), which consists of 180 LIRGs and 22 ULIRGs in the local universe at redshifts $z < 0.088$. They are contained in the IRAS Revised Bright Galaxy Sample (RBGS; Sanders et al. 2003), a complete sample of 629 extragalactic objects having $60 \mu\text{m}$ fluxes above 5.24 Jy at Galactic latitudes $|b| > 5^\circ$. These U/LIRGs have been observed in the multiwavelength bands, by the IR telescopes of Spitzer (e.g., Imanishi et al. 2007; Díaz-Santos et al. 2010; Petric et al. 2011; Inami et al. 2013; Stierwalt et al. 2013), AKARI (e.g., Imanishi et al. 2008; Lee et al. 2012; Inami et al. 2018), Herschel (e.g., Díaz-Santos et al. 2013, 2014; Chu et al. 2017; Lu et al. 2017), and X-ray telescopes of Chandra (e.g., Iwasawa et al. 2011; Torres-Albà et al. 2018), and NuSTAR (Teng et al. 2015; Ricci et al. 2017a, 2021; Privon et al. 2020; Yamada et al. 2021). Here, we select the same targets as in Yamada et al. (2021), the 57 local U/LIRGs containing 84 individual galaxies observed with the hard X-ray telescopes NuSTAR and/or Swift/BAT. According to the detailed X-ray spectral analysis combining the available soft X-ray observations, our targets are comprised of 40 AGNs (two unobscured AGNs, 21 obscured AGNs, 16 CT AGNs, one jet-dominated AGN), and 44 starburst-dominant or hard X-ray-undetected sources.

Here, the source coordinates, redshift, merger stages, and the projected separation between the two nuclei are taken from Table 1 of Yamada et al. (2021). Based on high-spatial-resolution images (e.g., Stierwalt et al. 2013), the merger stages are classified into five stages: stage A (galaxy pairs before a first encounter), stage B (post-first encounter with symmetric galaxy disks but showing signature of tidal tails), stage C (showing some signatures of mergers, such as tidal tails, amorphous disks), stage D (two nuclei within a common envelope), and stage N (no signatures of mergers or massive neighbors). In the same manner as Yamada et al. (2021), we hereafter call stage A–B galaxies as early mergers, stage C–D as late mergers, and stage N as nonmergers.

¹ When the values of the star formation rates (SFR) and stellar masses (M_*) are referred from previous works, we correct these values assuming Salpeter (1955) by decreasing 0.15 and 0.24 dex, or values assuming Kroupa (2001) by subtracting 0.02 and 0.03 dex, respectively (e.g., Santini et al. 2014; Speagle et al. 2014).

Table 1. Basic Information of our Sample

ID	IRAS Name	Object Name	z	M	D_{12}	D_{12}	AGN	Type	$\log(L_{\text{IR}})$	IRS
					(arcsec)	(kpc)			(L_{\odot})	
(1)	(2)	(3)	(4)	(5)	(6)	(7)	(8)	(9)	(10)	(11)
ID01	F00085–1223	NGC 34	0.0196	D	S	S	Y	Obs	11.49	Y
ID02	F00163–1039 ^a	MCG–02-01-052/MCG–02-01-051	0.0272	B
ID03	F00163–1039 N	MCG–02-01-052	0.0273	B	56.1	30.7	n	n	[11.48]	n
ID04	F00163–1039 S	MCG–02-01-051	0.0271	B	56.1	30.7	n	n	11.48	Y
ID05	F00344–3349	ESO 350–38	0.0206	C	5.2	2.2	Y?	n	11.28	Y
ID06	F00402–2349 ^a	NGC 232/NGC 235	0.0224	B
ID07	F00402–2349 W	NGC 232	0.0226	B	120.8	54.7	n	n	[11.44]:	Y
ID08	F00402–2349 E	NGC 235	0.0222	B	120.8	54.7	Y	Obs	[11.44]:	Y
ID09	F00506+7248	MCG+12-02-001	0.0157	C	0.9	0.3	Y	CT	11.50	Y
ID10	F01053–1746 ^b	IC 1623A/IC 1623B	0.0202	C	15.7	6.4	n	n/n	11.71	n/Y
ID11	F02071–1023 ^a	NGC 833/NGC 835	0.0132	A
ID12	F02071–1023 W2	NGC 833	0.0129	A	56.4	15.3	Y	Obs	[11.05]:	Y
ID13	F02071–1023 W	NGC 835	0.0136	A	56.4	15.3	Y	Obs	[11.05]:	Y
ID14	F02071–1023 E	NGC 838	0.0128	A	148.8	39.1	n	n	[11.05]:	Y
ID15	F02071–1023 S	NGC 839	0.0129	A	148.8	39.1	n	n	[11.05]:	Y
ID16	F02401–0013	NGC 1068	0.0038 [†]	N	n	n	Y	CT	11.40	Y
ID17	F03117+4151 ^a	UGC 2608/UGC 2612	0.0276	N
ID18	F03117+4151 N	UGC 2608	0.0233	N	n	n	Y	CT	11.41	Y
ID19	F03117+4151 S	UGC 2612	0.0318	N	n	n	n	n	[11.41]	Y
ID20	F03164+4119	NGC 1275	0.0176	N	n	n	Y	Jet	11.26	Y
ID21	F03316–3618	NGC 1365	0.0055 [†]	N	n	n	Y	Obs	11.00	Y
ID22	F04454–4838	ESO 203–1	0.0529	B	7.5	7.7	n	n	11.86	Y
ID23	F05054+1718 ^a	CGCG 468-002W/CGCG 468-002E	0.0171	B
ID24	F05054+1718 W	CGCG 468-002W	0.0175	B	29.5	10.3	Y	Obs	[11.22]:	Y
ID25	F05054+1718 E	CGCG 468-002E	0.0168	B	29.5	10.3	n	n	[11.22]:	Y
ID26	F05189–2524	IRAS F05189–2524	0.0426	D	S	S	Y	Obs	12.16	Y
ID27	F06076–2139 ^b	IRAS F06076–2139/2MASS 06094601–2140312	0.0374	C	8.3	6.2	Y	Obs/n	11.65	Y/n
ID28	F08354+2555	NGC 2623	0.0185	D	S	S	Y	Obs	11.60	Y
ID29	F08520–6850 ^b	ESO 060–IG016 West/East	0.0451	B	15.4	13.6	Y	n/Obs	11.82	n/Y
ID30	F08572+3915	IRAS F08572+3915	0.0580	D	4.4	5.6	Y	Obs	12.16	Y
ID31	F09320+6134	UGC 5101	0.0394	D	S	S	Y	Obs	12.01	Y
ID32	F09333+4841 ^a	MCG+08-18-012/MCG+08-18-013	0.0255	A
ID33	F09333+4841 W	MCG+08-18-012	0.0252	A	65.3	33.6	n	n	[11.34]	n
ID34	F09333+4841 E	MCG+08-18-013	0.0259	A	65.3	33.6	n	n	11.34	Y
ID35	F10015–0614 ^a	MCG–01-26-013/NGC 3110	0.0165	A
ID36	F10015–0614 S	MCG–01-26-013	0.0161	A	108.8	36.5	n	n	[11.37]	n
ID37	F10015–0614 N	NGC 3110	0.0169	A	108.8	36.5	n	n	11.37	Y
ID38	F10038–3338	ESO 374–IG032	0.0340	D	S	S	Y?	n	11.78	Y
ID39	F10257–4339	NGC 3256	0.0094	D	5.1	1.0	n	n	11.64	Y
ID40	F10565+2448	IRAS F10565+2448	0.0431	D	7.4	6.7	n	n	12.08	Y

Table 1 *continued*

Table 1 (*continued*)

ID	IRAS Name	Object Name	z	M	D_{12}	D_{12}	AGN	Type	$\log(L_{\text{IR}})$	IRS
					(arcsec)	(kpc)			(L_{\odot})	
(1)	(2)	(3)	(4)	(5)	(6)	(7)	(8)	(9)	(10)	(11)
ID41	F11257+5850 ^b	NGC 3690 West/East	0.0103	C	22.0	4.6	Y	CT/n	11.93	Y/Y
ID42	F12043–3140 ^b	ESO 440–58/MCG–05-29-017	0.0230	B	11.8	5.5	n	n/n	11.43	Y/Y
ID43	F12112+0305	IRAS F12112+0305	0.0733	D	3.0	4.1	n	n	12.36	Y
ID44	F12243–0036 ^a	NGC 4418/MCG+00-32-013	0.00735	A
ID45	F12243–0036 NW	NGC 4418	0.0073 [†]	A	179.9	29.4	Y?	n	11.19	Y
ID46	F12243–0036 SE	MCG+00-32-013	0.0074 [†]	A	179.9	29.4	n	n	[11.19]	n
ID47	F12540+5708	Mrk 231	0.0422	D	S	S	Y	Obs	12.57	Y
ID48	F12590+2934 ^b	NGC 4922S/NGC 4922N	0.0238	C	22.1	10.6	Y	n/Obs	11.38	n/Y
ID49	F13126+2453	IC 860	0.0112	N	n	n	n	n	11.14	Y
ID50	13120–5453	IRAS 13120–5453	0.0308	D	S	S	Y	CT	12.32	Y
ID51	F13188+0036	NGC 5104	0.0186	N	n	n	n	n	11.27	Y
ID52	F13197–1627	MCG–03-34-064	0.0165	N	n	n	Y	Obs	11.28	Y
ID53	F13229–2934	NGC 5135	0.0137	N	n	n	Y	CT	11.30	Y
ID54	F13362+4831 ^b	Mrk 266B/Mrk 266A	0.0278	B	10.1	5.6	Y	CT/Obs	11.56	Y/Y
ID55	F13428+5608	Mrk 273	0.0378	D	0.9	0.7	Y	Obs	12.21	Y
ID56	F14348–1447	IRAS F14348–1447	0.0827	D	3.4	5.2	Y	CT	12.39	Y
ID57	F14378–3651	IRAS F14378–3651	0.0681	D	S	S	n	Y	12.23	Y
ID58	F14544–4255 ^b	IC 4518A/IC 4518B	0.0159	B	35.5	11.5	Y	Obs/n	11.23	Y/n
ID59	F15250+3608	IRAS F15250+3608	0.0552	D	0.7	0.8	n	n	12.08	Y
ID60	F15327+2340 ^b	Arp 220W/Arp 220E	0.0181	D	1.0	0.4	Y	CT/n	12.28	Y(u)
ID61	F16504+0228 ^b	NGC 6240S/NGC 6240N	0.0245	D	1.7	0.8	Y	CT	11.93	Y(u)
ID62	F16504+0228 ^a	NGC 6285/NGC 6286	0.0186	B
ID63	F16577+5900 N	NGC 6285	0.0190	B	91.0	34.5	n	n	[11.37]	Y
ID64	F16577+5900 S	NGC 6286	0.0183	B	91.0	34.5	Y	CT	11.37	Y
ID65	F17138–1017	IRAS F17138–1017	0.0173	D	S	S	Y	Obs	11.49	Y
ID66	F18293–3413	IRAS F18293–3413	0.0182	N	S	S	n	n	11.88	Y
ID67	F19297–0406	IRAS F19297–0406	0.0857	D	S	S	n	n	12.45	Y
ID68	F20221–2458 ^b	NGC 6907/NGC 6908	0.0104	B	43.9	9.4	n	n/n	11.11	Y/n
ID69	20264+2533 ^a	NGC 6921/MCG+04-48-002	0.0142	A
ID70	20264+2533 W	NGC 6921	0.0145	A	91.4	26.5	Y	CT	[11.11]	n
ID71	20264+2533 E	MCG+04-48-002	0.0139	A	91.4	26.5	Y	Obs	11.11	Y
ID72	F20550+1655 ^b	II Zw 096/IRAS F20550+1655 SE	0.0353	C	11.6	8.1	n	n/n	11.94	Y/Y
ID73	F20551–4250	ESO 286–19	0.0430	D	S	S	n	n	12.06	Y
ID74	F21453–3511	NGC 7130	0.0162	N	n	n	Y	CT	11.42	Y
ID75	F23007+0836 ^a	NGC 7469/IC 5283	0.0162	A
ID76	F23007+0836 S	NGC 7469	0.0163	A	79.7	26.2	Y	Unobs	11.65	Y
ID77	F23007+0836 N	IC 5283	0.0160	A	79.7	26.2	n	n	[11.65]	n
ID78	F23128–5919	ESO 148–2	0.0446	C	4.5	3.9	Y	CT	12.06	Y
ID79	F23157+0618	NGC 7591	0.0165	N	n	n	n	n	11.12	Y
ID80	F23254+0830 ^a	NGC 7674/MCG+01-59-081	0.0292	A

Table 1 *continued*

Table 1 (*continued*)

ID	IRAS Name	Object Name	<i>z</i>	<i>M</i>	<i>D</i> ₁₂ (arcsec)	<i>D</i> ₁₂ (kpc)	AGN	Type	log(<i>L</i> _{IR}) (<i>L</i> _⊙)	IRS
(1)	(2)	(3)	(4)	(5)	(6)	(7)	(8)	(9)	(10)	(11)
ID81	F23254+0830 W	NGC 7674	0.0289	A	33.3	19.5	Y	Obs	11.56	Y
ID82	F23254+0830 E	MCG+01-59-081	0.0295	A	33.3	19.5	n	n	[11.56]	n
ID83	23262+0314 ^a	NGC 7679/NGC 7682	0.0171	A
ID84	23262+0314 W	NGC 7679	0.0171	A	269.8	93.8	Y	Unobs	11.11	Y
ID85	23262+0314 E	NGC 7682	0.0171	A	269.8	93.8	Y	Obs	[11.11]	n

NOTE—Columns: (1) Target ID; (2) IRAS name. “a” marks 13 total systems of resolved pairs to our targets. “b” marks 12 U/LIRGs (24 individual galaxies) that are too close to be separated by the Hershel PACS 70 μm images or UV-to-near-IR images; (3) object name; (4) redshift from NASA/IPAC Extragalactic Database (NED); (5) merger stage based on the high-spatial-resolution images (e.g., [Stierwalt et al. 2013](#)); (6–7) projected separation between the two nuclei in arcseconds and kiloparsecs. S and n mean that a single nucleus is observed in merging and nonmerging U/LIRGs, respectively; (8) Y and n mark the presence of a hard X-ray-detected AGN or not, respectively. Y? marks AGN candidates among the hard X-ray-undetected sources identified by the multiwavelength SED analysis (see Section 4.2.4); (9) X-ray classification (Unobs = unobscured AGN, Obs = obscured AGN, CT = CT AGN, Jet = jet-dominant AGN, and n = hard X-ray-undetected sources); (10) logarithmic total IR luminosity in units of L_\odot ([Armus et al. 2009](#)). Values in brackets should be upper limits due to contamination from nearby much brighter (or equally bright with the suffix “:”) IR sources; (11) Y and n mark detection and nondetection with Spitzer/IRS in the 10–20 μm (SH) or 19–38 μm (LH) band, respectively ([Alonso-Herrero et al. 2012](#); [Mazzarella et al. 2012](#); [Inami et al. 2013](#)). The (u) means that the two nuclei are not divided. All information in Column (2–11) are referred from [Yamada et al. \(2021\)](#).

[†]Throughout the paper, redshift-independent measurements of the luminosity distance are utilized for the multiwavelength results (e.g., luminosities) of the closest objects at $z < 0.01$, NGC 1068 (14.4 Mpc; [Tully 1988](#); [Bauer et al. 2015](#)), NGC 1365 (17.3 Mpc; [Venturi et al. 2018](#)), and NGC 4418/MCG+00-32-013 (34 Mpc; e.g., [Ohyama et al. 2019](#)).

(This table is available in its entirety in machine-readable form.)

Some of the pair galaxies are too close to be separated by the other wavelength bands. Particularly, the spatial distributions of far-IR emissions within the GOALS sources are poorly determined because of the limitations in the angular resolution of pre-Herschel data (IRAS, ISO, and AKARI). [Chu et al. \(2017\)](#) provided the total system fluxes and component fluxes (where possible) in all Herschel bands for the GOALS sample. The beam profiles have a mean FWHM value of 5''.6 for the Photodetector Array Camera and Spectrometer (PACS; [Pilbratt et al. 2010](#)) 70 μm band, the shortest wavelength band of Herschel data. After the cross-matching with multiwavelength catalogs (Section 3), we treat each interacting pair as a total system for 11 U/LIRGs (22 individual galaxies) that are too close (with a projected separation of $\lesssim 20''$) to be resolved by the Hershel PACS images, whose flux densities of individual galaxies are summed in all wavelength bands. Since we do not obtain any fluxes for IC 4518B but for a total system in the UV-to-near-IR bands, the other wavelength photometries are also combined as total fluxes of IC 4518A and IC 4518B (35''.5). Here, the 12 pairs are unresolved among 84 galaxies, and thus our sample has 72 individual sources in 57 local U/LIRGs.

Finally, to investigate the difference between the results of multiwavelength SED analysis by using the combined photometry of a total system and separated photometries of the individual galaxies, we duplicate add the 13 total systems of resolved pairs (with a projected separation of $\gtrsim 30''$) to our targets (see Section 4.4). Therefore, our sample host 85 sources consisting of 72 individual sources and 13 systems of resolved pairs.

3. MULTIWAVELENGTH OBSERVATIONS

For the 57 U/LIRGs (containing 84 individual sources in [Yamada et al. 2021](#)), we compiled the multiwavelength data from hard X-ray to radio bands. As noted in Section 2, the system fluxes of the close interacting pairs are calculated by adding the component fluxes. We note that neither the upper limits nor low-significant ($< 5\sigma$) values were utilized unless otherwise stated. While considering the spatial resolutions of individual instruments, we took care to utilize the multiwavelength photometries whose apertures sufficiently cover the fluxes derived from the extended emission of each target. In the following sections, we describe the multiwavelength data for each telescope. The characteristics of the multiwavelength surveys are summarized in Table 2.

Table 2. Characteristics of the Multiwavelength Catalogs Utilized in This Work

Class	Instrument	Band	Wavelength	ΔR (FWHM)	Area Coverage	Ref.
(1)	(2)	(3)	(4)	(5)	(6)	(7)
Hard X-ray	Swift/BAT	14–195 keV	0.0064–0.0886 nm	1170''	All sky	1,2,3
	NuSTAR	3–79 keV	0.016–0.413 nm	18''	Targeted obs.	3,4
	Suzaku/HXD-PIN	10–70 keV	0.018–0.124 nm	...	Targeted obs.	3,5
Soft X-ray	XMM-Newton	0.1–15 keV	0.083–12.40 nm	~6''	Targeted obs.	3,6
	Chandra	0.2–10 keV	0.12–6.20 nm	~0.5''	Targeted obs.	3,7
	Suzaku/XIS	0.2–12 keV	0.10–6.20 nm	96''–120''	Targeted obs.	3,5
	Swift/XRT	0.3–10 keV	0.12–4.13 nm	8.''8	Targeted obs.	1,3
UV	GALEX	FUV	152.8 (134.4–178.6) nm	4.''2	24,790 deg ²	8,9
	GALEX	NUV	231.0 (177.1–283.1) nm	5.''2	24,790 deg ²	8,9
Optical	Pan-STARRS	<i>g</i>	481.1 (394.3–559.3) nm	1.''47	$\delta \geq -30^\circ$ (3π)	10,11
	Pan-STARRS	<i>r</i>	615.6 (538.6–703.6) nm	1.''31	$\delta \geq -30^\circ$ (3π)	10,11
	Pan-STARRS	<i>i</i>	750.4 (677.8–830.4) nm	1.''19	$\delta \geq -30^\circ$ (3π)	10,11
	Pan-STARRS	<i>z</i>	866.9 (802.8–934.6) nm	1.''14	$\delta \geq -30^\circ$ (3π)	10,11
	Pan-STARRS	<i>y</i>	961.3 (910.1–1083.9) nm	1.''09	$\delta \geq -30^\circ$ (3π)	10,11
	SkyMapper	<i>u</i>	350.0 (306.7–386.7) nm	3.''1	$\delta \lesssim 0^\circ$ (2π)	10,12,13
	SkyMapper	<i>v</i>	387.9 (355.0–421.7) nm	2.''9	$\delta \lesssim 0^\circ$ (2π)	10,12,13
	SkyMapper	<i>g</i>	501.6 (410.3–657.0) nm	2.''6	$\delta \lesssim 0^\circ$ (2π)	10,12,13
	SkyMapper	<i>r</i>	607.7 (492.5–723.2) nm	2.''4	$\delta \lesssim 0^\circ$ (2π)	10,12,13
	SkyMapper	<i>i</i>	773.3 (692.9–864.7) nm	2.''3	$\delta \lesssim 0^\circ$ (2π)	10,12,13
	SkyMapper	<i>z</i>	912.0 (815.9–1067.9) nm	2.''3	$\delta \lesssim 0^\circ$ (2π)	10,12,13
	SDSS	<i>u</i>	355.1 nm	1.''53	14,555 deg ²	14,15
	SDSS	<i>g</i>	468.6 nm	1.''44	14,555 deg ²	14,15
	SDSS	<i>r</i>	616.5 nm	1.''32	14,555 deg ²	14,15
	SDSS	<i>i</i>	748.1 nm	1.''26	14,555 deg ²	14,15
	SDSS	<i>z</i>	893.1 nm	1.''29	14,555 deg ²	14,15
Near-IR	2MASS	<i>J</i>	1.235 (1.081–1.407) μ m	~2.''5	All sky	10,16,17
	2MASS	<i>H</i>	1.662 (1.479–1.823) μ m	~2.''5	All sky	10,16,17
	2MASS	<i>K_s</i>	2.159 (1.954–2.355) μ m	~2.''5	All sky	10,16,17
Mid-IR	WISE	W1	3.353 (2.754–3.872) μ m	6.''1	All sky	10,18
	WISE	W2	4.603 (3.963–5.341) μ m	6.''4	All sky	10,18
	WISE	W3	11.56 (7.443–17.261) μ m	6.''5	All sky	10,18
	WISE	W4	22.09 (19.52–27.91) μ m	12.''0	All sky	10,18
	AKARI	S9W	8.228 (5.846–12.188) μ m	5.''5	All sky	10,19,20
	AKARI	L18W	17.61 (13.61–28.67) μ m	5.''7	All sky	10,19,20
Far-IR	Herschel	PACS blue	70 μ m (60–85) μ m	5.''6	Targeted obs. [†]	21,22
	Herschel	PACS green	100 μ m (85–130) μ m	6.''8	Targeted obs. [†]	21,22
	Herschel	PACS red	160 μ m (130–210) μ m	11.''3	Targeted obs. [†]	21,22
	Herschel	PSW	250 μ m	18.''1	Targeted obs. [†]	21,23
	Herschel	PMW	350 μ m	25.''2	Targeted obs. [†]	21,23
	Herschel	PLW	500 μ m	36.''6	Targeted obs. [†]	21,23
Radio	VLA (VLASS)	3.0 GHz	99.9 mm	2.5''	$\delta \geq -40^\circ$ (3.3π)	24
	VLA (NVSS)	1.4 GHz	214.1 mm	45''	$\delta \geq -40^\circ$ (3.3π)	25
	VLA (FIRST)	1.4 GHz	214.1 mm	5''	10,575 deg ²	26
	VLA (WENSS)	325.125 MHz	922.1 mm	54''	$\delta \geq +30^\circ$ (π)	27
	VLA (VLSSr)	73.8 MHz	4.06 m	75''	$\delta \geq -40^\circ$ (3.3π)	28
	MOST (SUMSS)	843 MHz	355.6 mm	45''	$\delta \leq -30^\circ$ (π)	29,30
	MWA (GLEAM)	170–231 MHz	1.50 (1.30–1.76) m	120''	$\delta \leq +30^\circ$ (3π)	31,32
	MWA (GLEAM)	147–154 MHz	1.99 (1.95–2.04) m	120''	$\delta \leq +30^\circ$ (3π)	31,32
	MWA (GLEAM)	72–80 MHz	3.94 (3.75–4.16) m	120''	$\delta \leq +30^\circ$ (3π)	31,32
	GMRT (TGSS)	147.5 (140–156) MHz	2.03 (1.92–2.14) m	25''	$\delta \geq -53^\circ$ (3.6π)	33

NOTE—Comments: (1) wavelength class; (2–3) instrument and its wavelength band; (4) wavelength range for the X-ray bands, effective wavelength for the UV-to-far-IR bands, and the typical wavelength for the radio bands. Bandwidth is denoted in parentheses; (5) angular resolution; (6) area coverage of each survey; (7) References of column (3)–(6).

References: (1) Gehrels et al. (2004); (2) Oh et al. (2018); (3) Yamada et al. (2021) and the references therein; (4) Harrison et al. (2013); (5) Mitsuda et al. (2007); (6) Jansen et al. (2001); (7) Garmire et al. (2003); (8) Bianchi et al. (2017); (9) Morrissey et al. (2007); (10) Spanish Virtual Observatory (SVO) Filter Profile Service (<http://svo2.cab.inta-csic.es/theory/fps/>); (11) Chambers et al. (2016); (12) Wolf et al. (2018); (13) Onken et al. (2019); (14) Albareti et al. (2017); (15) Ahumada et al. (2020) and the information (scope and image quality) on the DR16 website (<https://www.sdss.org/dr16/>); (16) Cohen et al. (2003); (17) Skrutskie et al. (2006); (18) Wright et al. (2010); (19) Murakami et al. (2007); (20) Ishihara et al. (2010); (21) Chu et al. (2017); (22) Poglitsch et al. (2010); (23) Griffin et al. (2010); (24) Gordon et al. (2021); (25) Condon et al. (1998); (26) Helfand et al. (2015); (27) Rengelink et al. (1997); (28) Lane et al. (2014); (29) Mauch et al. (2003); (30) Mauch et al. (2008); (31) Hurley-Walker et al. (2017); (32) Hurley-Walker et al. (2019); (33) Intema et al. (2017).

[†] All of U/LIRGs in GOALS sample are mapped by the Herschel with both the PACS and SPIRE (see Chu et al. 2017).

3.1. X-ray Spectra

Among 57 U/LIRGs, Yamada et al. (2021) carried out the broadband X-ray spectral analysis for 49 U/LIRG systems by using all of the available NuSTAR, Chandra (Garmire et al. 2003), XMM-Newton (Jansen et al. 2001), and Suzaku (Mitsuda et al. 2007) data observed by 2020 April. They also performed the analysis of Swift/X-Ray Telescope (XRT; Burrows et al. 2005) data when no other soft X-ray data were obtained, and utilized the Swift/BAT spectra in the 105-month catalog (Oh et al. 2018) if detected. Considering that X-ray spectral works support the clumpy nature of AGN tori (see e.g., Liu & Li 2014; Furui et al. 2016; Tanimoto et al. 2018, 2019; Buchner et al. 2019), these best-fitting models were provided with a Monte Carlo-based model from a clumpy torus (XCLUMPY; Tanimoto et al. 2019), which enables us to constrain the torus covering fractions for individual AGNs (e.g., Ogawa et al. 2019, 2021; Tanimoto et al. 2020, 2022; Yamada et al. 2020, 2021; Uematsu et al. 2021; Inaba et al. 2022). The broadband X-ray spectral analysis for three other sources UGC 2608, NGC 5135, and NGC 7469 was also conducted with XCLUMPY (Yamada et al. 2020; Ogawa et al. 2021). Therefore, we compiled these X-ray results of 52 U/LIRG systems with XCLUMPY to compare the results from the multiwavelength SED decomposition with an updated CLUMPY model (Section 4.1).

For the other five U/LIRGs, Yamada et al. (2021) only analyzed the NuSTAR data because their spectra show complex features. Instead of the XCLUMPY model, we analyzed their NuSTAR spectra ($\sim 3\text{--}70$ keV) by adopting the best-fitting models in previous works for three nonmerging LIRGs NGC 1068 (M2d in Bauer et al. 2015), NGC 1275 (Model2 in Rani et al. 2018), NGC 1365 (final model for Observation 4 in Rivers et al. 2015), and two dual-AGN systems Mrk 266B/Mrk 266A (SW-R model in Iwasawa et al. 2020)² and NGC 6240S/NGC 6240N (sum of two AGN models with MYtorus in Puccetti et al. 2016), respectively.

The best-fitting spectral models were applied in the multiwavelength SEDs. By following the same manner as Yamada et al. (2021), we calculated the 5σ upper limits in the 8–24 keV band from the NuSTAR

counts for the hard X-ray–undetected sources, by using the HEASARC tool WebPIMMS v4.11a assuming a power law of $\Gamma = 1.8$ (e.g., Ueda et al. 2014; Ricci et al. 2017b) with Galactic absorption, whose hydrogen column density was fixed at the value of Willingale et al. (2013). The 2–7 keV upper limits were provided from the XMM-Newton/MOS (MOS1 and MOS2) for IC 5283 and MCG+01-59-081, since their NuSTAR 8–24 keV fluxes were smaller than those of the interacting companion that causes the high contamination.

3.2. UV Photometry

The far-UV (FUV; $\lambda_{\text{eff}} \sim 152.8$ nm) and near-UV (NUV; $\lambda_{\text{eff}} \sim 231.0$ nm) photometries were compiled from the latest version of the Galaxy Evolution Explore (GALEX; Martin et al. 2005; Bianchi et al. 2011) satellite catalog (GR6plus7 data release; Bianchi et al. 2017).³ The GALEX observation area covers almost all of the sky ($\gtrsim 90\%$). Cross-matching the optical positions of the individual nuclei and the UV peak positions, we extracted the GALEX photometries (FUV_mag and NUV_mag). To ensure reliable data, we finally selected the data with Fexf = 0 and Nexf = 0, where the Fexf and Nexf represent the extended flags for FUV and NUV bands, respectively.

3.3. Optical Photometry

The optical photometries were taken from the large catalogs with three ground-base telescopes, Pan-STARRS1 (PS1) DR2 (e.g., Chambers et al. 2016; Flewelling et al. 2020; Magnier et al. 2020a,b,c; Waters et al. 2020), SkyMapper Southern Survey DR1 and DR2 (Wolf et al. 2018; Onken et al. 2019), and SDSS DR16 (Ahumada et al. 2020). The current coverage areas are $\sim 3/4$ sky (north of $\delta = -30^\circ$) for Pan-STARRS, $\sim 1/2$ sky (south of $\delta = 0^\circ$) for SkyMapper, and $\sim 1/3$ sky (a large part of the northern area) for SDSS. We preferentially used the Pan-STARRS mean object magnitudes in g , r , i , z , and y bands. Since most of our targets are extended sources, we calculated the flux densities from their Kron magnitudes (Kron 1980), which were corrected for the missing fluxes (about 10%)⁴ by multiplying 100/90 (or -0.115 mag). When the Pan-STARRS data were not available, we applied the SkyMapper data in u , v , g , r , i , and z bands. Since the Petrosian magnitudes for extended sources were given in the SkyMapper catalog, we adopted them and corrected for the missing

² The torus reflection component reproduced by the SW-R model (Ikeda et al. 2009) is defined only in the 1–100 keV band. Assuming the power-law model with the same slope as in the 80–100 keV band, we approximately expanded the X-ray model to the 100–200 keV spectra in Figures E1 and E7.

³ The GALEX observations utilized in this paper can be accessed via 10.17909/t9-pyxy-kg53.

⁴ <https://outerspace.stsci.edu/display/PANSTARRS/PS1+Kron+photometry+of+extended+sources>

fluxes by -0.130 mag (Graham et al. 2005) assuming the typical Sersic index to be 3 (e.g., Haan et al. 2011). We finally chose the SDSS photometry (cmodelMag) in u , g , r , i , and z bands for the other sources, and for NGC 4418/MCG+00-32-013 and Mrk 266B/Mrk 266A because the Pan-STARRS photometries of these two systems were >0.4 mag fainter than those of SDSS values.

We extracted the optical photometry from these catalogs in each of three bins, $u-v$, $g-z$, and y bands. The averaged differences of the optical magnitudes, ΔMag (SkyMapper – Pan-STARRS) = 0.07, 0.11, -0.12 , -0.16 , and ΔMag (SDSS – Pan-STARRS) = 0.14, 0.11, 0.02, -0.19 for g , r , i , and z bands, respectively. Here, we systematically added the 10% uncertainties (~ 0.115 mag) for the whole optical flux densities as a systematic error derived from the different measurements. We excluded five pieces of the optical photometry for NGC 232 (SkyMapper v -band), ESO 374-IG032 (SkyMapper v -band), IRAS F12112+0305 (Pan-STARRS y -band), and NGC 6907/NGC 6908 (SkyMapper $u-v$ bands) because their flux densities were much smaller than those in other optical bands by a factor of 3–10.

3.4. Near-IR Photometry

In the near-IR bands, we utilized the data of the Two Micron All Sky Survey (2MASS; Skrutskie et al. 2006).⁵ The effective wavelengths of 2MASS filters are $1.235\ \mu\text{m}$, $1.662\ \mu\text{m}$, and $2.159\ \mu\text{m}$ for J , H , and K_s bands, respectively (Turner 2011). The data of our targets were taken from the extended catalog. Since the values were not presented only for IRAS F17138–1017, we took its values from the point source catalog. Finally, we extracted the data with `cc_flg = “000”` to avoid the effects of artifacts.

3.5. Mid-IR Photometry

The mid-IR data were compiled from the Wide-field IR Survey Explorer (WISE; Wright et al. 2010) and AKARI (Murakami et al. 2007).⁶ We employed the photometry in W1 ($3.4\ \mu\text{m}$), W2 ($4.6\ \mu\text{m}$), W3 ($12\ \mu\text{m}$), and W4 ($22\ \mu\text{m}$) bands from the ALLWISE catalog (Cutri et al. 2021), or ALLSKY catalog (Cutri & et al. 2012) if not obtained. We primarily utilized the “gmag” (elliptical aperture magnitude), or secondarily “mpro” (instrumental profile-fit photometry magnitude), with `w1-4sat=0` and `w1-4cc_map=0`. The AKARI fluxes in

S9W ($9\ \mu\text{m}$) and L18W ($18\ \mu\text{m}$) bands were obtained from AKARI/IRC mid-IR all-sky Survey (Ishihara et al. 2010), where we selected the data with `q_S09=0` & `X09=0` for S9W, and `q_S18=0` & `X18=0` for L18W, respectively.

3.6. Far-IR Photometry

We applied the far-IR fluxes presented by Chu et al. (2017), using the Herschel Space Observatory (Pilbratt et al. 2010) Photodetector Array Camera and Spectrometer (PACS; Poglitsch et al. 2010) and the Spectral and Photometric Imaging Receiver (SPIRE; Griffin et al. 2010). For all the PACS bands ($70\ \mu\text{m}$, $100\ \mu\text{m}$, $160\ \mu\text{m}$) and SPIRE bands ($250\ \mu\text{m}$, $350\ \mu\text{m}$, $500\ \mu\text{m}$), they computed the total system fluxes and component fluxes of individual galaxies (where possible) for the entire GOALS sample. The aperture radius was set by the band with the largest beam size for each instrument: usually the $160\ \mu\text{m}$ band for PACS, and the $500\ \mu\text{m}$ band for SPIRE.

3.7. Radio Photometry

Radio surveys with large sky coverages have been performed over a wide frequency range (see e.g., Shimwell et al. 2019; Stein et al. 2021). In our study, we utilized eight kinds of wide-area radio catalogs, which have been conducted with four main telescopes: Karl G. Jansky Very Large Array (VLA), Molonglo Observatory Synthesis Telescope (MOST; Mills 1981; Robertson 1991), Murchison Widefield Array (MWA; Lonsdale et al. 2009; Tingay et al. 2013), and Giant Metrewave Radio Telescope (GMRT; Swarup 1991). The catalogs are described below:

The catalogs of the VLA observations:

- (1) The Very Large Array Sky Survey (VLASS; Gordon et al. 2021), observing the entire sky north of $\delta = -40^\circ$ (82% sky region) at 3 GHz.
- (2) The NRAO VLA Sky Survey (NVSS; Condon et al. 1998) covering the sky north of $\delta = -40^\circ$ at 1.4 GHz.
- (3) The Faint Images of the Radio Sky at Twenty-centimeters (FIRST; Helfand et al. 2015), observing in $10,575\ \text{deg}^2$ of sky coverage ($8,444\ \text{deg}^2$ in the north Galactic cap and $2,131\ \text{deg}^2$ in the southern cap) at 1.4 GHz.
- (4) The Westerbork Northern Sky Survey (WENSS; Rengelink et al. 1997), a low-frequency radio survey that will cover the whole sky north of $\delta = +30^\circ$ at $325.125\ \text{MHz}$.

⁵ The Digital Object Identifier (DOI) of the 2MASS catalog is [10.26131/IRSA2](https://doi.org/10.26131/IRSA2).

⁶ The DOIs of the WISE and AKARI catalogs are [10.26131/IRSA1](https://doi.org/10.26131/IRSA1) and [10.26131/IRSA181](https://doi.org/10.26131/IRSA181), respectively.

- (5) The VLA Low-frequency Sky Survey Redux (VLSSr; Cohen et al. 2007; Lane et al. 2014), covering the sky north of $\delta = -40^\circ$ at 73.8 MHz.

The catalogs of the other radio observations:

- (6) The Sydney University Molonglo Sky Survey (SUMSS) catalog, Version 2.1r (updated in 2012; Mauch et al. 2003, 2008) with MOST, covering the sky south of $\delta = -30^\circ$ at 843 MHz. The data of IRAS F13120–5453 are not listed in the original catalog but are obtained from Allison et al. (2014).
- (7) The GaLactic and Extragalactic All-sky MWA (GLEAM; Hurley-Walker et al. 2017) survey, covering 24,831 deg² over sky south of $\delta = +30^\circ$ and Galactic latitudes outside 10° of the Galactic plane, excluding some areas such as the Magellanic Clouds, across 72–231 MHz. Hurley-Walker et al. (2019) also presented the GLEAM catalog of the Galactic plane (2,860 deg²); in which only the system of MCG+04-48-002 and NGC 6921 was contained, but their fluxes were not utilized because both galaxies are not divided by the MWA. To get similar data from VLA catalogs for northern-sky targets, we picked out the fluxes in the 170–231 MHz, 147–154 MHz, and 72–80 MHz bands.
- (8) The TIFR GMRT Sky Survey (TGSS; Intema et al. 2017), observing 36,900 deg² of the sky north of $\delta = -53^\circ$ ($\sim 90\%$ sky), at 147.5 MHz (with a bandwidth of 140–156 MHz).

We basically utilized the integrated fluxes referred from these radio catalogs. Although only the peaked fluxes were presented in the VLSSr catalog, they should be the same as integrated fluxes for unresolved point sources because of the large beam size (75''; see Table 2). To avoid flux underestimates due to the resolved-out extended emission, we basically employed the radio catalogs excluding the two catalogs observed with the high-spatial-resolution instruments: VLASS (2'') and FIRST (5'').⁷ For the faint sources that any data are not obtained, we adopted the 5σ upper limits from the TGSS catalog (<24.5 mJy at 150 MHz). Additionally, we used the fluxes of these faint sources from the VLASS (3.0 GHz) and FIRST (1.4 GHz) catalogs if detected at the $\gtrsim 5\sigma$ level⁸, or the 5σ upper limits (<0.44 and <1.00 mJy, respectively).

⁷ Since the uncertainties of FIRST flux densities were not provided, we assume them as 10% uncertainties.

⁸ We utilized the VLASS fluxes for the low-significance radio sources, NGC 833 (3.3 σ) and MCG+01-59-081 (4.4 σ).

3.8. Correction for Galactic Extinction

The magnitudes in the FUV, NUV, $u-y$, J , H , K_s , W1 and W2 bands were corrected for the Galactic extinction by following Schlegel et al. (1998), hereafter SFD. We adopted the correction factors, R_λ ($= A_\lambda / E(B-V)$ SFD), where A_λ is the extinction at the λ band in units of magnitude, calculated by $A_\lambda = 1.086\tau_\lambda$ from Bianchi et al. (2017) for GALEX, Schlafly & Finkbeiner (2011) for Pan-STARRS, Wolf et al. (2018) for SkyMapper, and Yuan et al. (2013) for the other telescopes:

- GALEX:

$$[R_{\text{FUV}}, R_{\text{NUV}}] = [8.06, 7.95]$$

- Pan-STARRS:

$$\begin{aligned} [R_g, R_r, R_i, R_z, R_y] \\ = [3.172, 2.271, 1.682, 1.322, 1.087] \end{aligned}$$

- SkyMapper:

$$\begin{aligned} [R_u, R_v, R_g, R_r, R_i, R_z] \\ = [4.294, 4.026, 2.986, 2.288, 1.588, 1.206] \end{aligned}$$

- SDSS:

$$\begin{aligned} [R_u, R_g, R_r, R_i, R_z] \\ = [4.39, 3.30, 2.31, 1.71, 1.29] \end{aligned}$$

- 2MASS:

$$[R_J, R_H, R_Ks] = [0.72, 0.46, 0.306]$$

- WISE:

$$[R_{\text{W1}}, R_{\text{W2}}] = [0.18, 0.16]$$

The magnitudes of $E(B-V)$ reddening and the flux densities of the UV-to-radio photometries corrected for the Galactic extinction in our sample are summarized in Table E1 ($\lambda < 1 \mu\text{m}$), Table E2 ($\lambda = 1\text{--}200 \mu\text{m}$), and Table E3 ($\lambda > 200 \mu\text{m}$).

4. MULTIWAVELENGTH SED MODEL AND BEST-FIT PARAMETERS

To best constrain the properties of polar dust, we update the latest multiwavelength SED-fitting code X-CIGALE (Yang et al. 2020a) by implementing the IR CLUMPY model (Section 4.1), whose geometry is the same as in XCLUMPY. The UV-to-IR SEDs are analyzed with the modified code for all targets (Section 4.2). For the radio data, we perform the fitting of radio photometry after the UV-to-IR SED decomposition (Section 4.3). We finally combine the results of X-ray spectral analysis (Yamada et al. 2021), UV-to-IR SED decomposition, and radio fitting. The validity of the best-fit parameters are evaluated in Section 4.4.

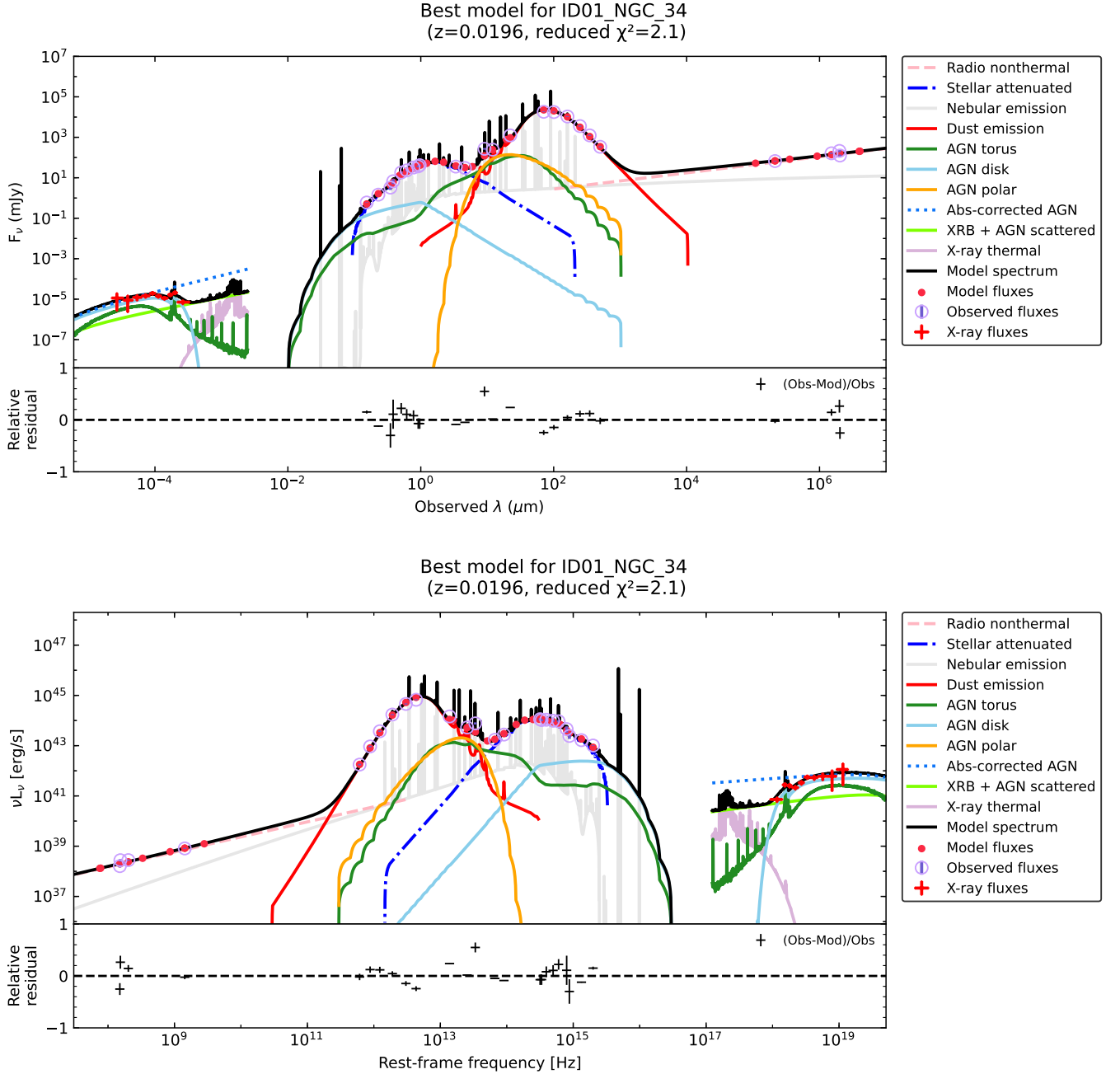


Figure 1. An example of the hard-X-ray-to-radio SED and best-fitting models for a stage-D merger NGC 34 (ID01). Upper panel: observed wavelength vs. flux density. Lower panel: rest-frame frequency vs. luminosity. The bottom panels show the residuals in the UV-to-radio bands. The individual curves show the SED models of radio non-thermal emission (pink dashed), attenuated stellar emission (blue dash-dotted), nebular emission (gray), dust emission (red), AGN torus (green), escaped AGN disk (cyan), polar dust (orange), absorption-corrected AGN X-ray emission (blue dotted), the X-ray emission from AGN scatters and X-ray binaries (light green), and X-ray thermal emission (light purple). Purple and red circles represent the observed and model flux densities, respectively. Red crosses in the X-ray band denote the NuSTAR spectra analyzed by Yamada et al. (2021). The results for all targets are given in Figures E1–E10.

The tables of best-fitting parameters and supplemental measurements of each target are listed in Appendix A. The results of a mock analysis (i.e., the test for the reliability of the estimates, given the uncertainty of the photometry) are shown in Appendix B. The comparison of our results with the previous works is discussed in Appendix C, and the comparison of the results with a different AGN model (SKIRTOR; Stalevski et al. 2016) is in Appendix D. The hard X-ray to radio multiwavelength SEDs and their best-fitting models are presented in Figure 1 and Figures E1–E10 (see Appendix E).

4.1. New Implementation of CLUMPY for X-CIGALE

4.1.1. AGN Model in Multiwavelength SED

The combination of X-ray and IR data enables us to constrain the distribution of the gas and dust in the AGNs (e.g., Hickox & Alexander 2018). For making the analysis consistent with the XCLUMPY X-ray spectra, Miyaji et al. (2019) have modified the CIGALE package, a fitting code to model the UV-to-radio SEDs of galaxies (Burgarella et al. 2005; Noll et al. 2009; Boquien et al. 2019), to include an implementation of CLUMPY (Nenkova et al. 2008a,b). They conduct the X-ray spectral analysis with XCLUMPY and the UV-to-IR SED decomposition with CLUMPY as a module, and successfully estimate the torus parameters of an AKARI-selected CT AGN, such as X-ray absorbing column, torus optical depth, torus angular width, and inclination angle. Recent works (Tanimoto et al. 2020; Ogawa et al. 2021) show that these clumpy torus models mostly present the larger covering fraction in the IR band than those in X-rays, consistent with the presence of the polar dust (see e.g., Asmus et al. 2016; Asmus 2019; López-Gonzaga et al. 2016; López-Gonzaga & Jaffe 2016; Höning & Kishimoto 2017; Höning 2019; Lyu & Rieke 2018; Buat et al. 2021; Toba et al. 2021a; Andonie et al. 2022).

Yang et al. (2020a) develop a new X-ray module for CIGALE, allowing it to fit SEDs, named X-CIGALE (but their X-ray model does not consider the absorption from the target, our Galaxy, and/or the intergalactic medium).⁹ Torus models are mainly classified by their dust distribution such as smooth, clumpy, and two-phase (clumpy and smooth) models. The current version of X-CIGALE (CIGALE v2020.0) includes two AGN models of a classical smooth torus model by Fritz et al. (2006) and a modern two-phase model (SKIRTOR) by Stalevski et al. (2012, 2016). They also implement the

model of polar-dust extinction (e.g., Lyu & Rieke 2018; Höning 2019). For maintaining energy conservation in the scheme of X-CIGALE, the polar dust model considers the radiative energy absorbed by their dust. The model of polar dust assumes the isotropic dust re-radiation and the “gray body” model (e.g., Casey 2012).

Since a clumpy distribution of the dust is necessary to prevent the destruction of grains (e.g., Krolik & Begelman 1988), many works adopt the SKIRTOR model in X-CIGALE (e.g., Yang et al. 2020a, 2022; Buat et al. 2021). However, conducting the SED fit by a self-consistent AGN model with X-CIGALE and XCLUMPY is difficult because the torus component of SKIRTOR has different geometry and parameter definitions from those of XCLUMPY. Thus we use the CLUMPY module by combining the SKIRTOR’s polar dust component.

4.1.2. Differences between CLUMPY and SKIRTOR

The CLUMPY model assumes an isotropic emission of the central source commonly adopted in the literature (e.g., Schartmann et al. 2005; Höning et al. 2006). Strong correlations between X-ray and nuclear 12 μm fluxes (i.e., least biased by extra-nuclear emission) are reported for both Seyfert 1 and 2 galaxies (e.g., Gandhi et al. 2009; Asmus et al. 2015). When taking the X-ray emission as an isotropic tracer for the AGN luminosity, the low scatter of the mid-IR/X-ray luminosity correlation suggests that the mid-IR emission is also close to isotropic. The reason is that the hollow cone is visible to the observer at any inclination in the inflowing disk and outflowing polar dust (Höning & Kishimoto 2017; Höning 2019). The intrinsic SED of the central AGN disk emission in CLUMPY follows the piecewise power-law distribution in Rowan-Robinson (1995), where the CLUMPY model adopts $\lambda_{\text{RJ}} = 1 \mu\text{m}$ (wavelength marking the onset of the Rayleigh-Jeans tail). CLUMPY model results in a Gaussian angular distribution. A density gradient along the polar angle is proportional to $\exp(-\theta^2/\sigma^2)$, where θ is the elevation angle and σ is torus angular width (typically $\sim 20^\circ$; e.g., Ogawa et al. 2021; Yamada et al. 2021). Whereas, SKIRTOR considers the anisotropy of the central source (Netzer 1987) and employs larger $\lambda_{\text{RJ}} = 5 \mu\text{m}$ than that in CLUMPY. SKIRTOR assumes a sharp-edged angular distribution of high-density clumps embedded in a smooth component with low density. A density gradient along the polar angle is proportional to $\exp(-x|\cos(90^\circ - \theta)|)$ in SKIRTOR, where x is a torus density angular parameter typically fixed to 1.0 (e.g., Yang et al. 2020a).

Stalevski et al. (2016) demonstrate that the difference in the input SED shape of the central engine (e.g., λ_{RJ})

⁹ Yang et al. (2022) improve the X-CIGALE code mainly related to AGN intrinsic X-ray anisotropy, X-ray binary emission, AGN accretion-disk SED shape, and AGN radio emission (new version as CIGALE v2022.1).

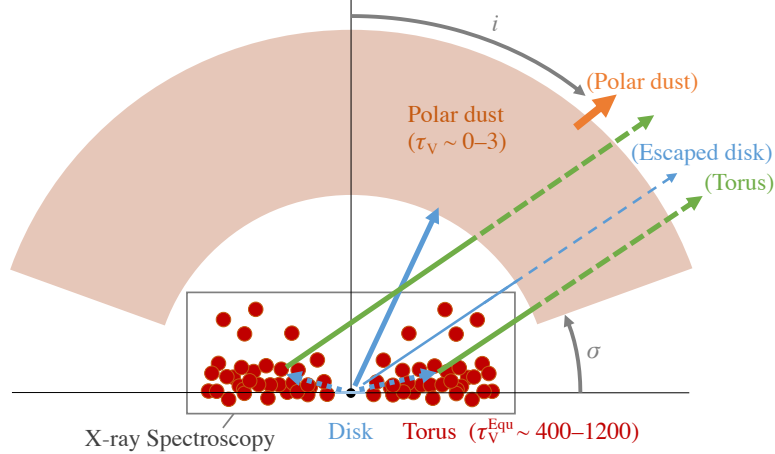


Figure 2. A schematic picture of the AGN structure assumed in the updated CLUMPY model. Central black circle and blue bar represent the SMBH and accretion disk, respectively. Brown circles show the clumps of torus, whose structure is constrained by the X-ray spectroscopy with XCLUMPY. Light-brown annular sector illustrates the polar dust. Green arrays mark the torus reflection emission. Blue thick (solid and dotted) arrays are the AGN disk emission, while a blue thin array is the escaped disk emission via the clump gaps. These emissions are attenuated by the polar dust, marked as dashed lines. Orange arrow shows the dust re-radiation from the polar dust. The symbols “ σ ” and “ i ” mean the torus angular width and inclination angle, respectively.

has little effect on the resulting dust emission: what matter is the total amount of emission from the central engine.¹⁰ By comparing the results obtained with the clumpy torus model of isotropic disk radiation, Stalevski et al. (2012) report that the anisotropic assumption only reduces dust fluxes by a factor of at most 2, keeping roughly the similar shape of IR SEDs. On the other hand, the smooth component in SKIRTOR can produce a more attenuated silicate feature and have a stronger near-IR emission than without the smoothly distributed element (Stalevski et al. 2012, 2016; see also Efstathiou et al. 2022). Moreover, the dependence of the dust distribution on θ in SKIRTOR tends to be less and may cause a stronger near-IR emission than in CLUMPY (Gaussian angular distribution). Although we find such a trend by examining how much of the differences in the results derived from the fits with CLUMPY and SKIRTOR (see Appendix D), both models consequently present similar intrinsic AGN luminosities for almost all of the U/LIRGs in our sample (Figure D1). Hence, our multiwavelength SED analysis is less affected by the model assumption between CLUMPY and SKIRTOR.

4.1.3. Implementation of CLUMPY Model

Figure 2 shows a schematic picture of our updated CLUMPY model containing the polar dust component. The model assumes the situation of an AGN structure

consisting of (1) an accretion disk at $\ll 1$ pc scale, (2) a clumpy torus at $\lesssim 10$ pc scale, and (3) polar dust at $\gtrsim 10$ pc scale (see Section 4.2.3). In the torus model of CLUMPY, the radial distribution of clumps is a power law with an index of q (i.e., r^{-q}), and the angular distribution is a Gaussian distribution. The number of clumps along a line-of-sight path ($N_{\text{clump}}^{\text{LOS}}$) is described by:

$$N_{\text{clump}}^{\text{LOS}}(\theta) = N_{\text{clump}}^{\text{Equ}} \exp(-\theta^2/\sigma^2), \quad (1)$$

where $N_{\text{clump}}^{\text{Equ}}$ is the number of clumps along the equatorial plane. The updated CLUMPY considers dust absorption, re-emission, and scattering (Nenkova et al. 2008a,b), except for the scattering effect in the smooth polar-dust region. Since the total mass of polar dust is much smaller than that contained in the torus, the X-ray spectrum is almost unaffected by the polar dust component at energies above a few keV (e.g. Liu et al. 2019). Thus, the clump distribution derived from the X-ray spectroscopy with XCLUMPY (e.g., Yamada et al. 2021) traces the structure of the clumpy torus without the polar dust. A part of the disk emission is escaped via the clump gap, keeping the shape of its intrinsic AGN SED. Considering the optical depth of a single clump of the torus with $\tau_V = 40-120$ in this work (corresponds to $\tau_\lambda > 1$ in the UV-to-optical bands, the escape probability, P_{esc} , is calculated by $P_{\text{esc}} \simeq \exp(-N_{\text{clump}}^{\text{LOS}})$ (see also Equation A4 in Nenkova et al. 2008a and Section 2.2 in Nenkova et al. 2008b).

The distribution of the polar dust is determined by the region with $\theta \geq \sigma$ (or the region with the angle between

¹⁰ <https://sites.google.com/site/skirtorus/sed-library>

the polar axis and edge of the torus in SKIRTOR). By limiting the range of the polar dust temperature between 100–250 K, the polar dust model in this work reflects the extended dust at $\gtrsim 10$ pc (see Section 4.2.3 and 6.5). We allow the line-of-sight optical depth (τ_V) of polar dust as a typical range in previous studies, $\tau_V \lesssim 3$ (e.g., Buat et al. 2021; Toba et al. 2021a; see Section 4.2.3 and 6.2). The value is much smaller than the equatorial optical depth of the torus ($\tau_V^{\text{Equ}} \sim 400\text{--}1200$), where the number of clumps is 10 (Section 4.2.2). Here, the distributions of polar dust and the galaxy’s interstellar medium (ISM) are not distinguished. Finally, to keep energy conservation, the dust extinction and re-radiation of polar dust in the UV-to-IR bands are included in the same manner as the original X-CIGALE code.

4.2. UV-to-IR SED Fitting with CLUMPY

By using the X-CIGALE code with the CLUMPY implementation, we conduct the UV-to-IR SED decomposition, whose best-fit parameters are adopted for the radio fitting (Section 4.3). The details of the UV-to-IR SED model are described for the host galaxy (stellar emission, nebular emission, and dust emission; Section 4.2.1), torus (torus and escaped disk emission; Section 4.2.2), and polar dust emission (Section 4.2.3 and 4.2.4). The models and parameters we adopted are summarized in Table 3.

4.2.1. Host Galaxy Model

We utilize a delayed star formation history (SFH) model to allow for an instantaneous burst of the starburst activities (e.g., Ciesla et al. 2015; Nersesian et al. 2019). The parameter ranges of the SFH model are mainly referred from the works with CIGALE code for local Herschel-selected galaxies (Buat et al. 2018) and U/LIRGs (Paspaliaris et al. 2021). The stellar emission is modeled as a 5 Gyr simple stellar population (BC03; Bruzual & Charlot 2003). Here, the Chabrier (2003) IMF, solar metallicity, and the standard nebular emission model (see Inoue 2011) are adopted. We consider the attenuation law for the stellar continuum of Calzetti et al. (2000), where the nebular emission is reddened with a Milky Way extinction curve (Cardelli et al. 1989). The reddening of the nebular emission, $E(B-V)_{\text{line}}$ is a free parameter, while the ratio of the reddening of the emission lines and whole stellar continuum, $E(B-V)_{\text{star}}/E(B-V)_{\text{line}}$, was found to be 0.44 for local starbursts (Calzetti 2001). Since the contribution of the UV bump for local galaxies is small ($\sim 1/3$ of that of the MW bump) and can be ignored as it affects the near-UV magnitude by only 0.1 mag (Salim et al. 2018),

we fix the amplitude at zero. Recent works report that the extinction curves show a great diversity in power-law slope (e.g., Salim et al. 2018; Salim & Narayanan 2020), whose range of the slopes is covered from -0.8 to 0.0 . We fit the cold dust emission from the host galaxy with the physical dust model from Draine et al. (2014), the updated model of the previous one (Draine & Li 2007). The parameter ranges of `qph` (q_{ph} ; 0.47–2.50), `umin` (1–50) and `alpha` (2.0 or 2.5) are referred from recent works (e.g., Buat et al. 2018, 2021). The dust fraction in photo-dissociation regions (PDRs) is fixed to 0.02 (e.g., Draine & Li 2007; Dale et al. 2012; Magdis et al. 2012; Buat et al. 2018).

4.2.2. Torus Model (CLUMPY and SKIRTOR)

For the torus component, we adopt the CLUMPY model implemented in the X-CIGALE code (Model I). The number of clumps along the equator of $N_{\text{clump}}^{\text{Equ}} = 10$, the ratio of the outer to inner radii of $Y = 20$, and the radial clumpy distribution index of $q = 0.5$ are assumed to make the analysis consistent with XCLUMPY (Tanimoto et al. 2019). The torus optical depth in the V band is a free parameter (τ_V ; 40, 80, or 120), while the torus angular width (σ ; 15° to 70° in steps of 5°) and inclination angle (i ; 30° , 60° , or 80°) are fixed as be the closest values to the parameters of the best-fitting model in the X-ray works (Yamada et al. 2020, 2021; Ogawa et al. 2021).¹¹ For the systems whose individual galaxies have different inclinations (NGC 6921/MCG+04-48-002 and NGC 7679/NGC 7682), we select $\sigma = 20^\circ$ and $i = 60^\circ$ as typical values in the X-ray results. The UV-to-IR SEDs of starburst-dominant or hard X-ray-undetected sources are modeled without AGN component ($f_{\text{AGN}} = 0$), while allowing the AGN fraction in the IR band to free between 0.05–0.8 for AGNs.

We also perform the SED decomposition with the SKIRTOR model (Model II; see Appendix D). A torus density radial parameter (q) and torus density angular parameter (x) are fixed to be 1.0 (e.g., Stalevski et al. 2016; Yang et al. 2020a).¹² The equatorial optical depth at $9.7\text{ }\mu\text{m}$ ($\tau_{9.7}$) is a free parameter (5, 9, or 11). The angular distribution of clumps has a sharp edge corresponding to the angle between the equatorial plane and edge of the torus (Δ). Here, the unobscured and ob-

¹¹ Since the reduced χ^2 is larger than 10 for IRAS F08572+3915, its inclination of 80° is chosen that present the smallest χ^2 . For NGC 1068, NGC 1275, NGC 1365, Mrk 266B/Mrk 266A, and NGC 6240S/NGC 6240N, we assume σ to be a typical value of 20° (e.g., Yamada et al. 2021; Ogawa et al. 2021), and select the inclination angle showing the smallest χ^2 from 30° , 60° , and 80° .

¹² We confirm that the results and discussion are unchanged even if $q = 0.5$ to keep consistency with CLUMPY model.

Table 3. Summary of Models and Input Parameters in the UV-to-IR SED Fitting

Model	Module	Parameter	Value
SFH model	shfdelayedbq	<code>tau_main</code> (Myr)	1000, 3000, 5000
		<code>age_main</code> (Myr)	4500, 7000, 9500, 12000
		<code>age_bq</code> (Myr)	10, 20, 100
		<code>r_sfr</code>	1, 3.16, 10, 31.6, 100, 1000
Stellar emission	bc03	<code>imf</code>	1 (Chabrier)
		<code>metallicity</code>	0.02
Nebular emission	nebular	<code>logU</code>	-3.0
		<code>f_esc</code>	0.0
		<code>f_dust</code>	0.0
		<code>lines_width</code> (km s ⁻¹)	300
Attenuation law	dustatt_modified_starburst	<code>E_BV_lines</code>	0.1, 0.25, 0.5, 0.75, 1.0, 1.5, 2.0
		<code>E_BV_factor</code>	0.44
		<code>uv_bump_wavelength</code> (nm)	217.5
		<code>uv_bump_width</code> (nm)	35.0
		<code>uv_bump_amplitude</code>	0.0
		<code>powerlaw_slope</code>	-0.8, -0.4, 0.0
		<code>Ext_law_emission_lines</code>	1 (Milky Way)
		<code>Rv</code>	3.1
Dust emission	dl2014	<code>qpah</code> (= q_{pah})	0.47, 1.12, 2.50
		<code>umin</code>	1, 5, 10, 25, 50
		<code>alpha</code>	2.0, 2.5
		<code>gamma</code>	0.02
AGN (torus/disk)	CLUMPY (Model I)	<code>Y_ratio</code> (= Y)	20
		<code>tau_V</code> (= τ_V)	40, 80, 120
		<code>N_0</code> (= $N_{\text{clump}}^{\text{Equ}}$)	10
		<code>q</code> (= q)	0.5
		<code>sigma</code> (= σ ; degree)	15 to 70 (per bin 5; fixed)
		<code>inclination</code> (= i ; degree)	30, 60, 80 (fixed)
		<code>fracAGN</code> (= f_{AGN})	0.0 (for starburst-dominant sources), or 0.05, 0.1, 0.2, 0.3, 0.4, 0.5, 0.6, 0.7, 0.8 (for AGNs)
		<code>R</code> (= Y)	20
		<code>t</code> (= $\tau_{9.7}$)	5, 9, 11
		<code>oa</code> (= Δ ; degree)	30, 40, 60 (fixed)
AGN (polar)	CLUMPY/SKIRTOR	<code>i</code> (= i ; degree)	30, 60, 80 (fixed)
		<code>fracAGN</code> (= f_{AGN})	0.0 (for starburst-dominant sources), or 0.05, 0.1, 0.2, 0.3, 0.4, 0.5, 0.6, 0.7, 0.8 (for AGNs)
		<code>law</code>	0 (SMC)
		<code>EBV</code> (= $E(B - V)$; mag)	0.0 (fixed), or 0.05, 0.3, 0.8
		<code>temperature</code> (= T_{polar} ; K)	100, 150, 200, 250
		<code>emissivity</code> (= β)	1.6

scured AGNs are determined by the inclination angle above $i < 90^\circ - \Delta$ or not, respectively. To keep fully consistency between the SKIRTOR-based AGN classification and X-ray classification in our sample (Table 1), we convert the torus angular width (σ) of $[10^\circ\text{--}15^\circ, 15^\circ\text{--}25^\circ, 25^\circ\text{--}70^\circ]$ to the Δ of $[30^\circ, 40^\circ, 60^\circ]$, respectively.

4.2.3. Polar Dust Model

In the polar dust model, we adopt the Small Magellanic Cloud (SMC; Prevot et al. 1984) extinction curve, which is preferred from AGN observations (e.g., Hopkins et al. 2004; Salvato et al. 2009; Bongiorno et al. 2012; Buat et al. 2021). The reddening $E(B-V)$ is free (0.05, 0.3, and 0.8; e.g., Buat et al. 2021; Paspaliaris et al. 2021; Toba et al. 2021a; Yang et al. 2022), or setting $E(B-V) = 0$ if no significant AGN contribution ($f_{\text{AGN}} = 0$). The emissivity (β) is fixed at 1.6 as a typical value (e.g., Draine & Lee 1984; Casey 2012; Yang et al. 2020a). The previous IR works indicate the temperature of polar dust (T_{polar}) is \sim 100–200 K (e.g., Lopez-Rodriguez et al. 2018; Lyu & Rieke 2018; Hönig 2019), while the temperature of the torus is \gtrsim 300 K (e.g., Tristram et al. 2009; Tristram & Schartmann 2011). Recent high-spatial-resolution mid-IR observation of the nearby Seyfert 2 galaxy, the Circinus galaxy, with Very Large Telescope Interferometer also supports the similar temperatures (\sim 370 K within the subparsec-scale central region and \sim 200 K in outer polar dust regions; Isbell et al. 2022). These temperatures are much larger than those expected for a galaxy’s ISM heated only by star formation (\sim 20–60 K; e.g., Casey 2012; Clements et al. 2018; da Cunha et al. 2021). Although the higher temperature dust above 300 K should radiate the near-IR emission from a ring-like dust structure on the subparsec central region (e.g., Krolik 2007; Schartmann et al. 2014; Baba et al. 2018; Hönig 2019; Lyu & Rieke 2021; Gámez Rosas et al. 2022; Matsumoto et al. 2022), the material of the inner edge of a torus and accompanying polar dust would be difficult to distinguish by both near-IR and X-ray observations. Therefore, we select the range of the polar dust temperature within 100–250 K, and clarify that (1) the estimates of the physical properties of extended (\gtrsim 10 pc; see also Section 6.5) polar dust that are not taken into account for the hot ($>$ 300 K) dust component on the subparsec region and (2) the central hot dust emission are predominantly considered as the torus emission in this study.

4.2.4. Significance Test for Torus and Polar-dust Emission

We examine the Bayesian information criterion (BIC; Schwarz 1978) for two kinds of fits with and without the AGN (torus and polar dust) component. Using the χ^2 statistics, the BIC is provided by the equation as $\text{BIC} =$

$\chi^2 + k \times \ln(N)$, where k is the number of free parameters and N is the number of photometric data (Ciesla et al. 2018; Buat et al. 2019). Among the sources yielding a poor fit with reduced χ^2 above 6, the three galaxies, ESO 350–38, ESO 374–IG032, and NGC 4418, show the $\Delta\text{BIC} = \text{BIC}_{\text{woAGN}} - \text{BIC}_{\text{wAGN}} > 6$ (significantly improvement with a posterior probability above 95%; Raftery 1995). Thus, we re-classify these three galaxies as AGN candidates and select the inclination angle providing the smallest χ^2 .

Furthermore, we conduct the significance test for the polar dust component in the UV-to-IR SED analysis. The left panel of Figure 3 presents the fraction of sources showing $\text{BIC} > 6$ for a polar dust component with two kinds of torus models. We find that the analysis with SKIRTOR provides larger fractions of the AGNs showing significant polar dust contribution than with CLUMPY. This stronger significance of mid-IR polar dust emission can be explained by the flatter SED slope of the torus component in the SKIRTOR model due to the strong near-IR emission from smooth low-density dust (Section 4.1.2 and Appendix D). Although the sample is quite limited to the nine AGNs, the signatures of polar-dust radiation are reported by high-resolution mid-IR images and interferometry (NGC 1068, NGC 1365, NGC 3690 West, Mrk 231, MCG–03-34-064, NGC 5135, IC 4518W, NGC 7469, and NGC 7674; López-Gonzaga et al. 2014, 2016; López-Gonzaga & Jaffe 2016; Asmus et al. 2016; Asmus 2019; Lopez-Rodriguez et al. 2017, 2018; Mattila et al. 2018; Gámez Rosas et al. 2022).¹³ Six of these AGNs hosting polar dust emissions do not show any significant BIC values with these torus models (right panel of Figure 3). This is mainly because the available photometries of them in the near-IR (2MASS) and/or mid-IR (WISE and AKARI) bands are insufficient to give a diagnosis, which may be derived by the artifacts related to their IR emission from extended or comprehensive morphology. So, we adopt the polar dust model for the AGNs with one or more signs from mid-IR images, interferometry, and BIC tests by SED analysis with CLUMPY and SKIRTOR. For the seven AGNs without any signs of polar dust contribution, most of whose IR photometries are available, we treat them as AGNs without polar dust emission by applying $E(B-V) = 0$, i.e., returning to the original torus model. Impres-

¹³ The presence of polar dust in Mrk 231 is implied by near-to-mid-IR polarimetry (López-Rodriguez et al. 2017), and in NGC 3690 West by detecting the time variability of nucleus IR SED due to the tidal disruption event radiating the polar dust emission (Mattila et al. 2018).

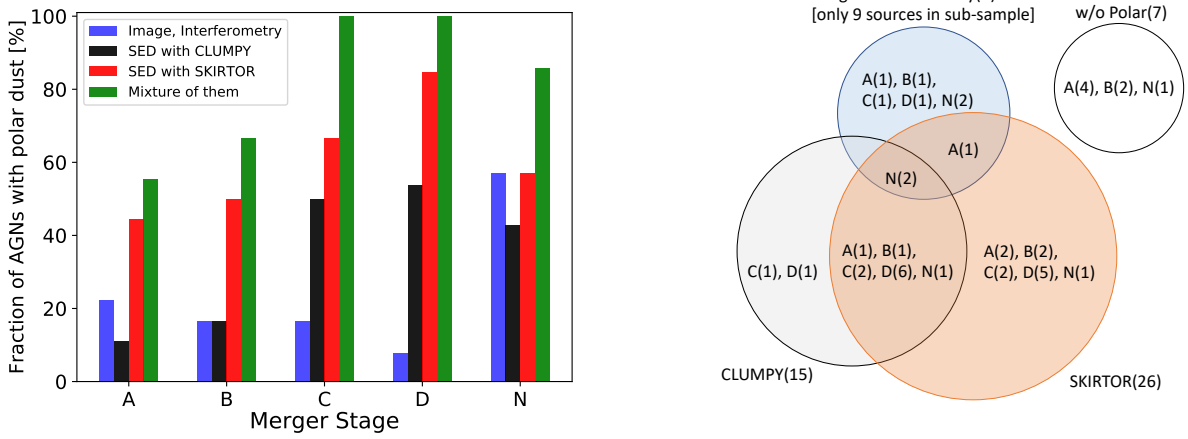


Figure 3. Left panel: Histogram of the fraction of the sources that shows some signatures of the presence of polar dust emission for the AGNs with merger stage. Each signature derived from the high-resolution image (e.g., Asmus 2019) and interferometry (e.g., López-Gonzaga et al. 2016; López-Gonzaga & Jaffe 2016) in the mid-IR band (blue), the UV-to-IR SED decomposition with CLUMPY (black) and with SKIRTOR (red) are color-coded. Green histogram illustrates the fraction for the AGNs with one or more signs of polar dust emission (green). Right panel: Venn diagram of the sources with/without the signs of polar dust emission. The numbers of the sources for individual categories and merger stages are illustrated in parentheses.

sively, we find that these AGNs are in early mergers and nonmergers, while all of the AGNs in late mergers show the signatures of polar dust emission, as discussed in Section 6.5.2. Finally, we list the best fitting parameters in the tables of Appendix A (e.g., Table A1–A5).

4.3. Radio Fitting

By fixing the best-fitting parameters obtained by the UV-to-IR SED analysis, we finally conduct the radio SED decomposition. The radio model is composed of the continuum from the nebular emission (free-free, free-bound, and two-photon continua)¹⁴, which also radiates UV-to-IR emission (Section 4.2.1), and independent synchrotron emission from AGN and/or starburst (Boquien et al. 2019). We parameterized a correlation coefficient between total-IR luminosity and monochromatic radio luminosity of the synchrotron emission at 1.4 GHz ($q_{\text{IR}} = \log L_{\text{IR}} / L_{1.4\text{GHz}}$), and the power-law slope of synchrotron emission (α_{radio}) derived from the low-frequency radio emission in the 0.1–4 m or 0.07–3.0 GHz bands. We choose the parameter ranges of q_{IR} between −1.50 and +3.50 with a step of 0.01 (e.g., Yun et al. 2001; U et al. 2012; Vardoulaki et al. 2015), and α_{radio} between 0.00 and 1.50 with a step of 0.01 (e.g., Murphy 2013; Toba et al. 2019b). If only a sin-

gle radio photometry or upper limit values are available, we fix α_{radio} to be 0.5, a median value in the <5 GHz bands among local U/LIRGs (Murphy 2013), consistent with the averaged value of the estimates in our study ($\alpha_{\text{radio}} = 0.48 \pm 0.16$). The best-fitting parameters and radio luminosities are listed in Table A3, and the combined hard X-ray to radio multiwavelength SEDs and their best-fitting models are shown in Figures 1 and Appendix E.

4.4. Best-fit Parameters and Their Validity

We have performed the multiwavelength SED analysis for the local U/LIRGs, covering the hard X-ray to radio wavelength bands. The best-fit parameters of individual sources are summarized in Tables A1–A5, and the averaged values of these results are shown in Table 4. The histogram of the reduced χ^2 of the UV-to-IR SED decomposition for the 72 individual targets in our sample is displayed in Figure 4. The SED decomposition of some targets shows a relatively large χ^2 above 5, which is mainly caused by the noisy photometric data in the UV or optical band (Figures E1–E10 in Appendix E). Conducting a mock analysis, we confirm that the best-fit parameters derived from our multiwavelength SED decomposition are less affected by photometric uncertainties (see Appendix B). However, the SED fitting of IRAS F08572+3915 shows a large reduced χ^2 over 10 because the model presents weaker near-IR fluxes than the photometric data. Its SED is moderately reproduced with SKIRTOR (with reduced χ^2 of 6.7). Although its AGN luminosity may be underestimated (at

¹⁴ The model of the nebular component covers the UV to radio 1 m emission. To expand the available wavelength, we assume the slope between the fluxes in the 0.8 and 1 m bands to the 1–10 m radio emission for the nebular component, where it is less dominant than the synchrotron component.

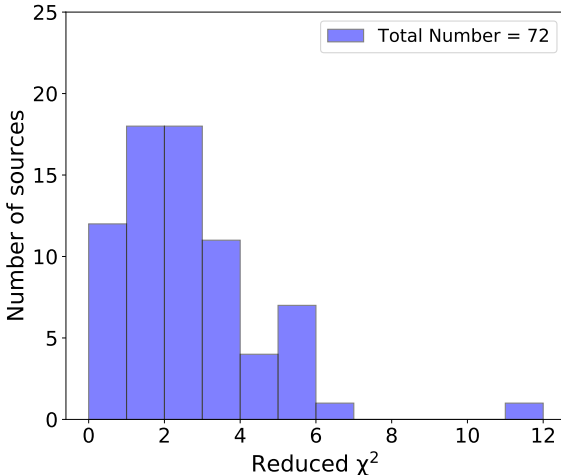


Figure 4. Histogram of the reduced χ^2 derived from the UV-to-IR SED decomposition for the 72 individual targets in our sample.

worse ~ 0.4 dex), the AGN luminosities for the other sources derived with CLUMPY are well consistent with the values with SKIRTOR (Appendix D). Thus, we utilize the results from the multiwavelength analysis with CLUMPY for all targets to discuss their characteristics of the host galaxy and AGN.

Next, we investigate the significance of the AGN feature in the multiwavelength SED decomposition. Figure 5 shows the histogram of the ΔBIC on the different fits with and without the AGN component for the 72 individual targets in our sample (see also Section 4.2.4). Remarkably, most of the sources are distributed around the threshold of $\Delta\text{BIC} = 6$, regardless of whether the sources are the AGNs (hard X-ray-detected AGNs and three newly identified AGN candidates by the diagnostics of $\Delta\text{BIC} > 6$) or the other sources (starburst-dominant or hard X-ray-undetected sources). This indicates that the AGNs in U/LIRGs are difficult to detect only with the SED decomposition. Therefore, the strong constraints on the AGN structure derived from the X-ray spectral analysis will effectively solve the complex SEDs in the IR band.

We evaluate the effects on the results if unresolved photometries are utilized. For the stellar mass (M_*) and SFR, the comparison of our results and previous works of SED analysis by using the photometry of total systems are presented in Appendix E. Figure 6 presents the differences in the results derived from the combined photometry of a total system and the separated photometries of individual galaxies for the 13 resolved pairs. The stellar masses and SFRs are not affected by using

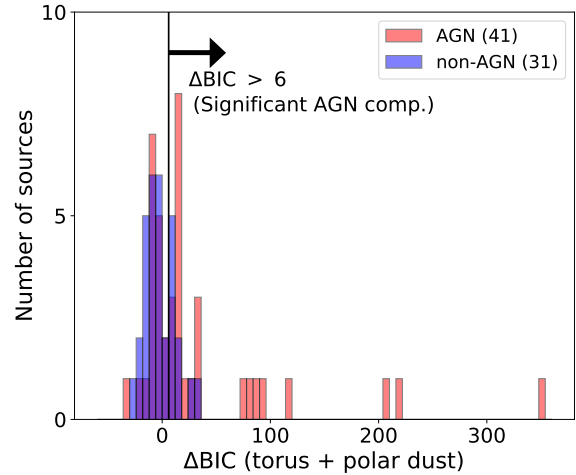


Figure 5. Histogram of ΔBIC ($= \text{BIC}_{\text{woAGN}} - \text{BIC}_{\text{wAGN}}$) for the 72 individual targets in our sample. The black solid line shows the threshold of $\Delta\text{BIC} = 6$ as the significant differences (posterior probability above 95%) in two fits with and without adding the AGN (torus and polar dust) component. The red histogram shows the number of the hard X-ray-detected AGNs and three newly identified AGN candidates. The blue histogram is the number of the other sources, i.e., starburst-dominant sources or hard X-ray-undetected sources.

the summed fluxes of individual galaxies. On the other hand, for the 10 pairs hosting AGNs, the UV-to-IR torus (L_{torus}) and polar dust luminosities (L_{polar}), and intrinsic (bolometric) AGN disk luminosities ($L_{\text{AGN,int}}$) derived from the combined photometries become larger than those from separated ones. According to the SED models in Figures E1–E10, the slope of the IR SEDs of the starburst component is similar to the one of the AGN (see also Section 5.4). This makes it difficult to accurately extract the AGN contribution from the IR SED when the photometries of a starburst-dominant source and a galaxy hosting an AGN are mixed. The overestimation of AGN luminosities for unresolved sources is found to be ~ 0.2 dex, which is a small effect on the following discussion.

5. RESULTS: MULTIWAVELENGTH EMISSION FROM U/LIRGS

Before the discussion on the properties of polar dust in U/LIRGs (Section 6), we first study the characteristics of the multiwavelength radiation, which are helpful to understand the detailed environments from the nucleus to galactic scales. We also aim to investigate unique features for future works to explore buried AGNs in

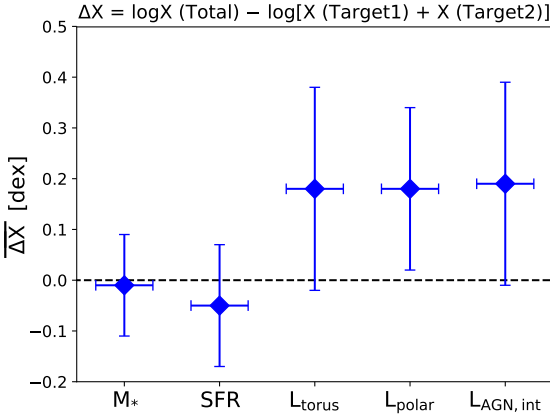


Figure 6. The differences in M_* , SFR, L_{torus} , L_{polar} , and $L_{\text{AGN,int}}$ derived from the UV-to-IR SED analysis by using the combined photometry of a total system and separated photometries of the individual galaxies for 13 resolved pairs. Diamonds and these uncertainties denote the averaged values and 1σ dispersions, respectively.

U/LIRGs at higher redshift. For these purposes, we here examine the SFR– M_* relation as an indicator of the host galaxy’s properties (Section 5.1). Next, we evaluate the activities of AGNs and starbursts by focusing on the radio emission (Section 5.2), WISE IR color (Section 5.3), and averaged multiwavelength SEDs (Section 5.4). Finally, we discuss the properties of AGNs in U/LIRGs by comparing the X-ray and other wavelength luminosities corrected for the torus absorption (Section 5.5). The main findings are summarized in Section 5.6.

5.1. Characteristics of Host Galaxies

We investigate the properties of host galaxies in U/LIRGs by using the measurements of stellar masses (M_*) and SFRs. A strong correlation between these quantities for the majority of star-forming galaxies has been well reported (e.g., Brinchmann et al. 2004; Noeske et al. 2007; Elbaz et al. 2007; Speagle et al. 2014; Saintonge et al. 2016; Tomczak et al. 2016; Pearson et al. 2018), called the main sequence (MS). Generally, galaxies above the MS are qualified as “starburst”, while galaxies below the relation are passive galaxies in terms of their star-formation activity. Thus, the comparison of these physical quantities enables us to understand the galaxy’s evolution in the populations.

Figure 7 shows the averaged values of M_* and SFR compared with merger stages. The M_* is almost similar for all merger stages, while the SFR increases with merger stage. The left panel of Figure 8 presents the

SFR– M_* relation obtained by the multiwavelength SED analysis for our U/LIRGs color-coded by the merger stages. We overplot the values of Palmer–Green (PG) quasars at $z < 0.1$ as gray diamonds. For these quasars, the SFRs are estimated by the UV-to-IR SED decomposition (Lyu et al. 2017) and stellar masses are referred from Xie et al. (2021) based on the high-resolution optical and near-IR images (Zhang et al. 2016) or the M_* – M_{BH} relation of Greene et al. (2020).¹⁵ For comparison, we also plot some MS relations for SDSS star-forming galaxies at $0.015 \leq z \leq 0.1$ (Elbaz et al. 2007), a large homogeneous collection of star-forming galaxies out to $z \sim 6$ (the relation at $z \approx 0$ is adopted; Speagle et al. 2014), and SDSS DR7 galaxies with $0.01 < z < 0.05$ and $M_* > 10^8 M_\odot$ on the basis of SFRs derived from UV and mid-IR (12 or 22 μm) luminosities (Saintonge et al. 2016).

The previous IR SED analysis of local U/LIRGs using the photometry of unresolved total systems by Shangguan et al. (2019) decouples the contributions of AGN and starburst emission and suggests the whole U/LIRGs are above the MS. On the other hand, using the separated photometry of individual sources as possible in the SED fitting, we find that some component sources in early mergers sit on or lie below the MS. The early mergers and PG quasars have wide ranges of SFRs above and below the MS, while the late mergers have the highest SFRs above the MS. Except for some early mergers, the distributions of the stellar masses are comparable in both U/LIRGs and PG quasars. As a result, the average specific SFR, sSFR (= SFR/ M_*), is much larger in late mergers ($\log(\text{sSFR}/\text{yr}^{-1}) = -8.51 \pm 0.58$) than those in early mergers (-9.58 ± 0.98), nonmergers (-9.50 ± 0.51), and PG quasars (-10.16 ± 0.64). Interestingly, this is well consistent with the recent high-resolution simulations of gas-rich major mergers (Blecha et al. 2018), which predicts the starbursts with the highest sSFR (-8.4 in a logarithmic scale) in the final phase of mergers. Although the progenitor of quasars are not necessarily triggered by mergers (e.g., Xie et al. 2021), these results support that the starburst activities in U/LIRGs are triggered in early mergers, and suppressed after late mergers with high sSFR (e.g., Di Matteo et al. 2005; Hopkins et al. 2008; Ellison et al. 2013; Barrera-Ballesteros et al. 2015; Shangguan et al. 2019; U et al. 2019; Yamada et al. 2021).

¹⁵ The values of M_{BH} are referred from Veilleux et al. (2009a) by averaging the results from different measurements, including spheroid luminosity, spheroid velocity dispersion, reverberation mapping, and virial relation (see Zhang et al. 2016).

Table 4. Averaged Values of Best-fit Parameters and Accompanying Results.

No.	Parameter	Merger Stage					
		A	B	C	D	A–B	C–D
Free parameters (UV-to-IR SED analysis; Section 4.2)							
1	$\log(\tau_{\text{main}})$ (Myr)	3.38 ± 0.23	3.42 ± 0.22	3.50 ± 0.12	3.53 ± 0.09	3.40 ± 0.23	3.52 ± 0.10
2	$\log(\text{age_main})$ (Myr)	3.89 ± 0.12	3.85 ± 0.10	3.91 ± 0.07	3.89 ± 0.06	3.87 ± 0.11	3.89 ± 0.07
3	$\log(\text{age_bq})$ (Myr)	1.65 ± 0.22	1.68 ± 0.21	1.55 ± 0.32	1.39 ± 0.31	1.67 ± 0.22	1.44 ± 0.32
4	$\log(r_{\text{sfr}})$	1.12 ± 0.79	1.39 ± 0.88	1.57 ± 0.77	2.19 ± 0.64	1.24 ± 0.84	2.01 ± 0.74
5	$E_{\text{BV}}\text{lines}$	0.72 ± 0.51	0.99 ± 0.43	0.83 ± 0.38	1.37 ± 0.29	0.84 ± 0.50	1.22 ± 0.41
6	powerlaw_slope	-0.47 ± 0.24	-0.41 ± 0.31	-0.39 ± 0.27	-0.35 ± 0.29	-0.45 ± 0.27	-0.36 ± 0.29
7	q_{pah}	1.19 ± 0.58	1.16 ± 0.68	0.85 ± 0.38	0.80 ± 0.54	1.17 ± 0.62	0.82 ± 0.50
8	u_{min}	10.18 ± 11.07	15.49 ± 15.10	25.15 ± 14.95	29.93 ± 15.15	12.50 ± 13.25	28.57 ± 15.25
9	α_{pah}	2.19 ± 0.20	2.20 ± 0.23	2.18 ± 0.22	2.31 ± 0.22	2.19 ± 0.22	2.27 ± 0.23
10	τ_{V}	81.51 ± 8.95	85.26 ± 6.15	74.31 ± 22.58	73.37 ± 23.63	83.01 ± 8.16	73.67 ± 23.31
11	f_{AGN}	0.16 ± 0.13	0.11 ± 0.04	0.26 ± 0.18	0.18 ± 0.19	0.14 ± 0.11	0.20 ± 0.19
12	$E(B - V)$ (mag)	0.40 ± 0.26	0.25 ± 0.17	0.39 ± 0.19	0.33 ± 0.27	0.33 ± 0.23	0.35 ± 0.25
13	T_{polar} (K)	164.03 ± 37.97	173.29 ± 8.66	134.10 ± 27.44	132.57 ± 33.06	168.15 ± 29.25	133.06 ± 31.40
Fixed Parameters (UV-to-IR SED analysis; Section 4.2)							
14	σ (degree)	24.4 ± 14.6	19.2 ± 1.9	24.2 ± 9.3	19.2 ± 2.7	22.3 ± 11.7	20.8 ± 6.1
15	i (degree)	54.4 ± 18.9	63.3 ± 7.5	61.7 ± 16.7	60.0 ± 15.2	58.0 ± 16.0	60.5 ± 15.7
Free Parameters (radio fitting; Section 4.3)							
16	$\alpha_{\text{radio}}^{\dagger}$	0.54 ± 0.16	0.52 ± 0.07	0.52 ± 0.14	0.38 ± 0.15	0.54 ± 0.13	0.43 ± 0.16
17	q_{ir}^{\dagger}	2.39 ± 0.41	2.26 ± 0.29	2.50 ± 0.19	2.57 ± 0.27	2.34 ± 0.37	2.55 ± 0.25
Accompanying results							
18	$\log(M_*)$ (M_{\odot})	10.23 ± 0.91	10.42 ± 0.39	10.43 ± 0.35	10.35 ± 0.52	10.31 ± 0.74	10.37 ± 0.48
19	$\log(\text{SFR})$ ($M_{\odot} \text{ yr}^{-1}$)	0.49 ± 0.82	1.06 ± 0.55	1.53 ± 0.38	1.98 ± 0.32	0.74 ± 0.77	1.86 ± 0.40
20	$\log(\text{sSFR})$ (yr^{-1})	-9.74 ± 1.08	-9.36 ± 0.80	-8.90 ± 0.49	-8.36 ± 0.54	-9.58 ± 0.98	-8.51 ± 0.58
21	$\log(L_{1.4\text{GHz}})^{\dagger}$ (erg s $^{-1}$)	38.19 ± 0.88	38.75 ± 0.52	39.09 ± 0.30	39.47 ± 0.44	38.44 ± 0.80	39.36 ± 0.44
22	q_{excess}	0.12 ± 0.08	0.11 ± 0.11	0.08 ± 0.02	0.08 ± 0.03	0.11 ± 0.10	0.08 ± 0.03
23	$\log(L_{6,\text{AGN}})$ (erg s $^{-1}$)	42.39 ± 0.95	42.77 ± 0.60	43.30 ± 0.48	43.52 ± 0.50	42.54 ± 0.85	43.45 ± 0.50
24	$\log(L_{12,\text{t}})$ (erg s $^{-1}$)	43.03 ± 0.83	43.31 ± 0.49	43.93 ± 0.50	44.09 ± 0.52	43.14 ± 0.73	44.04 ± 0.52
25	$\log(L_{12,\text{p}})$ (erg s $^{-1}$)	43.24 ± 0.29	43.07 ± 0.75	43.10 ± 0.24	43.46 ± 0.75	43.16 ± 0.55	43.35 ± 0.65
26	$\log(L_{12,\text{AGN}})$ (erg s $^{-1}$)	43.21 ± 0.85	43.52 ± 0.53	44.04 ± 0.40	44.23 ± 0.53	43.34 ± 0.75	44.17 ± 0.50
27	$\log(L_{\text{torus}})$ (erg s $^{-1}$)	43.18 ± 0.80	43.43 ± 0.44	43.98 ± 0.45	44.14 ± 0.50	43.28 ± 0.69	44.09 ± 0.49
28	$\log(L_{\text{polar}})$ (erg s $^{-1}$)	43.62 ± 0.54	43.40 ± 0.18	44.07 ± 0.39	44.29 ± 0.59	43.53 ± 0.43	44.22 ± 0.55
29	$\log(L_{\text{AGN,int}})$ (erg s $^{-1}$)	43.49 ± 0.71	43.80 ± 0.36	44.35 ± 0.45	44.53 ± 0.57	43.61 ± 0.62	44.47 ± 0.54
30	$\log(M_{\text{BH}})$ (M_{\odot})	7.80 ± 0.41	7.83 ± 0.24	7.34 ± 0.28	7.83 ± 0.46	7.81 ± 0.35	7.67 ± 0.47
31	$\log(\lambda_{\text{Edd}})$	-2.43 ± 1.01	-2.17 ± 0.47	-1.15 ± 0.45	-1.29 ± 0.67	-2.33 ± 0.85	-1.24 ± 0.61
32	$\log(R_{\text{polar}})$ (pc)	1.77 ± 0.59	1.56 ± 0.05	2.24 ± 0.45	2.35 ± 0.40	1.68 ± 0.45	2.32 ± 0.42

NOTE—Comments: The table summarizes the averaged values of each parameter for individual merger stages. (1–13) Free parameters as listed in Table 3 (see Section 4.2); (14–15) Two fixed parameters of torus angular width and inclination angle as listed in Table 3 (Section 4.2); (16–17) free parameters of the radio fitting (Section 4.3); (18–20) stellar mass (M_*), SFR, and specific SFR (sSFR = SFR/M_*) as listed in Table A2; (21–22) rest-frame radio 1.4 GHz luminosity and radio-excess parameter (q_{excess}) as listed in Table A3 (see Section 5.2); (23–26) rest-frame 6 μm luminosity of AGN (torus and polar dust) component, rest-frame 12 μm luminosities of the torus, polar dust, and total AGN component (see Table A4); (27–32) UV-to-IR (mainly IR) luminosities (torus, polar dust, and AGN components), SMBH mass, Eddington ratio, and physical sizes of the polar dust structure (Section 6.5) as listed in Table A5.

† The values of the sources whose α_{radio} is fixed at 0.5 are excluded.

The right panel of Figure 8 denotes the SFR– M_* relation for U/LIRGs with or without AGNs. Red stars mark the hard X-ray-detected AGNs and three AGNs that are re-classified by the significance test with BIC values (Section 4.2.4), while dark gray circles mark the starburst-dominant or hard X-ray-undetected sources. The U/LIRGs but several early mergers below the MS show similar distributions regardless of the presence or absence of AGNs. About 50% of the AGNs in late mergers are CT AGNs and, among the hard X-ray-

undetected sources, there are few CT AGN candidates based on their 3σ upper limits in the 8–24 keV band (Yamada et al. 2021). These results support that the obscuration of the AGNs is not related to the difference in the SFR– M_* distribution with and without AGNs. A similar result in the IR band for local U/LIRGs of GOALS sample is reported by Shangguan et al. (2019), who evaluate the presence of AGNs when the IR SED fit is significantly improved by adding the torus component. Their AGN classification is based on the signa-

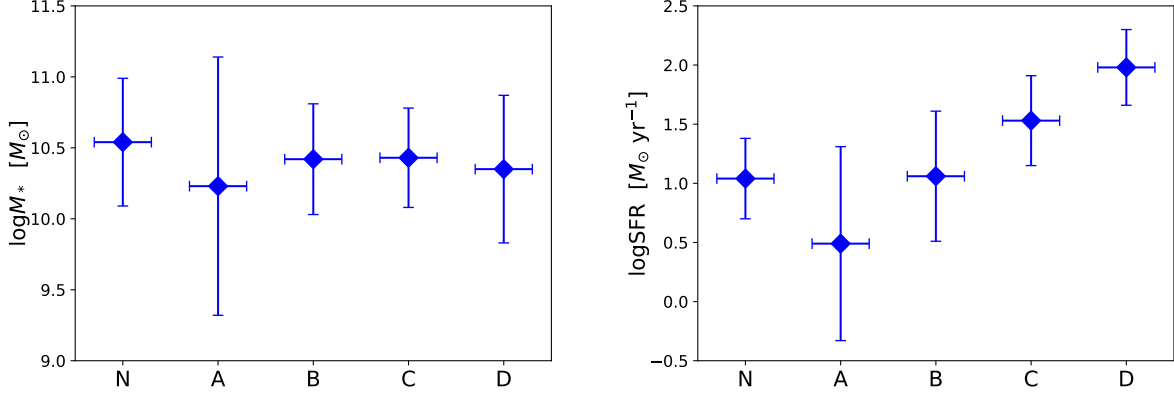


Figure 7. Left panel: averaged values of logarithmic M_* compared with merger stages. Right panel: averaged values of logarithmic SFR compared with merger stages.

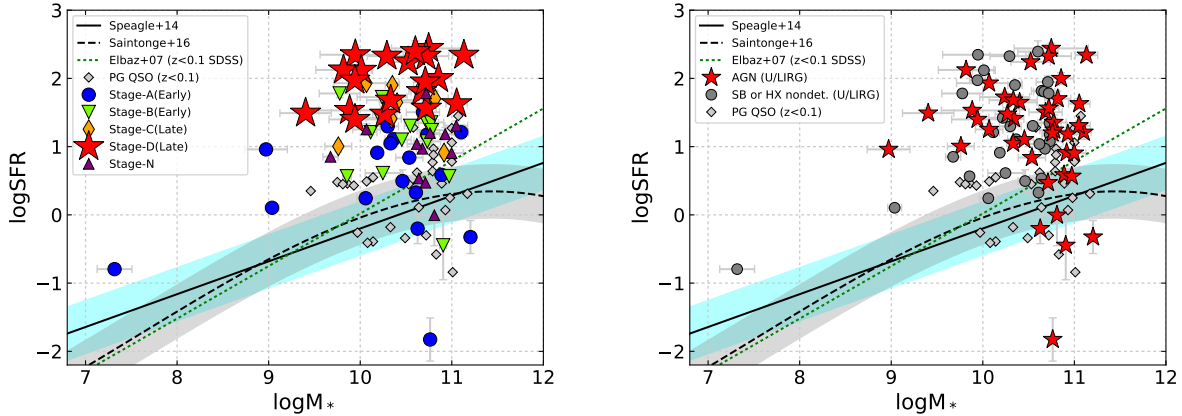


Figure 8. Left panel: logarithmic stellar mass in M_\odot vs. logarithmic SFR in $M_\odot \text{ yr}^{-1}$. The blue circles, green triangles, orange diamonds, red stars, and purple triangles represent the sources in stages A, B (early mergers), C, D (late mergers), and N (nonmergers) U/LIRGs, respectively. The gray diamonds illustrate the PG QSOs at $z < 0.1$, whose SFRs are estimated by the UV-to-IR SED decomposition (Lyu et al. 2017). The black dotted curve and cyan area denote the MS and 1σ uncertain reported by Speagle et al. (2014), while the dashed solid curve and shading represent those reported by Saintonge et al. (2016). The green dotted line is the MS among $z < 0.1$ SDSS galaxies Elbaz et al. (2007). Right panel: the same but the sources are classified by AGNs in U/LIRGs (red star), starburst-dominant or hard X-ray-nondetected sources in U/LIRGs (gray circle), and PG QSOs (gray diamond).

ture of strong mid-IR emission from the AGNs. Thus, no matter which classifications of hard X-ray or mid-IR observations we select, the SFR– M_* relation implies the small influence of the AGN activities on the starburst activities in the phase of U/LIRGs.

5.2. Origin of Radio Emission from U/LIRGs

Radio observation is a potential approach to reveal a mixture of starburst and AGN activities in U/LIRGs. About 10% of AGNs radiate strong synchrotron emission primarily from the powerful relativistic jets in the radio band, observable as radio-loud AGNs (e.g., Begel-

man et al. 1984). The other AGNs are classified as radio-quiet AGNs, whose radio emissions are derived from a wide range of possible mechanisms: star formation, AGN-driven wind, free-free emission from photoionized gas, low power jets, and the innermost accretion disc coronal activities (e.g., Panessa et al. 2019; Kawamuro et al. 2022). Thanks to the long wavelengths, radio observations can overcome the effects of dust obscuration in U/LIRGs and investigate their central engines, particularly starbursts and/or AGNs (e.g., Condon et al.

1991; Lonsdale et al. 2003; Murphy 2013; Vardoulaki et al. 2015).

5.2.1. Radio Slope

For star-forming galaxies, the radio emission typically appears as a power law spectrum ($S_\nu \propto \nu^{-\alpha}$) from thermal and non-thermal emission associated with the formation of massive stars. The thermal emission is produced by the young massive O/B stars dominating the ionization in HII regions, and the non-thermal emission is produced by supernova remnants of the more massive stars than $\gtrsim 8 M_\odot$, accelerating cosmic-ray electrons (e.g., Helou et al. 1985; Condon 1992). Under such conditions, the thermal bremsstrahlung free-free emission from the HII regions has a flat slope ($\alpha \sim 0.1$), while the non-thermal free-free emission shows a steep slope ($\alpha \sim 0.8$; e.g., Niklas et al. 1997). The contribution of non-thermal emission is much larger at frequencies below 10 GHz than the thermal emission, as confirmed by the best-fit models of synchrotron (pink) and nebular free-free (gray) emission in the radio band (see Figure 1 and Figures E1–E10). However, since the AGNs also radiate the synchrotron emission with a similar slope to the starburst emission ($\alpha \sim 0.8$; e.g., Krolik 1999; Niklas et al. 1997; but see the study of radio-slope map by Vardoulaki et al. 2015 and Linden et al. 2019), this makes difficult to separate the starburst and AGN radio emission. For U/LIRGs, the nuclear radio emission should have flat spectra due to optically-thick free-free absorption (Condon et al. 1991; Clemens et al. 2008; Leroy et al. 2011; Murphy et al. 2013; Murphy 2013), and thus the radio slope could not be a tracer of AGNs but an indicator of the surrounding environment of the nuclear starbursts and AGNs.

The top panels of Figure 9 display the radio slope within the 0.07–3.0 GHz band, α_{radio} , (Section 4.3) as a function of the SFR and the fraction of the AGN luminosity in the IR band. The previous radio study of U/LIRGs performed by Murphy (2013) reports that the median value of the radio slope at $\lesssim 5$ GHz for U/LIRGs is 0.5, and the slopes decrease with merger stage. The values in our work are well consistent with their median value and decreasing trend. The flat slope in late mergers with high SFRs ($\alpha_{\text{radio}} \sim 0.0\text{--}0.5$) can be explained by the optically-thick free-free absorption due to the rich environment of the nuclear region.¹⁶ In the right panel, the hard X-ray-detected AGNs and three

newly-identified AGN candidates are characterized as the positive values of the fraction of AGN luminosity. As mentioned above, the AGN fraction (i.e., the dominance of AGN activity) is not correlated with the radio slope for U/LIRGs.

5.2.2. Radio-IR Correlation Coefficient

Alternatively, the correlation coefficient, q_{IR} (= $\log L_{\text{IR}}/L_{1.4\text{GHz}}$; see Section 4.3), can be a complementary parameter to unveil the presence of AGNs in U/LIRGs. For star-forming galaxies, a tight correlation between radio and IR luminosities is reported (e.g., Kennicutt 1998; Bonzini et al. 2015), whose luminosity ratio is expressed by q_{IR} . For the AGN-dominant sources, the value should be small due to the powerful synchrotron emission from the AGN (e.g., Yun et al. 2001; U et al. 2012). We investigate the distribution of q_{IR} as a function of the SFR and the fraction of the AGN luminosity (bottom panels of Figure 9). Except for three outliers below the criteria specified as radio-excess ($q_{\text{IR}} < 1.64$, marked by gray dotted line; Yun et al. 2001), these U/LIRGs are distributed around the typical value of star-forming galaxies, ~ 2.64 (black dashed line; Bell 2003), without regard for merger stage and SFR. Remarkably, the sources having larger fractions of AGN luminosity tend to show smaller q_{IR} , indicating the strong radio emission due to the synchrotron radiation from the AGNs. Not only the sources with $q_{\text{IR}} < 1.64$ (Yun et al. 2001), but those with $q_{\text{IR}} < 2$ have AGNs for the U/LIRGs in our sample.

5.2.3. Radio Excess Parameter

In the left panel of Figure 10, we also compare the SFR and radio 1.4 GHz luminosities ($L_{1.4\text{GHz}}$) for U/LIRGs. The black dashed line is the empirical correlation from the radio-far-IR luminosity relation and the conversion factor between SFR and far-IR luminosity for star-forming galaxies in Kennicutt (1998), assuming Chabrier IMF (see also Bonzini et al. 2015):

$$\log(L_{1.4\text{GHz}}/\text{erg s}^{-1}) = \log(\text{SFR}) + 37.60. \quad (2)$$

Our targets roughly follow the empirical relation. Delvecchio et al. (2017) introduce a new diagnostics for AGNs by using the radio excess parameter, $q_{\text{excess}} = \log(L_{1.4\text{GHz}}/\text{SFR})$. They suggest that the sources having $q_{\text{excess}} > 38.130 \times (1+z)^{0.013}$ in $(\text{erg s}^{-1})/(M_\odot \text{ yr}^{-1})$ are likely attributable to AGN activities. As shown in the right panel, the radio-excess sources in our samples have $f_{\text{AGN}} > 0$ (i.e., hosting AGNs) in the IR band.

As a whole, the radio-excess sources in U/LIRGs host AGNs detected in the IR and X-ray bands. Whereas, the other major population of radio-quiet sources in

¹⁶ The AGNs with high-Eddington ratios also show the flat radio slope (Laor et al. 2019; Yang et al. 2020b), whose contribution of the radio emission may be smaller than those of starbursts as discussed on the correlation coefficient (q_{IR}).

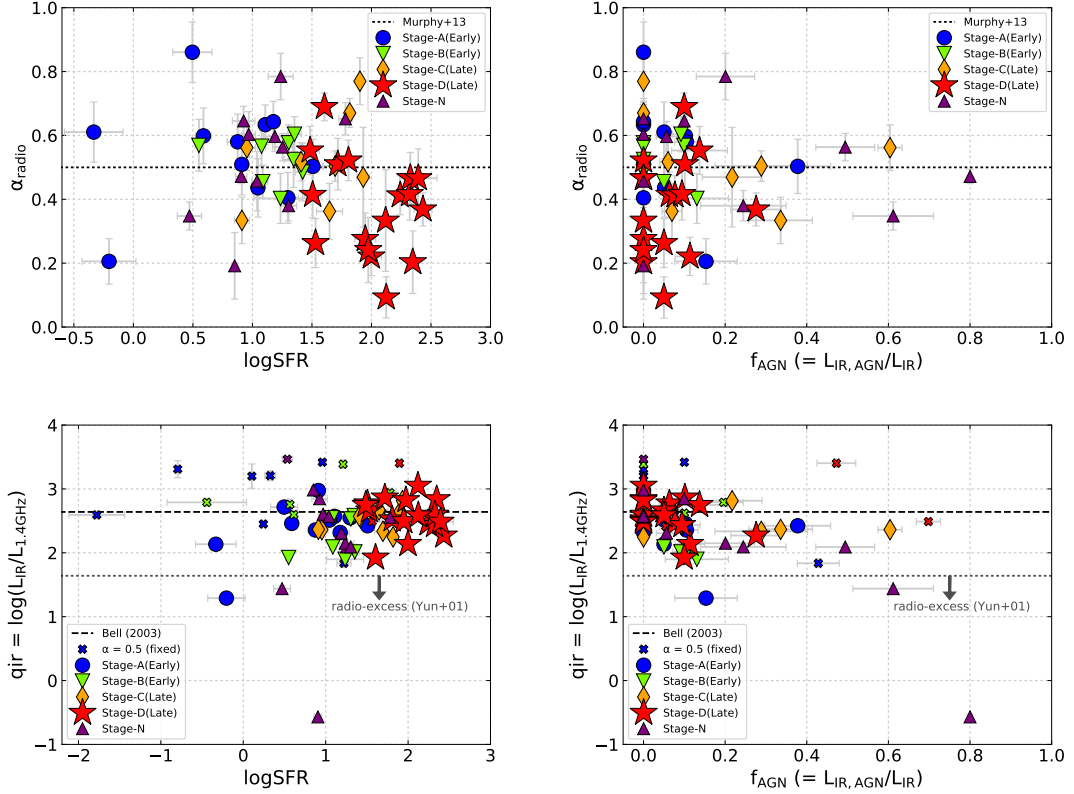


Figure 9. Top panels: logarithmic SFR vs. α_{radio} (left) and fraction of AGN luminosity in the IR band vs. α_{radio} (right), excluding the sources whose α_{radio} is fixed at 0.5. The sources with $f_{\text{AGN}} = 0.0$ mean the U/LIRGs which do not have AGNs. The dashed line is the median of low-frequency (<5 GHz) α_{radio} among U/LIRGs reported by Murphy (2013). Bottom panels: logarithmic SFR vs. q_{IR} (left) and fraction of AGN luminosity in the IR band vs. q_{IR} (right). The dashed line is the averaged values reported in Bell (2003), and the dotted gray line illustrates the threshold for radio-excess ($q_{\text{IR}} < 1.64$) as a tracer of an AGN (Yun et al. 2001; U et al. 2012). Large symbols are the same in Figure 8, while small crosses denote the sources where $\alpha_{\text{radio}} = 0.5$ is assumed in the radio fitting.

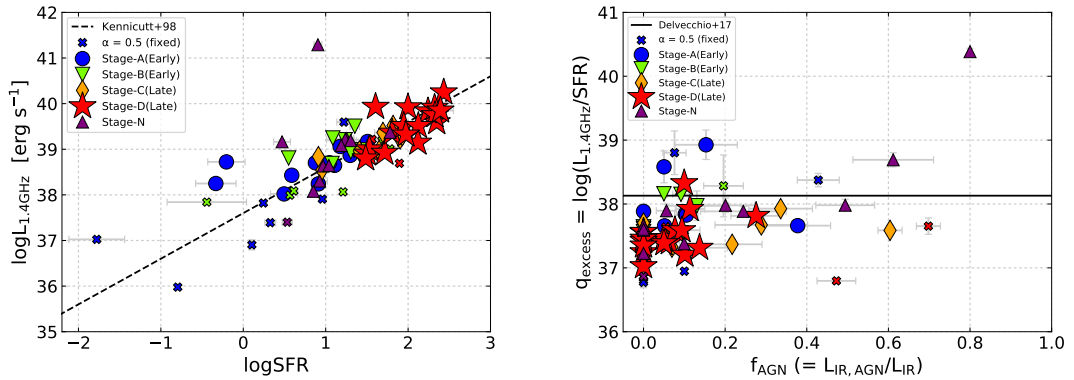


Figure 10. Left panel: logarithmic SFR vs. logarithmic radio luminosity at 1.4 GHz. The black dashed line is obtained by the empirical radio-far-IR relation in star-forming galaxies in Kennicutt (1998), assuming Chabrier IMF (see Bonzini et al. 2015). Right panel: fraction of AGN luminosity in the IR band (f_{AGN}) vs. radio excess parameter (q_{excess}). The sources with $f_{\text{AGN}} = 0.0$ mean the U/LIRGs which do not have AGNs. The black solid curve shows the threshold of radio-excess sources at $z \approx 0.0$ (Delvecchio et al. 2017). The symbols are the same in Figure 9.

U/LIRGs are indistinguishable from AGNs or not. The same results are reported for AKARI-selected star-forming galaxies with and without AGNs (Morić et al. 2010), indicating that the AGNs in U/LIRGs are typical radio-quiet AGNs in star-forming galaxies (i.e., the large contribution of the radio emission from the intense starbursts). Therefore, although sources with high q_{excess} values likely contain AGNs, the radio emission reflects the intensity of the starburst activities (e.g., SFR) for the majority of U/LIRGs.

5.3. WISE Color: New Wedge of Buried AGNs

Near-IR to mid-IR observations have been thought of as a promising tool to detect the AGN emission in U/LIRGs (e.g., Veilleux et al. 2009b; Petric et al. 2011; Imanishi & Saito 2014; Imanishi et al. 2020; Díaz-Santos et al. 2017). A large part of the emission from central AGNs in U/LIRGs is absorbed by the surrounding materials such as the torus with a large covering fraction (e.g., Imanishi et al. 2006, 2008; Ricci et al. 2017a; Yamada et al. 2019) and re-radiated chiefly in the mid-IR wavelength. The $\sim 3\text{--}30 \mu\text{m}$ SEDs of the reprocessed dust emission heated by the AGN is characterized as a steep power-law slope (e.g., Laurent et al. 2000; Stern et al. 2005; Assef et al. 2010). Indeed, the IR color selection with WISE has been exploited to search for the optically obscured AGNs (e.g., Jarrett et al. 2011; Stern et al. 2012; Mateos et al. 2012, 2013; Assef et al. 2013, 2018; Secrest et al. 2015; Toba et al. 2015; Ellison et al. 2017; Satyapal et al. 2017; Weston et al. 2017; Goulding et al. 2018a; Pfeifle et al. 2022).

5.3.1. $W1-W2$ Color

Figure 11 presents the WISE $W1-W2$ (or $[3.4]-[4.6]$) in Vega magnitude) color as a function of SFR (left) and AGN fraction in the IR band (right).¹⁷ Here, the WISE magnitudes are corrected for Galactic extinction (Section 3.8). Stern et al. (2012) introduce a simple mid-IR color criterion of $[3.4] - [4.6] > 0.8$ by using the WISE-selected sources in the Cosmic Evolution Survey (COSMOS; Scoville et al. 2007). Similarly, Satyapal et al. (2014) report that a more inclusive $[3.4] - [4.6] > 0.5$ cut identifies AGNs in low- z ($z < 0.2$) mergers selected from the SDSS survey (Ellison et al. 2013). For our U/LIRGs, we find that all late mergers have $\log \text{SFR} \gtrsim 1.5$ and $[3.4] - [4.6] \gtrsim 0.5$, while most early mergers and nonmergers have smaller

SFRs and $[3.4] - [4.6] \lesssim 0.5$, making it easy to select the IR-luminous late mergers. However, the comparison between WISE color and AGN fraction suggests that the hard X-ray-detected and newly-identified AGN candidates (i.e., $f_{\text{AGN}} > 0$) are not distinguished from the other starburst-dominant or hard X-ray-undetected sources by the $[3.4]-[4.6]$ color. These results indicate that for U/LIRGs, the $[3.4]-[4.6]$ criteria could not necessarily discriminate between the intense starbursts and the AGNs discovered with the hard X-ray observations (e.g., Ricci et al. 2016, 2017a; Yamada et al. 2021).

5.3.2. WISE Color-color Diagram

Figure 12 shows the WISE color-color diagram ($[3.4]-[4.6]$ versus $[4.6]-[12]$) for our sample. The AGN wedges that have been well utilized for the low- z galaxies are overplotted (Jarrett et al. 2011; Mateos et al. 2012; Blecha et al. 2018). Almost all late mergers are located within the AGN wedge that is based on the hydrodynamics and radiative transfer simulation of gas-rich mergers (dashed line; see Equation (1) in Blecha et al. 2018). In late mergers, it is notable that the values of $[4.6]-[12]$ magnitudes decrease with the values of $[3.4]-[4.6]$ magnitudes for the AGNs, while they increase for the other sources. Particularly, the AGNs with $[4.6]-[12] \lesssim 3$ in stage D mergers (IRAS F05189-2524, IRAS F08572+3915, UGC 5101, ESO 374-IG032, and Mrk 231) show the excess in the $\sim 3\text{--}10 \mu\text{m}$ wavelength relative to the best-fit SED models with updated CLUMPY model (Figures E1-E10), corresponding to the dust emission at the temperature of $\sim 300\text{--}1000$ K (e.g., Lyu & Rieke 2021). The contribution of the near-IR emission from the old stellar population (e.g., Polletta et al. 2007) is extracted by the multiwavelength SED analysis, the origin of the $\sim 3\text{--}10 \mu\text{m}$ excess can be explainable by the additional nuclear hot dust heated by the AGNs, such as inner part of the dusty disk and/or hot polar dust within the inner parsecs (e.g., Hönig et al. 2013; García-Bernete et al. 2017, 2022; Lyu et al. 2017; Lyu & Rieke 2021; Mattila et al. 2018; Mizukoshi et al. 2022). The near-IR excess in a sample of type 1 AGN is well reported (Netzer et al. 2007; Mor et al. 2009; Mor & Netzer 2012) and this hot dust component can also be part of the known outflows in Mrk 231 (e.g., Feruglio et al. 2015; Morganti et al. 2016; Veilleux et al. 2016). The strong near-IR emission from the dusty disk, hot polar dust, or both is a unique feature of buried AGNs in late mergers.

Although the complete selection of hard X-ray-detected AGNs by the WISE color seems to be difficult, some buried AGNs in local U/LIRGs are characterized by the near-IR excess appearing in the improved AGN

¹⁷ The WISE photometry of Mrk 231, a stage D merger hosting the AGN with high λ_{Edd} , is not utilized in the SED analysis due to the flag of $w1\text{-}3\text{sat} \approx 0.06$ ($W1, W2, W3 = 7.80 \pm 0.01, 6.58 \pm 0.01, 3.54 \pm 0.01$, respectively), but is only provided in Figures 11-12 since it will be a small effect on the WISE colors.

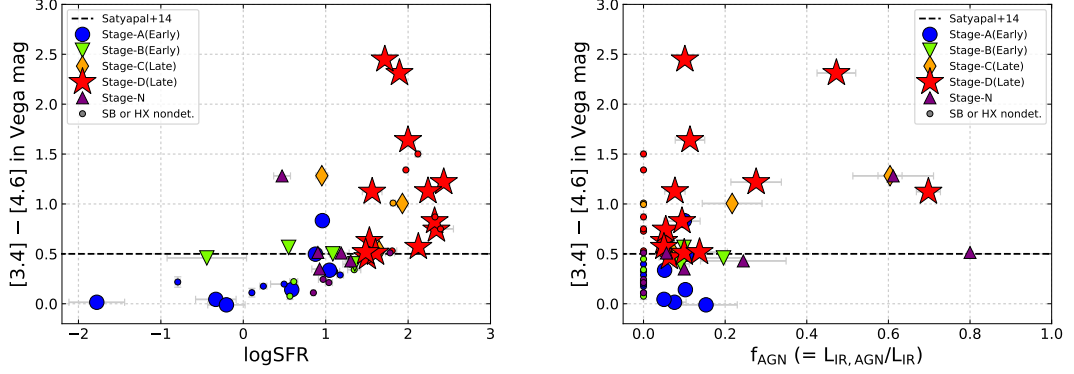


Figure 11. WISE W1–W2 color as a function of SFR (left) and the fraction of AGN luminosity in the IR band (right). Dashed line illustrates the W1 – W2 > 0.5 threshold (Satyapal et al. 2014).

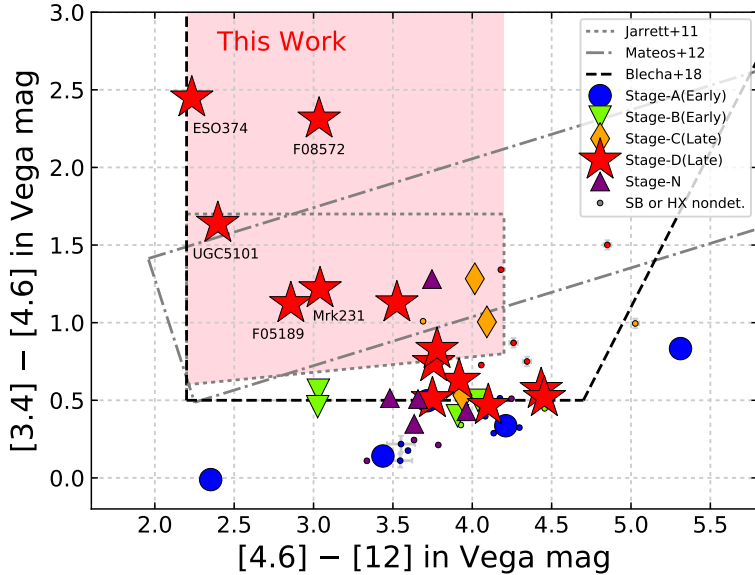


Figure 12. WISE color–color diagram. The AGN selection wedges are illustrated as the areas within the dotted gray (Jarrett et al. 2011), dash-dotted gray (Mateos et al. 2012), and black dashed (Blecha et al. 2018) boxes, and the pink shaded area is presented in This work, respectively. Large symbols are the same in Figure 8, while small circles illustrate the sources where $f_{AGN} = 0.0$ (starburst-dominant or hard X-ray–nondetected sources).

color selection (pink shade);

$$2.2 < [4.6] - [12] < 4.2, \text{ and} \\ [3.4] - [4.6] > 0.1 \times ([4.6] - [12]) + 0.38, \quad (3)$$

which are the combination of the previous AGN wedge for QSOs, Seyfert galaxies, and obscured AGNs (dotted line; see Equation (1) in Jarrett et al. 2011) and the higher $[3.4]$ – $[4.6]$ region. Among our local U/LIRGs within the new wedge, the selection purity of the AGNs in stage C–D mergers is $72^{+11}_{-12}\%$ (9/12). Here the fraction and uncertainty are the 50th and 16th–84th quantiles of a binomial distribution, respectively, calculated with the beta function (Cameron 2011).

By contrast, the completeness of selecting AGNs with the new wedge is low ($40\% \pm 10\%$; 9/23). Considering that only the most luminous AGNs (e.g., IRAS F05189–2524, IRAS F08572+3915, and Mrk 231) tend to be selected, the low completeness suggests the difficulty of the identification of low-luminous AGNs in late mergers. We also need to keep in mind that this criterion should be adopted for local U/LIRGs since it includes the typical criteria for QSOs and normal AGNs (Jarrett et al. 2011). Thus,

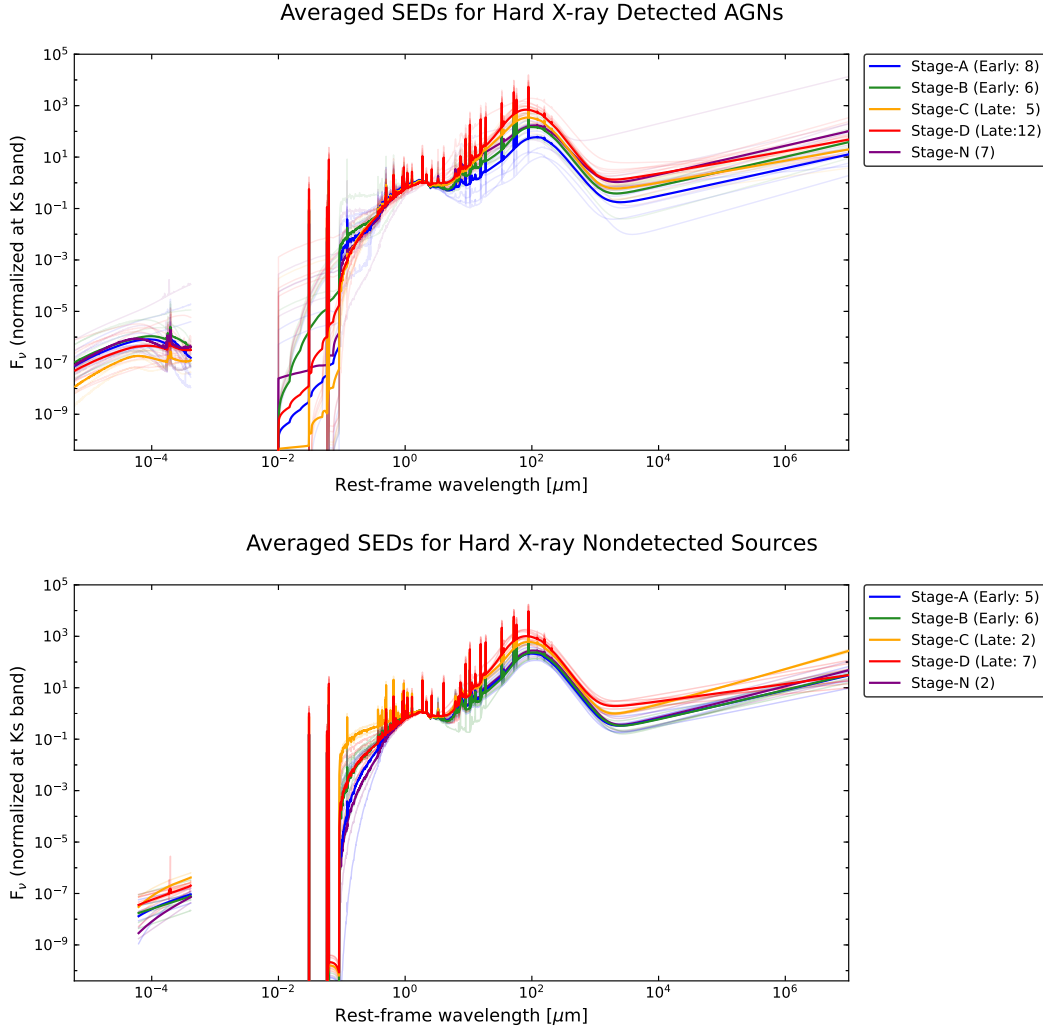


Figure 13. Top panel: rest-frame wavelength vs. flux density normalized at K_s band for the hard X-ray-detected AGNs. Bottom panel: the same but for the soft X-ray-detected galaxies among starburst-dominant or hard X-ray-nondetected sources. The solid curves represent the averaged SEDs for the sources in stage A (blue), stage B (green), stage C (orange), stage D (red) and stage N (purple) U/LIRGs. Values in parentheses are the number of sources. The light-colored curves show the SEDs for individual sources.

this new WISE color–color diagram for local U/LIRGs provides valuable information on the presence of the luminous AGNs hosting the dusty disk, hot polar dust, or both within the inner parsecs.

5.4. Averaged SEDs in U/LIRGs

To further understand the characteristics of the hard X-ray to radio emission in local U/LIRGs, in Figure 13 we illustrate the SEDs for all sources whose X-ray spectra above $\gtrsim 1$ keV are analyzed by Yamada et al. (2021). The K_s ($2.159 \mu\text{m}$) band (near the peak of the stellar emission) is selected for the normalization since it is less affected by dust extinction and contamination from AGN-heated hot dust (e.g., Kim et al. 2002; Marconi

& Hunt 2003; Skrutskie et al. 2006; Vika et al. 2012).¹⁸ The left panel shows the best-fit models of 36 single and two unresolved dual hard X-ray-detected AGNs (Mrk 266B/Mrk 266A and NGC 6240S/NGC 6240N), but excluding three newly identified AGN candidates. Here, the complex X-ray absorption lines in NGC 1365 are ignored as it is a dramatically variable feature, mainly caused by highly ionized species of Fe in a high-velocity outflow (Rivers et al. 2015). On the other hand, the right panel shows those of two starburst-dominant

¹⁸ The results are almost unchanged even if the normalization is chosen in the H band, which is also a reliable tracer of the stellar luminosity (e.g., Marconi & Hunt 2003; Hainline et al. 2011).

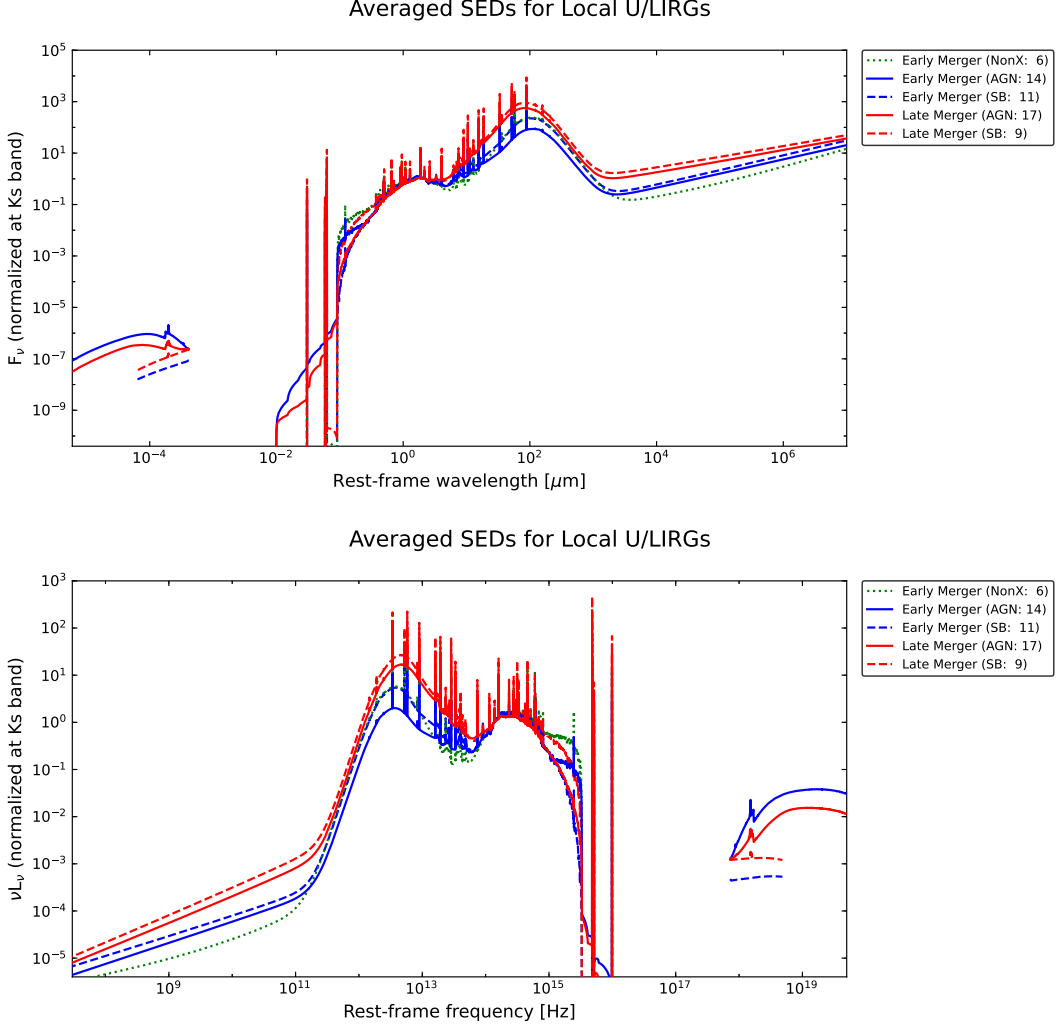


Figure 14. Top panel: rest-frame wavelength vs. flux density normalized at K_s band. Bottom panel: rest-frame frequency vs. luminosity normalized at K_s band. The dotted green curve shows the averaged SEDs for the sources whose X-ray spectra above $\gtrsim 1$ keV are not obtained in stage A–B (early) mergers. The solid curves represent the averaged SEDs for the hard X-ray-detected AGNs in stage A–B (early mergers; blue) and stage C–D (late mergers; red). The dashed curves are the same ones for the soft X-ray-detected galaxies among starburst-dominant or hard X-ray-nondetected sources. Values in parentheses are the number of sources. These SED templates are available in Table 5.

sources detected in the hard X-ray band (IC 1623A and NGC 3256) and 20 hard X-ray-undetected sources. Since the $\lesssim 3$ keV spectra are complex due to the Galactic extinction and the optically thin thermal emission in the host galaxy, we plot the best-fit models of the X-ray spectra in the 3–200 keV band for AGNs and 3–20 keV for the other sources.

These SEDs exhibit several common features in the UV-to-radio bands regardless of the presence or absence of AGNs. First, they have a dip in the UV-to-optical wavelength, even though the SEDs are corrected for Galactic extinction. The UV emission from the stellar populations and/or AGN disk is absorbed by the

gas and dust of the host galaxy, torus, and polar dust. Second, the IR-to-radio fluxes relative to the K_s band increase with merger stage due to the re-radiation from the dust of AGNs and primarily intense starbursts (Section 5.1 and Section 5.2). Third, the increase of the IR emission causes the steep slope in the near-to-mid-IR band to appear as the features in WISE [3.4]–[4.6] color (Section 5.3).

Figure 14 presents the averaged SEDs for AGNs and the other sources in both early and late mergers, whose X-ray spectra above $\gtrsim 1$ keV are analyzed. We also plot the averaged UV-to-radio SEDs for the sources whose X-ray spectra above $\gtrsim 1$ keV are not obtained, all of which

Averaged SEDs for Local U/LIRGs

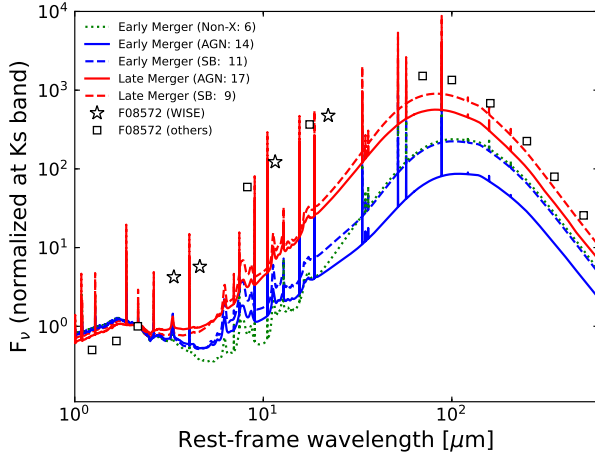


Figure 15. Enlarged picture of the IR (1–600 μm) wavelength of the left panel in Figure 14 (rest-frame wavelength vs. flux density normalized at K_s band). Stars and squares mark the photometry of WISE and other IR instruments (2MASS, AKARI, and Herschel) for the AGN in IRAS F08572+3915.

are in early mergers. These averaged SED templates in Figure 14 are available in Table 5. By comparing the AGNs (solid curves) and the others (dashed and dotted curves), we find that the averaged SEDs of the latter population show stronger far-IR fluxes than those of the former. This support that the starburst-dominant sources have cooler dust than AGNs. Whereas, the UV-to-radio SEDs of AGNs and non-AGN sources holistically resemble each other, regardless of the merger stage. The difference in the far-IR fluxes is smaller than the scattering among the individual sources as shown in Figure 13. This resemblance makes it difficult to identify the AGNs in U/LIRGs.

In Figure 15, we compare the averaged SEDs and the photometry of the buried AGNs in IRAS F08572+3915, which is one of the most luminous AGNs in our sample and is well selected by the WISE color–color diagram (Section 5.3). We find that the source shows the flux peak at shorter IR wavelengths than in normal U/LIRGs. This suggests the presence of a large amount of hot dust, which can be a unique feature of the luminous AGNs deeply hidden by gas and dust. Regardless of the presence of the IR-excess features, the X-ray spectra of AGNs and others are completely different (Figure 14). The AGNs have much larger X-ray fluxes than those in the starburst-dominant or hard X-ray-undetected sources. According to the X-ray spectral analysis in Yamada et al. (2021), the observed X-rays of AGNs become dimmed with merger stage due to

Table 5. Averaged SED Templates in Our Targets

Column Name	Format	Unit	Description
Class	LONG		Classification
Wavelength	DOUBLE	μm	Wavelength
Frequency	DOUBLE	Hz	Frequency
Normed_FNU	DOUBLE		Flux density at each wavelength
Normed_LNU	DOUBLE		Luminosity at each wavelength

(This table is available in its entirety in machine-readable form.)

the increase of the hydrogen column density, while for the starburst-dominant sources, the soft X-rays dominated by the X-ray binary emission in the host galaxy (e.g., Mineo et al. 2012) become brighter in late mergers with high SFRs than in early mergers. Overall, the AGNs show a significant X-ray excess relative to the other wavelength emission, as represented by the comparison between observed X-ray luminosity and SFR in Section 6.3 of Yamada et al. (2021). Therefore, despite the effects of the X-ray weakness (Section 5.5), the excess of X-ray fluxes relative to the UV-to-radio SEDs should be an incomparable characteristic enabling us to reveal the true energy sources (intense starbursts and/or buried AGNs) in U/LIRGs.

5.5. X-ray Weak AGNs in IR-luminous Galaxies

We finally investigate the multiwavelength AGN luminosities corrected for the absorption of the host galaxy, torus, and polar dust. Yamada et al. (2021) estimate the de-absorbed 2–10 keV AGN luminosities and find that the ratio of the bolometric AGN luminosity to the X-ray luminosity is quite large for the AGNs in late mergers. This X-ray weakness has been thought of as a particular property of the AGNs in local U/LIRGs (e.g., Teng et al. 2014, 2015), and its origin (e.g., the optically thick failed winds launched from an inner region of the disk) is discussed in Yamada et al. (2021). For understanding the AGN activities in U/LIRGs through cosmic history, it is at least necessary to probe whether the X-ray weakness is a common feature for both low- z and high- z U/LIRGs.

5.5.1. 6 μm Luminosity vs. 2–10 keV Luminosity

Figure 16 illustrates the relation between monochromatic luminosity of the AGN emission at rest-frame 6 μm derived from the multiwavelength SED decomposition ($L_{6,\text{AGN}}$) and unabsorbed (i.e., de-absorbed) X-ray luminosity in the rest-frame 2–10 keV band ($L_{\text{X},\text{unabs}}$). Many studies report that the mid-IR and X-ray luminosities of the AGN component are strongly correlated over a wide luminosity ranges (e.g., Lutz et al. 2004;

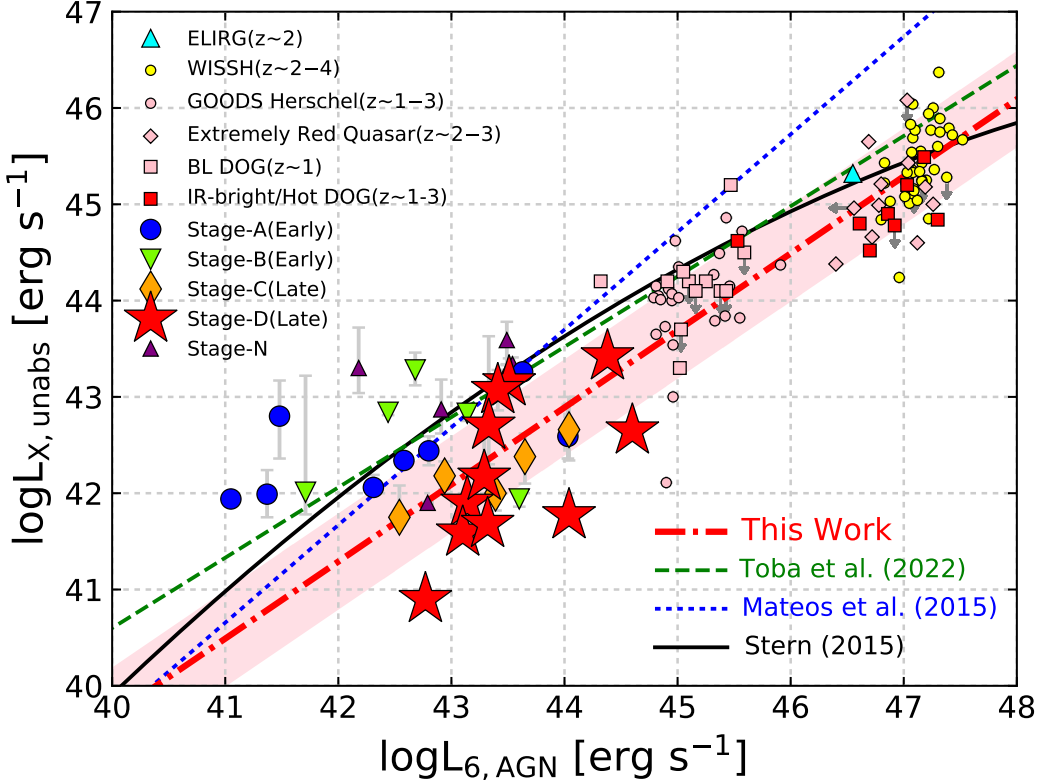


Figure 16. Rest-frame $6 \mu\text{m}$ luminosity contributed from AGNs vs. unabsorbed (absorption-corrected) rest-frame 2–10 keV luminosity for AGNs in various IR-luminous galaxies. The cyan triangle indicates an ELIRG at $z \sim 2$ (Toba et al. 2021b). The yellow circles represent WISSH quasars at $z \sim 2$ –4 (Martocchia et al. 2017; Zappacosta et al. 2020). The pink circles indicate mid-IR luminous quasars at $z \sim 1$ –3 in the GOODS-Herschel fields (Del Moro et al. 2016) while pink diamonds show extremely red quasars at $z \sim 2$ –3 (Goulding et al. 2018b). The pink and red squares mark broad-line DOGs at $z \sim 1$ (Zou et al. 2020) and IR-bright/hot DOGs at $z \sim 1$ –3 (Ricci et al. 2017c; Vito et al. 2018; Zappacosta et al. 2018; Toba et al. 2020a), respectively. Their colors (cyan, yellow, pink, and red) are largely categorized by the typical N_{H} of the populations (see the text). The other symbols are the same in Figure 8. The green dashed and blue dotted lines illustrate the linear relation using a sample drawn from the eROSITA Final Equatorial Depth Survey (Toba et al. 2022a) and the Bright Ultra-hard XMM-Newton Survey (Mateos et al. 2015), respectively. The black solid curve denotes the 2D polynomial relations from Stern (2015). Red dash-dotted line and the pink shaded area are the best-fitting relation and its 1σ dispersion among stage C–D mergers and the high- z IR-luminous sources, respectively.

Ramos Almeida et al. 2007; Gandhi et al. 2009; Ichikawa et al. 2012, 2017; Asmus et al. 2015; Mateos et al. 2015; Stern 2015; García-Bernete et al. 2016; Chen et al. 2017; Toba et al. 2019a, 2022a). Here, we plot the values for local U/LIRGs color-coded by merger stages, and overplot those for IR-luminous galaxies corresponding to high- z U/LIRGs: an extremely luminous IR galaxy (ELIRG) at $z \sim 2$ (Toba et al. 2021b); WISE/SDSS selected hyper-luminous (WISSH) quasars at $z \sim 2$ –4 (Martocchia et al. 2017; Zappacosta et al. 2020); mid-IR luminous quasars at $z \sim 1$ –3 from the GOODS-Herschel fields (Del Moro et al. 2016); extremely red quasars at $z \sim 2$ –3 (Goulding et al. 2018b); dust-obscured galaxies (DOGs) with broad optical/UV emission lines (BL

DOGs) at $z \sim 1$ (Zou et al. 2020); and IR-bright DOGs at $z \sim 1$ (Toba et al. 2020a) and hot DOGs at $z \sim 1$ –3 (Ricci et al. 2017c; Vito et al. 2018; Zappacosta et al. 2018).¹⁹ The values of $L_{6,\text{AGN}}$ and $L_{\text{X},\text{unabs}}$ for high- z IR-luminous galaxies are presented in their references mostly by the IR SED decomposition and X-ray spectral analysis, respectively. The AGNs are unobscured

¹⁹ The $L_{6,\text{AGN}}$ of extremely red quasars in Goulding et al. (2018b) and hot DOGs in Ricci et al. (2017c) are provided by assuming that the $6 \mu\text{m}$ emission is AGN-dominant (see e.g., Del Moro et al. 2016 for extremely red quasars; e.g., Stern et al. 2014; Assef et al. 2016, 2020; Tsai et al. 2018; Zappacosta et al. 2018 for hot DOGs).

($\lesssim 10^{22} \text{ cm}^{-2}$) for an ELIRG (cyan), weakly obscured ($\sim 10^{21}\text{--}10^{23} \text{ cm}^{-2}$) for WISSH quasars (yellow), moderately obscured ($\sim 10^{22}\text{--}10^{24} \text{ cm}^{-2}$) for mid-IR luminous quasars in the GOODS-Herschel fields, extremely red quasars, and BL DOGs (pink), and heavily obscured ($\gtrsim 10^{23} \text{ cm}^{-2}$) for IR-bright/hot DOGs (red). Moreover, we compare these values with the typical relation obtained from the SDSS-selected low- z Seyfert galaxies (Stern 2015), the Bright Ultra-hard XMM-Newton Survey (BUXS; Mateos et al. 2015), and the eROSITA Final Equatorial Depth Survey (eFEDS; Toba et al. 2022a).

We find that several late mergers of local U/LIRGs lie below the typical $L_{6,\text{AGN}}\text{--}L_{X,\text{unabs}}$ relation, supporting the X-ray weakness. For late mergers (stage C and D) and high- z IR-luminous galaxies, we conduct a Bayesian maximum likelihood method of Kelly (2007) between the two parameters. The resulting linear function is

$$\log(L_{X,\text{unabs}}) = 0.80 \log(L_{6,\text{AGN}}) + 7.69, \quad (4)$$

and the 1σ dispersion is ± 0.50 dex (red dashed line and pink shaded area). The correlation coefficient is $r = 0.92 \pm 0.02$, confirming a tight correlation for low- z and high- z IR-luminous sources. These AGNs in the IR-luminous sources at $z \sim 0\text{--}4$ are obscured sources and show smaller de-absorbed X-ray luminosities relative to the mid-IR luminosities than the typical relations. In particular, most AGNs in IR-bright/hot DOGs are heavily obscured ($\gtrsim 10^{23} \text{ cm}^{-2}$) and explicitly X-ray weak among them (e.g., Ricci et al. 2017c; Toba et al. 2020a), sharing similarity with the X-ray weak AGNs in late mergers for local U/LIRGs (Yamada et al. 2021).

5.5.2. Optical to X-ray Spectral Index

Additionally, we display the comparison between Eddington ratio (λ_{Edd}) and the optical to X-ray spectral index (α_{OX} ; Tananbaum et al. 1979) in Figure 17. The definition of α_{OX} is provided by using the monochromatic luminosity at rest-frame 2500 Å of the intrinsic AGN disk emission ($L_{2500,\text{disk}}$) and the de-absorbed monochromatic luminosity at rest-frame 2 keV ($L_{2\text{keV},\text{unabs}}$) as below:

$$\alpha_{\text{OX}} = \frac{\log(L_{2\text{keV},\text{unabs}}/L_{2500,\text{disk}})}{\log(\nu_{2\text{keV}}/\nu_{2500})}. \quad (5)$$

The $L_{2500,\text{disk}}$ is obtained by multiwavelength SED analysis in this work, and $L_{2\text{keV},\text{unabs}}$ is calculated from the best-fit models of the broadband X-ray spectra (Section 3.1). The α_{OX} probes the balance between the accretion disk and hot corona activities, radiating optical and X-ray emission respectively. Several works report a moderate correlation between the Eddington ratio and α_{OX} (e.g., Lusso et al. 2010; Chiarello et al.

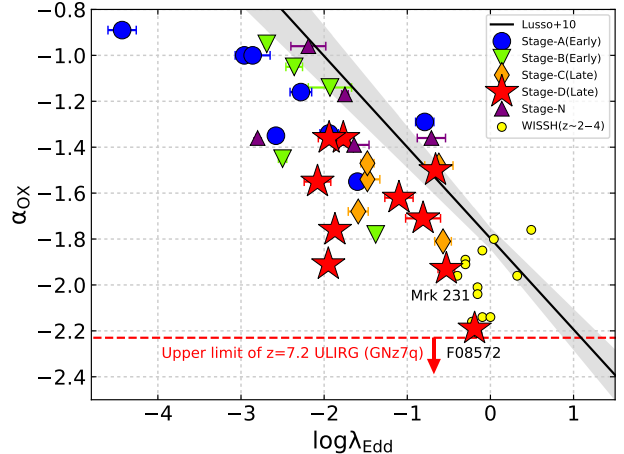


Figure 17. Logarithmic Eddington ratio vs. α_{OX} computed using extinction-corrected 2500 Å and unabsorbed 2 keV luminosities. The black solid curve represents the best-fit relation among local and high- z AGNs, respectively (Lusso et al. 2010). The gray shaded area shows its 1σ uncertainty. The upper limit of a ULIRG at $z = 7.2$ (GNz7q; Fujimoto et al. 2022) is shown as a red dashed line since its SMBH mass and Eddington ratios are not constrained. Yellow circles mark the WISSH quasars in $z \sim 2\text{--}4$ (Zappacosta et al. 2020). The other symbols are the same in Figure 8.

2018) for X-ray selected AGNs and a typical relation of Lusso et al. (2010) is illustrated by a black solid line in Figure 17. We overplot the values of WISSH quasars (yellow circles; Martocchia et al. 2017; Zappacosta et al. 2020), and the upper limit of α_{OX} (< -2.23) provided with deep Chandra observation for a $z = 7.2$ red quasar GHZ7q, classified as U/LIRG (red dashed line; Fujimoto et al. 2022).

Although the Eddington ratios contain uncertainties of about ± 0.5 dex originating from the M_{BH} measurements (Yamada et al. 2021), some AGNs in stage D mergers show much smaller α_{OX} than the typical relation. The distribution of α_{OX} for X-ray selected and optical-selected AGNs (Just et al. 2007; Lusso et al. 2010; Dong et al. 2012; Martocchia et al. 2017; Chiarello et al. 2018) mostly covers from -1.0 to -2.0 . Whereas, we find that the local stage-D mergers with the largest AGN luminosities (Mrk 231 and IRAS F08572+3915), many WISSH quasars, and GHZ7q lie $\alpha_{\text{OX}} \lesssim -2$. The caveat is that the X-ray luminosity of GHZ7q is only corrected for Galactic absorption, but the Chandra observation of GHZ7q confirms the lack of rest-frame hard X-rays, and the significant UV emission suggests the AGN is not heavily obscured. Its bolometric AGN luminosity estimated by the optical-to-millimeter SED analysis is $(1.7 \pm 0.1) \times$

10^{46} erg s $^{-1}$, which is ~ 7 times larger than that of IRAS F08572+3915 ($L_{\text{AGN,int}} \sim 2.5 \times 10^{45}$ erg s $^{-1}$). Unless the AGN of GHz7q has an extreme Eddington ratio above $\lambda_{\text{Edd}} \sim 10$, the upper limit of α_{OX} suggests the possibility that the AGN is also X-ray weak.

5.5.3. X-ray Weakness as a Common Feature

In summary, considering the small values of $L_{\text{X,unabs}}/L_{6,\text{AGN}}$ ratio and α_{OX} , the de-absorbed multiwavelength SEDs support that the *X-ray weakness may be a common feature* among the AGNs in IR-luminous galaxies over cosmic history ($z \sim 0\text{--}7$). Intriguingly, the strong AGN-driven outflows have been discovered from the $z \lesssim 1$ U/LIRGs (e.g., Chen et al. 2020) and the high- z IR-luminous galaxies such as WISSH quasars (Bischetti et al. 2017; Travascio et al. 2020; Vietri et al. 2022), extremely red quasars (Zakamska et al. 2016; Hamann et al. 2017; Goulding et al. 2018b), and IR-bright and hot DOGs (e.g., Ricci et al. 2017c; Toba et al. 2017a,b; Wu et al. 2018; Finnerty et al. 2020). As discussed in Section 6.1.6 of Yamada et al. (2021) for local late-stage U/LIRGs, the physical mechanism of the extreme X-ray weakness (e.g., the X-ray attenuation due to overionized optically-thick failed winds at $\sim 10^2\text{--}10^3 r_g$) can enhance the UV-driven winds, which may effectively trigger the massive outflows in low- z and high- z U/LIRGs.

5.6. Summary of Multiwavelength Features

Here, we summarize the multiwavelength features of local U/LIRGs. The component galaxies in early mergers have a wide range of SFRs above and below the MS, while galaxies in late mergers have the highest SFRs above the MS. Similar SFR– M_* distributions of AGNs and non-AGN sources imply the small influence of the AGN activities on the star formation in the phase of U/LIRGs (Section 5.1). The flat slope of radio emission in late mergers may be caused by the optically-thick free-free absorption due to the rich environment of the nuclear region. The SFRs are correlated with radio luminosity, indicating the major origin of the radio emission is from the starburst emission except for the radio-excess AGNs (Section 5.2). In the WISE color-color diagram, we propose a new wedge of the buried AGNs in late mergers. The strong near-IR emission of the hard X-ray-detected AGNs in late mergers suggests that they host the dusty disk and/or hot polar dust within the inner parsecs (Section 5.3). The averaged SEDs suggest that the excess of the X-rays is an incomparable characteristic enabling us to reveal the true energy sources (intense starbursts and/or buried AGNs) in U/LIRGs (Section 5.4). The absorption-corrected AGN SEDs show the extreme X-ray weakness

relative to the other wavelengths. This may be a common feature among the AGNs in IR-luminous galaxies over the cosmic history ($z \sim 0\text{--}7$), whose mechanism will be related to their massive outflows (Section 5.5). In short, our results support that (1) the intense starburst and buried AGNs occur in late mergers and (2) these buried AGNs may have dusty disks and/or hot polar dust, whose X-ray weakness may be related to the massive outflows.

6. DISCUSSION I: EVOLUTION OF POLAR DUST IN U/LIRGS

In this Section, we investigate the structure of polar dust in U/LIRGs based on the results of the multiwavelength SED analysis. The detailed results of the polar dust are discussed on the obscuration and luminosity (Section 6.1), gas-to-dust ratio (Section 6.2), the contribution to the IR AGN luminosity (Section 6.3), polar dust temperature (Section 6.4), and the unified view of the polar dust structure in U/LIRGs (Section 6.5).

6.1. Obscuration and Luminosity

The top left panel of Figure 18 presents the histograms of the line-of-sight extinction in the V band by the torus ($A_{V,\text{torus}}^{(\text{LOS})}$), while the bottom left panel shows for polar dust extinction ($A_{V,\text{polar}}^{(\text{LOS})}$). The dust extinction of the polar dust is calculated with $R_V = 3.1$ (Cardelli et al. 1989) and given when $90^\circ - i > \sigma$ (Section 4.1.3). We note that the values are much smaller than those of torus due to the initial condition of $E(B - V) = 0\text{--}0.8$ mag (Section 4.2.2 and 4.2.3; see e.g., Buat et al. 2021). We compare the histograms of different groups of unobscured, obscured, and CT AGNs. As expected from the dominance of the torus in the dust extinction, the $A_{V,\text{torus}}^{(\text{LOS})}$ becomes larger with the line-of-sight AGN obscuration in the X-ray band. Whereas, $A_{V,\text{polar}}^{(\text{LOS})}$ does not show any positive correlation with the X-ray obscuration. Considering that the hydrogen column densities mainly reflect the absorption by the broad line region and/or torus for obscured AGNs (e.g., Tanimoto et al. 2020; Ogawa et al. 2021; Andonie et al. 2022)²⁰, the decorrelation between $A_{V,\text{polar}}^{(\text{LOS})}$ and AGN types will be derived by the difference in the scales of the torus (~ 1 pc) and the extended polar dust emission ($\sim 10\text{--}1000$ pc; see Section 6.5) whose typical temperatures are allowed between 100–250 K (Section 4.2.3).

²⁰ Particularly for U/LIRGs, the AGNs show the dramatic variability in N_{H} , supporting the presence of compact-scale (a few parsecs) obscurer (Laha et al. 2020; Yamada et al. 2021).

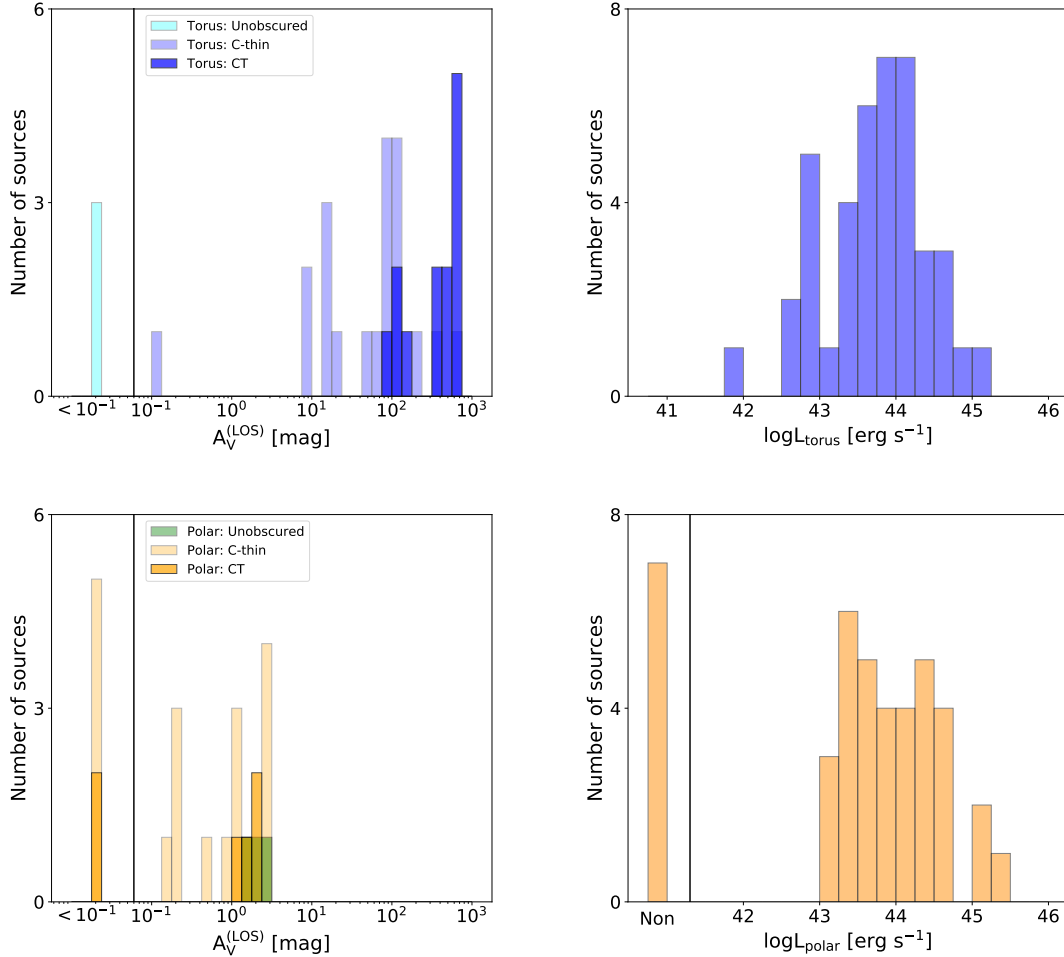


Figure 18. Top left panel: histogram of the line-of-sight extinction in the V band by the torus $A_{V,\text{torus}}^{(\text{LOS})}$ (top). These are divided by the X-ray AGN classification (unobscured, Compton-thin, and CT AGNs; Yamada et al. 2021). Bottom left panel: the same for the polar dust extinction, $A_{V,\text{polar}}^{(\text{LOS})}$ (bottom). The seven sources showing $90^\circ - i > \sigma$ (i.e., $A_{V,\text{polar}}^{(\text{LOS})} = 0$) are excluded. Top right panel: histogram of the torus (top) luminosity in the UV-to-IR band. Bottom right panel: the same for polar dust luminosity. The number of AGNs whose best-fit SED models do not include a polar dust component is shown on the left side.

In the top right panel, we illustrate the distributions of the integrated UV-to-IR (mainly IR) torus (L_{torus}), and in the bottom right panel for polar dust luminosities (L_{polar}). They cover the ranges of $\log L_{\text{torus}}/(\text{erg s}^{-1}) \sim 42\text{--}45$ and $\log L_{\text{polar}}/(\text{erg s}^{-1}) \sim 43\text{--}45.5$, respectively. Although seven sources show no signatures of the polar dust emission (Section 4.2.4), the distribution of the polar dust luminosities is larger than that of the torus ones. This is in agreement with the high-spatial-resolution mid-IR imaging by Asmus (2019), who reports that a large part of the mid-IR luminosities is derived from the extended emission.

6.2. Gas-to-dust Ratio

The comparison between X-ray absorption and dust extinction has been investigated to evaluate the gas-to-

dust ratio. The X-rays trace all material of gas and dust (N_{H}), and the optical-to-IR emission primarily traces the dust component (A_{V}). Maiolino et al. (2001) report that the $N_{\text{H}}/A_{\text{V}}$ ratios are larger than the Galactic value ($N_{\text{H}}/A_{\text{V}} = 1.87 \times 10^{21} \text{ cm}^{-2} \text{ mag}^{-1}$; Draine 2003), while for unobscured AGNs those are smaller (see also Burtscher et al. 2016). Recent works with the torus models of CLUMPY and XCLUMPY, but not including the polar dust component, (Miyaji et al. 2019; Tanimoto et al. 2020; Ogawa et al. 2021) support that the $N_{\text{H}}/A_{\text{V}}$ values are higher than or similar to the Galactic value for obscured AGNs, but smaller for unobscured AGNs. Ogawa et al. (2021) suggest that the trend could be explained if the torus angular widths are overestimated in the IR band due to the contamination from the polar dust emission.

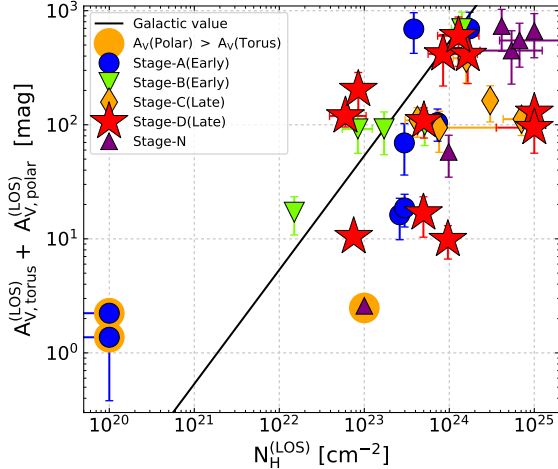


Figure 19. Line-of-sight hydrogen column density $N_{\text{H}}^{(\text{LOS})}$ derived from X-ray spectra vs. $A_{V,\text{torus}}^{(\text{LOS})}$, and polar dust, $A_{V,\text{polar}}^{(\text{LOS})}$ (if $90^\circ - i > \sigma$, $A_{V,\text{polar}}^{(\text{LOS})} = 0$). Solid line shows the Galactic gas-to-dust ratio ($N_{\text{H}}/A_{\text{V}} = 1.87 \times 10^{21} \text{ cm}^{-2} \text{ mag}^{-1}$; Draine 2003). Large orange circles mark the AGNs showing $A_{V,\text{polar}}^{(\text{LOS})} > A_{V,\text{torus}}^{(\text{LOS})}$. The other symbols are the same in Figure 8.

Our SED decomposition provides the values of $A_{V,\text{torus}}^{(\text{LOS})}$ and $A_{V,\text{polar}}^{(\text{LOS})}$. In Figure 19, we compare the X-ray obscuration and dust extinction. The three AGNs with $A_{V,\text{torus}}^{(\text{LOS})} < A_{V,\text{polar}}^{(\text{LOS})}$ have a wide range of gas-to-dust ratios. As mentioned in Section 6.1, both parameters may trace the different regions of a compact torus in X-rays and extended polar dust in the optical-to-IR bands, respectively. Except for them, the AGNs with $N_{\text{H}} > 10^{22} \text{ cm}^{-2}$ in our U/LIRGs show $A_{V,\text{torus}}^{(\text{LOS})} > A_{V,\text{polar}}^{(\text{LOS})}$, meaning the small contribution of the polar dust component to the dust extinction. We find that the obscured AGNs have similar or higher $N_{\text{H}}/A_{\text{V}}$ ratios than the Galactic one, indicating that the materials on the compact (a few parsecs) scales in the U/LIRGs show a large gas-to-dust ratio.

Similarly, it is reported that the gas-to-dust mass ratio ($M_{\text{gas}}/M_{\text{dust}}$) is $\sim 200\text{--}300$ for local ULIRGs (e.g., Seaquist et al. 2004), which is larger than the Galactic value. These results may be explainable mainly by two scenarios. The first scenario is that the A_{V} decreases by the destruction of the small dust grains by supernova shocks and/or expelled by strong AGN winds (e.g., Draine & Salpeter 1979; Jones et al. 1994; Savage & Sembach 1996; Maiolino et al. 2001; Gaskell et al. 2004; Liang et al. 2004; Rupke et al. 2008; Mannucci et al. 2010; Roseboom et al. 2012; Asano et al. 2013; Rémy-Ruyer et al. 2014). The second is that the N_{H} increases

by dust-free gas clouds covering the line-of-sight in BLR of the AGN (e.g., Granato et al. 1997; Burtscher et al. 2016; Ichikawa et al. 2019; Ogawa et al. 2021; Mizukoshi et al. 2022). More investigations are needed to reveal the origin of the large gas-to-dust ratios in U/LIRGs.

3.3. Contribution to the IR AGN Luminosity

The torus and polar dust luminosities in the UV-to-IR bands are primarily determined by the total AGN luminosity times their apparent covering fractions (and/or large volumes). Considering the averaged torus angular width is $\sigma \sim 20^\circ$ (Ogawa et al. 2021; Yamada et al. 2021), the apparent covering fractions of polar dust can be expected as $\Omega/4\pi = 1 - \sin(20^\circ) \sim 0.66$. The polar dust luminosities are ~ 2 times larger than those of the torus component (left panel of Figure 20; see also Section 6.1). If polar dust is likely the dust component of the AGN-driven outflows, their activities should be correlated with the Eddington ratios. Although it is natural under the situation that the polar dust luminosities are proportional to the AGN luminosities, we confirm the positive correlation between the polar dust luminosities and Eddington ratios in our sample.

In the X-rays, it is thought that the torus covering fractions of Compton-thin matters becomes smaller with larger Eddington ratios due to the radiation pressure from the AGN (Ricci et al. 2017d, 2022). By analyzing the broadband X-ray spectra with XCLUMPY, Yamada et al. (2021) find that the individual torus covering fraction for AGNs in U/LIRGs follow the typical relation, except for two buried AGNs with $\lambda_{\text{Edd}} \sim 1$ in stage-D mergers. On the other hand, the torus angular width (or covering fraction) in the IR band with CLUMPY (Ichikawa et al. 2015; García-Bernete et al. 2019) are larger than those of X-ray results with XCLUMPY, supporting the significant polar dust emission (Ogawa et al. 2021).

Several works with other AGN models calculate the torus covering fractions in the IR band by using the conversion factor from the $L_{\text{torus}}/L_{\text{AGN,int}}$ (e.g., Stalevski et al. 2016; Ichikawa et al. 2019). However, considering that the polar dust is thought to be a hollow-cone structure (e.g., Höning 2019; Isbell et al. 2022), it is difficult to calculate the true covering fractions of the polar dust assuming the uniform conical distribution (Yang et al. 2020a). In Figure 21, we investigate the UV-to-IR luminosities relative to the intrinsic AGN disk luminosity ($L_{\text{AGN,int}}$) for the torus and polar dust components, as a function of the Eddington ratio. As noted above, the $L_{\text{torus}}/L_{\text{AGN,int}}$ ratios are smaller than those of polar dust, and both simple luminosity ratios are not well correlated with Eddington ratios.

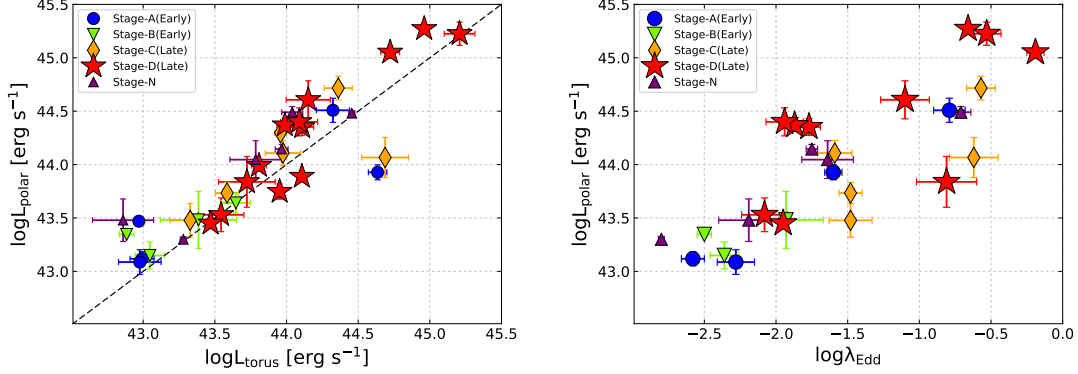


Figure 20. Left panel: logarithmic torus luminosity vs. logarithmic polar-dust luminosity in the UV-to-IR bands. Right panel: logarithmic Eddington ratio vs. logarithmic polar-dust luminosity. The symbols are the same in Figure 8.

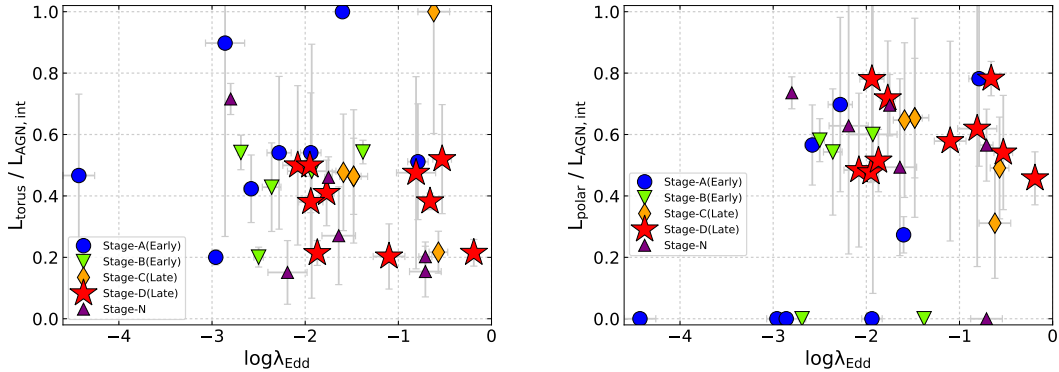


Figure 21. Left panel: logarithmic Eddington ratio vs. ratio of the torus and intrinsic AGN luminosities. Two AGNs whose luminosity ratio above 1 are plotted as $L_{\text{torus}}/L_{\text{AGN,int}} = 1$. Right panel: logarithmic Eddington ratio vs. ratio of polar dust and intrinsic AGN luminosities. The symbols are the same in Figure 8.

We find that the AGNs with $L_{\text{polar}}/L_{\text{AGN,int}} > 0.5$ have the Eddington ratios of $\log \lambda_{\text{Edd}} \gtrsim -3.0$. In the X-ray band, Fabian et al. (2008) proposed the $N_{\text{H}}-\lambda_{\text{Edd}}$ diagram to evaluate the presence of outflow, where dusty clouds are pushed away by radiation pressure against the gravitational force. In our sample, the AGNs with higher Eddington ratios than the criteria show multi-scale outflows, such as UFO, ionized outflow, and molecular outflows (Yamada et al. 2021). Recently, Venanzi et al. (2020) compute similar diagnostics for the IR-dominant outflows (i.e., polar dust). When the AGN radiative acceleration and gravity are equal ($a_{\text{AGN}} = a_{\text{g}}$), the dusty outflows are pushed away for the AGNs with $\log \lambda_{\text{Edd}} \gtrsim -2.5$ assuming $N_{\text{H}} \approx 10^{22} \text{ cm}^{-2}$ or $\log \lambda_{\text{Edd}} \gtrsim -3.0$ assuming $N_{\text{H}} \approx 10^{21.5} \text{ cm}^{-2}$ (see also Alonso-Herrero et al. 2021). Thus, the decline of the polar dust luminosity for low-Eddington AGNs is consistent with the theoretical prediction of the IR-dominant dusty winds caused by the radiation pressure.

6.4. Polar Dust Temperature

In this study, we newly constrain the polar dust temperature (T_{polar}) for the AGNs in U/LIRGs, thanks to the combination of X-ray spectroscopy and multiwave-length SED analysis. Figure 22 provides the relation between the polar dust luminosity and its temperature. For these AGNs with signs of the polar dust emission, we find that the averaged values of polar dust luminosity increase from early mergers ($\log(L_{\text{polar}}/\text{erg s}^{-1}) = 43.53 \pm 0.43$) to late mergers (44.22 ± 0.55 ; see Table 4). On the other hand, the polar dust temperature appears to decrease with merger stage. Here, it is notable that the T_{polar} mostly lie in the range of ~ 100 – 200 K, which are in good agreement with the researches of the IR interferometric observations and IR SED analysis as listed in Section 4.2.3. Even though the SED fitting with the range of T_{polar} within 100–300 K is examined, we confirm that the results are almost unchanged.

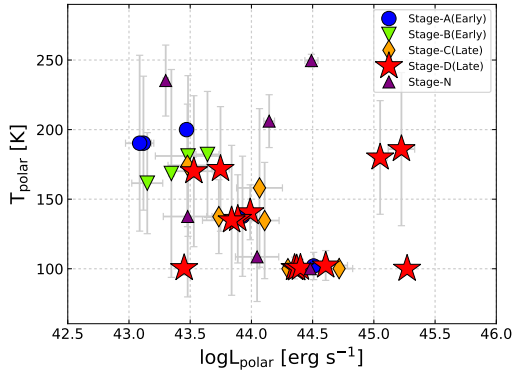


Figure 22. Logarithmic polar-dust luminosity vs. polar-dust temperature. The symbols are the same in Figure 8.

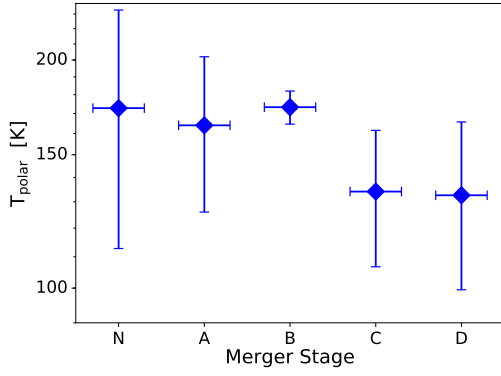


Figure 23. Differences in the polar-dust temperature with merger stage, described in the logarithmic scale. Diamonds and uncertainties represent the averaged value and 1σ dispersions, respectively.

To confirm the trend of the polar dust temperature, we also compare the averaged values with merger stages as illustrated in Figure 23. Notably, the temperatures of late mergers (~ 130 K) decline from the values of early mergers or nonmergers (~ 170 K). Although the allowed range is above 100 K, these averaged values are much larger than the dust temperature of the ISM in local U/LIRGs and high- z submillimeter galaxies (~ 20 –60 K; e.g., Casey 2012; Clements et al. 2018; da Cunha et al. 2021). All AGNs in late mergers show significant signs of the presence of polar dust emission (Section 4.2.4). Taking into account the high AGN luminosities (proportional to polar dust luminosity; Section 6.3) in late mergers, the decline of the dust temperature within the inner parsecs seems to be unlikely. The preferable reason is that the polar dust emission is radiated farther away from the center (see also e.g., Lyu & Rieke 2018; Buat

et al. 2021), implying the development of the physical size of the polar dust structure.

6.5. Polar Dust Structure

6.5.1. Physical Size of the Polar Dust

Finally, we estimate the physical size of the polar dust for local U/LIRGs by using the polar dust temperature. For a simple analytic model, the luminosity absorbed by dust grains at a distance (r) from the central radiation source, L_{abs} , is calculated by the following equation (see also e.g., Barvainis 1987; Hönig & Kishimoto 2011; Venanzi et al. 2020):

$$L_{\text{abs}} = 16\pi r^2 Q_{\text{abs};P}(T)\sigma_{\text{SB}}T^4, \quad (6)$$

where $Q_{\text{abs};P}(T)$ is the Planck mean absorption efficiency and σ_{SB} is Stefan–Boltzmann constant. The polar dust model in our multiwavelength SED analysis assumes the dust emissivity of $\beta = 1.6$ (e.g., Draine & Lee 1984; Casey 2012; Yang et al. 2020a), and the $Q_{\text{abs};P}(T)$ is proportional to $T^{1.6}$. The typical scales of polar dust (R_{polar}) can be estimated by solving the equation:

$$R_{\text{polar}} = r_{\text{sub}} \times (T_{\text{polar}}/1500 \text{ K})^{-2.8}. \quad (7)$$

The r_{sub} is the sublimation radius at the temperature of $T_{\text{sub}} = 1500$ K and can be calculated by $r_{\text{sub}} = 0.4 \times (L_{\text{AGN,int}}/10^{45} \text{ erg s}^{-1})^{1/2}$ pc in the CLUMPY model (Nenkova et al. 2008a,b). Table A5 lists the estimates of R_{polar} for the U/LIRGs in our sample.

In the top panel of Figure 24, we present the relation between the intrinsic (bolometric) AGN disk luminosity and R_{polar} . The linear regression analysis in log–log space is performed for the targets by using the Bayesian maximum-likelihood method (Kelly 2007). The best-fitting relation (red dashed line) is

$$\log(R_{\text{polar}}) = 0.78 \log(L_{\text{AGN,int}}/\text{erg s}^{-1}) - 32.40. \quad (8)$$

Its 1σ dispersion is ± 0.35 dex and the correlation coefficient is 0.80, implying a tight relation.

It is notably that the radius of the polar dust emission measured by the high-spatial-resolution imaging in the mid-IR 12 μm band (Asmus 2019) for U/LIRGs (gray diamond) and normal galaxies (gray square) are well consistent with the best-fitting relation. For NGC 1068, the compact radius of the mid-IR emission (~ 54 pc) relative to the AGN luminosity is in good agreement with our estimate ($R_{\text{polar}} \sim 45$ pc). The distribution of the R_{polar} obtained from our methods and by the mid-IR images (Asmus 2019) shows a steeper slope (~ 0.8) than the relationship with the constant temperature (0.5). This supports that the typical polar dust temperatures

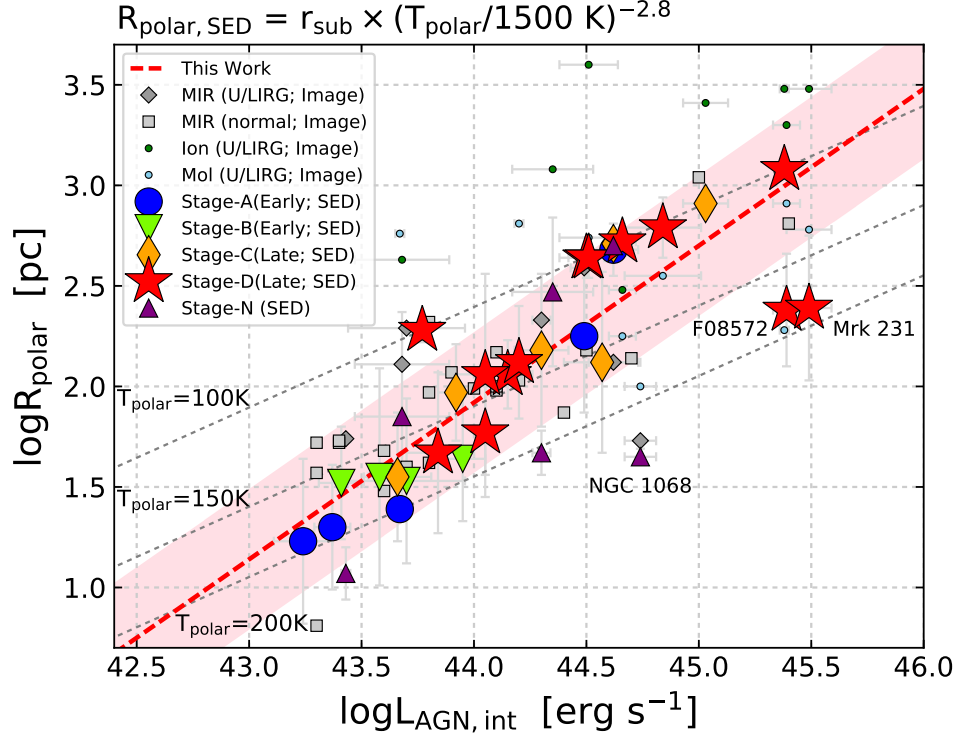


Figure 24. Top panel: logarithmic intrinsic AGN luminosity vs. logarithmic physical size of the dominant IR emission from the polar dust, estimated from the sublimation radius and polar dust temperature. The dashed red line and pink shade show the best-fitting linear relation and its 1σ dispersion among the AGNs, respectively. The green circles illustrate the physical size of ionized outflows measured with optical IFU observations, and light blue circles mark the size of molecular outflows measured with submillimeter observations in the subsample of our U/LIRGs (Fluetsch et al. 2019, 2021). The gray diamonds and small circles denote the sizes of extended mid-IR emission for U/LIRGs and non-U/LIRG sources respectively (Asmus 2019). For the size of molecular outflows and extended mid-IR region, the bolometric AGN luminosities of U/LIRGs are adopted to the estimates in this study, while those of non-U/LIRGs are calculated as the X-ray luminosity (Asmus 2019) times 20 (e.g., Vasudevan & Fabian 2007). The other symbols are the same in Figure 8. Bottom panel: schematic picture of the AGN structure (polar dust, NLR, torus, failed winds, accretion disk, and SMBH) in U/LIRGs.

decrease with AGN luminosity or physical size of the polar dust (R_{polar}).

It should be emphasized that Equation (6) can be generally applied to an optically thin, continuous dust environment. Whereas, the extinction of the polar dust in the V band is not ($A_{V,\text{polar}}^{(\text{LOS})} \sim 1-3$; see Section 6.1). A plausible explanation of this discrepancy is that the polar dust consists of optically thin layers of otherwise optically thick dust clouds, where the temperature and emission profile is dominated by direct heating from the central source (Hönig & Kishimoto 2010, 2011).²¹ This is consistent with the radiative hydrodynamic (RHD) simulations expecting that the polar dust structure would be smoothly distributed with most substructure being filamentary and/or clumpy (Wada et al. 2009; Wada 2012; Schartmann et al. 2011; Dorodnitsyn et al. 2012; Chan & Krolik 2016, 2017; Dorodnitsyn & Kallman 2017; Williamson et al. 2019).

If the polar dust structure is a bipolar hollow cone with the opening angle of $\theta_1-\theta_2$, its volume (V_{polar}) is calculated by:

$$\begin{aligned} V_{\text{polar}} &= 2 \times (4/3)\pi r^3 \times 2\pi[1 - (\cos(\theta_2))]/4\pi \\ &\quad - 2 \times (4/3)\pi r^3 \times 2\pi[1 - (\cos(\theta_1))]/4\pi \\ &= (4/3)\pi r^3[\cos(\theta_1) - \cos(\theta_2)]. \end{aligned} \quad (9)$$

The conical structure of the polar dust model in our study can be described as a simple case of $\theta_1 = 0^\circ$ and $\theta_2 = 90^\circ - \sigma$. Lyu & Rieke (2018) introduce a power-law dust density profile, $\rho(r) \propto r^{-\alpha}$, and the value of α is $0 < \alpha \lesssim 2$ based on the previous observational studies (Behar 2009; Faucher-Giguère & Quataert 2012; Feruglio et al. 2015; Revalski et al. 2018). The total mass of the extended ($\gtrsim 10$ pc) polar dust within the radius of r , $M_{\text{polar}}(r)$, follows the mass profile of $dM_{\text{polar}}/dr \propto (dV_{\text{polar}}/dr)\rho(r) \propto r^{2-\alpha}$. Assuming that the polar dust emission depends on their mass, a large part of the polar dust emission is derived from the large-scale structure at $r \sim R_{\text{polar}}$. However, the polar dust sizes for three AGNs in NGC 1068, IRAS F08572+3915, and Mrk 231 are much smaller than the best-fitting relation. Interestingly, Feruglio et al. (2015) investigate the spatial distribution of the intense molecular CO(2–1) outflows in Mrk 231 with Atacama Large Millimeter/submillimeter

Array (ALMA) and report that its mass profile (or the outflow filling factor) follows $\alpha \approx 2$. This suggests that the polar dust emission in Mrk 231 is derived from the whole structure. Although the spatial distribution for NGC 1068 and IRAS F08572+3915 is unclear, the density profile may cause the seemingly hot and compact emission from the polar dust. Except for these three AGNs, the R_{polar} is thought to be the spatial scale of the polar dust detected in the mid-IR images (Asmus 2019). Thus, the best-fitting relation between AGN luminosity and R_{polar} suggests that the IR-luminous polar dust structure expands from a few tens parsec (early mergers) to kiloparsec scales (late mergers).

6.5.2. Scenario of the Outflowing Polar Dust

To distinguish whether the polar dust is (1) the galactic ISM or dust near the edge of NLR being illuminated by the AGN or (2) the outflowing dusty winds launched from the inner edge of the torus, we investigate the spatial sizes of the ionized and molecular outflows for our U/LIRGs (Table A5). Fluetsch et al. (2021) analyze the optical integral field unit (IFU) data of 26 local U/LIRGs with Very Large Telescope (VLT)/Multi Unit Spectroscopic Explorer (MUSE). From the literature, they also include 31 galaxies with spatially resolved multiphase outflow information (e.g., Rupke & Veilleux 2013; Rupke et al. 2017). For eight U/LIRGs in our sample (small-green circles), they estimate the radius of the ionized outflow based on the extent of the broad H α component. Fluetsch et al. (2019) investigate the molecular outflows primarily by using CO data from the ALMA archive in a sample of 45 local galaxies. The radius of the molecular outflows is measured for nine U/LIRGs in our targets (light-blue circles). We find that the sizes of ionized and molecular outflows are similar to or larger than those of the polar dust size, supporting that the materials outside the polar dust are outflowing.

Many works predict that the polar dusty outflows are launched from the surface of the inner torus (e.g., Hönig & Kishimoto 2010; Hönig et al. 2012, 2013; Gallagher et al. 2015; Ishibashi et al. 2018). The semi-analytical disk and wind models suggest that the dusty winds can be launched by the AGN radiation pressure and the heated dust itself (Venanzi et al. 2020). Similarly, RHD simulations also support that dusty winds are naturally driven (e.g., Schartmann et al. 2014; Wada et al. 2016, 2018; Williamson et al. 2019, 2020). Some observational attempts to test this hypothesis have been performed by analyzing the IR SEDs (e.g., Lyu & Rieke 2018) and by comparing the polar dust luminosities with the strength

²¹ The polar dust temperature assuming the gray body model is different from the inverse peak-wavelength temperature (T_{peak}) measured by Wein's displacement law (i.e., $\lambda_{\text{peak}} = 2.898 \times 10^3 \mu\text{m K}/T_{\text{peak}}$, which only applies to perfect black bodies; Casey 2012). Though the assumption of the emitter (e.g., gray body or smooth distribution with clumps) may cause a systematic uncertainty of the polar dust temperature, the results of the decrease in T_{polar} with merger stage will be almost unchanged.

of the multiphase outflows (e.g., Alonso-Herrero et al. 2021).

Since the polar dust emission does not show the emission/absorption lines, it is difficult to estimate its velocity. For the starburst galaxy M 82, Yoshida et al. (2011) carry out the spectropolarimetry of the optical emission lines. The outflowing dust grains are predicted to polarize the continuum and emission lines emanating from the nuclear starburst region, acting as “moving mirrors” for nuclear light. By comparing the velocities between the normal and polarized emission lines, they find that the velocity of the polar dust (v_{polar}) decreases from $\sim 200 \text{ km s}^{-1}$ at a few hundred parsecs to $\sim 20\text{--}30 \text{ km s}^{-1}$ at 1–1.2 kpc. For the U/LIRGs hosting nuclear starbursts and AGNs, the minimum velocity of the polar dust should be $\gtrsim 30 \text{ km s}^{-1}$ at 1 kpc. The typical lifetime of the U/LIRGs containing submillimeter galaxies at $z \sim 1\text{--}2$ ($t_{\text{U/LIRG}}$) are $\sim 30\text{--}100 \text{ Myr}$ (Hopkins et al. 2006, 2008; Meier et al. 2010; Hickox et al. 2012; Inayoshi et al. 2018) or at most 300 Myr (Swinbank et al. 2006; Meng et al. 2010; Privon et al. 2013). The migration length of the outflowing dusts can be roughly estimated by the velocity ($v_{\text{polar}} \gtrsim 30 \text{ km s}^{-1}$) times the U/LIRG lifetime ($t_{\text{U/LIRG}} \gtrsim 30 \text{ Myr}$), i.e., $\gtrsim 1 \text{ kpc}$. The smaller fraction of the AGNs with signs of polar dust emission for early mergers than that for late mergers also supports the evolution of the polar dust (Section 4.2.4). Although the possible contribution of the polar dust emission from the non-outflowing dust in the NLR should not be rejected, the polar dust seems to be dusty winds as expected by recent simulations. Thus, the polar dust size (R_{polar}) increases from a few tens of parsec (early mergers) to kiloparsec scales (late mergers), indicating that the polar dust is likely the expanding (i.e., evolving) dusty outflows.

6.5.3. Unified View of the Polar Dust Structure in U/LIRGs

In the bottom panel of Figure 24, we present the schematic picture of the polar dust structure in U/LIRGs. The polar dust sizes, estimated from the polar dust temperature and dust sublimation radius, increase with AGN luminosity (or merger stage). The polar dust temperature decrease with the polar dust size from $\sim 200 \text{ K}$ (a few tens of parsec) to $\sim 100 \text{ K}$ (kiloparsec scale). Considering the typical dust density profile of $0 < \alpha \lesssim 2$, their sizes corresponds to the outer structure of the extended polar dust (Section 6.5.1). The polar dust sizes are smaller than those of ionized and molecular outflows, and their expansion with merger stage can be explained by the polar dust velocity and U/LIRG lifetime (Section 6.5.2).

At the parsec-scale regions, RHD simulations show that the innermost torus structure is formed by radiation-driven fountain-like outflows (e.g., Wada et al. 2018). A multiphase dynamic nature of torus (pink ellipses) and circumnuclear region (CND; yellow ocher) in the $r \lesssim$ tens of parsecs torus region is confirmed by recent ALMA observations (e.g., Izumi et al. 2016, 2018). Hönig (2019) mentions that the polar dust is expected to be launched by the inner edge of the torus due to the AGN radiation (coming from the AGN disk or vicinity of the SMBH). As noted in Section 6.5.1, the polar dust structure would be smoothly distributed with most substructure being filamentary and/or clumpy, as expected by RHD simulations (Wada 2012; Schartmann et al. 2011; Williamson et al. 2019), although we simply describe it by a smooth distribution. According to these results, the schematic picture illustrates the AGN structures, containing the polar dust, NLR, torus, failed winds around the torus, accretion disk, and SMBH in the early-to-late merging U/LIRGs.

6.5.4. Polar Dust vs. Molecular Outflow

This study indicates that the multiwavelength SED analysis is one of the key means to evaluate the activities of the dust components of large-scale outflows. In Figure 25, we compare the polar dust luminosities with the molecular outflow velocity ($V_{\text{out,mol}}$; left panel) and mass transfer rates ($\dot{M}_{\text{out,mol}}$; right panel). Yamada et al. (2021) lists the values of $V_{\text{out,mol}}$ and $\dot{M}_{\text{out,mol}}$ for local U/LIRGs by referring the previous works based on the broad CO emission lines and OH absorption lines (e.g., González-Alfonso et al. 2017; Laha et al. 2018 and references therein). We find that the polar dust luminosity and $V_{\text{out,mol}}$ show no significant relation. This may be due to the dispersion of the slope of the dust density profiles (α), or the dispersion of the size of the molecular outflows relative to the polar dust size (Figure 24). Whereas, the polar dust luminosity and mass transfer rates of the molecular outflows show a positive correlation. This may be a reasonable result by taking into account that the polar dust luminosities depend on their mass (particularly containing the large-scale mass at $r \sim R_{\text{polar}}$; Section 6.5.1). We calculate the best-fitting relation by using the Bayesian maximum-likelihood method as below:

$$\log(L_{\text{polar}}) = 0.77 \log(\dot{M}_{\text{out,mol}}) + 42.79, \quad (10)$$

where the 1σ dispersion is $\pm 0.67 \text{ dex}$ and the correlation coefficient is 0.71. Since the sample is quite limited, further studies using large samples are necessary to establish the general relation between polar dust (i.e., dusty winds) and molecular outflows.

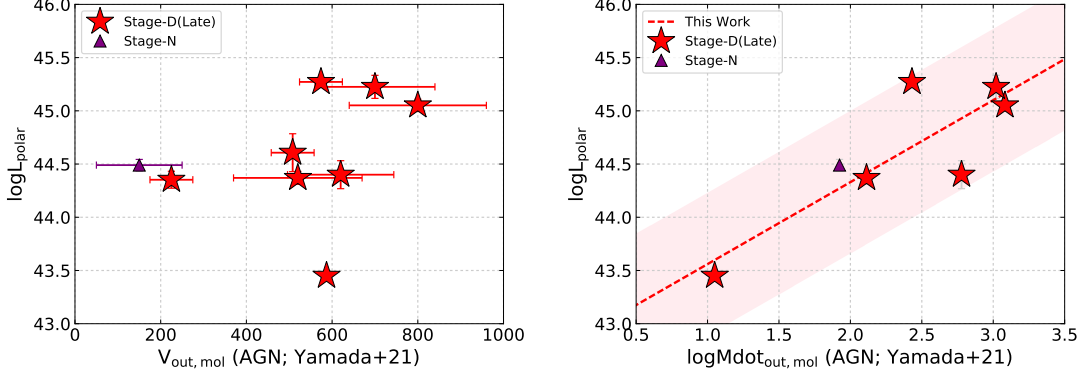


Figure 25. Polar-dust luminosity as a function of molecular outflow velocity (left) and logarithmic mass transfer rate of molecular outflow (right) referred from Yamada et al. (2021). The red dashed line and pink shaded area mark the best-fitting relation and its 1σ dispersion. The symbols are the same in Figure 8.

7. DISCUSSION II: COEVOLUTION PROCESS OF GALAXY, SMBH, AND OUTFLOW

7.1. Activities of Starburst and AGN

To understand the origin of the coevolution of galaxies and SMBHs, their growth rates are well studied. Numerical simulations of galaxy mergers predict that the SFR, AGN luminosities, and obscuration of the central AGN increase with merger stage (e.g., Di Matteo et al. 2005; Hopkins et al. 2006, 2008; Narayanan et al. 2010; Anglés-Alcázar et al. 2017; Blecha et al. 2018; Kawaguchi et al. 2020; Yutani et al. 2022). The observational studies using multiwavelength data support their increases with merger stage (e.g., Imanishi et al. 2010; Lee et al. 2012; Ellison et al. 2013; Satyapal et al. 2014; Ricci et al. 2017a, 2021; Koss et al. 2018; Pfeifle et al. 2019; Shangguan et al. 2019; Yamada et al. 2019, 2021).

By combining the broadband X-ray spectroscopy and multiwavelength SED decomposition, this study estimates the SFRs and AGN luminosities for a large sample of 72 resolved sources in U/LIRGs, which are treated separately divided into 41 hard X-ray-detected AGNs (containing 36 single AGNs, 2 unresolved dual AGN systems, and 3 newly identified AGNs) and 31 other sources (starburst-dominant or hard X-ray-undetected sources). In Figure 26, we investigate the distribution of SFR (left) and intrinsic (bolometric) AGN luminosity (right) as a function of projected separation between two galaxies. For the starburst-dominant or hard X-ray-undetected sources, we refer to the AGN luminosities estimated from the [O IV] 25.89 μm luminosity ($L_{[\text{O IV}]}$; small crosses) in Yamada et al. (2021). They confirm that these values are consistent with the 3σ upper limits of the predicted 2–10 keV AGN luminosity from the X-ray counts by assuming $N_{\text{H}} \leq 10^{25} \text{ cm}^{-2}$ and $L_{\text{X,unabs}} - L_{[\text{O IV}]}$ relation (Liu et al. 2014). We note

that the dispersion of the low values of SFRs and AGN luminosities for the early mergers with the ~ 10 –40 kpc are caused by the faint companion galaxies that are not IR-luminous galaxies. Focusing on the largest values of individual merger stages, our results support that the SFRs and AGN luminosities increase with projected separation and merger stage, consistent with the results in Section 5.6.

In Figure 27, we compare the SFRs and bolometric AGN luminosities in our sample. By the same method in Yamada et al. (2021), we draw the galaxy–SMBH “simultaneous evolution” relation (see also e.g., Ueda et al. 2018), where the growing systems keeping the SFR– $L_{\text{AGN,int}}$ relation are expected to establish the local $M_{\text{bulge}} - M_{\text{BH}}$ relation. Here, the relation assumes the fraction of stellar mass that are taken back to the ISM (return fraction) as $R = 0.41$ (Chabrier 2003), the ratio of stellar masses to SMBH masses in the local universe as $A \sim 200$ (Kormendy & Ho 2013), and a radiative efficiency as $\eta = 0.05$ (Ueda et al. 2014). The detailed explanations are presented in Yamada et al. (2021). The relation is described as

$$\log(L_{\text{AGN,int}}) = \log(\text{SFR}/M_{\odot} \text{ yr}^{-1}) + 42.94. \quad (11)$$

The hard X-ray-detected and newly identified AGNs in U/LIRGs follows the simultaneous coevolution relation, consistent with the results by Yamada et al. (2021). For the AGNs in our sample excluding non-mergers and outliers with $\log\text{SFR} < 0$, we calculate the best-fitting relation based on the Bayesian maximum-likelihood method:

$$\log(L_{\text{AGN,int}}) = 0.89 \log(\text{SFR}) + 42.71. \quad (12)$$

The 1σ uncertainty is ± 0.66 dex and the correlation coefficient is 0.54. As mentioned in Appendix C (see Figure C3), the AGN luminosities in Yamada et al. (2021)

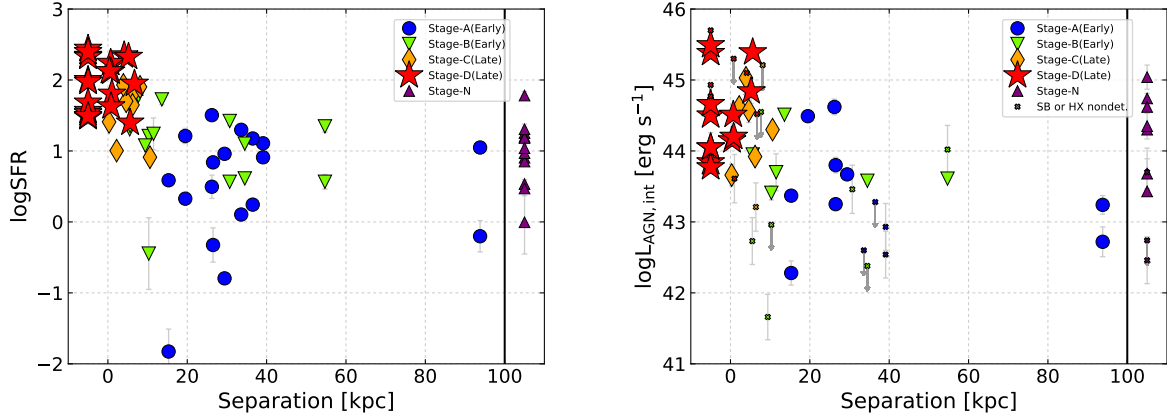


Figure 26. SFR and intrinsic AGN luminosity as a function of projected separation between two galaxies in units of kiloparsecs. Single nuclei in merging (stage D) and nonmerging (stage N) sources are plotted on the left (negative value) and right sides, respectively. Large symbols are the same in Figure 8, while small crosses illustrate the starburst-dominant or hard X-ray–nondetected sources.

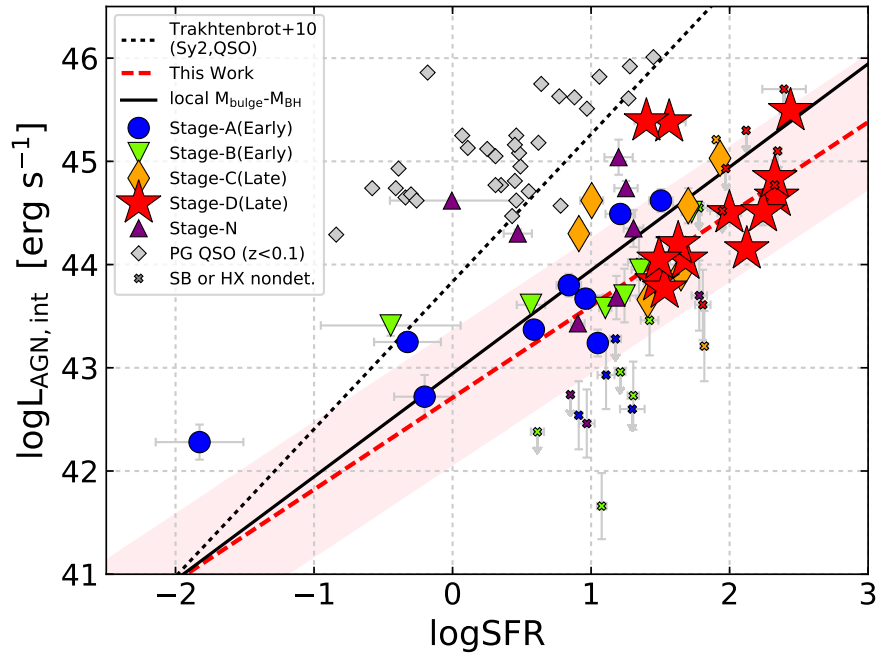


Figure 27. Logarithmic SFR vs. intrinsic AGN luminosity. Black dotted line denotes the typical relation among low-z Seyfert 2s, QUEST QSOs, and high-z QSOs (Trakhtenbrot & Netzer 2010). The red dashed line and pink shaded area mark the best-fitting relation and its 1σ dispersion for the AGNs in U/LIRGs, excluding the nonmergers and AGNs with $\log\text{SFR} < 0$. The black solid line is the galaxy–SMBH ‘simultaneous evolution’ line for $A = 200$ (see also Ueda et al. 2018). The large symbols are the same in Figure 8. The small crosses mark the starburst-dominant or hard X-ray–nondetected sources, whose $L_{\text{AGN,int}}$ values are derived from the [O IV] luminosities (Yamada et al. 2021).

are larger than the values in this work, and then their typical relation is ~ 0.4 dex brighter in the AGN luminosity. Their AGN luminosities are derived from the averages of four different measurements; the [O IV] luminosity (e.g., Gruppioni et al. 2016), bolometric AGN fraction (e.g., Díaz-Santos et al. 2017), and IR SED decomposition and Spitzer/IRS spectral fitting (Alonso-Herrero et al. 2012; Shangguan et al. 2019). Its systematic scatter related to the application of the averaged values is reported as about ± 0.27 dex. Our best-fitting relation with the 1σ uncertainty is overlapped on not only the relation of Yamada et al. (2021) but the simultaneous coevolution relation (black solid line). This supports that the AGNs in U/LIRGs are exactly in the coevolution phase of galaxies and SMBHs.

Yamada et al. (2021) report that the AGNs in stage D mergers show the multiphase massive outflows at subparsec to kiloparsec scales, that is, UFOs (e.g., Feruglio et al. 2015; Tombesi et al. 2015; Mizumoto et al. 2019; Smith et al. 2019), ionized outflows (e.g., Fischer et al. 2013; Rich et al. 2015; Kakkad et al. 2018; Fluetsch et al. 2021; Toba et al. 2022b), and molecular outflows with velocities above 500 km s^{-1} (e.g., González-Alfonso et al. 2017; Laha et al. 2018; Fluetsch et al. 2019). As discussed in Section 6.3 and 6.5, the polar dust luminosities are $\sim 2/3 \times L_{\text{AGN,int}}$, and the physical sizes increase with AGN luminosities from a few tens of parsec to kiloparsec scales. In short, the polar dust luminosities and sizes are the largest in the stage D mergers with high AGN luminosities. Moreover, we plot the quantities of PG quasars at $z \lesssim 0.1$ (Lyu et al. 2017) and empirical relation for local AGNs and quasars (Trakhtenbrot & Netzer 2010). They lie in the AGN-dominant region above the coevolution relation, which should have strong gas outflows (e.g., Woo et al. 2020). The coexistence of intense starbursts, luminous AGNs, and massive outflows (UFOs, ionized outflows, molecular outflows, and dusty winds) particularly in the phase of U/LIRGs support a standard AGN feedback scenario that the AGN-driven outflows suppress star-forming activities and ULIRGs eventually transit to the unobscured quasars (e.g., Di Matteo et al. 2005; Hopkins et al. 2008; Alexander & Hickox 2012; Ananna et al. 2022; see also Yamada et al. 2021).

7.2. Mass Growth of Galaxy and SMBH

According to the obtained SFRs and AGN luminosities, we evaluate the total growth masses of galaxies and SMBHs. The increase in the stellar mass (ΔM_*) can be calculated by the SFR times the growth timescale (t_{growth}). The mass accretion rates (\dot{M}_{BH}) are estimated by using a radiative efficiency ($\eta = 0.05$; Ueda et al.

2014) and the light speed (c) as

$$\dot{M}_{\text{BH}} = L_{\text{AGN,int}} \times (1 - \eta) / (\eta c^2). \quad (13)$$

The increase in the SMBH mass (ΔM_{BH}) corresponds to the \dot{M}_{BH} times t_{growth} . Here, the multiwavelength SED analysis presents the SFRs and AGN luminosities for the U/LIRGs in the various merger stages. Since the history of these quantities during the U/LIRG lifetime ($t_{\text{U/LIRG}} \sim 30\text{--}100$ Myr; Section 6.5.2) is unclear, we compute the increased masses assuming t_{growth} is 30 Myr as a time scale of early mergers or late mergers. For the three resolved dual AGN systems in stage A mergers (NGC 833/NGC 835, NGC 6921/MCG+04-48-002, and NGC 7679/NGC 7682), we also calculate the total mass of the two galaxies and SMBHs after the galaxy collision, containing the increased masses from their starburst and AGN activities for 30 Myr.

Figure 28 describes the relation between the stellar masses and SMBH masses for the hard X-ray-detected AGNs in our sample. We plot the local $M_{\text{bulge}} - M_{\text{BH}}$ relation (Kormendy & Ho 2013), scaled relation assuming Chabrier IMF, and a typical $M_* - M_{\text{BH}}$ relation for classical bulges and ellipticals (Reines & Volonteri 2015). The stellar masses are obtained by our SED fitting, while the SMBH masses are referred from Yamada et al. (2021). The distributions of these masses in our U/LIRGs at $z < 0.1$ are well consistent with the study of $z < 0.3$ U/LIRGs by Farrah et al. (2022). The caveat is that the SMBH masses we refer are derived from the averaged values of the four kinds of different measurements: stellar mass to SMBH mass relation (e.g., Reines & Volonteri 2015), $M - \sigma_*$ relation (e.g., Gültekin et al. 2009), photometric bulge luminosity (e.g., Veilleux et al. 2009a; Winter et al. 2009; Haan et al. 2011), and various other methods such as the flux density of old stellar emission at $2 \mu\text{m}$ (Caramete & Biermann 2010), velocity dispersion of [O III] emission (Alonso-Herrero et al. 2012), water masers (Lodato & Bertin 2003; Klöckner & Baan 2004; Izumi et al. 2016), and so on. Although the systematic differences appear to depend on neither the intrinsic AGN luminosity nor Eddington ratio (Yamada et al. 2021), systematic uncertainties of the averaged SMBH masses are not negligible (at most ± 0.5 dex; gray error bars). Thus, the figure does not necessarily indicate that the SMBH masses are a bit small relative to the local relations.

We overplot the expected masses due to the starbursts and AGN activities for 30 Myr (arrows) and the additional collision of two galaxies (empty stars). For the two stage-D mergers with low stellar masses of $\log(M_*/M_\odot) \sim 9.0\text{--}9.5$ (IRAS F08572+3915 and IRAS F17138–1017), their galaxies and SMBHs are

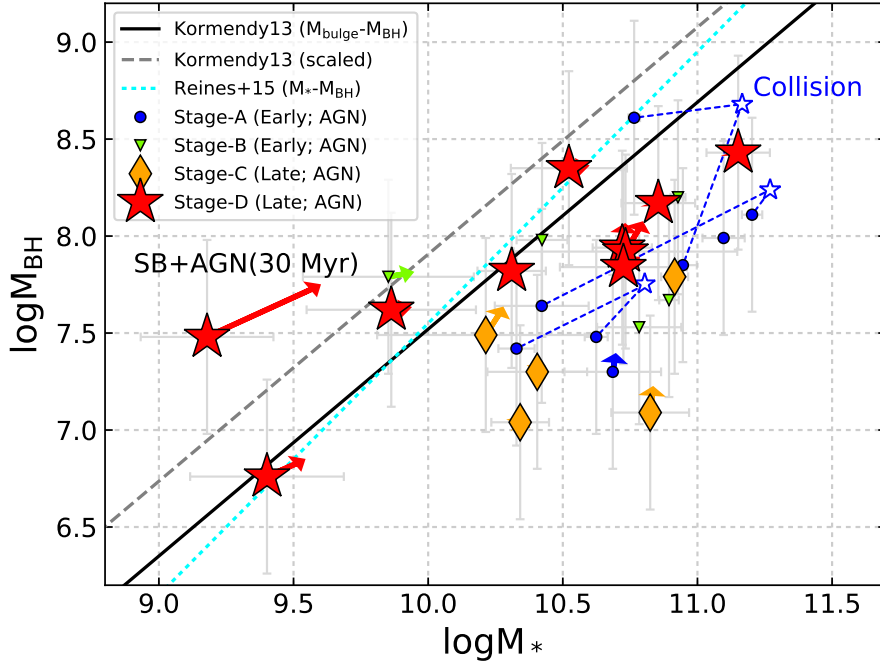


Figure 28. Logarithmic stellar mass vs. logarithmic SMBH mass referred from Yamada et al. (2021) for the AGNs in stage C (orange diamond) and stage D (red star) U/LIRGs. Solid arrows represent the expected masses of the galaxy and SMBH if they evolve with the constant growth rates (SFR and \dot{M}_{BH}) for 30 Myr. For three dual-AGN systems in stage A mergers, the merged masses of the two sources including the mass increase for 30 Myr are marked as empty blue stars with dotted lines. The black solid line denotes the local bulge mass (M_{bulge}) and SMBH mass (M_{BH}) relation for classical bulges and elliptical galaxies (Kormendy & Ho 2013). The dashed line shows the scaled relation that has bulge masses scaled down by 0.33 dex to consider the difference in the adopted mass-to-light ratios, and blue dotted line presents the typical M_{*} - M_{BH} relation for classical bulges and ellipticals (Reines & Volonteri 2015).

rapidly growing thanks to the starburst and AGN activities. We find that, however, the increased masses for the other U/LIRGs are small by these activities even though some of the stage-D U/LIRGs have the highest SFRs ($\sim 100\text{--}300 M_{\odot} \text{ yr}^{-1}$) and AGN luminosities ($\log L_{\text{AGN,int}} \sim 45.0\text{--}45.5$). Notably, the galaxy collision causes rapid growth for these high-mass systems.

Soltan's argument (Soltan 1982), one of the well-known discussions on the cosmic growth of SMBHs, suggests that the SMBHs are thought to have grown primarily by the gas accretion, not SMBH-SMBH coalescence. This requirement is imposed to explain the SMBH mass density at redshift z and the accreting gas mass density from $z = \infty$ to 0 (Yu & Tremaine 2002; Shankar et al. 2004). Because the SMBH-SMBH coalescence conserves the SMBH mass density, the argument does not reject the presence of ubiquitous merger events (e.g., Enoki et al. 2004; Jahnke & Macciò 2011). In this context, the growth events keeping the balanced SFR- $L_{\text{AGN,int}}$ relation triggered by galaxy mergers (see Figure 27; see also e.g., Di Matteo et al. 2005) should be helpful to con-

struct the local $M_{\text{bulge}}\text{--}M_{\text{BH}}$ relation. Whereas we need to keep in mind that, focusing on individual galaxies, the galaxy collision generates such high-mass galaxies with $\log(M_{*}/M_{\odot}) \gtrsim 10$). Therefore, our results indicate that galaxy merger is a vital process to establish the local $M_{\text{bulge}}\text{--}M_{\text{BH}}$ relation and build up the high-mass galaxies such as local elliptical galaxies.

7.3. Perspective of the Galaxy-SMBH Coevolution in Mergers

Finally, we summarize the perspective of the merger-driven coevolution of galaxies and SMBHs as described in the schematic picture of Figure 29. The SFRs and intrinsic (bolometric) AGN luminosities increase with merger stage, where the galaxy growth occurs first and rapid mass accretion delivered from the host galaxy to the SMBH is triggered later (Section 7.1). The merger process in the SFR- $L_{\text{AGN,int}}$ diagram should be a key mechanism to drive the balanced growth of galaxies and SMBHs in the cosmic history (e.g., Madau & Dickinson 2014; Ueda et al. 2014; Aird et al. 2015) and then to es-

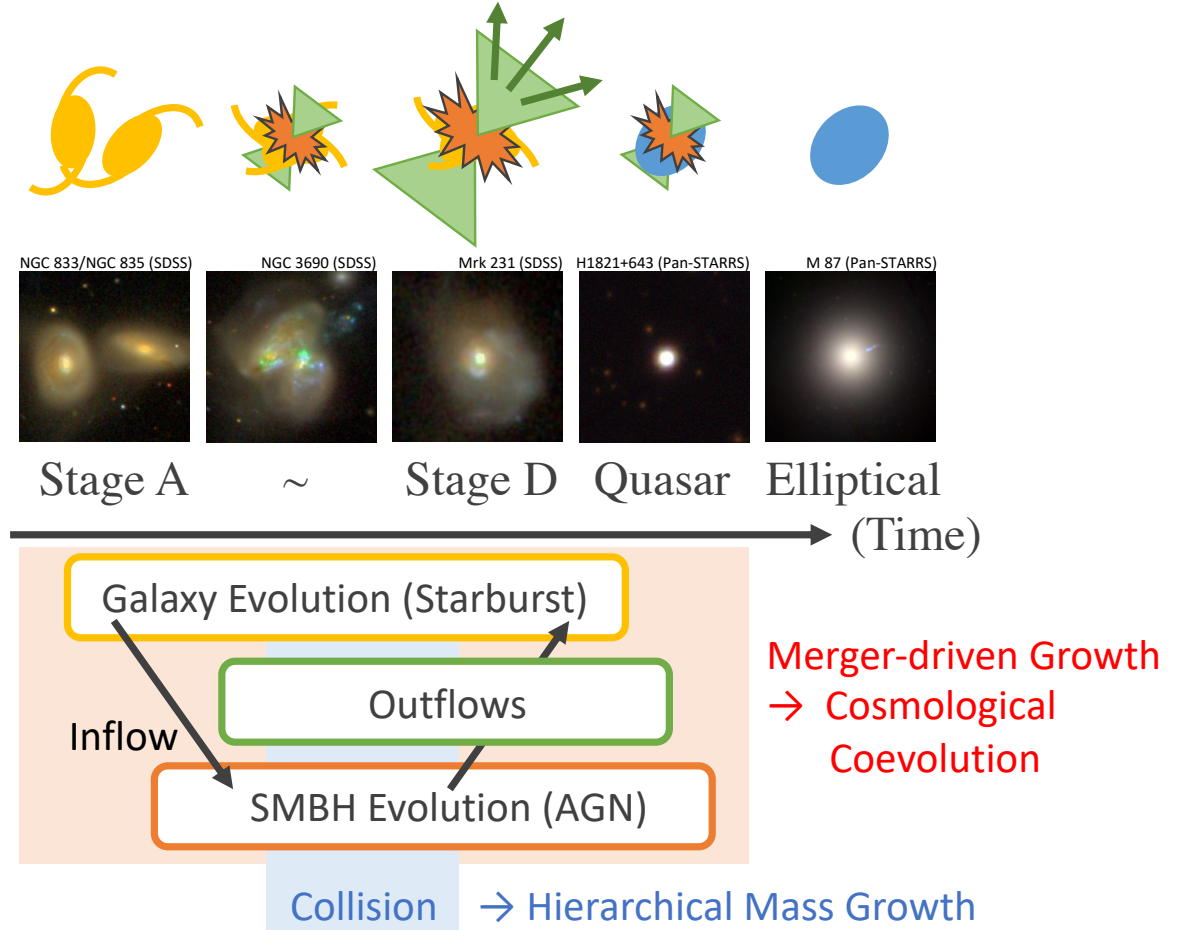


Figure 29. Schematic picture of merger-driven coevolution of galaxies and SMBHs. Middle panels are compiled from Pan-STARRS DR2 and SDSS DR16 images (Section 3.3), whose sources are merging U/LIRGs (NGC 833/NGC 835, NGC 3690, Mrk 231) and post-merger candidates (a quasar H1821+643, e.g., Jadhav et al. 2021; and an elliptical galaxy M87, e.g., Longobardi et al. 2015).

tablish the local $M_{\text{bulge}}-M_{\text{BH}}$ relation (e.g., Kormendy & Ho 2013). Moreover, galaxy collision is another important process to induce hierarchical mass growth and build up the high mass system such as local elliptical galaxies (Section 7.2).

Yamada et al. (2021) find that the AGNs in stage D mergers show the multiphase outflows at subparsec to kiloparsec scales, e.g., UFOs, ionized outflows, and molecular outflows. They also unveil that the AGNs with high Eddington ratios as $\lambda_{\text{Edd}} \sim 1$ have moderate N_{H} ($\sim 10^{23} \text{ cm}^{-2}$), where dusty clouds at parsec scales are pushed away by radiation pressure against the gravitational force as predicted with the $N_{\text{H}}-\lambda_{\text{Edd}}$ diagram (e.g., Fabian et al. 2008, 2009; Ricci et al. 2017d, 2022). The recent high-spatial-resolution ALMA and Chandra observations support the feedback effects on the torus by evaporating a portion of the gas (Kawamuro et al.

2021), while the AGNs in U/LIRGs are deeply buried by massive inflows and/or outflows (Yamada et al. 2021). The X-ray weakness in U/LIRGs should make it easy to launch the massive outflows efficiently (Section 5.5). By combining the X-ray spectroscopy and multiwavelength SED fitting, we constrain the physical parameters of polar dust structure (e.g., IR luminosity, temperature, and spatial scales) that is thought to be launched by the AGN radiation pressure and the heated dust itself (Section 6.5; see also Venanzi et al. 2020; Alonso-Herrero et al. 2021). The polar dust emission may be negligible for some low-Eddington AGNs ($\lambda_{\text{Edd}} \lesssim 10^{-3}$) in early mergers (Section 4.2.4 and 6.3). For the AGNs showing significant polar dust emission, the physical size of polar dust increases with merger stage from a few tens of parsec to kiloparsec scales. These results indicate that the massive outflows connecting to galaxy scales

are nurtured by the rapid accretion SMBHs and rich environments in U/LIRGs.

The coexistence of intense starburst, AGNs, and large-scale massive outflows in local U/LIRGs support a standard AGN feedback scenario (see also Chen et al. 2020). According to the scenario, the U/LIRGs will transit to the unobscured AGNs (Section 7.1). It is still unclear whether the star-forming activities are quenched due to the high specific SFRs (see e.g., Section 5.1) or the AGN feedback by the massive outflows. Considering the balanced starburst and AGN activities in the merger sequence, the massive outflows would present some kind of physical connection between galaxies and SMBHs. To completely understand the role of massive outflows in late mergers, it is needed to more researches of the mass transport mechanism and the effects on star formation in the host galaxy. In the near future, the high-spatial-resolution IR images will be presented by the Mid-InfraRed Instrument (MIRI; Rieke et al. 2015; Wright et al. 2015) onboard the James Webb Space Telescope (5–28 μm), and The Mid-Infrared Multi-field Imager for gaZing at the UnKnown Universe (MIMIZUKU; Kamizuka et al. 2020) on The University of Tokyo Atacama Observatory (TAO; Yoshii et al. 2010) 6.5m ground-based telescope (2–38 μm). Combining the multiwavelength images with such as these telescopes and ALMA will allow us to study the distribution of the warm and cold outflowing matters, and better constrain the relationship between the outflows and star-forming activities.

8. CONCLUSION

The purpose of this work is (1) to understand the features of multiwavelength emissions in U/LIRGs, (2) to reveal the structure of the outflowing polar dust, and (3) to investigate the activities of host galaxies, SMBHs, and outflows for testing whether the merger process is a vital factor to establish the local $M_{\text{bulge}}-M_{\text{BH}}$ relation. To achieve these goals, we have performed a hard X-ray to radio multiwavelength SED decomposition for the 57 local U/LIRGs (containing 84 individual galaxies) observed with NuSTAR and/or Swift/BAT (Yamada et al. 2021). We compile the broadband X-ray spectra and multiwavelength wide-survey catalogs in the UV to radio bands. After the cross-matching with them, we finally obtain the multiwavelength photometries of the sample consisting of 72 resolved sources and 13 duplicated systems of resolved pairs, which are spatially divided in the Herschel PACS 70 μm bands. We modify the latest SED-fitting code X-CIGALE by implementing the infrared (IR) CLUMPY model, allowing the multi-

wavelength study with the consistent X-ray torus model (XCLUMPY). Adopting the torus parameters obtained by the X-ray fitting (Yamada et al. 2021), we constrain the properties of host galaxies, AGN tori, and polar dust. Here, we described the main results as follows.

1. The sample has 36 single and two unresolved dual AGNs detected in the hard X-ray band (Yamada et al. 2021). For all targets, we perform the BIC test for two kinds of UV-to-IR SED fitting with and without AGN (torus and polar dust) components. Although it is difficult to reliably identify AGNs solely by the SED fitting, we newly identify three AGN candidates by the diagnostics of $\Delta\text{BIC} > 6$. We also examine the significance of the polar dust component for these AGNs. The AGNs in late mergers support the presence of polar dust emission, while some AGNs in early mergers or nonmergers show no signatures (Section 4.2.4).
2. The component galaxies in early mergers have a wide range of SFRs above and below the main sequence (MS), while galaxies in late mergers have the highest SFRs above the MS. Similar SFR– M_* distributions of AGNs and the others imply that the small influence of the AGN activities on the star formation in the phase of U/LIRGs (Section 5.1).
3. The flat slope of radio emission in late mergers may be caused by the optically-thick free-free absorption due to the rich environment of the nuclear region. Most AGNs in U/LIRGs are radio-quiet. The SFRs are correlated with radio luminosity, indicating that starburst emission is dominant (Section 5.2).
4. In the WISE color–color diagram, we propose a new wedge of the buried AGNs in late mergers, which show the $\sim 3\text{--}10 \mu\text{m}$ excess. This can be explainable by the inner part of the dusty disk and/or hot polar dust within the inner parsecs (Section 5.3).
5. The averaged SEDs suggest that the strength of the X-rays is the best means to reveal the true energy sources (intense starbursts and/or buried AGNs) in U/LIRGs (Section 5.4). The absorption-corrected AGN SEDs show X-ray weakness relative to the other wavelengths. This may be a common feature among the AGNs in IR-luminous galaxies over the cosmic history ($z \sim 0\text{--}7$), whose mechanism will be related to their massive outflows (Section 5.5).

6. Although polar-dust extinction is much smaller than torus extinction, the UV-to-IR (mainly IR) polar dust luminosities are ~ 2 times larger than the torus ones because of the seemingly large covering fractions (and/or large volumes) of polar dust. The AGNs with the signs of polar dust emission (Section 4.2.4) have $\log \lambda_{\text{Edd}} \gtrsim -3.0$ (Section 6.3).
7. The polar-dust temperature decreases with merger stages. We estimate the physical size of the polar dust by the temperature and dust sublimation radius, consistent with the high-spatial-resolution mid-IR images (Asmus 2019). Their sizes increase with AGN luminosity from a few tens of parsec (early mergers) to kiloparsec scales (late mergers), indicating that the polar dust is likely the expanding (i.e., evolving) dusty outflows (Section 6.5).
8. The SFRs and intrinsic (bolometric) AGN luminosities increase with merger stage. The comparison between these quantities suggests that the starbursts occur first and AGNs arise later, and overall their growth rates follow the simultaneous coevolution relation that can establish the local $M_{\text{bulge}}-M_{\text{BH}}$ mass relation (Section 7.1).
9. Considering the Soltan argument, the balanced $\text{SFR}-L_{\text{AGN,int}}$ relation helps the construction of local $M_{\text{bulge}}-M_{\text{BH}}$ relation. Whereas, galaxy collision is also a key process to build up high-mass galaxies such as local elliptical galaxies (Section 7.2).
10. Yamada et al. (2021) and this work suggest that the AGNs in late mergers show the multiphase outflows at subparsec to kiloparsec scales, that is, UFOs, ionized outflows, molecular outflows, and expanding dusty winds. The coexistence of intense starburst, AGNs, and large-scale massive outflows support a standard AGN feedback scenario (Section 7.3).

We thank the anonymous referee for constructive comments and suggestions that helped improve the quality of the paper. S.Y. acknowledges Dr. Taiki Kawamuro and Dr. Kohei Ichikawa for their helpful discussion. This work is financially supported by JSPS KAKENHI grant numbers 19J22216 and 22K20391 (S.Y.); 17K05384 and 20H01946 (Y.U.); 18J01050, 19K14759, and 22H01266 (Y.T.); 21J13894 (S.O.); 22J22795 (R.U.); and 21K03632 (M.I.). S.Y. is grateful for support from RIKEN Special Postdoctoral Re-

searcher Program. M.H.E. and T.M. acknowledge support by UNAM-DGAPA PAPIIT IN111319 and CONACYT Investigación Científica Básica 252531. H.M.E. also thanks support from a postdoctoral fellowship from UNAM-DGAPA. C.R. acknowledges support from the Fondecyt Iniciacion grant 11190831 and ANID BASAL project FB210003.

This research has made use of data and/or software provided by the High Energy Astrophysics Science Archive Research Center (HEASARC), which is a service of the Astrophysics Science Division at NASA/GSFC. This work makes use of data obtained from the NuSTAR Data Analysis Software (NuSTARDAS) jointly developed by the ASI Science Data Center (ASDC, Italy) and the California Institute of Technology (USA). This publication makes use of data obtained with Chandra, supported by the Chandra X-ray Observatory Center at the Smithsonian Astrophysical Observatory, and with XMM-Newton, an ESA science mission with instruments and contributions directly funded by ESA Member States and NASA. This study makes use of data obtained from the Suzaku satellite, a collaborative mission between the space agencies of Japan (JAXA) and the USA (NASA). The scientific results reported in this article are based on observations made by UK Swift Science Data Centre at the University of Leicester.

This research makes use of the SIMBAD database, operated at CDS, Strasbourg, France (Wenger et al. 2000), and the Aladin sky atlas, developed at CDS, Strasbourg Observatory, France (Bonnarel et al. 2000; Boch & Fernique 2014). Also, this research makes use of data from the NASA/IPAC Extragalactic Database (NED) and NASA/IPAC Infrared Science Archive (IRSA), operated by JPL/California Institute of Technology under contract with the National Aeronautics and Space Administration (see also IPAC DOIs: Skrutskie et al. 2003; Wright et al. 2019; AKARI Team 2020).

This research is based on observations with GALEX, operated for NASA by the California Institute of Technology under NASA contract NAS5-98034. The GALEX data presented in this paper were obtained from the Mikulski Archive for Space Telescopes (MAST) at the Space Telescope Science Institute (see also MAST DOI: Bianchi 2020).

The Pan-STARRS1 Surveys (PS1) and the PS1 public science archive have been made possible through contributions by the Institute for Astronomy, the University of Hawaii, the Pan-STARRS Project Office, the Max-Planck Society and its participating institutes, the Max Planck Institute for Astronomy, Heidelberg and the Max Planck Institute for Extraterrestrial Physics, Garching, The Johns Hopkins University, Durham University, the

University of Edinburgh, the Queen’s University Belfast, the Harvard-Smithsonian Center for Astrophysics, the Las Cumbres Observatory Global Telescope Network Incorporated, the National Central University of Taiwan, the Space Telescope Science Institute, the National Aeronautics and Space Administration under Grant No. NNX08AR22G issued through the Planetary Science Division of the NASA Science Mission Directorate, the National Science Foundation Grant No. AST-1238877, the University of Maryland, Eotvos Lorand University (ELTE), the Los Alamos National Laboratory, and the Gordon and Betty Moore Foundation.

The national facility capability for SkyMapper has been funded through ARC LIEF grant LE130100104 from the Australian Research Council, awarded to the University of Sydney, the Australian National University, Swinburne University of Technology, the University of Queensland, the University of Western Australia, the University of Melbourne, Curtin University of Technology, Monash University and the Australian Astronomical Observatory. SkyMapper is owned and operated by The Australian National University’s Research School of Astronomy and Astrophysics. The survey data were processed and provided by the SkyMapper Team at ANU. The SkyMapper node of the All-Sky Virtual Observatory (ASVO) is hosted at the National Computational Infrastructure (NCI). Development and support of the SkyMapper node of the ASVO have been funded in part by Astronomy Australia Limited (AAL) and the Australian Government through the Commonwealth’s Education Investment Fund (EIF) and National Collaborative Research Infrastructure Strategy (NCRIS), particularly the National eResearch Collaboration Tools and Resources (NeCTAR) and the Australian National Data Service Projects (ANDS).

Funding for the SDSS IV has been provided by the Alfred P. Sloan Foundation, the U.S. Department of Energy Office of Science, and the Participating Institutions. SDSS acknowledges support and resources from the Center for High-Performance Computing at the University of Utah. The SDSS web site is www.sdss.org. SDSS is managed by the Astrophysical Research Consortium for the Participating Institutions of the SDSS Collaboration including the Brazilian Participation Group, the Carnegie Institution for Science, Carnegie Mellon University, Center for Astrophysics — Harvard & Smithsonian (CfA), the Chilean Participation Group, the French Participation Group, Instituto de Astrofísica de Canarias, The Johns Hopkins University, Kavli Institute for the Physics and Mathematics of the Universe (IPMU) / University of Tokyo, the Korean Participation Group, Lawrence Berkeley National

Laboratory, Leibniz Institut für Astrophysik Potsdam (AIP), Max-Planck-Institut für Astronomie (MPIA Heidelberg), Max-Planck-Institut für Astrophysik (MPA Garching), Max-Planck-Institut für Extraterrestrische Physik (MPE), National Astronomical Observatories of China, New Mexico State University, New York University, University of Notre Dame, Observatório Nacional / MCTI, The Ohio State University, Pennsylvania State University, Shanghai Astronomical Observatory, United Kingdom Participation Group, Universidad Nacional Autónoma de México, University of Arizona, University of Colorado Boulder, University of Oxford, University of Portsmouth, University of Utah, University of Virginia, University of Washington, University of Wisconsin, Vanderbilt University, and Yale University.

This publication makes use of data products from the 2MASS, which is a joint project of the University of Massachusetts and the Infrared Processing and Analysis Center/California Institute of Technology, funded by the National Aeronautics and Space Administration and the National Science Foundation. This publication makes use of data products from the WISE, which is a joint project of the University of California, Los Angeles, and the Jet Propulsion Laboratory/California Institute of Technology, funded by the National Aeronautics and Space Administration. This research is based on observations with AKARI, a JAXA project with the participation of ESA. Herschel is an ESA space observatory with science instruments provided by European-led Principal Investigator consortia and with important participation from NASA.

This work makes use of the data from the VLA, operated by the National Radio Astronomy Observatory (NRAO). The NRAO is a facility of the National Science Foundation operated under a cooperative agreement by Associated Universities, Inc. This study makes use of data obtained from the MOST, operated with the support of the Australian Research Council and the Science Foundation for Physics within the University of Sydney. This scientific work makes use of the Murchison Radio-astronomy Observatory, operated by CSIRO. We acknowledge the Wajarri Yamatji people as the traditional owners of the Observatory site. Support for the operation of the MWA is provided by the Australian Government (NCRIS), under a contract to Curtin University administered by Astronomy Australia Limited. We acknowledge the Pawsey Supercomputing Centre which is supported by the Western Australian and Australian Governments. We thank the staff of the GMRT that made these observations possible. GMRT is run by the National Centre for Radio Astrophysics of the Tata Institute of Fundamental Research.

Facilities: NuSTAR, Swift, XMM-Newton, Chandra, Suzaku, GALEX, Pan-STARRS, SkyMapper, SDSS, 2MASS, WISE, AKARI, Herschel, VLA, MOST, MWA, GMRT.

Software: XCLUMPY (Tanimoto et al. 2019), HEAsoft (v6.25), XSPEC(v12.10.1; Arnaud 1996), NuSTAR-DAS(v1.8.0), CIAO(v4.11), SAS (v17.0.0; Gabriel et al. 2004), TOPCAT (Taylor 2006), X-CIGALE (Boquien et al. 2019; Yang et al. 2020a).

APPENDIX

A. BEST-FITTING RESULTS

Here, we present the best-fit parameters derived from the UV-to-IR SED decomposition, WISE W1–W4 magnitude, (Table A1 and A2) and the results of the radio fitting (Table A3). In Table A4 we list the logarithmic AGN luminosities in the X-ray, optical, and IR

bands. The obscuration and UV-to-IR luminosities for the torus and polar dust component, Eddington ratios, and the spatial scales of the multiphase outflows (Section 6.5) are summarized in Table A5. The multiwavelength SEDs and the best-fit SED models are presented in Appendix E.

Table A1. Best-fitting Parameters of the UV-to-IR SED Decomposition

ID	Name	f_{AGN}	τ_V	σ (°)	i (°)	$E(B - V)_{\text{polar}}$ (mag)	T_{polar} (K)	χ^2_{red}
								(9)
ID01	NGC 34	0.06±0.03	95±28	20	60	0.07±0.12	170±54	2.1
ID02	MCG-02-01-052/MCG-02-01-051	0.00 ^(f)	1.5
ID03	MCG-02-01-052	0.00 ^(f)	4.5
ID04	MCG-02-01-051	0.00 ^(f)	0.6
ID05	ESO 350-38	0.60±0.03	41±7	20	80	0.11±0.17	100±1	2.5
ID06	NGC 232/NGC 235	0.05±0.01	93±28	20	60	1.7
ID07	NGC 232	0.00 ^(f)	2.0
ID08	NGC 235	0.10±0.01	87±29	20	60	2.4
ID09	MCG+12-02-001	0.06±0.02	96±28	20	60	0.55±0.29	174±44	1.8
ID10	IC 1623A/IC 1623B	0.00 ^(f)	3.3
ID11	NGC 833/NGC 835	0.10±0.01	87±31	15	60	0.55±0.29	201±52	1.7
ID12	NGC 833	0.08±0.03	82±32	15	60	3.7
ID13	NGC 835	0.10±0.02	91±30	15	60	0.16±0.26	190±48	1.8
ID14	NGC 838	0.00 ^(f)	1.3
ID15	NGC 839	0.00 ^(f)	3.6
ID16	NGC 1068	0.49±0.07	79±33	20	80	0.39±0.31	250±5	5.3
ID17	UGC 2608/UGC 2612	0.26±0.05	63±30	15	80	0.8
ID18	UGC 2608	0.20±0.07	64±32	15	80	1.0
ID19	UGC 2612	0.00 ^(f)	4.1
ID20	NGC 1275	0.80±0.01	41±8	20	30	0.80±0.01	100±1	5.6
ID21	NGC 1365	0.10±0.01	83±32	20	30	0.80±0.02	235±25	1.6
ID22	ESO 203-1	0.00 ^(f)	1.4
ID23	CGCG 468-002W/CGCG 468-002E	0.17±0.04	81±32	15	60	0.05±0.02	126±35	2.1
ID24	CGCG 468-002W	0.20±0.05	85±32	15	60	0.06±0.07	162±36	4.0
ID25	CGCG 468-002E	0.00 ^(f)	2.1
ID26	IRAS F05189-2524	0.70±0.03	40±3	15	60	0.80±0.04	100±1	3.8
ID27	IRAS F06076-2139/2MASS 06094601-2140312	0.07±0.02	94±28	20	60	0.55±0.29	137±27	0.8

Table A1 *continued*

Table A1 (*continued*)

ID	Name	f_{AGN}	τ_V	σ	i	$E(B-V)_{\text{polar}}$	T_{polar}	χ^2_{red}
				(°)	(°)			
(1)	(2)	(3)	(4)	(5)	(6)	(7)	(8)	(9)
ID28	NGC 2623	0.05±0.01	104±21	20	60	0.05±0.02	100±5	3.5
ID29	ESO 060-IG016 West/East	0.10±0.01	80±31	20	60	1.0
ID30	IRAS F08572+3915	0.47±0.05	49±24	20	80	0.05±0.02	180±41	11.8
ID31	UGC 5101	0.11±0.04	45±16	15	60	0.30±0.05	101±8	3.7
ID32	MCG+08-18-012/MCG+08-18-013	0.00 ^(f)	3.0
ID33	MCG+08-18-012	0.00 ^(f)	4.5
ID34	MCG+08-18-013	0.00 ^(f)	1.4
ID35	MCG-01-26-013/NGC 3110	0.00 ^(f)	1.5
ID36	MCG-01-26-013	0.00 ^(f)	2.3
ID37	NGC 3110	0.00 ^(f)	3.9
ID38	ESO 374-IG032	0.10±0.02	54±25	20	30	0.05±0.06	172±45	5.9
ID39	NGC 3256	0.00 ^(f)	1.7
ID40	IRAS F10565+2448	0.00 ^(f)	5.2
ID41	NGC 3690 West/East	0.29±0.11	88±31	45	30	0.58±0.31	158±57	2.6
ID42	ESO 440-58/MCG-05-29-017	0.00 ^(f)	1.7
ID43	IRAS F12112+0305	0.00 ^(f)	5.7
ID44	NGC 4418/MCG+00-32-013	0.29±0.03	117±10	20	80	0.65±0.23	150±1	3.2
ID45	NGC 4418	0.10±0.01	82±28	20	80	0.63±0.24	200±1	3.4
ID46	MCG+00-32-013	0.00 ^(f)	4.9
ID47	Mrk 231	0.28±0.06	79±33	25	60	0.42±0.29	186±55	0.3
ID48	NGC 4922S/NGC 4922N	0.34±0.08	81±32	20	60	0.38±0.19	135±42	0.8
ID49	IC 860	0.00 ^(f)	3.1
ID50	IRAS 13120-5453	0.05±0.01	49±22	20	80	0.23±0.28	100±5	2.0
ID51	NGC 5104	0.00 ^(f)	2.8
ID52	MCG-03-34-064	0.61±0.10	48±20	20	60	0.79±0.06	206±19	1.8
ID53	NGC 5135	0.06±0.02	79±33	15	80	0.38±0.31	138±58	1.0
ID54	Mrk 266B/Mrk 266A	0.09±0.02	98±26	20	60	0.10±0.18	182±45	1.6
ID55	Mrk 273	0.08±0.02	73±33	15	60	0.78±0.09	101±6	2.4
ID56	IRAS F14348-1447	0.09±0.04	71±33	20	80	0.40±0.31	102±11	2.6
ID57	IRAS F14378-3651	0.00 ^(f)	2.4
ID58	IC 4518A/IC 4518B	0.13±0.08	79±33	20	60	0.39±0.31	181±58	0.3
ID59	IRAS F15250+3608	0.00 ^(f)	2.8
ID60	Arp 220W/Arp 220E	0.05±0.01	110±18	20	60	0.72±0.18	141±20	6.2
ID61	NGC 6240S/NGC 6240N	0.10±0.01	104±23	20	30	0.05±0.06	136±32	1.4
ID62	NGC 6285/NGC 6286	0.05±0.01	82±33	20	80	0.38±0.31	172±74	4.5
ID63	NGC 6285	0.00 ^(f)	2.3
ID64	NGC 6286	0.05±0.01	82±33	20	80	0.44±0.31	168±75	5.5
ID65	IRAS F17138-1017	0.14±0.07	81±33	20	60	0.37±0.30	135±54	5.1
ID66	IRAS F18293-3413	0.00 ^(f)	0.9
ID67	IRAS F19297-0406	0.00 ^(f)	2.1
ID68	NGC 6907/NGC 6908	0.00 ^(f)	2.5
ID69	NGC 6921/MCG+04-48-002	0.10±0.01	86±31	20	60	0.4
ID70	NGC 6921	0.05±0.01	82±33	20	80	0.8
ID71	MCG+04-48-002	0.11±0.03	91±29	20	60	0.7

Table A1 *continued*

Table A1 (*continued*)

ID	Name	f_{AGN}	τ_V	σ	i	$E(B - V)_{\text{polar}}$	T_{polar}	χ^2_{red}
				(°)	(°)	(mag)	(K)	
(1)	(2)	(3)	(4)	(5)	(6)	(7)	(8)	(9)
ID72	II Zw 096/IRAS F20550+1655 SE	0.00 ^(f)	3.7
ID73	ESO 286-19	0.00 ^(f)	2.3
ID74	NGC 7130	0.24±0.10	79±32	25	80	0.38±0.31	109±32	1.6
ID75	NGC 7469/IC 5283	0.34±0.09	77±33	15	30	0.34±0.36	102±11	0.4
ID76	NGC 7469	0.38±0.08	75±33	15	30	0.72±0.20	102±10	0.6
ID77	IC 5283	0.00 ^(f)	1.2
ID78	ESO 148-2	0.22±0.07	45±18	20	80	0.16±0.24	100±3	2.6
ID79	NGC 7591	0.00 ^(f)	2.3
ID80	NGC 7674/MCG+01-59-081	0.41±0.04	71±32	40	30	0.06±0.07	137±48	0.7
ID81	NGC 7674	0.43±0.05	60±29	40	30	0.06±0.08	138±43	0.6
ID82	MCG+01-59-081	0.00 ^(f)	0.3
ID83	NGC 7679/NGC 7682	0.07±0.03	90±30	20	60	0.49±0.31	181±57	1.7
ID84	NGC 7679	0.05±0.01	88±31	15	30	0.44±0.32	190±63	1.1
ID85	NGC 7682	0.15±0.08	82±32	60	60	1.7

NOTE—Comments: (1–2) ID and object name; (3) fraction of AGN luminosity in the IR band. The symbol “(f)” means that the value is fixed; (4) optical depth of each clump at V band; (5–6) torus angular width and inclination; (7) $E(B - V)$ of the polar dust; (8) temperature of the polar dust; (9) reduced χ^2 for the UV-to-IR SED decomposition.

(This table is available in its entirety in machine-readable form.)

Table A2. Properties of Host Galaxies and WISE Color

ID	Name	$\log M_*$	$\log \text{SFR}$	$\log \text{sSFR}$	W1	W2	W3	W4
(1)	(2)	(M_\odot)	($M_\odot \text{ yr}^{-1}$)	(yr)	(mag)	(mag)	(mag)	(mag)
		(3)	(4)	(5)	(6)	(7)	(8)	(9)
ID01	NGC 34	10.31±0.13	1.51±0.07	-8.80±0.14	9.82±0.01	9.35±0.01	5.25±0.01	2.05±0.01
ID02	MCG-02-01-052/MCG-02-01-051	10.37±0.13	1.47±0.06	-8.90±0.14
ID03	MCG-02-01-052	9.85±0.05	0.57±0.02	-9.29±0.05	12.25±0.02	12.17±0.02
ID04	MCG-02-01-051	10.22±0.15	1.42±0.06	-8.80±0.17	10.80±0.01	10.35±0.01	5.89±0.01	2.95±0.01
ID05	ESO 350-38	9.74±0.16	0.95±0.07	-8.79±0.17	10.79±0.01	9.50±0.01	5.49±0.01	2.10±0.01
ID06	NGC 232/NGC 235	11.07±0.06	1.35±0.04	-9.72±0.07
ID07	NGC 232	10.73±0.13	1.35±0.08	-9.38±0.15	9.66±0.01	9.32±0.01	5.40±0.01	2.71±0.01
ID08	NGC 235	10.93±0.03	0.55±0.03	-10.38±0.04	10.03±0.01	9.47±0.01	6.44±0.01	3.71±0.01
ID09	MCG+12-02-001	10.34±0.11	1.41±0.06	-8.93±0.12	...	8.92±0.01	4.49±0.01	1.45±0.01
ID10	IC 1623A/IC 1623B	10.64±0.11	1.82±0.03	-8.82±0.11	9.22±0.01	8.21±0.01	4.52±0.01	1.54±0.01
ID11	NGC 833/NGC 835	11.16±0.07	0.37±0.24	-10.80±0.25
ID12	NGC 833	10.76±0.02	-1.78±0.34	-12.54±0.34	9.50±0.01	9.49±0.01	...	5.71±0.04
ID13	NGC 835	10.95±0.05	0.59±0.07	-10.36±0.08	8.91±0.01	8.77±0.01	5.33±0.01	3.32±0.01
ID14	NGC 838	10.36±0.09	1.11±0.06	-9.26±0.11	9.32±0.01	9.00±0.01	4.70±0.01	2.14±0.01
ID15	NGC 839	10.19±0.04	0.91±0.03	-9.27±0.05	9.60±0.01	9.09±0.01	4.91±0.01	1.81±0.01
ID16	NGC 1068	10.07±0.15	1.25±0.08	-8.82±0.17
ID17	UGC 2608/UGC 2612	11.05±0.10	1.36±0.07	-9.68±0.12
ID18	UGC 2608	10.75±0.11	1.24±0.11	-9.51±0.15	...	8.70±0.01	5.09±0.01	2.33±0.01
ID19	UGC 2612	10.64±0.13	0.53±0.06	-10.11±0.14	...	10.39±0.01	7.55±0.01	5.88±0.04
ID20	NGC 1275	9.70±0.20	0.91±0.05	-8.79±0.20	8.03±0.01	7.52±0.01	4.04±0.01	1.07±0.01
ID21	NGC 1365	10.94±0.08	0.93±0.09	-10.01±0.13	6.30±0.01	5.95±0.01	2.32±0.01	...
ID22	ESO 203-1	9.78±0.22	1.78±0.06	-8.00±0.23	...	12.15±0.01	7.92±0.01	4.36±0.01
ID23	CGCG 468-002W/CGCG 468-002E	10.95±0.10	0.87±0.20	-10.07±0.22
ID24	CGCG 468-002W	10.89±0.04	-0.44±0.48	-11.34±0.48	9.93±0.01	9.47±0.01	6.44±0.01	...
ID25	CGCG 468-002E	10.11±0.07	1.21±0.04	-8.90±0.08	6.67±0.01	3.08±0.01
ID26	IRAS F05189-2524	10.72±0.11	1.56±0.12	-9.16±0.16	8.77±0.01	7.65±0.01	4.79±0.01	1.77±0.01
ID27	IRAS F06076-2139/2MASS 06094601-2140312	10.41±0.19	1.65±0.11	-8.76±0.21	11.31±0.01	10.78±0.01	6.84±0.01	3.81±0.01
ID28	NGC 2623	9.86±0.31	1.53±0.05	-8.33±0.32	10.39±0.01	9.76±0.01	5.84±0.01	2.60±0.01
ID29	ESO 060-IG016 West/East	9.85±0.32	1.68±0.04	-8.17±0.32	3.69±0.01
ID30	IRAS F08572+3915	9.18±0.25	1.89±0.02	-7.28±0.25	10.25±0.02	7.94±0.02	4.90±0.02	2.04±0.02
ID31	UGC 5101	10.85±0.14	2.00±0.09	-8.86±0.16	10.10±0.01	8.46±0.01	6.07±0.01	3.20±0.01
ID32	MCG+08-18-012/MCG+08-18-013	10.28±0.10	1.30±0.06	-8.98±0.11
ID33	MCG+08-18-012	9.04±0.08	0.10±0.02	-8.93±0.08	13.78±0.03	13.67±0.03	10.13±0.07	...
ID34	MCG+08-18-013	10.30±0.12	1.30±0.09	-9.00±0.15	10.84±0.01	10.44±0.01	6.36±0.01	...
ID35	MCG-01-26-013/NGC 3110	10.68±0.12	1.26±0.09	-9.42±0.15
ID36	MCG-01-26-013	10.06±0.10	0.24±0.04	-9.82±0.11	11.42±0.01	11.24±0.01	7.64±0.01	5.15±0.03
ID37	NGC 3110	10.73±0.09	1.18±0.04	-9.56±0.09	9.19±0.01	8.90±0.01	4.76±0.01	2.57±0.01
ID38	ESO 374-IG032	10.43±0.20	1.72±0.05	-8.71±0.21	10.60±0.01	8.16±0.01	5.92±0.01	3.19±0.01
ID39	NGC 3256	10.67±0.12	1.81±0.06	-8.86±0.13	7.58±0.01	7.05±0.01	...	-0.44±0.01
ID40	IRAS F10565+2448	10.71±0.13	1.95±0.09	-8.76±0.16	11.06±0.01	...	6.24±0.01	3.17±0.01
ID41	NGC 3690 West/East	10.82±0.14	1.69±0.10	-9.13±0.18
ID42	ESO 440-58/MCG-05-29-017	10.55±0.06	1.30±0.04	-9.24±0.08
ID43	IRAS F12112+0305	9.95±0.39	2.35±0.03	-7.60±0.39	12.36±0.01	11.63±0.01	7.57±0.01	4.28±0.01
ID44	NGC 4418/MCG+00-32-013	9.28±0.13	0.82±0.08	-8.47±0.15
ID45	NGC 4418	8.97±0.23	0.96±0.05	-8.01±0.24	10.15±0.01	9.32±0.01	4.01±0.01	0.40±0.01
ID46	MCG+00-32-013	7.32±0.19	-0.80±0.03	-8.11±0.19	14.11±0.03	13.89±0.04	10.34±0.08	7.77±0.16
ID47	Mrk 231	10.73±0.42	2.43±0.08	-8.30±0.42	7.80±0.01	6.58±0.01	3.54±0.01	0.57±0.01
ID48	NGC 4922S/NGC 4922N	10.92±0.05	0.91±0.06	-10.00±0.08

Table A2 *continued*

Table A2 (*continued*)

ID	Name	$\log M_*$	$\log \text{SFR}$	$\log \text{sSFR}$	W1	W2	W3	W4
(1)	(2)	(M_\odot)	($M_\odot \text{ yr}^{-1}$)	(yr)	(mag)	(mag)	(mag)	(mag)
		(3)	(4)	(5)	(6)	(7)	(8)	(9)
ID49	IC 860	9.68±0.08	0.85±0.02	-8.82±0.09	10.62±0.01	10.51±0.01	7.17±0.01	2.93±0.01
ID50	IRAS 13120–5453	11.15±0.12	2.34±0.07	-8.81±0.14	9.58±0.01	8.83±0.01	5.08±0.01	1.91±0.01
ID51	NGC 5104	10.68±0.06	0.97±0.06	-9.71±0.09	9.62±0.01	9.38±0.01	5.74±0.01	3.18±0.01
ID52	MCG–03–34–064	10.71±0.10	0.47±0.10	-10.24±0.14	9.20±0.01	7.92±0.01	4.17±0.01	1.53±0.01
ID53	NGC 5135	10.93±0.17	1.19±0.10	-9.74±0.20	8.61±0.01	8.10±0.01	4.44±0.01	1.62±0.01
ID54	Mrk 266B/Mrk 266A	10.76±0.14	1.35±0.06	-9.41±0.15	9.88±0.01	9.48±0.01	5.57±0.01	2.56±0.01
ID55	Mrk 273	10.52±0.22	2.24±0.05	-8.28±0.22	10.50±0.01	9.37±0.01	5.85±0.01	2.16±0.01
ID56	IRAS F14348–1447	10.73±0.24	2.32±0.06	-8.40±0.24	12.12±0.01	11.29±0.01	7.52±0.01	3.95±0.01
ID57	IRAS F14378–3651	10.29±0.21	2.33±0.03	-7.96±0.21	12.24±0.02	11.37±0.02	7.11±0.02	3.42±0.02
ID58	IC 4518A/IC 4518B	10.78±0.16	1.24±0.22	-9.55±0.27
ID59	IRAS F15250+3608	10.01±0.12	2.12±0.02	-7.89±0.13	12.34±0.02	10.84±0.02	5.99±0.01	2.40±0.01
ID60	Arp 220W/Arp 220E	9.82±0.30	2.12±0.04	-7.69±0.31	9.71±0.01	9.14±0.01	4.70±0.01	0.76±0.01
ID61	NGC 6240S/NGC 6240N	11.02±0.11	1.60±0.05	-9.42±0.12	8.85±0.01	8.34±0.01	4.59±0.01	1.35±0.01
ID62	NGC 6285/NGC 6286	10.61±0.07	1.35±0.03	-9.26±0.08
ID63	NGC 6285	10.25±0.19	0.61±0.05	-9.63±0.20	10.89±0.01	10.66±0.01	...	4.62±0.01
ID64	NGC 6286	10.42±0.09	1.09±0.04	-9.34±0.10	9.90±0.02	9.40±0.02	5.37±0.01	3.51±0.02
ID65	IRAS F17138–1017	9.40±0.29	1.48±0.08	-7.92±0.30	9.63±0.02	9.11±0.02	4.66±0.01	1.84±0.01
ID66	IRAS F18293–3413	10.72±0.12	1.78±0.06	-8.94±0.13	8.88±0.01	8.37±0.01	4.12±0.01	1.42±0.01
ID67	IRAS F19297–0406	10.60±0.22	2.39±0.16	-8.21±0.27	11.94±0.02	11.19±0.02	6.85±0.02	3.46±0.02
ID68	NGC 6907/NGC 6908	10.73±0.14	1.08±0.03	-9.66±0.15
ID69	NGC 6921/MCG+04-48-002	11.15±0.09	0.94±0.13	-10.22±0.16
ID70	NGC 6921	11.20±0.04	-0.33±0.25	-11.54±0.25	8.67±0.01	8.62±0.01	...	5.01±0.02
ID71	MCG+04-48-002	10.42±0.17	0.88±0.09	-9.55±0.19	9.30±0.01	8.80±0.01	5.08±0.01	2.90±0.01
ID72	II Zw 096/IRAS F20550+1655 SE	10.35±0.08	1.90±0.02	-8.45±0.08	11.37±0.02	10.38±0.02	5.35±0.01	...
ID73	ESO 286–19	9.94±0.09	1.97±0.02	-7.97±0.09	11.30±0.01	9.96±0.01	5.78±0.01	...
ID74	NGC 7130	11.06±0.11	1.30±0.07	-9.76±0.13	8.98±0.01	8.55±0.01	4.59±0.01	1.74±0.01
ID75	NGC 7469/IC 5283	10.83±0.17	1.49±0.08	-9.34±0.19
ID76	NGC 7469	10.69±0.18	1.51±0.08	-9.18±0.20	8.29±0.01	...	3.83±0.01	0.77±0.01
ID77	IC 5283	10.46±0.08	0.50±0.16	-9.97±0.18	10.30±0.01	10.10±0.01
ID78	ESO 148–2	10.21±0.40	1.93±0.05	-8.28±0.41	11.02±0.01	10.01±0.01	5.92±0.01	2.63±0.01
ID79	NGC 7591	10.62±0.11	1.04±0.04	-9.58±0.11	9.54±0.01	9.33±0.01	5.54±0.01	2.91±0.01
ID80	NGC 7674/MCG+01-59-081	11.21±0.06	1.25±0.10	-9.96±0.11
ID81	NGC 7674	11.10±0.08	1.22±0.09	-9.88±0.12	...	8.05±0.01	4.66±0.01	2.04±0.01
ID82	MCG+01-59-081	10.61±0.09	0.33±0.07	-10.28±0.11
ID83	NGC 7679/NGC 7682	10.77±0.03	1.06±0.02	-9.72±0.04
ID84	NGC 7679	10.33±0.07	1.05±0.02	-9.28±0.07	9.63±0.01	9.30±0.01	5.09±0.01	2.75±0.01
ID85	NGC 7682	10.62±0.04	-0.20±0.23	-10.83±0.23	10.20±0.01	10.21±0.01	7.86±0.02	5.21±0.03

NOTE—Comments: (1–2) ID and object name; (3) logarithmic stellar mass; (4) logarithmic SFR; (5) logarithmic specific SFR (sSFR); (6)–(9) W1, W2, W3, and W4 magnitudes (Vega) from ALLWISE catalog (Section 3.5 and 5.3). The W1 and W2 magnitudes are corrected for Galactic extinction (Section 3.8).

(This table is available in its entirety in machine-readable form.)

Table A3. Results of the Radio Fitting

ID	Name	α_{radio}	q_{ir}	$\log L_{1.4\text{GHz}}$	q_{excess}	χ^2_{red}
		(3)	(4)	(5) (erg s $^{-1}$)	(6)	(7)
(1)	(2)					
ID01	NGC 34	0.41 \pm 0.07	2.77 \pm 0.06	38.91 \pm 0.04	21.25 \pm 0.08	2.1
ID02	MCG -02-01-052/MCG -02-01-051	0.44 \pm 0.09	2.54 \pm 0.05	39.03 \pm 0.05	21.42 \pm 0.08	1.4
ID03	MCG -02-01-052	0.5 ^(f)	2.76 \pm 0.08	37.99 \pm 0.07	21.28 \pm 0.07	4.2
ID04	MCG -02-01-051	0.49 \pm 0.09	2.50 \pm 0.05	38.99 \pm 0.05	21.42 \pm 0.08	0.5
ID05	ESO 350-38	0.56 \pm 0.07	2.36 \pm 0.04	38.54 \pm 0.04	21.44 \pm 0.08	2.1
ID06	NGC 232/NGC 235	0.68 \pm 0.06	2.43 \pm 0.05	39.20 \pm 0.04	21.70 \pm 0.06	1.8
ID07	NGC 232	0.52 \pm 0.09	2.58 \pm 0.05	38.98 \pm 0.04	21.49 \pm 0.09	1.8
ID08	NGC 235	0.57 \pm 0.08	1.93 \pm 0.05	38.81 \pm 0.04	22.11 \pm 0.05	2.2
ID09	MCG+12-02-001	0.52 \pm 0.06	2.57 \pm 0.05	38.96 \pm 0.04	21.41 \pm 0.07	1.7
ID10	IC 1623A/IC 1623B	0.67 \pm 0.05	2.25 \pm 0.05	39.52 \pm 0.04	21.56 \pm 0.05	2.7
ID11	NGC 833/NGC 835	0.61 \pm 0.07	2.49 \pm 0.05	38.41 \pm 0.05	21.90 \pm 0.25	1.6
ID12	NGC 833	0.5 ^(f)	2.59 \pm 0.06	37.02 \pm 0.06	22.66 \pm 0.34	3.1
ID13	NGC 835	0.60 \pm 0.09	2.46 \pm 0.05	38.43 \pm 0.05	21.70 \pm 0.08	1.6
ID14	NGC 838	0.63 \pm 0.06	2.57 \pm 0.05	38.65 \pm 0.04	21.39 \pm 0.08	1.2
ID15	NGC 839	0.51 \pm 0.10	2.98 \pm 0.06	38.24 \pm 0.05	21.18 \pm 0.05	3.3
ID16	NGC 1068	0.56 \pm 0.04	2.09 \pm 0.05	39.23 \pm 0.04	21.83 \pm 0.09	3.6
ID17	UGC 2608/UGC 2612	0.79 \pm 0.07	2.25 \pm 0.05	39.37 \pm 0.04	21.86 \pm 0.08	0.8
ID18	UGC 2608	0.78 \pm 0.07	2.15 \pm 0.05	39.22 \pm 0.04	21.83 \pm 0.11	1.0
ID19	UGC 2612	0.5 ^(f)	3.47 \pm 0.03	37.40 \pm 0.02	20.72 \pm 0.07	4.0
ID20	NGC 1275	0.47 \pm 0.02	-0.57 \pm 0.03	41.29 \pm 0.03	24.24 \pm 0.05	3.6
ID21	NGC 1365	0.65 \pm 0.05	2.85 \pm 0.04	38.30 \pm 0.03	21.23 \pm 0.10	2.3
ID22	ESO 203-1	0.5 ^(f)	2.94 \pm 0.07	39.01 \pm 0.06	21.08 \pm 0.08	1.3
ID23	CGCG 468-002W/CGCG 468-002E	0.5 ^(f)	2.76 \pm 0.06	38.47 \pm 0.05	21.45 \pm 0.20	2.0
ID24	CGCG 468-002W	0.5 ^(f)	2.79 \pm 0.06	37.84 \pm 0.05	22.14 \pm 0.48	3.4
ID25	CGCG 468-002E	0.5 ^(f)	3.39 \pm 0.06	38.07 \pm 0.03	20.71 \pm 0.05	2.3
ID26	IRAS F05189-2524	0.5 ^(f)	2.49 \pm 0.05	39.22 \pm 0.05	21.51 \pm 0.13	3.7
ID27	IRAS F06076-2139/ 2MASS 06094601-2140312	0.36 \pm 0.09	2.67 \pm 0.05	38.97 \pm 0.05	21.18 \pm 0.12	0.7
ID28	NGC 2623	0.26 \pm 0.08	2.66 \pm 0.05	39.00 \pm 0.04	21.32 \pm 0.07	3.1
ID29	ESO 060-IG016 West/East	0.5 ^(f)	2.62 \pm 0.05	39.19 \pm 0.05	21.36 \pm 0.06	1.0
ID30	IRAS F08572+3915	0.5 ^(f)	3.40 \pm 0.07	38.69 \pm 0.04	20.65 \pm 0.04	11.3
ID31	UGC 5101	0.22 \pm 0.06	2.14 \pm 0.05	39.92 \pm 0.04	21.78 \pm 0.09	3.3
ID32	MCG+08-18-012/MCG+08-18-013	0.41 \pm 0.08	2.56 \pm 0.05	38.85 \pm 0.04	21.41 \pm 0.07	2.7
ID33	MCG+08-18-012	0.5 ^(f)	3.20 \pm 0.19	36.91 \pm 0.11	20.66 \pm 0.11	3.9
ID34	MCG+08-18-013	0.40 \pm 0.08	2.55 \pm 0.05	38.87 \pm 0.04	21.42 \pm 0.10	1.3
ID35	MCG-01-26-013/NGC 3110	0.64 \pm 0.05	2.31 \pm 0.05	39.06 \pm 0.04	21.66 \pm 0.10	1.4
ID36	MCG-01-26-013	0.5 ^(f)	2.45 \pm 0.06	37.82 \pm 0.05	21.43 \pm 0.07	2.2
ID37	NGC 3110	0.64 \pm 0.06	2.32 \pm 0.05	39.06 \pm 0.04	21.74 \pm 0.06	3.4
ID38	ESO 374-IG032	0.51 \pm 0.08	2.87 \pm 0.05	38.92 \pm 0.04	21.06 \pm 0.06	5.3
ID39	NGC 3256	0.52 \pm 0.06	2.52 \pm 0.06	39.36 \pm 0.05	21.41 \pm 0.08	1.3
ID40	IRAS F10565+2448	0.28 \pm 0.08	2.50 \pm 0.05	39.51 \pm 0.04	21.42 \pm 0.10	4.8
ID41	NGC 3690 West/East	0.50 \pm 0.05	2.34 \pm 0.05	39.37 \pm 0.04	21.53 \pm 0.11	2.2
ID42	ESO 440-58/MCG-05-29-017	0.58 \pm 0.06	2.53 \pm 0.04	38.95 \pm 0.03	21.49 \pm 0.05	1.5
ID43	IRAS F12112+0305	0.20 \pm 0.10	2.84 \pm 0.06	39.59 \pm 0.04	21.10 \pm 0.05	5.2
ID44	NGC 4418/MCG+00-32-013	0.5 ^(f)	3.21 \pm 0.07	37.89 \pm 0.05	20.93 \pm 0.10	3.1
ID45	NGC 4418	0.5 ^(f)	3.42 \pm 0.05	37.91 \pm 0.03	20.80 \pm 0.06	3.2
ID46	MCG+00-32-013	0.5 ^(f)	3.31 \pm 0.13	35.98 \pm 0.07	20.63 \pm 0.07	4.2
ID47	Mrk 231	0.37 \pm 0.05	2.27 \pm 0.05	40.25 \pm 0.04	21.67 \pm 0.09	0.3
ID48	NGC 4922S/NGC 4922N	0.33 \pm 0.07	2.37 \pm 0.05	38.84 \pm 0.04	21.78 \pm 0.07	0.9

Table A3 *continued*

Table A3 (*continued*)

ID	Name	α_{radio}	q_{ir}	$\log L_{1.4\text{GHz}}$ (erg s $^{-1}$)	q_{excess}	χ^2_{red}
(1)	(2)	(3)	(4)	(5)	(6)	(7)
ID49	IC 860	0.19 ± 0.10	2.98 ± 0.06	38.08 ± 0.04	21.08 ± 0.05	2.8
ID50	IRAS 13120–5453	$0.5^{(\text{f})}$	2.41 ± 0.05	39.98 ± 0.04	21.49 ± 0.08	1.9
ID51	NGC 5104	0.60 ± 0.07	2.60 ± 0.05	38.63 ± 0.04	21.52 ± 0.07	2.6
ID52	MCG–03-34-064	0.35 ± 0.04	1.44 ± 0.05	39.16 ± 0.04	22.55 ± 0.11	2.5
ID53	NGC 5135	0.60 ± 0.05	2.31 ± 0.05	39.08 ± 0.04	21.75 ± 0.10	0.9
ID54	Mrk 266B/Mrk 266A	0.60 ± 0.06	2.01 ± 0.04	39.50 ± 0.04	22.01 ± 0.07	1.5
ID55	Mrk 273	0.41 ± 0.06	2.46 ± 0.05	39.83 ± 0.04	21.44 ± 0.06	2.2
ID56	IRAS F14348–1447	0.42 ± 0.08	2.43 ± 0.05	39.91 ± 0.04	21.44 ± 0.08	2.3
ID57	IRAS F14378–3651	0.47 ± 0.08	2.60 ± 0.05	39.75 ± 0.04	21.28 ± 0.04	2.1
ID58	IC 4518A/IC 4518B	0.40 ± 0.08	1.90 ± 0.06	39.21 ± 0.06	21.83 ± 0.23	0.7
ID59	IRAS F15250+3608	0.33 ± 0.16	3.05 ± 0.07	39.15 ± 0.05	20.88 ± 0.05	2.6
ID60	Arp 220W/Arp 220E	0.09 ± 0.06	2.59 ± 0.05	39.51 ± 0.04	21.24 ± 0.06	5.3
ID61	NGC 6240S/NGC 6240N	0.69 ± 0.04	1.93 ± 0.04	39.93 ± 0.04	22.18 ± 0.06	1.5
ID62	NGC 6285/NGC 6286	0.44 ± 0.05	2.23 ± 0.04	39.29 ± 0.04	21.79 ± 0.05	4.2
ID63	NGC 6285	$0.5^{(\text{f})}$	2.60 ± 0.06	38.09 ± 0.05	21.33 ± 0.07	2.1
ID64	NGC 6286	0.46 ± 0.05	2.09 ± 0.04	39.25 ± 0.04	22.01 ± 0.06	5.0
ID65	IRAS F17138–1017	0.55 ± 0.08	2.75 ± 0.06	38.80 ± 0.04	21.17 ± 0.09	4.6
ID66	IRAS F18293–3413	0.65 ± 0.05	2.56 ± 0.04	39.37 ± 0.03	21.44 ± 0.07	0.8
ID67	IRAS F19297–0406	0.47 ± 0.09	2.49 ± 0.05	39.85 ± 0.04	21.31 ± 0.16	1.9
ID68	NGC 6907/NGC 6908	0.57 ± 0.06	2.55 ± 0.05	38.69 ± 0.04	21.47 ± 0.06	2.8
ID69	NGC 6921/MCG+04-48-002	0.59 ± 0.08	2.32 ± 0.05	38.84 ± 0.04	21.76 ± 0.14	0.4
ID70	NGC 6921	0.61 ± 0.09	2.13 ± 0.05	38.25 ± 0.05	22.44 ± 0.25	0.7
ID71	MCG+04-48-002	0.58 ± 0.09	2.36 ± 0.05	38.70 ± 0.05	21.68 ± 0.10	0.6
ID72	II Zw 096/IRAS F20550+1655 SE	0.77 ± 0.07	2.65 ± 0.06	39.23 ± 0.05	21.18 ± 0.05	3.1
ID73	ESO 286–19	0.24 ± 0.10	2.82 ± 0.07	39.32 ± 0.06	21.20 ± 0.06	2.2
ID74	NGC 7130	0.38 ± 0.05	2.09 ± 0.04	39.19 ± 0.03	21.74 ± 0.08	1.3
ID75	NGC 7469/IC 5283	0.53 ± 0.08	2.37 ± 0.05	39.19 ± 0.04	21.56 ± 0.09	0.4
ID76	NGC 7469	0.50 ± 0.08	2.42 ± 0.05	39.17 ± 0.04	21.51 ± 0.09	0.5
ID77	IC 5283	0.86 ± 0.09	2.72 ± 0.06	38.02 ± 0.05	21.38 ± 0.17	1.1
ID78	ESO 148–2	0.47 ± 0.16	2.81 ± 0.08	39.30 ± 0.06	21.22 ± 0.08	2.4
ID79	NGC 7591	0.46 ± 0.09	2.57 ± 0.05	38.64 ± 0.05	21.46 ± 0.06	2.1
ID80	NGC 7674/MCG+01-59-081	0.43 ± 0.06	1.73 ± 0.05	39.75 ± 0.05	22.36 ± 0.11	0.8
ID81	NGC 7674	$0.5^{(\text{f})}$	1.84 ± 0.07	39.60 ± 0.06	22.23 ± 0.11	0.6
ID82	MCG+01-59-081	$0.5^{(\text{f})}$	3.21 ± 0.08	37.39 ± 0.06	20.92 ± 0.09	0.6
ID83	NGC 7679/NGC 7682	0.32 ± 0.08	2.21 ± 0.05	39.02 ± 0.04	21.82 ± 0.05	1.5
ID84	NGC 7679	0.44 ± 0.09	2.51 ± 0.05	38.70 ± 0.04	21.51 ± 0.05	1.0
ID85	NGC 7682	0.21 ± 0.07	1.29 ± 0.05	38.72 ± 0.04	22.78 ± 0.23	1.5

NOTE—Comments: (1–2) ID and object name; (3) radio spectral index of the power-law synchrotron emission. The symbol “(f)” means that the value is fixed; (4) the far-IR/radio correlation coefficient; (5) rest-frame radio 1.4 GHz luminosity; (6) radio-excess parameter $q_{\text{excess}} = \log(L_{1.4\text{GHz}}/\text{SFR})$; (7) reduced χ^2 for the combination of the radio fitting and UV-to-IR SED decomposition.

(This table is available in its entirety in machine-readable form.)

Table A4. Summary of the logarithmic AGN luminosities

ID (1)	Name (2)	$L_{6,\text{AGN}}$ (3)	$L_{12,\text{t}}$ (4)	$L_{12,\text{p}}$ (5)	$L_{12,\text{AGN}}$ (6)	$L_{12,\text{nuc}}$ (7)	$L_{\text{X,unabs}}$ (8)	$L_{2\text{keV,unabs}}$ (9)	$L_{2500,\text{disk}}$ (10)	α_{OX} (11)
ID01	NGC 34	43.14	43.46	43.70	43.89	43.10	$41.90^{+0.10}_{-0.10}$	41.63	43.07	-1.55
ID05	ESO 350-38	43.23	43.87	42.93	43.92	43.84	...
ID06	NGC 232/NGC 235	43.01	43.59	...	43.59	...	$43.28^{+0.18}_{-0.16}$	42.98	43.24	-1.10
ID08	NGC 235	42.68	43.25	...	43.25	43.29	$43.28^{+0.18}_{-0.16}$	42.97	42.84	-0.95
ID09	MCG+12-02-001	42.54	43.15	43.09	43.42	...	$41.75^{+0.33}_{-0.08}$	41.48	42.88	-1.54
ID11	NGC 833/NGC 835	42.49	42.77	43.32	43.43	...	$42.33^{+0.28}_{-0.24}$	42.04	42.54	-1.19
ID12	NGC 833	41.37	41.95	...	41.95	...	$41.99^{+0.25}_{-0.24}$	41.78	41.51	-0.89
ID13	NGC 835	42.31	42.89	42.75	43.13	...	$42.06^{+0.13}_{-0.03}$	41.67	42.59	-1.35
ID16	NGC 1068	43.54	43.93	44.52	44.62	43.80	$43.34^{+0.07}_{-0.08}$...	43.96	...
ID17	UGC 2608/UGC 2612	43.84	44.48	...	44.48	...	$43.59^{+0.19}_{-0.25}$	43.48	44.55	-1.41
ID18	UGC 2608	43.49	44.12	...	44.12	...	$43.59^{+0.19}_{-0.25}$	43.33	44.26	-1.36
ID20	NGC 1275 [†]	43.88	44.43	43.10	44.45	44.21	...	43.19	43.84	-1.25
ID21	NGC 1365	42.79	43.23	43.44	43.65	42.51	$41.90^{+0.01}_{-0.01}$	41.71	42.65	-1.36
ID23	CGCG 468-002W/CGCG 468-002E	42.98	43.55	42.39	43.58	...	$42.84^{+0.04}_{-0.03}$	42.49	43.14	-1.25
ID24	CGCG 468-002W	42.44	42.97	42.83	43.21	...	$42.84^{+0.04}_{-0.03}$	42.51	42.64	-1.05
ID26	IRAS F05189-2524	44.38	44.92	43.89	44.95	44.87	$43.42^{+0.01}_{-0.02}$	43.30	44.60	-1.50
ID27	IRAS F06076-2139/ 2MASS 06094601-2140312	42.94	43.55	43.50	43.82	...	$42.18^{+0.15}_{-0.14}$	41.92	43.14	-1.47
ID28	NGC 2623	42.77	43.37	42.11	43.39	43.61	$40.90^{+0.11}_{-0.11}$	40.64	43.00	-1.91
ID29	ESO 060-IG016 West/East	43.60	44.14	...	44.14	...	$41.94^{+0.07}_{-0.08}$	41.69	43.73	-1.78
ID30	IRAS F08572+3915	44.04	44.70	44.79	45.05	45.13	$41.77^{+0.06}_{-0.07}$	41.52	44.61	-2.19
ID31	UGC 5101	43.51	44.05	42.97	44.08	44.35	$43.15^{+0.25}_{-0.15}$	42.77	43.72	-1.36
ID38	ESO 374-IG032	43.39	43.93	43.43	44.05	43.28	...
ID41	NGC 3690 West/East	44.04	44.70	42.89	44.70	...	$42.66^{+0.34}_{-0.32}$	42.55	43.80	-1.48
ID44	NGC 4418/MCG+00-32-013	42.33	43.11	43.55	43.68	43.32	...
ID45	NGC 4418	42.24	42.75	43.49	43.56	43.70	42.89	...
ID47	Mrk 231	44.60	45.20	44.92	45.38	...	$42.65^{+0.02}_{-0.02}$	42.28	44.71	-1.93
ID48	NGC 4922S/NGC 4922N	43.39	44.02	42.86	44.05	...	$42.00^{+0.20}_{-0.18}$	41.74	43.52	-1.68
ID50	IRAS 13120-5453	43.29	43.94	43.00	43.99	...	$42.17^{+0.59}_{-0.11}$	41.91	43.88	-1.76
ID52	MCG-03-34-064	43.49	43.95	44.18	44.38	44.00	$43.27^{+0.06}_{-0.07}$	43.08	43.53	-1.17
ID53	NGC 5135	42.18	42.82	42.04	42.89	43.23	$43.30^{+0.42}_{-0.26}$	43.01	42.90	-0.96
ID54	Mrk 266B/Mrk 266A	43.07	43.56	43.69	43.93	42.71	43.17	-1.18
ID55	Mrk 273	43.41	43.94	42.91	43.98	...	$43.07^{+0.21}_{-0.21}$	42.78	43.73	-1.36
ID56	IRAS F14348-1447	43.33	44.05	43.27	44.12	...	$42.70^{+0.93}_{-0.40}$	42.46	44.07	-1.62
ID58	IC 4518A/IC 4518B	43.14	43.39	43.81	43.95	43.54	$42.83^{+0.06}_{-0.08}$	42.55	42.93	-1.14
ID60	Arp 220W/Arp 220E	43.10	43.70	43.64	43.97	...	$41.59^{+0.02}_{-0.02}$	41.33	43.38	-1.79
ID61	NGC 6240S/NGC 6240N	43.45	44.01	43.52	44.14	43.57	43.42	-0.94
ID62	NGC 6285/NGC 6286	42.10	42.94	42.20	43.01	...	$42.01^{+1.21}_{-0.23}$	41.64	42.98	-1.51
ID64	NGC 6286	41.71	42.54	41.96	42.64	...	$42.01^{+1.21}_{-0.23}$	41.63	42.80	-1.45
ID65	IRAS F17138-1017	43.32	43.92	42.80	43.95	...	$41.68^{+0.09}_{-0.06}$	41.41	43.27	-1.71
ID69	NGC 6921/MCG+04-48-002	42.96	43.52	...	43.52	...	$42.96^{+0.40}_{-0.46}$	42.64	43.12	-1.19
ID70	NGC 6921	41.48	42.47	...	42.47	...	$42.80^{+0.37}_{-0.44}$	42.49	42.48	-1.00
ID71	MCG+04-48-002	42.80	43.37	...	43.37	...	$42.44^{+0.15}_{-0.15}$	42.12	43.02	-1.34
ID74	NGC 7130	42.91	43.71	42.75	43.75	43.18	$42.87^{+0.31}_{-0.25}$	42.55	43.58	-1.39
ID75	NGC 7469/IC 5283	43.76	44.35	43.20	44.38	...	$43.26^{+0.03}_{-0.02}$	43.06	43.85	-1.30
ID76	NGC 7469	43.63	44.21	43.07	44.24	43.83	$43.26^{+0.03}_{-0.02}$	43.07	43.84	-1.29
ID78	ESO 148-2	43.65	44.29	43.35	44.34	...	$42.38^{+0.24}_{-0.28}$	42.13	44.25	-1.81
ID80	NGC 7674/MCG+01-59-081	44.04	44.58	42.55	44.59	...	$42.59^{+0.33}_{-0.23}$	42.29	43.73	-1.55
ID81	NGC 7674	44.03	44.54	43.53	44.58	44.26	$42.59^{+0.33}_{-0.23}$	42.28	43.71	-1.55

Table A4 *continued*

Table A4 (*continued*)

ID (1)	Name (2)	$L_{6,\text{AGN}}$ (3)	$L_{12,\text{t}}$ (4)	$L_{12,\text{p}}$ (5)	$L_{12,\text{AGN}}$ (6)	$L_{12,\text{nuc}}$ (7)	$L_{\text{X},\text{unabs}}$ (8)	$L_{2\text{keV},\text{unabs}}$ (9)	$L_{2500,\text{disk}}$ (10)	α_{OX} (11)
ID83	NGC 7679/NGC 7682	42.67	43.16	43.47	43.65	...	$42.49^{+0.08}_{-0.07}$	42.21	42.70	-1.19
ID84	NGC 7679	42.58	42.96	43.34	43.49	42.74	$42.34^{+0.06}_{-0.04}$	42.06	42.47	-1.16
ID85	NGC 7682	41.05	42.13	...	42.13	...	$41.94^{+0.06}_{-0.06}$	41.68	41.94	-1.00

NOTE—Comments: (1–2) ID and object name; (3) logarithmic rest-frame 6 μm luminosity of AGN (torus and polar dust) component ($L_{6,\text{AGN}}$); (4)–(6) logarithmic rest-frame 12 μm luminosities of torus component ($L_{12,\text{t}}$), polar component ($L_{12,\text{p}}$), and both components ($L_{12,\text{AGN}}$); (7) logarithmic nuclear 12 μm luminosity ($L_{12,\text{nuc}}$) referred from Asmus et al. (2014, 2015); (8)–(9) logarithmic unabsorbed (absorption-corrected) AGN luminosities in the rest-frame 2–10 keV ($L_{\text{X},\text{unabs}}$) and 2 keV bands ($L_{2\text{keV},\text{unabs}}$); (10) logarithmic extinction-corrected intrinsic AGN disk luminosity in the rest-frame 2500 Å band ($L_{2500,\text{disk}}$); (11) X-ray to optical spectral index computed by $\alpha_{\text{OX}} \equiv \log(L''_{2\text{keV}}/L''_{2500})/\log(\nu_{2\text{keV}}/\nu_{2500})$, where $L''_{2\text{keV}} = L_{2\text{keV},\text{unabs}}/\nu_{2\text{keV}}$ and $L''_{2500} = L_{2500,\text{disk}}/\nu_{2500}$.

† Large fractions of the mid-IR and X-ray luminosities in NGC 1275 could be explained by the jet emission (e.g., Hitomi Collaboration et al. 2018; Rani et al. 2018).

(This table is available in its entirety in machine-readable form.)

Table A5. Summary of the Extinction, AGN Luminosities, and Polar Dust Sizes

ID	Name	$N_{\text{H}}^{(\text{LOS})}$ (10^{22} cm^{-2})	$A_{\text{V,torus}}^{(\text{LOS})}$ (mag)	$A_{\text{V,polar}}^{(\text{LOS})}$ (mag)	$\log L_{\text{torus}}$ (erg s^{-1})	$\log L_{\text{polar}}$ (erg s^{-1})	$\log L_{\text{AGN,int}}$ (erg s^{-1})	$\log M_{\text{BH}}$ (M_{\odot})	$\log \lambda_{\text{Edd}}$ (10)	$\log R_{\text{polar}}$ (pc)	$\log R_{\text{mir/i/o/mo}}$ (pc)
(1)	(2)	(3)	(4)	(5)	(6)	(7)	(8)	(9)	(10)	(11)	(12)
ID01	NGC 34	$50.3^{+10.3}_{-9.9}$	108.3 \pm 32.0	0.2 \pm 0.4	43.54 \pm 0.16	43.53 \pm 0.16	43.84 \pm 0.16	7.82	-2.08 \pm 0.16	1.67 \pm 0.40	$\cdots/\cdots/\cdots$
ID05	ESO 350-38	...	346.6 \pm 58.5	0	43.96 \pm 0.04	44.30 \pm 0.04	44.62 \pm 0.04	2.71 \pm 0.02	$\cdots/\cdots/\cdots$
ID06	NGC 232/NGC 235	$51.4^{+8.3}_{-6.1}$	106.7 \pm 32.3	...	43.75 \pm 0.02	44.01 \pm 0.02	44.01 \pm 0.02	8.20	-2.29 \pm 0.02	...	$\cdots/\cdots/\cdots$
ID08	NGC 235	$51.4^{+8.3}_{-6.1}$	99.4 \pm 33.7	...	43.35 \pm 0.03	43.61 \pm 0.03	43.61 \pm 0.03	8.20	-2.69 \pm 0.03	...	$\cdots/\cdots/\cdots$
ID09	MCG+12-02-001	$707.5^{+268.4}_{-277.1}$	110.3 \pm 31.5	1.7 \pm 0.9	43.33 \pm 0.14	43.48 \pm 0.16	43.66 \pm 0.15	7.04	-1.48 \pm 0.15	1.55 \pm 0.32	$\cdots/\cdots/\cdots$
ID11	NGC 833/NGC 835	...	17.4 \pm 6.2	1.7 \pm 0.9	42.91 \pm 0.07	43.17 \pm 0.04	43.31 \pm 0.06	1.21 \pm 0.31	$\cdots/\cdots/\cdots$
ID12	NGC 833	$26.1^{+1.2}_{-1.1}$	16.2 \pm 6.4	...	41.95 \pm 0.17	42.28 \pm 0.17	42.28 \pm 0.17	8.61	-4.43 \pm 0.17	...	$\cdots/\cdots/\cdots$
ID13	NGC 835	$29.8^{+0.8}_{-1.5}$	18.2 \pm 5.9	0.5 \pm 0.8	42.99 \pm 0.08	43.12 \pm 0.07	43.37 \pm 0.08	7.85	-2.58 \pm 0.08	1.30 \pm 0.31	$\cdots/\cdots/\cdots$
ID16	NGC 1068	\sim 1000	664.8 \pm 278.0	0	44.04 \pm 0.07	44.49 \pm 0.05	44.74 \pm 0.07	7.35	-0.71 \pm 0.07	1.65 \pm 0.04	$1.73/\cdots/2.00$
ID17	UGC 2608/UGC 2612	540^{+700}_{-310}	436.8 \pm 209.2	...	44.52 \pm 0.09	45.33 \pm 0.09	45.33 \pm 0.09	7.64	-0.42 \pm 0.09	...	$\cdots/\cdots/\cdots$
ID18	UGC 2608	540^{+700}_{-310}	447.1 \pm 220.0	...	44.22 \pm 0.16	44.22 \pm 0.16	45.04 \pm 0.17	7.64	-0.71 \pm 0.17	...	$\cdots/\cdots/\cdots$
ID20	NGC 1275 †	...	0.1 \pm 0.1	2.5 \pm 0.1	44.46 \pm 0.02	44.48 \pm 0.02	44.62 \pm 0.02	2.70 \pm 0.01	$\cdots/\cdots/\cdots$
ID21	NGC 1365	\sim 10	0.1 \pm 0.1	2.5 \pm 0.1	43.28 \pm 0.02	43.30 \pm 0.02	43.43 \pm 0.02	8.13	-2.80 \pm 0.02	1.07 \pm 0.13	$1.74/\cdots/\cdots$
ID23	CGCG 468-002W/CGCG 468-002E	$1.5^{+0.1}_{-0.1}$	16.2 \pm 6.4	0.2 \pm 0.1	43.55 \pm 0.12	43.64 \pm 0.12	43.91 \pm 0.12	7.67	-1.86 \pm 0.12	2.07 \pm 0.34	$\cdots/\cdots/\cdots$
ID24	CGCG 468-002W	$1.5^{+0.1}_{-0.1}$	16.9 \pm 6.3	0.2 \pm 0.2	43.05 \pm 0.10	43.15 \pm 0.13	43.41 \pm 0.10	7.67	-2.36 \pm 0.10	1.52 \pm 0.28	$\cdots/\cdots/\cdots$
ID26	IRAS F05189-2524	$7.5^{+0.1}_{-0.1}$	8.0 \pm 0.5	2.5 \pm 0.1	44.96 \pm 0.02	45.27 \pm 0.02	45.38 \pm 0.02	7.94	-0.66 \pm 0.02	3.08 \pm 0.01	$/3.48/2.28$
ID27	IRAS F06076-2139/	$42.2^{+24.0}_{-12.0}$	107.7 \pm 31.7	1.7 \pm 0.9	43.59 \pm 0.08	43.73 \pm 0.10	43.92 \pm 0.08	7.30	-1.48 \pm 0.08	1.97 \pm 0.24	$\cdots/\cdots/\cdots$
ID28	2MASS 06094601-2140312	$6.0^{+4.5}_{-2.1}$	119.3 \pm 23.9	0.2 \pm 0.1	43.47 \pm 0.02	43.45 \pm 0.02	43.77 \pm 0.02	7.62	-1.95 \pm 0.02	2.28 \pm 0.06	$\cdots/\cdots/\cdots$
ID29	NGC 2623	$8.4^{+4.0}_{-2.9}$	91.9 \pm 35.7	...	44.25 \pm 0.02	44.51 \pm 0.02	44.51 \pm 0.02	7.79	-1.38 \pm 0.02	...	$\cdots/\cdots/\cdots$
ID30	IRAS F08572+3915	$84.6^{+129.3}_{-28.3}$	417.9 \pm 199.3	0	44.72 \pm 0.07	45.05 \pm 0.06	45.39 \pm 0.06	7.48	-0.19 \pm 0.06	2.38 \pm 0.28	$\cdots/3.30/2.91$
ID31	UGC 5101	$96.3^{+4.3}_{-1.6}$	8.9 \pm 3.2	0.9 \pm 0.2	44.11 \pm 0.08	44.35 \pm 0.08	44.50 \pm 0.08	8.17	-1.77 \pm 0.08	2.64 \pm 0.10	$\cdots/\cdots/\cdots$
ID38	ESO 374-IG032	...	0.1 \pm 0.1	0.2 \pm 0.2	43.95 \pm 0.03	43.75 \pm 0.07	44.05 \pm 0.04	1.77 \pm 0.32	$\cdots/\cdots/\cdots$
ID41	NGC 3690 West/East	$302.6^{+60.6}_{-49.7}$	161.0 \pm 56.9	1.8 \pm 1.0	44.69 \pm 0.16	44.07 \pm 0.19	44.57 \pm 0.17	7.09	-0.62 \pm 0.17	2.12 \pm 0.45	$\cdots/\cdots/\cdots$
ID44	NGC 4418/MCG+00-32-013	...	991.4 \pm 86.0	0	43.38 \pm 0.03	43.90 \pm 0.03	44.10 \pm 0.03	1.95 \pm 0.01	$\cdots/\cdots/\cdots$
ID45	NGC 4418	...	695.0 \pm 238.8	0	42.97 \pm 0.02	43.47 \pm 0.02	43.67 \pm 0.02	1.39 \pm 0.01	$\cdots/\cdots/2.76$
ID47	Mrk 231	$8.5^{+0.2}_{-2.4}$	202.3 \pm 33.7	1.3 \pm 0.9	45.21 \pm 0.11	45.23 \pm 0.11	45.49 \pm 0.10	7.92	-0.53 \pm 0.10	2.39 \pm 0.36	$\cdots/3.48/2.78$
ID48	NGC 4922S/NGC 4922N	$75.9^{+285.1}_{-21.6}$	93.1 \pm 37.0	1.2 \pm 0.6	43.98 \pm 0.12	44.11 \pm 0.12	44.30 \pm 0.12	7.79	-1.59 \pm 0.12	2.18 \pm 0.38	$\cdots/\cdots/\cdots$
ID50	IRAS 13120-5453	$164.8^{+21.6}_{-20.5}$	413.0 \pm 183.4	0	43.99 \pm 0.06	44.37 \pm 0.06	44.66 \pm 0.06	8.43	-1.87 \pm 0.06	2.72 \pm 0.07	$\cdots/2.48/2.25$
ID52	MCG-03-34-064	$98.4^{+2.8}_{-2.4}$	55.3 \pm 23.1	2.5 \pm 0.2	43.97 \pm 0.04	44.14 \pm 0.04	44.30 \pm 0.04	7.95	-1.75 \pm 0.04	1.67 \pm 0.11	$2.33/\cdots/\cdots$
ID53	NGC 5135	670^{+1660}_{-280}	548.1 \pm 228.5	0	42.86 \pm 0.21	43.48 \pm 0.20	43.68 \pm 0.21	7.77	-2.19 \pm 0.21	1.85 \pm 0.52	$2.11/2.63/\cdots$
ID54	Mrk 266B/Mrk 266A	$700/6.8$	111.9 \pm 30.2	0.3 \pm 0.5	43.65 \pm 0.10	43.64 \pm 0.10	43.95 \pm 0.10	1.64 \pm 0.31	$\cdots/\cdots/\cdots$
ID55	Mrk 273	$49.6^{+5.5}_{-2.8}$	14.4 \pm 6.5	2.4 \pm 0.3	44.09 \pm 0.13	44.40 \pm 0.13	44.51 \pm 0.13	8.35	-1.94 \pm 0.13	2.64 \pm 0.10	$\cdots/3.60/2.74$
ID56	IRAS F14348-1447	$128.3^{+35.4}_{-35.0}$	602.6 \pm 277.5	0	44.15 \pm 0.15	44.61 \pm 0.18	44.84 \pm 0.17	7.84	-1.10 \pm 0.17	2.79 \pm 0.15	$\cdots/\cdots/2.55$
ID58	IC 4518A/IC 4518B	$17.1^{+0.5}_{-0.9}$	90.9 \pm 37.4	1.2 \pm 1.0	43.39 \pm 0.27	43.48 \pm 0.27	43.70 \pm 0.26	7.53	-1.93 \pm 0.26	1.53 \pm 0.41	$2.29/\cdots/\cdots$

Table A5 *continued*

Table A5 (*continued*)

ID	Name	$N_{\text{H}}^{(\text{LOS})}$ (10^{22} cm^{-2})	$A_{V,\text{torus}}^{(\text{LOS})}$ (mag)	$A_{V,\text{polar}}^{(\text{LOS})}$ (mag)	$\log L_{\text{torus}}$ (erg s $^{-1}$)	$\log L_{\text{polar}}$ (erg s $^{-1}$)	$\log L_{\text{AGN,int}}$ (erg s $^{-1}$)	$\log M_{\text{BH}}$ (M_{\odot})	$\log \lambda_{\text{Edd}}$	$\log R_{\text{polar}}$ (pc)	$\log R_{\text{mir/ir/o/mo}}$ (pc)
(1)	(2)	(3)	(4)	(5)	(6)	(7)	(8)	(9)	(10)	(11)	(12)
ID60	Arp 220W/Arp 220E	1000.0 $^{+n}_{-22.1}$	126.3 \pm 20.0	2.2 \pm 0.6	43.81 \pm 0.05	43.99 \pm 0.03	44.15 \pm 0.04	2.06 \pm 0.17	.../.../...
ID61	NGC 6240S/NGC 6240N	147/155	0.1 \pm 0.1	0.2 \pm 0.2	44.11 \pm 0.02	43.89 \pm 0.02	44.20 \pm 0.02	2.12 \pm 0.28	.../.../2.81
ID62	NGC 6285/NGC 6286	140.2 $^{+26.7}_{-34.6}$	690.5 \pm 276.1	0	43.06 \pm 0.05	43.50 \pm 0.02	43.75 \pm 0.05	7.98	-2.33 \pm 0.05	1.61 \pm 0.53	.../.../...
ID64	NGC 6286	140.2 $^{+26.7}_{-34.6}$	694.8 \pm 277.4	0	42.88 \pm 0.05	43.35 \pm 0.02	43.58 \pm 0.05	7.98	-2.51 \pm 0.05	1.55 \pm 0.54	.../.../...
ID65	IRAS F17138-1017	1000.0 $^{+n}_{-64.5}$	93.2 \pm 38.0	1.1 \pm 0.9	43.72 \pm 0.20	43.84 \pm 0.24	44.05 \pm 0.21	6.76	-0.81 \pm 0.21	2.06 \pm 0.50	.../.../...
ID69	NGC 6921/MCG+04-48-002	...	98.9 \pm 35.0	...	43.63 \pm 0.02	...	43.89 \pm 0.02/.../...
ID70	NGC 6921	173.1 $^{+27.8}_{-31.9}$	693.8 \pm 275.7	...	42.55 \pm 0.03	...	43.25 \pm 0.04	8.11	-2.96 \pm 0.04/.../...
ID71	MCG+04-48-002	72.7 $^{+14.8}_{-8.0}$	104.5 \pm 32.8	...	43.53 \pm 0.11	...	43.80 \pm 0.11	7.64	-1.94 \pm 0.11/.../...
ID74	NGC 7130	413.3 $^{+13.1}_{-7.4}$	734.0 \pm 292.7	0	43.78 \pm 0.18	44.05 \pm 0.18	44.35 \pm 0.18	7.89	-1.64 \pm 0.18	2.47 \pm 0.37	.../3.08/...
ID75	NGC 7469/IC 5283	<0.01	0.0 \pm 0.1	1.1 \pm 1.1	44.36 \pm 0.11	44.44 \pm 0.14	44.63 \pm 0.11	7.30	-0.77 \pm 0.11	2.68 \pm 0.14	.../.../...
ID76	NGC 7469	<0.01	0.0 \pm 0.1	2.2 \pm 0.6	44.32 \pm 0.12	44.51 \pm 0.11	44.62 \pm 0.11	7.30	-0.79 \pm 0.11	2.68 \pm 0.13	2.12/.../...
ID78	ESO 148-2	158.5 $^{+45.0}_{-47.6}$	383.4 \pm 151.1	0	44.36 \pm 0.10	44.72 \pm 0.11	45.03 \pm 0.10	7.49	-0.57 \pm 0.10	2.91 \pm 0.06	.../3.41/...
ID80	NGC 7674/MCG+01-59-081	29.6 $^{+2.5}_{-1.9}$	81.1 \pm 36.2	0.2 \pm 0.2	44.66 \pm 0.05	43.95 \pm 0.05	44.51 \pm 0.05	7.99	-1.58 \pm 0.05	2.26 \pm 0.42	.../.../...
ID81	NGC 7674	29.6 $^{+2.5}_{-1.9}$	69.1 \pm 33.1	0.2 \pm 0.2	44.64 \pm 0.06	43.93 \pm 0.07	44.49 \pm 0.06	7.99	-1.60 \pm 0.06	2.25 \pm 0.38	2.59/.../...
ID83	NGC 7679/NGC 7682	...	103.3 \pm 34.2	1.5 \pm 1.0	43.15 \pm 0.16	43.28 \pm 0.18	43.48 \pm 0.16	1.42 \pm 0.39	.../.../...
ID84	NGC 7679	<0.01	0.0 \pm 0.1	1.4 \pm 1.0	42.98 \pm 0.15	43.09 \pm 0.12	43.24 \pm 0.13	7.42	-2.28 \pm 0.13	1.23 \pm 0.41	.../.../...
ID85	NGC 7682	38.2 $^{+6.5}_{-7.0}$	691.4 \pm 268.8	...	42.67 \pm 0.22	...	42.72 \pm 0.21	7.48	-2.86 \pm 0.21/.../...

NOTE—Comments: (1–2) ID and object name; (3) line-of-sight hydrogen column density derived from X-ray spectral analysis (Section 3.1; Yamada et al. 2021); (4)–(5) line-of-sight extinction in the V band due to torus, $A_{V,\text{torus}}^{(\text{LOS})}$, and polar dust, $A_{V,\text{polar}}^{(\text{LOS})}$; (6)–(8) logarithmic UV-to-IR luminosities of torus component (L_{torus}), polar dust component (L_{polar}), and intrinsic AGN disk component ($L_{\text{AGN,int}}$); (9) SMBH mass estimated from the averaged value of four independent measurements in Yamada et al. (2021); (10) logarithmic Eddington ratio ($L_{\text{AGN,int}}/L_{\text{Edd}}$). The Eddington luminosity is defined as $L_{\text{Edd}} = 1.26 \times 10^{38} M_{\text{BH}}/M_{\odot}$; (11) physical size of polar dust, estimated by the polar dust temperature and dust sublimation radius (Section 6.5.1); (12) physical sizes of the polar dust emission detected in the mid-IR band (R_{mir} ; Asmus 2019), radius of ionized outflows (R_{io} ; Flütsch et al. 2021), and radius of molecular outflows (R_{mo} ; Flütsch et al. 2019).

[†] Large fractions of the X-ray and mid-IR luminosities in NGC 1275 could be explained by the jet emission (e.g., Hitomi Collaboration et al. 2018; Rani et al. 2018).

(This table is available in its entirety in machine-readable form.)

B. MOCK ANALYSIS

We evaluate the constrainability of a model parameter by the “mock analysis” of X-CIGALE. This is implemented in the previous version of CIGALE (see e.g., Buat et al. 2012, 2014; Ciesla et al. 2015; Lo Faro et al. 2017; Boquien et al. 2019; Toba et al. 2020b; Yang et al. 2020a). X-CIGALE uses the photometric data for each object based on the best-fit parameters. It allows the fluxes to vary within the uncertainties of the observations by adding a value taken from a Gaussian distribution with the same standard deviation as indicated by the photometric data.

Figure B1 shows the results of the mock analysis with the best-fit values compared to the mock values for the main parameters in this study. We find that the mean differences (the best-fit values – mock values) are small; $\Delta \log M_* = -0.01 \pm 0.11$, $\Delta \log \text{SFR} = -0.01 \pm 0.07$, $\Delta f_{\text{AGN}} = 0.00 \pm 0.03$, $\Delta \log L_{\text{AGN,int}} = 0.01 \pm 0.08$, $\Delta \log L_{\text{polar}} = -0.01 \pm 0.08$, and $\Delta T_{\text{polar}} = 0.21 \pm 18.19$. The deviation of the differences in T_{polar} is relatively large but consistent with the range of 1σ uncertainty of each object. Therefore, we conclude that these quantities are not sensitive to photometric uncertainties thanks to the multiwavelength SED analysis with the self-consistent AGN model.

C. COMPARISON WITH PREVIOUS SED STUDIES

Here, we examine the difference in the results of this study and previous SED works. For the local U/LIRGs in GOALS sample, Shangguan et al. (2019) performed the IR (1–500 μm) SED fitting and Paspaliaris et al. (2021) carried out the UV-to-submillimeter SED analysis. Our estimates of the SFRs are well consistent with their works (Figure C1). Whereas, we find that their stellar mass is smaller than those of our results (Figure C2). For the results of Shangguan et al. (2019), this may be explained by that the lack of optical photometric data that causes the overestimation of the fraction of the old-stellar population. In this case, the estimates of the luminosity from each star become small, and thus the total stellar mass will be overestimated. Although it is unclear why are the estimates of stellar mass by Paspaliaris et al. (2021) also larger, this may be affected by the difference in the contribution of the IR polar dust emission in our analysis that applies the torus parameters obtained from the X-ray fitting.

In the left panel of Figure C3, we compare the AGN luminosities in this study and those in Yamada et al. (2021). Their AGN luminosities are estimated by the averaged values of four different methods (e.g., the [O IV] luminosity, bolometric AGN fraction, and IR SED anal-

ysis). Its typical scatter is reported as ~ 0.27 dex when we adopt the averaged value. Particularly, the estimates using the [O IV] luminosities may be larger than those from other methods, which may be due to the contamination from the intense starburst emission in U/LIRGs (but see also Yamada et al. 2019). Even if the intrinsic AGN luminosities given by Yamada et al. (2021) are adopted, the main discussion on the $\text{SFR}-L_{\text{AGN,int}}$ relation is unchanged (see Section 7.1). The right panel of Figure C3 presents the comparison between the 12 μm luminosity of the AGN component (this study) and the nuclear 12 μm luminosities estimated with the high-spatial-resolution mid-IR images (Asmus 2019). Although there are a few differences, the multiwavelength SED analysis extracts the AGN emission that is consistent with the imaging studies.

D. COMPARISON WITH THE RESULTS OF SKIRTOR MODEL

In this study, we also performed the SED decomposition by using the AGN model as the SKIRTOR model (Stalevski et al. 2016) instead of the CLUMPY model. The σ values are converted from torus angular width (σ) of $[10^\circ\text{--}15^\circ, 15^\circ\text{--}25^\circ, 25^\circ\text{--}70^\circ]$ to angle between the equatorial plane and edge of the torus (Δ) of $[30^\circ, 40^\circ, 60^\circ]$, respectively. The smooth component in the SKIRTOR model shields the AGN disk emission at subparsec scales and re-radiates the strong near-IR emission relative to the clumpy torus model (Stalevski et al. 2012, 2016). In fact, the UV-to-IR SEDs of IRAS F08572+3915 that is not reproduced with CLUMPY ($\chi^2_{\text{red}} = 11.8$) due to the near-IR bump (as illustrated in the WISE color–color diagram in Section 5.3), while it is well fitted with SKIRTOR model ($\chi^2_{\text{red}} = 6.7$). The intrinsic AGN luminosities of IRAS F08572+3915 estimated with CLUMPY ($\log L_{\text{AGN,int}} = 45.39 \pm 0.06$) is smaller than that from SKIRTOR (45.82 ± 0.02). NGC 833, a stage A merger, is another outlier that shows the gap between the estimates with CLUMPY ($\log L_{\text{AGN,int}} = 42.28 \pm 0.17$) and SKIRTOR (42.91 ± 0.20 ; left panel of Figure D1), but the reason for the difference should be the poor photometry in the 5–70 μm band (see Figure E1). Except for the IRAS F08572+3915 and NGC 833, all sources show similar AGN luminosities with these models. Identically, the polar dust luminosities constrained with the SKIRTOR model are well consistent with the values with CLUMPY (right panel of Figure D1).

Additionally, we investigate the polar dust temperature derived from the fits with SKIRTOR (left panel of Figure D2). Due to the strong near-IR emission,

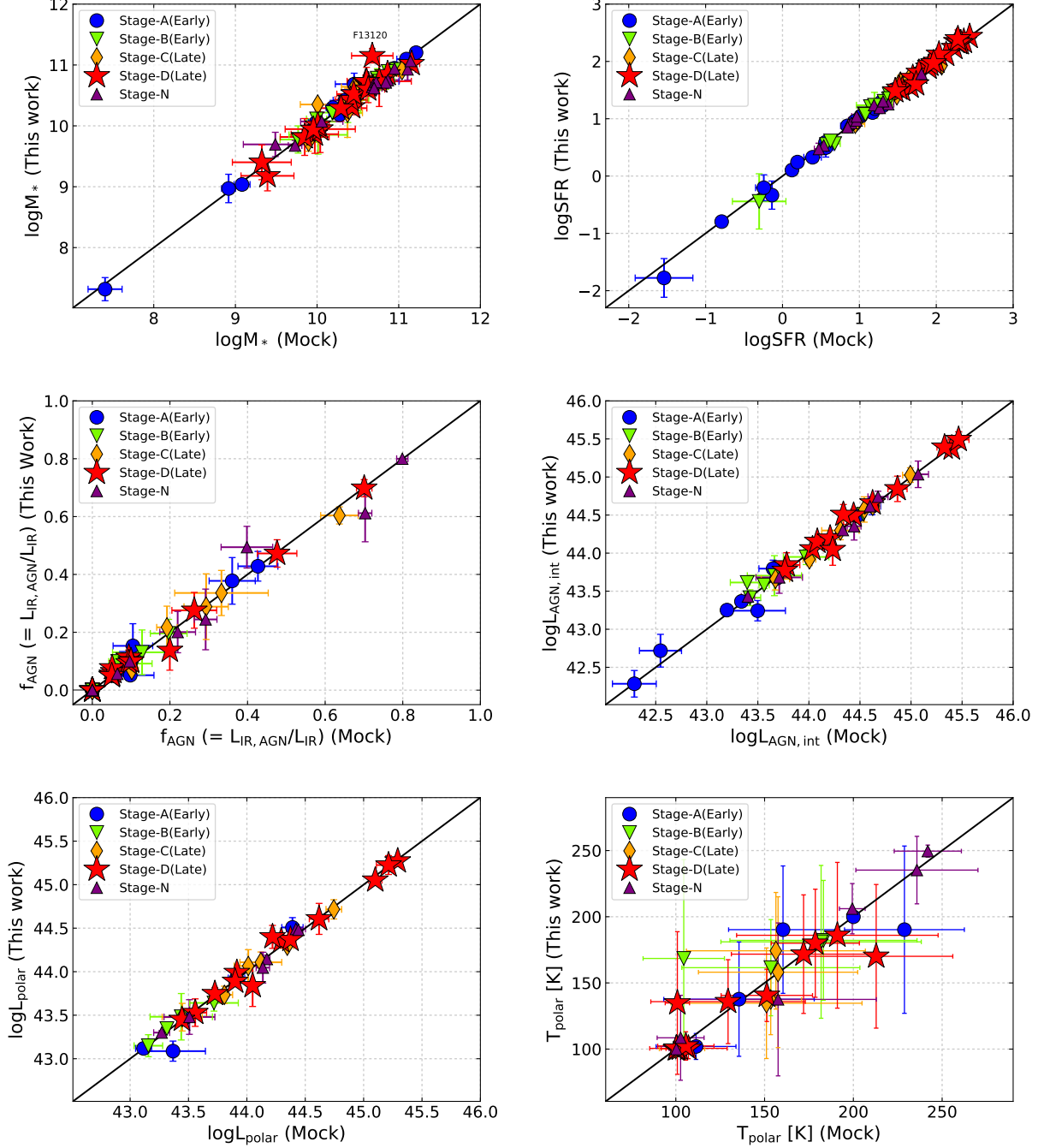


Figure B1. Comparison of the best-fit parameters and those derived from the mock analysis for the M_* (top left), SFR (top right), AGN fraction (middle left), intrinsic AGN luminosity (middle right), polar dust luminosity (bottom left), and polar dust temperature (bottom right). The symbols are the same in Figure 8.

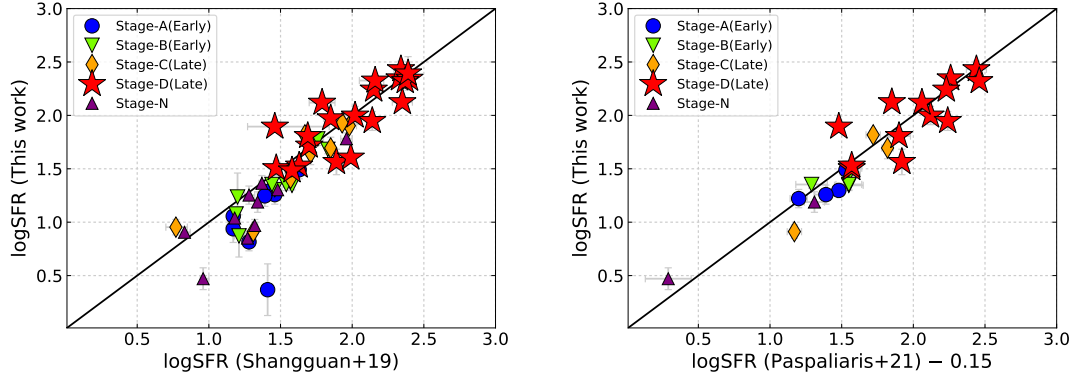


Figure C1. Left panel: comparison of SFRs estimated in Shangguan et al. (2019) and this work. Right panel: comparison of SFRs estimated in Paspaliaris et al. (2021) and this work. The former values are converted from Salpeter (1955) IMF to Chabrier (2003) IMF with 0.15 dex. The symbols are the same in Figure 8.

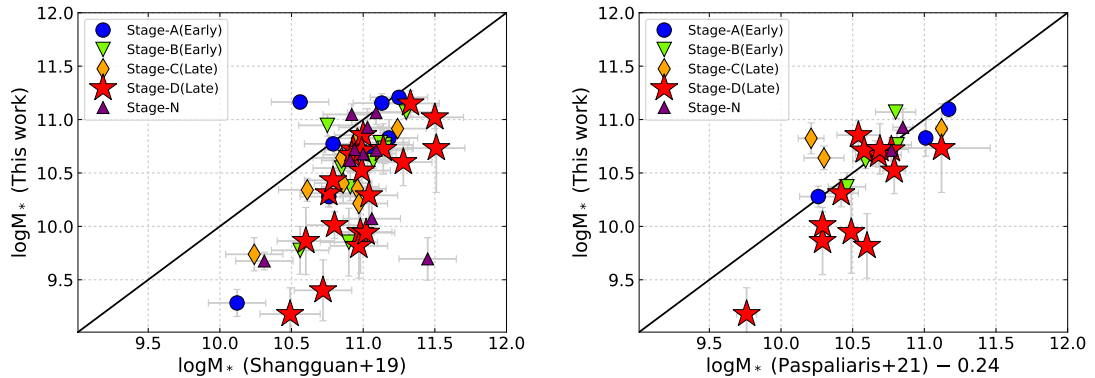


Figure C2. Left panel: comparison of M_* estimated in Shangguan et al. (2019) and this work. Right panel: comparison of M_* estimated in Paspaliaris et al. (2021) and this work. The former values are converted from Salpeter (1955) IMF to Chabrier (2003) IMF with 0.24 dex. The symbols are the same in Figure 8.

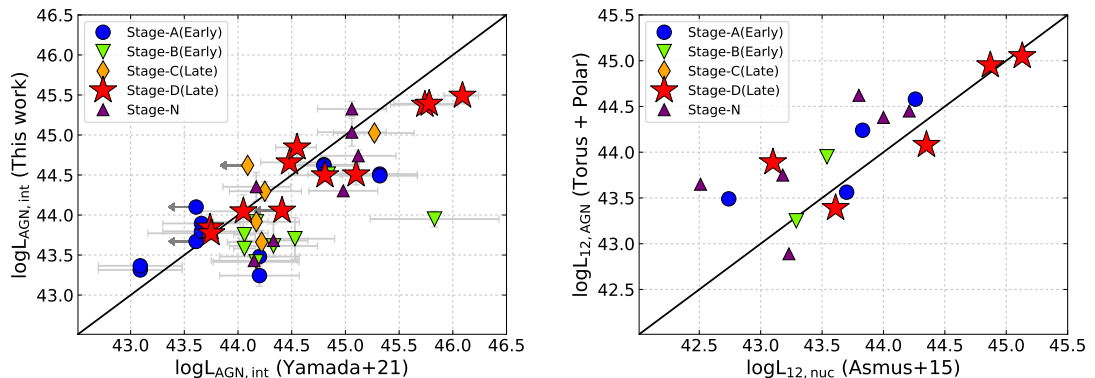


Figure C3. Left panel: comparison of $L_{\text{AGN},\text{int}}$ estimated in Yamada et al. (2021) and this work. Right panel: comparison with the AGN (torus and polar-dust components) 12 μm luminosity from UV-to-IR SED analysis ($L_{12\mu\text{m},\text{AGN}}$) and the nuclear 12 μm luminosity ($L_{12\mu\text{m},\text{nuc}}$; Asmus et al. 2015).

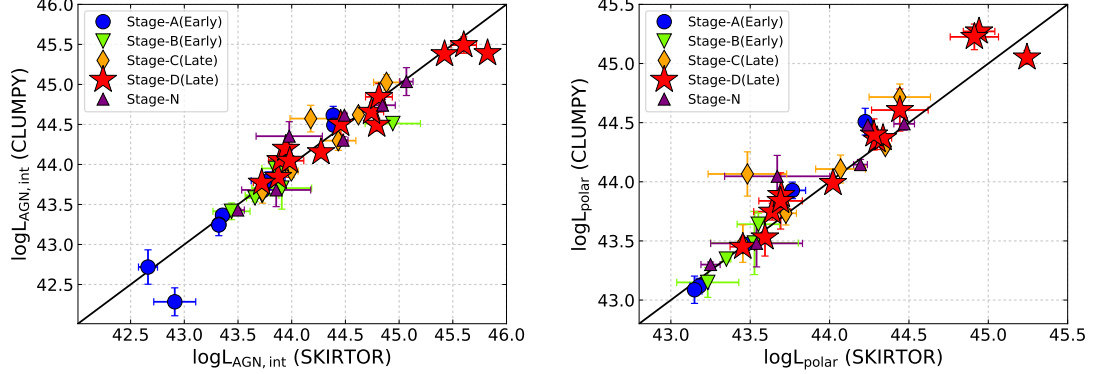


Figure D1. Left panel: comparison of intrinsic (bolometric) AGN luminosities derived with the CLUMPY model and SKIRTOR model. Right panel: comparison of polar-dust luminosities derived with CLUMPY model and SKIRTOR model. The symbols are the same in Figure 8.

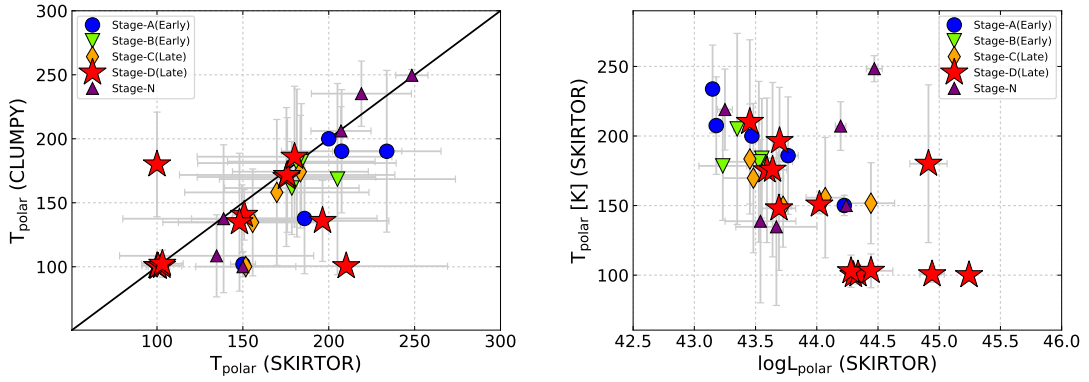


Figure D2. Left panel: comparison of polar dust temperatures derived with the CLUMPY model and SKIRTOR model. Right panel: logarithmic polar-dust luminosity vs. polar-dust temperature when SKIRTOR model is adopted. The symbols are the same in Figure 8.

the SEDs of the torus with SKIRTOR are flatter than with CLUMPY. In this case, a large part of the mid-IR emission will be modeled by the polar dust emission. This causes a larger fraction of the AGNs to show the signs of polar dust emission with SKIRTOR than with CLUMPY (Section 4.2.4). Hence, the polar temperature from the SKIRTOR model is larger than those from the CLUMPY model. In the right panel of Figure D2, we find that the results with SKIRTOR, that is, the trends of the large polar dust luminosities and low temperatures in late mergers, are consistent with the results with CLUMPY. We note that the estimates of the polar dust features by fixing the torus parameters with SKIRTOR are not self-consistent since the geometry of the XCLUMPY and SKIRTOR is different. Thus, it is preferred to adopt the results with CLUMPY particularly when we discuss the polar dust structure.

E. MULTIWAVELENGTH SED DECOMPOSITION

For convenience on the multiwavelength studies in our sample, we present the hard-X-ray-to-radio SEDs and the best fitting models at the observed frame in units of flux density in Figures E1. We also illustrate the SEDs and the best fitting models at the rest frame in units of luminosity in Figures E2–E10. The photometry data are summarized in Table E1–E3.

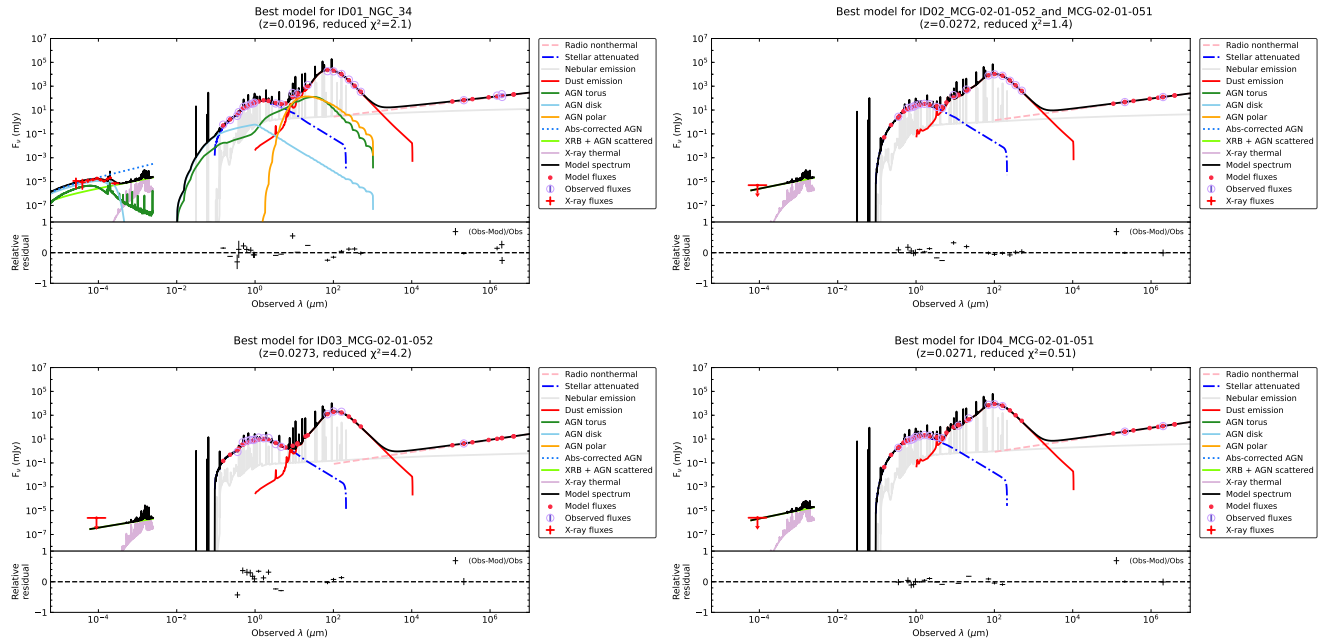


Figure E1. The hard-X-ray-to-radio SEDs and the best fitting models in units of flux density for our sample. The bottom panels show the residuals in the UV-to-radio bands. The individual curves are the same as in Figure 1. Purple and red circles represent the observed and model flux densities, respectively. Red crosses in the X-ray band denote the NuSTAR spectra (or, Swift/BAT for NGC 235 and XMM-Newton/MOS for IC 5283 and MCG+01-59-081). The red arrow and green triangles mark the 5σ upper limit.

(The complete figure set of 85 images is available.)

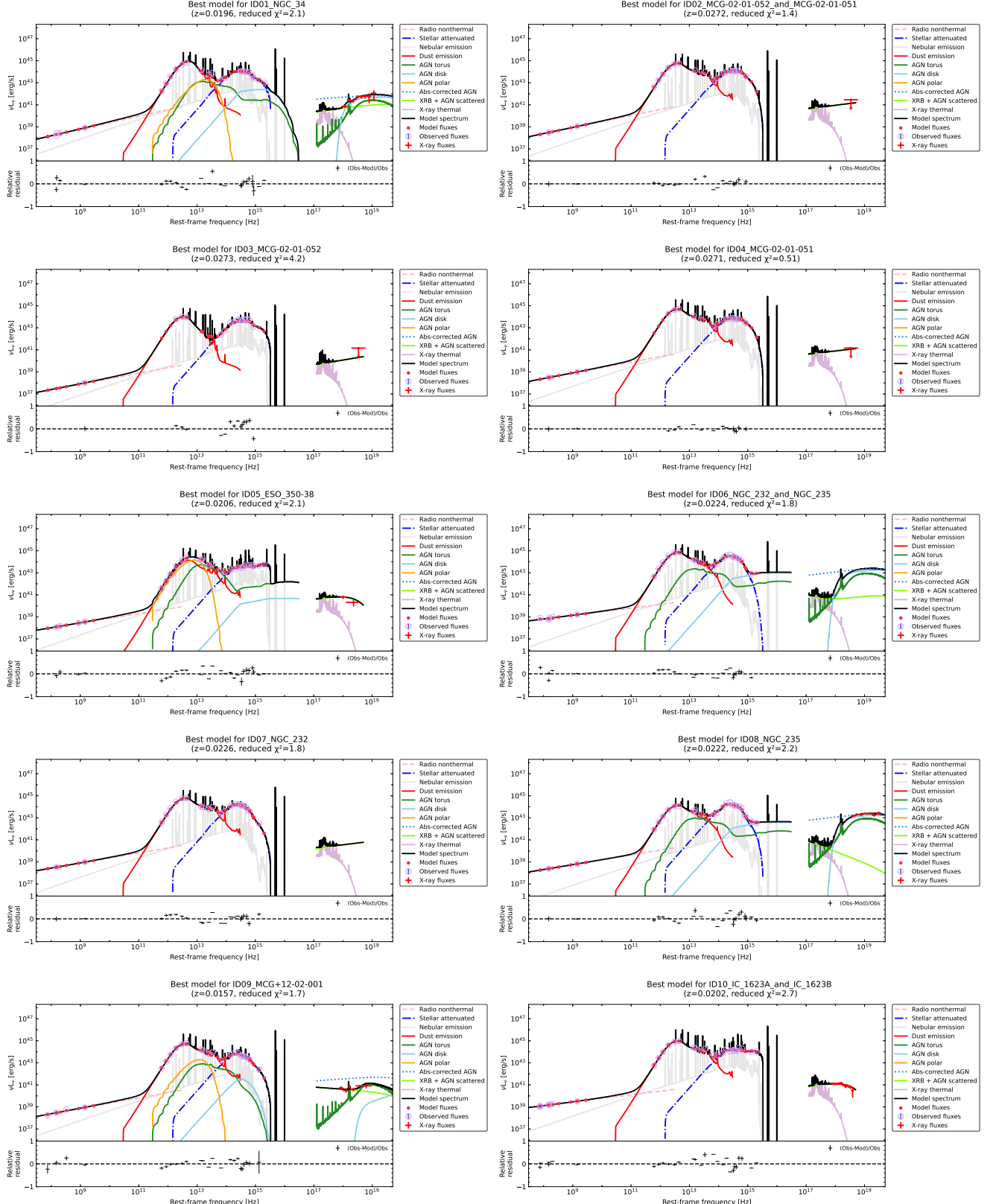


Figure E2. The hard-X-ray-to-radio SEDs and the best fitting models in units of luminosity for the sample of ID=1–10. The bottom panels show the residuals in the UV-to-radio bands. The individual curves are the same as in Figure 1. Purple and red circles represent the observed and model flux densities, respectively. Red crosses in the X-ray band denote the NuSTAR spectra (or, Swift/BAT for NGC 235 and XMM-Newton/MOS for IC 5283 and MCG+01-59-081). The red arrow and green triangles mark the 5σ upper limit.

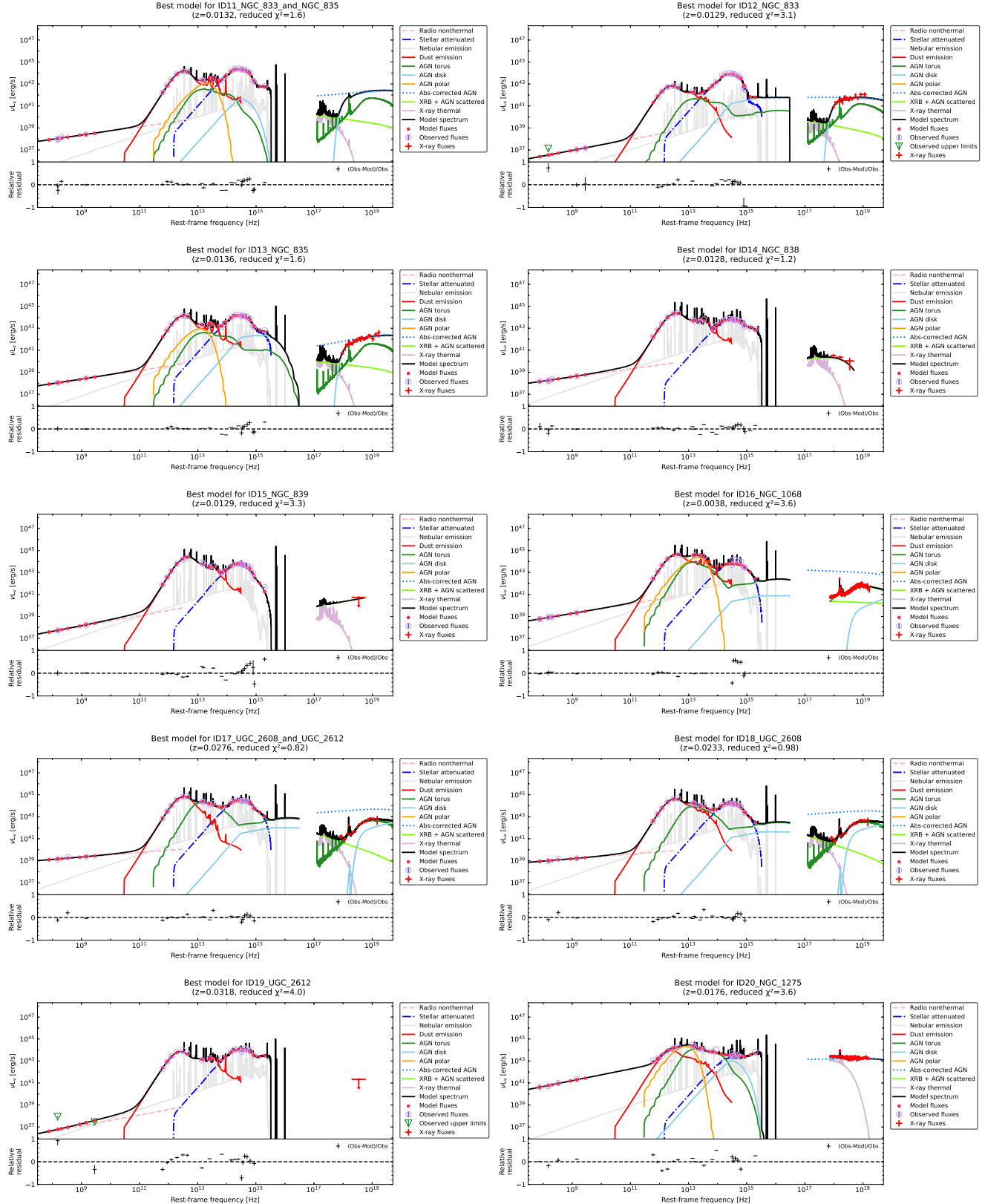


Figure E3. The same as in Figure E2 but for the sample of ID=11–20.

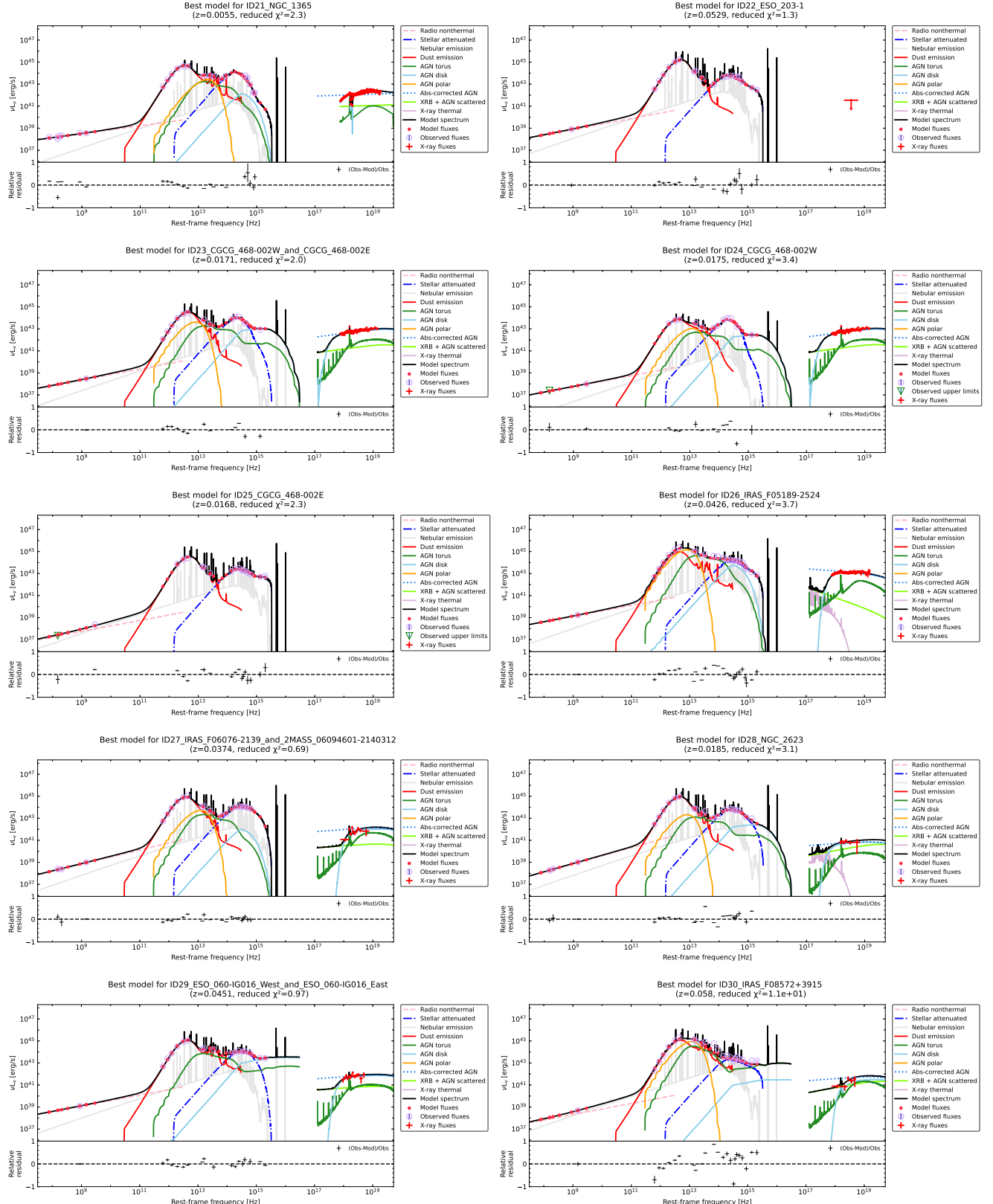


Figure E4. The same as in Figure E2 but for the sample of ID=21–30.

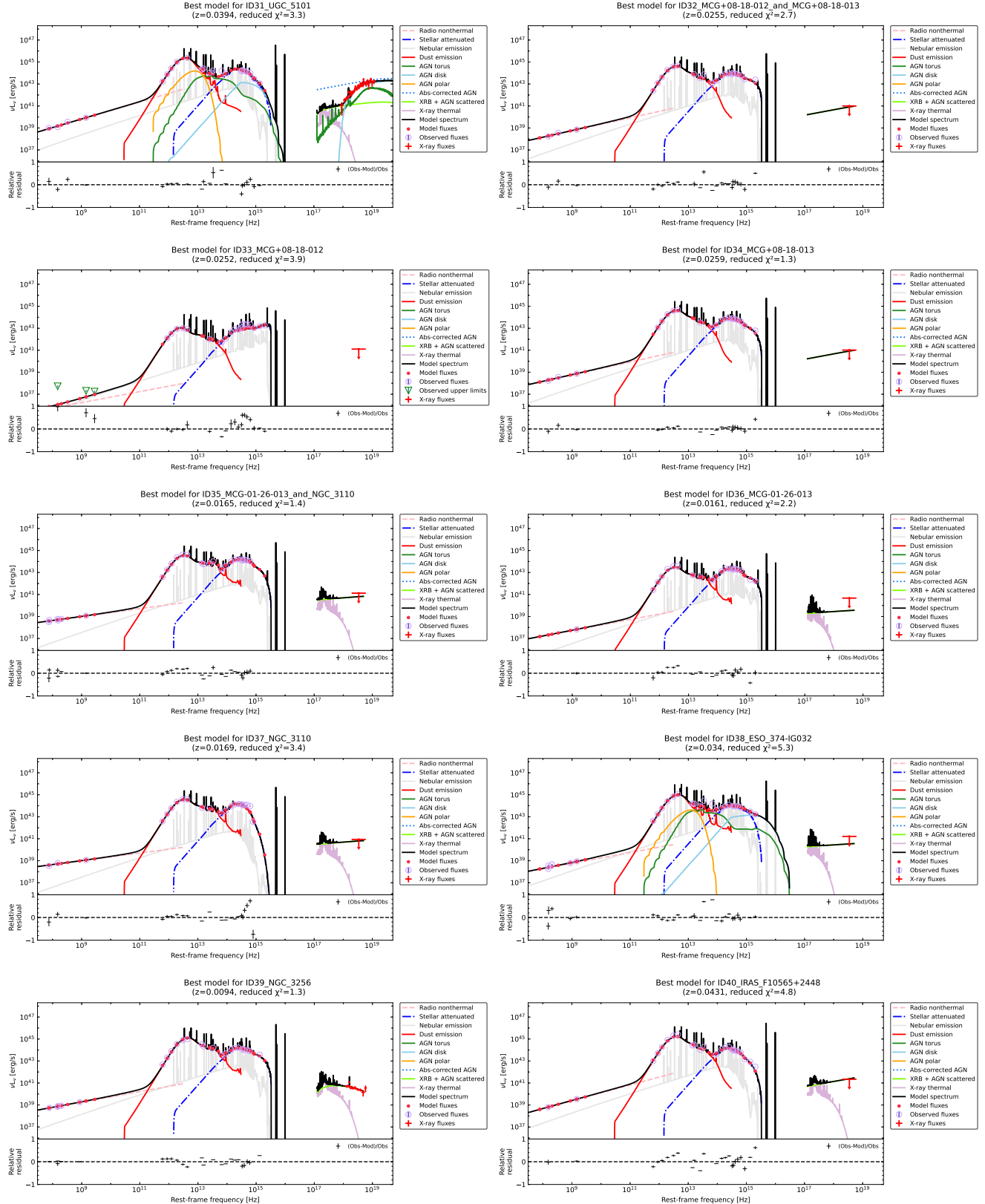


Figure E5. The same as in Figure E2 but for the sample of ID=31–40.

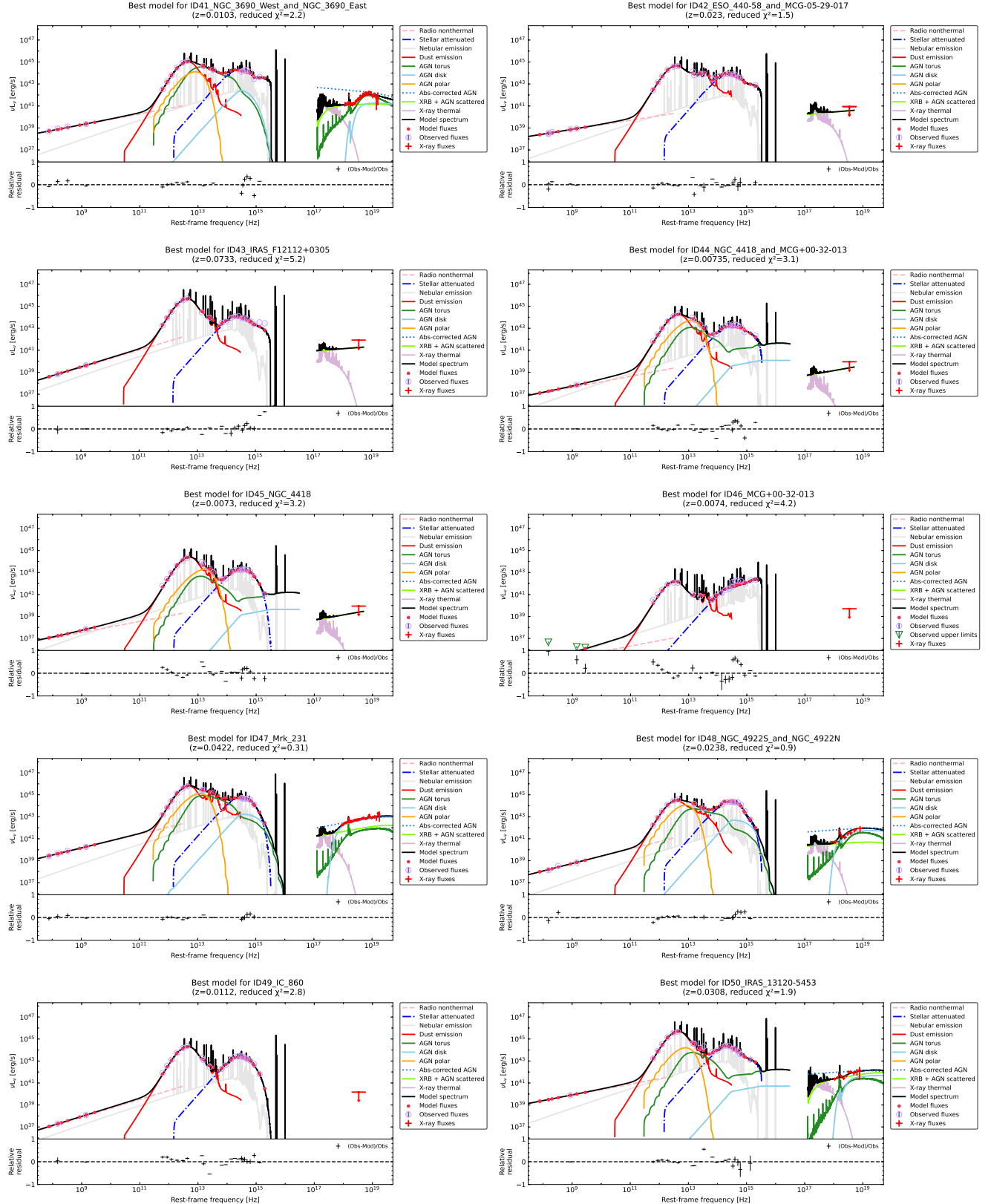


Figure E6. The same as in Figure E2 but for the sample of ID=41–50.

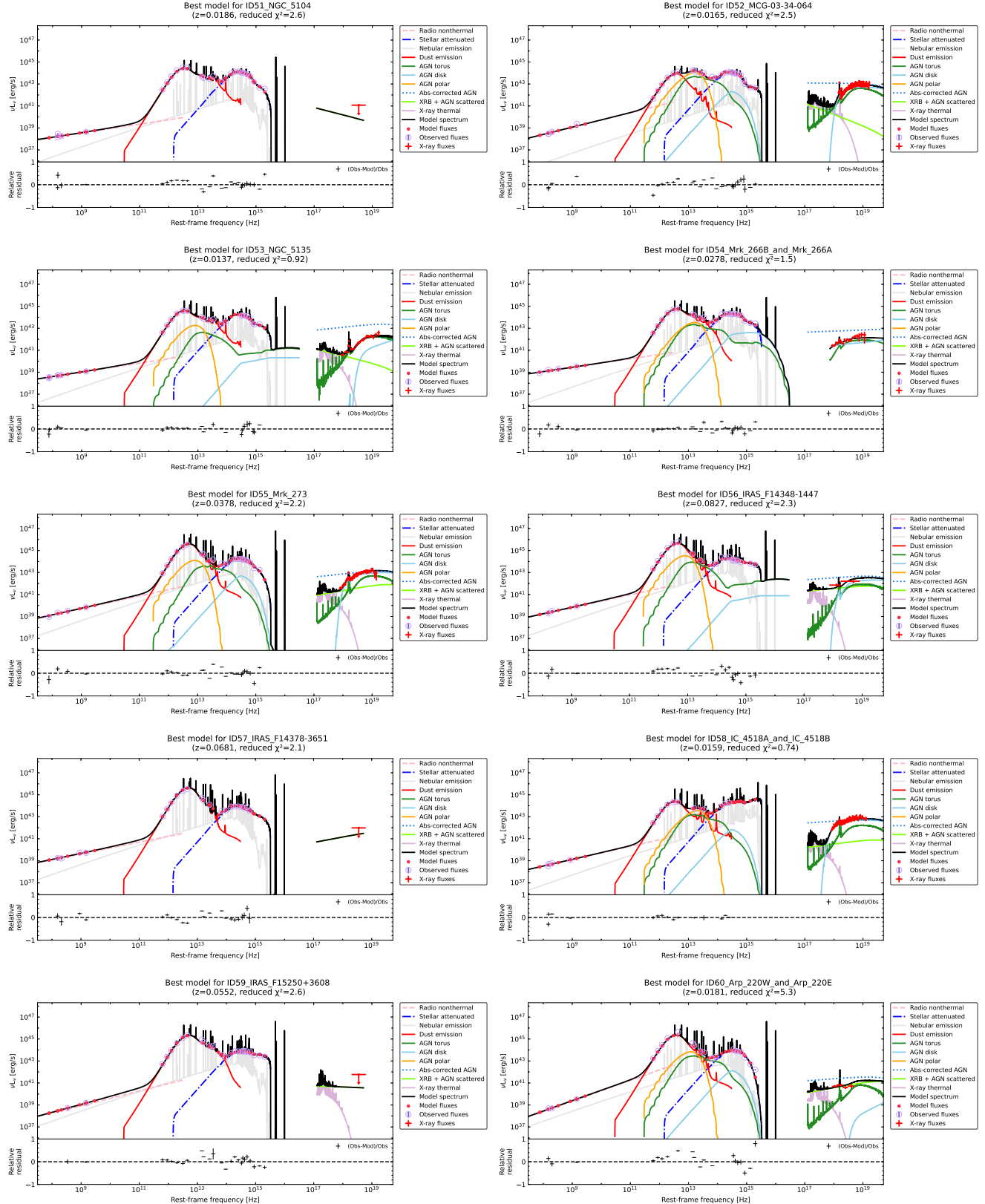


Figure E7. The same as in Figure E2 but for the sample of ID=51–60.

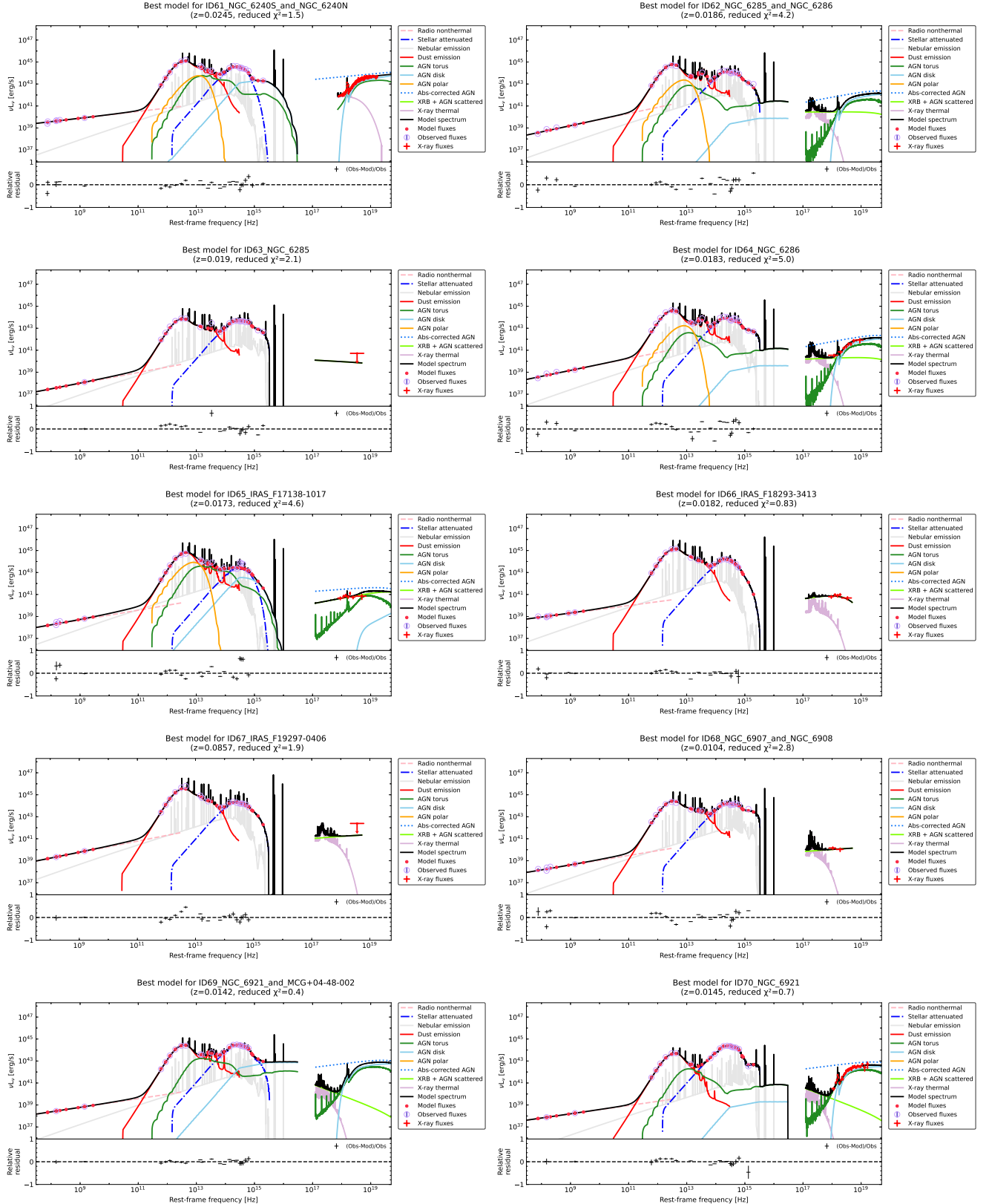


Figure E8. The same as in Figure E2 but for the sample of ID=61–70.

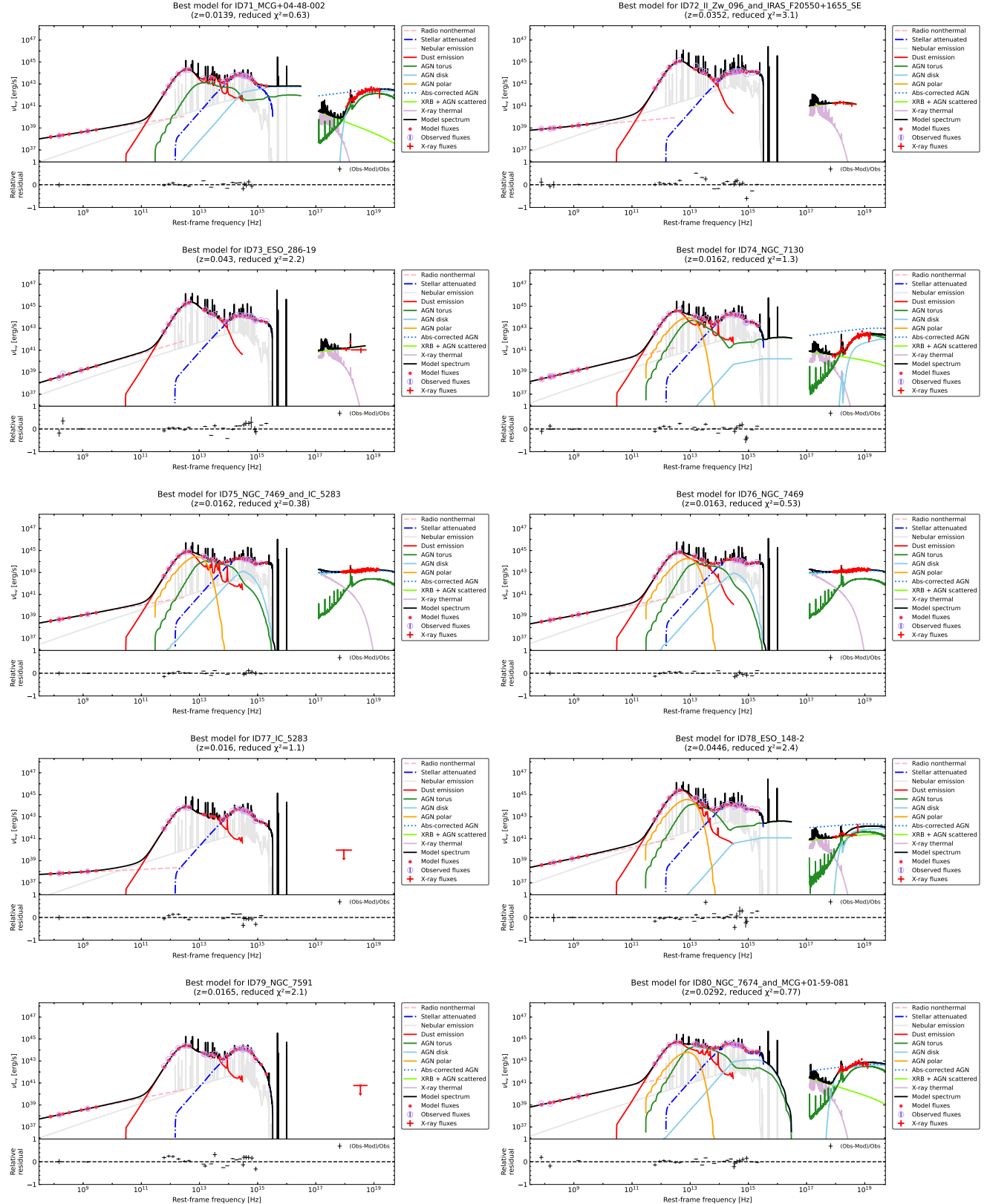


Figure E9. The same as in Figure E2 but for the sample of ID=71–80.

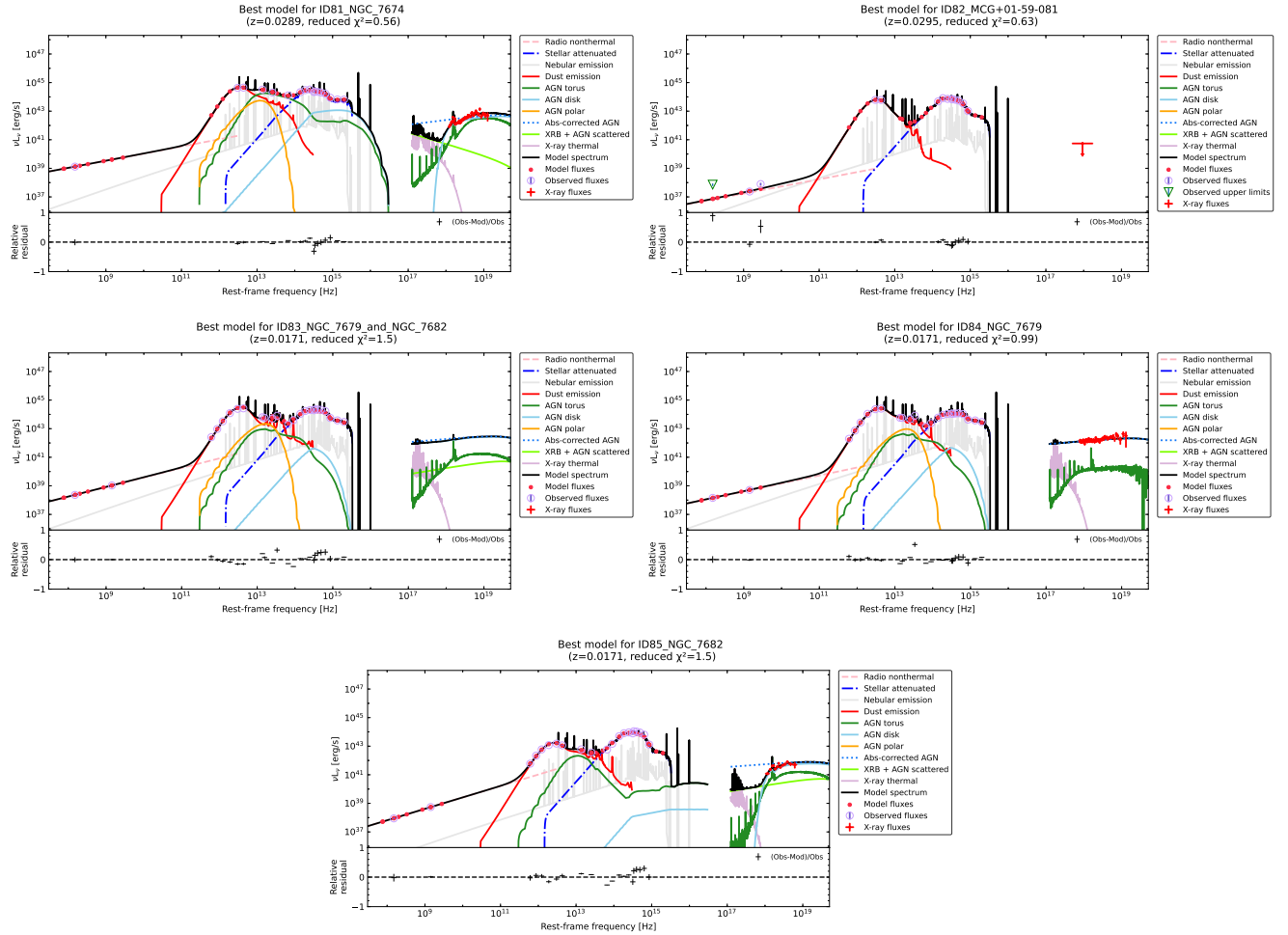


Figure E10. The same as in Figure E2 but for the sample of ID=81–85.

Table E1. Photometries of our targets in mJy ($\lambda < 1 \mu\text{m}$)

ID	Name	$E(B - V)$	FUV	NUV	u	v	F_{-uv}	g	r	i	F_{-griz}	y
(1)	(2)		152.8 nm	231.0 nm	350.0 nm	387.9 nm	SM	481.1 nm	615.6 nm	750.4 nm	866.9 nm	P
					354.3 nm		SD	501.6 nm	607.7 nm	773.3 nm	912.0 nm	SM
					(6)	(7)	(8)	(9)	(10)	(11)	(12)	(13)
												(14)
ID01	NGC 34	0.0268	0.598	1.463	3.26	6.72	SM	18.22	23.15	32.05	36.59	SM
ID02	MCG-02-01-052 /	0.0361	0.017	0.016	0.77	1.89		1.86	2.33	3.27	3.70	4.18
	MCG-02-01-051		2.72	...	SD	...	15.05	17.16	19.26	P
ID03	MCG-02-01-052	0.0361	0.27	1.54	1.74	1.93	24.05
		0.84	...	SD	5.44	7.15	8.41	8.37	P
		0.09	...		0.55	0.78	0.85	0.85	8.95
												0.92

Note— Columns: (1) target ID; (2) target name; (3) Galactic extinction estimated by Schlegel et al. (1998); (4–5) FUV and NUV flux densities from the GALEX database (GRplus7; Bianchi et al. 2017); (6–8) u -band and v -band flux densities, and the facility of these values, respectively. The adopted data of Pan-STARRS DR2 (f; e.g., Chambers et al. 2016), SkyMapper DR1 and DR2 (SK; e.g., Wolf et al. 2018), and SDSS DR16 (SD; Ahumada et al. 2020) are listed in Column (8); (9–13) g -band, r -band, i -band, z -band, $g-y$ bands and the facility of these values, respectively; (14) y -band flux density from Pan-STARRS. The Pan-STARRS photometries of $g-y$ bands are converted from the original Kron magnitudes by multiplying 100/90 (for 10% missing fluxes or 0.115 mag). The SkyMapper photometries of $u-z$ bands are converted from the original Petrosian magnitudes by multiplying 1.127 (e.g., 0.13 mag in case of typical Sersic index of 3; Graham et al. 2005; Haan et al. 2011). The flux densities are in units of mJy, and corrected for the Galactic extinction of Column (3), by applying the band passes as noted in the text. Their 1σ uncertainties are provided in the row just below. The uncertainties of $u-y$ bands are corrected by adding 10% of their flux densities to consider the dispersions among different kinds of measurements in their facilities.

(This table is available in its entirety in machine-readable form.)

Table E2. Photometries of our targets in mJy ($\lambda = 1\text{--}200 \mu\text{m}$)

ID	Name	<i>J</i>	<i>H</i>	K_s	W1	W2	S9W	W3	L18W	W4	PACS blue	PACS green	PACS red
(1)	(2)	1.235 μm	1.662 μm	2.159 μm	3.353 μm	4.603 μm	8.228 μm	11.56 μm	17.61 μm	22.09 μm	70 μm	100 μm	160 μm
ID01	NGC 34	35.67	30.43	269	245.26	...	1240.58	18210	17680	10650
		0.20	0.17	26	1.36	...	6.86	840	810	480
ID02	MCG-02-01-052/	30.59	33.25	31.82	18.32	14.43	178	...	517	...	8038	9876	7496
MCG-02-01-051	0.78	1.20	1.34	0.11	0.09	11	...	33	...	403	495	375	
ID03	MCG-02-01-052	13.53	11.78	12.44	3.82	2.27	1206	2081	1960	
		0.65	0.96	1.05	0.08	0.05	62	105	99	

NOTE—Columns: (1) target ID; (2) target name; (3–5) *J*-band, *H*-band, and K_s -band flux densities from the 2MASS extended catalog, except for IRAS F17138-1017 from point-source catalog (e.g., Skrutskie et al. 2006); (6–7), (9), and (11) W1, W2, W3, and W4 flux densities from ALLWISE catalog (updated version on February 16, 2021; Cutri et al. 2021) respectively; (8) and (10) S9W and L18W flux densities from AKARI/IRC mid-IR all-sky survey (Ishihara et al. 2010); (12–14) flux densities in PACS blue, green, and red bands from Herschel/PACS data (Chu et al. 2017); The flux densities are in units of mJy. The Galactic extinction in *J*, *H*, K_s , W1, and W2 bands are corrected by applying the band passes as noted in the text. Their 1σ uncertainties are provided in the row just below.
(This table is available in its entirety in machine-readable form.)

Table E3. Photometries of our targets in mJy ($\lambda > 200 \mu\text{m}$)

ID	Name	PSW 250 μm	PMW 350 μm	PLW 500 μm	NVSS 214.1 mm	SUMSS 355.6 mm	WENSS 922.1 mm	GLEAM1 325.125 MHz	GLEAM2 200.5 MHz	TGSS 150.5 MHz	GLEAM3 147.5 MHz	VLSSr 76 MHz	VLASS 73.8 MHz	VCLASS 3 GHz	FIRST 1.4 GHz
(1)	(2)	(3)	(4)	(5)	(6)	(7)	(8)	(9)	(10)	(11)	(12)	(13)	(14)	(15)	
ID01	NGC 34	3573	1239	339	66.9	162.1	212.3	125.5	[41.3]	...
ID02	MCG-02-01-052 / MCG-02-01-051	214 2862	75 1209	21 419	2.5 46.7	10.6	26.5	14.3	[1.5]	...
ID03	MCG-02-01-052	...	81	33	1.8	123.2	[32.7]	[33.6]
		4.3	13.6	[0.4]	[3.4]
		0.5	[<0.44]	[<1.0]
															...

NOTE— Columns: (1) target ID; (2) target name; (3–5) flux densities in PSW, PMW, and PLW bands from Herschel/SPIRE data (Chu et al. 2017); (6) 1.4 GHz flux densities from NVSS catalog (Condon et al. 1998); (7) 8.43 MHz flux densities from SUMSS catalog (Mauch et al. 2003); (8) 325.125 MHz flux densities from WENSS catalog (Rengelink et al. 1997); (9–10) and (12) 200.5 MHz (170–231 MHz), 150.5 MHz (147–154 MHz), and 76 MHz (72–80 MHz) flux densities from GLEAM catalog (Hurley-Walker et al. 2017). The values of $<5\sigma$ of GLEAM catalog are removed; (11) 147.5 MHz flux densities from TGSS catalog (Intema et al. 2017); (13) 73.8 MHz flux densities from VLSSr (Lane et al. 2014); (14) 3 GHz flux densities with the high angular resolution (2. $^{\prime\prime}$) from VLASS catalog (Gordon et al. 2021); (15) 1.4 GHz flux densities with the high angular resolution (5. $''$) from FIRST catalog (Becker et al. 1995; Helfand et al. 2015). Since the uncertainties of FIRST flux densities were not provided, we assume them as 10% uncertainties. The values in the square brackets for VLASS and FIRST data represent the flux densities and uncertainties that are not utilized in the radio fits (see Section 3.7 in details); The flux densities are in units of mJy. Their 1 σ uncertainties are provided in the row just below.

(This table is available in its entirety in machine-readable form.)

REFERENCES

- Ahumada, R., Prieto, C. A., Almeida, A., et al. 2020, ApJS, 249, 3, doi: [10.3847/1538-4365/ab929e](https://doi.org/10.3847/1538-4365/ab929e)
- Aird, J., Coil, A. L., Georgakakis, A., et al. 2015, MNRAS, 451, 1892, doi: [10.1093/mnras/stv1062](https://doi.org/10.1093/mnras/stv1062)
- AKARI Team. 2020, AKARI/IRC Point Source Catalogue, IPAC, doi: [10.26131/IRSA181](https://doi.org/10.26131/IRSA181)
- Albareti, F. D., Allende Prieto, C., Almeida, A., et al. 2017, ApJS, 233, 25, doi: [10.3847/1538-4365/aa8992](https://doi.org/10.3847/1538-4365/aa8992)
- Alexander, D. M., & Hickox, R. C. 2012, NewAR, 56, 93, doi: [10.1016/j.newar.2011.11.003](https://doi.org/10.1016/j.newar.2011.11.003)
- Allison, J. R., Sadler, E. M., & Meekin, A. M. 2014, MNRAS, 440, 696, doi: [10.1093/mnras/stu289](https://doi.org/10.1093/mnras/stu289)
- Alonso-Herrero, A., Pereira-Santaella, M., Rieke, G. H., & Rigopoulou, D. 2012, ApJ, 744, 2, doi: [10.1088/0004-637X/744/1/2](https://doi.org/10.1088/0004-637X/744/1/2)
- Alonso-Herrero, A., García-Burillo, S., Höning, S. F., et al. 2021, A&A, 652, A99, doi: [10.1051/0004-6361/202141219](https://doi.org/10.1051/0004-6361/202141219)
- Ananna, T. T., Urry, C. M., Ricci, C., et al. 2022, ApJL, 939, L13, doi: [10.3847/2041-8213/ac9979](https://doi.org/10.3847/2041-8213/ac9979)
- Andonie, C., Ricci, C., Paltani, S., et al. 2022, MNRAS, 511, 5768, doi: [10.1093/mnras/stac403](https://doi.org/10.1093/mnras/stac403)
- Anglés-Alcázar, D., Faucher-Giguère, C.-A., Quataert, E., et al. 2017, MNRAS, 472, L109, doi: [10.1093/mnrasl/slx161](https://doi.org/10.1093/mnrasl/slx161)
- Armus, L., Mazzarella, J. M., Evans, A. S., et al. 2009, PASP, 121, 559, doi: [10.1086/600092](https://doi.org/10.1086/600092)
- Arnaud, K. A. 1996, Astronomical Society of the Pacific Conference Series, Vol. 101, XSPEC: The First Ten Years, ed. G. H. Jacoby & J. Barnes, 17
- Asano, R. S., Takeuchi, T. T., Hirashita, H., & Nozawa, T. 2013, MNRAS, 432, 637, doi: [10.1093/mnras/stt506](https://doi.org/10.1093/mnras/stt506)
- Asmus, D. 2019, MNRAS, 489, 2177, doi: [10.1093/mnras/stz2289](https://doi.org/10.1093/mnras/stz2289)
- Asmus, D., Gandhi, P., Höning, S. F., Smette, A., & Duschl, W. J. 2015, MNRAS, 454, 766, doi: [10.1093/mnras/stv1950](https://doi.org/10.1093/mnras/stv1950)
- Asmus, D., Höning, S. F., & Gandhi, P. 2016, ApJ, 822, 109, doi: [10.3847/0004-637X/822/2/109](https://doi.org/10.3847/0004-637X/822/2/109)
- Asmus, D., Höning, S. F., Gandhi, P., Smette, A., & Duschl, W. J. 2014, MNRAS, 439, 1648, doi: [10.1093/mnras/stu041](https://doi.org/10.1093/mnras/stu041)
- Assef, R. J., Stern, D., Noiro, G., et al. 2018, ApJS, 234, 23, doi: [10.3847/1538-4365/aaa00a](https://doi.org/10.3847/1538-4365/aaa00a)
- Assef, R. J., Kochanek, C. S., Brodwin, M., et al. 2010, ApJ, 713, 970, doi: [10.1088/0004-637X/713/2/970](https://doi.org/10.1088/0004-637X/713/2/970)
- Assef, R. J., Stern, D., Kochanek, C. S., et al. 2013, ApJ, 772, 26, doi: [10.1088/0004-637X/772/1/26](https://doi.org/10.1088/0004-637X/772/1/26)
- Assef, R. J., Walton, D. J., Brightman, M., et al. 2016, ApJ, 819, 111, doi: [10.3847/0004-637X/819/2/111](https://doi.org/10.3847/0004-637X/819/2/111)
- Assef, R. J., Brightman, M., Walton, D. J., et al. 2020, ApJ, 897, 112, doi: [10.3847/1538-4357/ab9814](https://doi.org/10.3847/1538-4357/ab9814)
- Baba, S., Nakagawa, T., Isobe, N., & Shirahata, M. 2018, ApJ, 852, 83, doi: [10.3847/1538-4357/aa9f25](https://doi.org/10.3847/1538-4357/aa9f25)
- Barrera-Ballesteros, J. K., Sánchez, S. F., García-Lorenzo, B., et al. 2015, A&A, 579, A45, doi: [10.1051/0004-6361/201425397](https://doi.org/10.1051/0004-6361/201425397)
- Barvainis, R. 1987, ApJ, 320, 537, doi: [10.1086/165571](https://doi.org/10.1086/165571)
- Bauer, F. E., Arévalo, P., Walton, D. J., et al. 2015, ApJ, 812, 116, doi: [10.1088/0004-637X/812/2/116](https://doi.org/10.1088/0004-637X/812/2/116)
- Becker, R. H., White, R. L., & Helfand, D. J. 1995, ApJ, 450, 559, doi: [10.1086/176166](https://doi.org/10.1086/176166)
- Begelman, M. C., Blandford, R. D., & Rees, M. J. 1984, Reviews of Modern Physics, 56, 255, doi: [10.1103/RevModPhys.56.255](https://doi.org/10.1103/RevModPhys.56.255)
- Behar, E. 2009, ApJ, 703, 1346, doi: [10.1088/0004-637X/703/2/1346](https://doi.org/10.1088/0004-637X/703/2/1346)
- Bell, E. F. 2003, ApJ, 586, 794, doi: [10.1086/367829](https://doi.org/10.1086/367829)
- Bianchi, L. 2020, GALEX UV Unique Source Catalogs ("GUVcat") and Cross-Matches With Gaia and SDSS ("GUVmatch"), STScI/MAST, doi: [10.17909/T9-PYXY-KG53](https://doi.org/10.17909/T9-PYXY-KG53)
- Bianchi, L., Herald, J., Efremova, B., et al. 2011, Ap&SS, 335, 161, doi: [10.1007/s10509-010-0581-x](https://doi.org/10.1007/s10509-010-0581-x)
- Bianchi, L., Shiao, B., & Thilker, D. 2017, ApJS, 230, 24, doi: [10.3847/1538-4365/aa7053](https://doi.org/10.3847/1538-4365/aa7053)
- Bischetti, M., Piconcelli, E., Vietri, G., et al. 2017, A&A, 598, A122, doi: [10.1051/0004-6361/201629301](https://doi.org/10.1051/0004-6361/201629301)
- Blecha, L., Snyder, G. F., Satyapal, S., & Ellison, S. L. 2018, MNRAS, 478, 3056, doi: [10.1093/mnras/sty1274](https://doi.org/10.1093/mnras/sty1274)
- Boch, T., & Fernique, P. 2014, in Astronomical Society of the Pacific Conference Series, Vol. 485, Astronomical Data Analysis Software and Systems XXIII, ed. N. Manset & P. Forshay, 277
- Boettcher, E., Gallagher, John S., I., Ohyama, Y., et al. 2020, A&A, 637, A17, doi: [10.1051/0004-6361/201834880](https://doi.org/10.1051/0004-6361/201834880)
- Bongiorno, A., Merloni, A., Brusa, M., et al. 2012, MNRAS, 427, 3103, doi: [10.1111/j.1365-2966.2012.22089.x](https://doi.org/10.1111/j.1365-2966.2012.22089.x)
- Bonnarel, F., Fernique, P., Bienaymé, O., et al. 2000, A&AS, 143, 33, doi: [10.1051/aas:2000331](https://doi.org/10.1051/aas:2000331)
- Bonzini, M., Mainieri, V., Padovani, P., et al. 2015, MNRAS, 453, 1079, doi: [10.1093/mnras/stv1675](https://doi.org/10.1093/mnras/stv1675)
- Boquien, M., Burgarella, D., Roehlly, Y., et al. 2019, A&A, 622, A103, doi: [10.1051/0004-6361/201834156](https://doi.org/10.1051/0004-6361/201834156)
- Brinchmann, J., Charlot, S., White, S. D. M., et al. 2004, MNRAS, 351, 1151, doi: [10.1111/j.1365-2966.2004.07881.x](https://doi.org/10.1111/j.1365-2966.2004.07881.x)
- Bruzual, G., & Charlot, S. 2003, MNRAS, 344, 1000, doi: [10.1046/j.1365-8711.2003.06897.x](https://doi.org/10.1046/j.1365-8711.2003.06897.x)

- Buat, V., Boquien, M., Małek, K., et al. 2018, A&A, 619, A135, doi: [10.1051/0004-6361/201833841](https://doi.org/10.1051/0004-6361/201833841)
- Buat, V., Ciesla, L., Boquien, M., Małek, K., & Burgarella, D. 2019, A&A, 632, A79, doi: [10.1051/0004-6361/201936643](https://doi.org/10.1051/0004-6361/201936643)
- Buat, V., Noll, S., Burgarella, D., et al. 2012, A&A, 545, A141, doi: [10.1051/0004-6361/201219405](https://doi.org/10.1051/0004-6361/201219405)
- Buat, V., Heinis, S., Boquien, M., et al. 2014, A&A, 561, A39, doi: [10.1051/0004-6361/201322081](https://doi.org/10.1051/0004-6361/201322081)
- Buat, V., Mountrichas, G., Yang, G., et al. 2021, A&A, 654, A93, doi: [10.1051/0004-6361/202141797](https://doi.org/10.1051/0004-6361/202141797)
- Buchner, J., Brightman, M., Nandra, K., Nikutta, R., & Bauer, F. E. 2019, A&A, 629, A16, doi: [10.1051/0004-6361/201834771](https://doi.org/10.1051/0004-6361/201834771)
- Burgarella, D., Buat, V., Small, T., et al. 2005, ApJL, 619, L63, doi: [10.1086/423894](https://doi.org/10.1086/423894)
- Burrows, D. N., Hill, J. E., Nosek, J. A., et al. 2005, SSRv, 120, 165, doi: [10.1007/s11214-005-5097-2](https://doi.org/10.1007/s11214-005-5097-2)
- Burtscher, L., Davies, R. I., Graciá-Carpio, J., et al. 2016, A&A, 586, A28, doi: [10.1051/0004-6361/201527575](https://doi.org/10.1051/0004-6361/201527575)
- Calzetti, D. 2001, PASP, 113, 1449, doi: [10.1086/324269](https://doi.org/10.1086/324269)
- Calzetti, D., Armus, L., Bohlin, R. C., et al. 2000, ApJ, 533, 682, doi: [10.1086/308692](https://doi.org/10.1086/308692)
- Cameron, E. 2011, PASA, 28, 128, doi: [10.1071/AS10046](https://doi.org/10.1071/AS10046)
- Caramete, L. I., & Biermann, P. L. 2010, A&A, 521, A55, doi: [10.1051/0004-6361/200913146](https://doi.org/10.1051/0004-6361/200913146)
- Cardelli, J. A., Clayton, G. C., & Mathis, J. S. 1989, ApJ, 345, 245, doi: [10.1086/167900](https://doi.org/10.1086/167900)
- Casey, C. M. 2012, MNRAS, 425, 3094, doi: [10.1111/j.1365-2966.2012.21455.x](https://doi.org/10.1111/j.1365-2966.2012.21455.x)
- Chabrier, G. 2003, PASP, 115, 763, doi: [10.1086/376392](https://doi.org/10.1086/376392)
- Chambers, K. C., Magnier, E. A., Metcalfe, N., et al. 2016, arXiv e-prints, arXiv:1612.05560. <https://arxiv.org/abs/1612.05560>
- Chan, C.-H., & Krolik, J. H. 2016, ApJ, 825, 67, doi: [10.3847/0004-637X/825/1/67](https://doi.org/10.3847/0004-637X/825/1/67)
- . 2017, ApJ, 843, 58, doi: [10.3847/1538-4357/aa76e4](https://doi.org/10.3847/1538-4357/aa76e4)
- Chen, C.-T. J., Hickox, R. C., Goulding, A. D., et al. 2017, ApJ, 837, 145, doi: [10.3847/1538-4357/837/2/145](https://doi.org/10.3847/1538-4357/837/2/145)
- Chen, X., Akiyama, M., Ichikawa, K., et al. 2020, ApJ, 900, 51, doi: [10.3847/1538-4357/aba599](https://doi.org/10.3847/1538-4357/aba599)
- Chiataluce, E., Vagnetti, F., Tombesi, F., & Paolillo, M. 2018, A&A, 619, A95, doi: [10.1051/0004-6361/201833631](https://doi.org/10.1051/0004-6361/201833631)
- Chu, J. K., Sanders, D. B., Larson, K. L., et al. 2017, ApJS, 229, 25, doi: [10.3847/1538-4365/aa5d15](https://doi.org/10.3847/1538-4365/aa5d15)
- Cicone, C., Maiolino, R., Sturm, E., et al. 2014, A&A, 562, A21, doi: [10.1051/0004-6361/201322464](https://doi.org/10.1051/0004-6361/201322464)
- Ciesla, L., Elbaz, D., Schreiber, C., Daddi, E., & Wang, T. 2018, A&A, 615, A61, doi: [10.1051/0004-6361/201832715](https://doi.org/10.1051/0004-6361/201832715)
- Ciesla, L., Charmandaris, V., Georgakakis, A., et al. 2015, A&A, 576, A10, doi: [10.1051/0004-6361/201425252](https://doi.org/10.1051/0004-6361/201425252)
- Clemens, M. S., Vega, O., Bressan, A., et al. 2008, A&A, 477, 95, doi: [10.1051/0004-6361:20077224](https://doi.org/10.1051/0004-6361:20077224)
- Clements, D. L., Pearson, C., Farrah, D., et al. 2018, MNRAS, 475, 2097, doi: [10.1093/mnras/stx3227](https://doi.org/10.1093/mnras/stx3227)
- Cohen, A. S., Lane, W. M., Cotton, W. D., et al. 2007, AJ, 134, 1245, doi: [10.1086/520719](https://doi.org/10.1086/520719)
- Cohen, M., Wheaton, W. A., & Megeath, S. T. 2003, AJ, 126, 1090, doi: [10.1086/376474](https://doi.org/10.1086/376474)
- Condon, J. J. 1992, ARA&A, 30, 575, doi: [10.1146/annurev.aa.30.090192.003043](https://doi.org/10.1146/annurev.aa.30.090192.003043)
- Condon, J. J., Cotton, W. D., Greisen, E. W., et al. 1998, AJ, 115, 1693, doi: [10.1086/300337](https://doi.org/10.1086/300337)
- Condon, J. J., Huang, Z. P., Yin, Q. F., & Thuau, T. X. 1991, ApJ, 378, 65, doi: [10.1086/170407](https://doi.org/10.1086/170407)
- Cortijo-Ferrero, C., González Delgado, R. M., Pérez, E., et al. 2017, A&A, 606, A95, doi: [10.1051/0004-6361/201730669](https://doi.org/10.1051/0004-6361/201730669)
- Cutri, R. M., & et al. 2012, VizieR Online Data Catalog, II/311
- Cutri, R. M., Wright, E. L., Conrow, T., et al. 2021, VizieR Online Data Catalog, II/328
- da Cunha, E., Hodge, J. A., Casey, C. M., et al. 2021, ApJ, 919, 30, doi: [10.3847/1538-4357/ac0ae0](https://doi.org/10.3847/1538-4357/ac0ae0)
- Dale, D. A., Aniano, G., Engelbracht, C. W., et al. 2012, ApJ, 745, 95, doi: [10.1088/0004-637X/745/1/95](https://doi.org/10.1088/0004-637X/745/1/95)
- Del Moro, A., Alexander, D. M., Bauer, F. E., et al. 2016, MNRAS, 456, 2105, doi: [10.1093/mnras/stv2748](https://doi.org/10.1093/mnras/stv2748)
- Delvecchio, I., Smolčić, V., Zamorani, G., et al. 2017, A&A, 602, A3, doi: [10.1051/0004-6361/201629367](https://doi.org/10.1051/0004-6361/201629367)
- Di Matteo, T., Springel, V., & Hernquist, L. 2005, Nature, 433, 604, doi: [10.1038/nature03335](https://doi.org/10.1038/nature03335)
- Díaz-Santos, T., Charmandaris, V., Armus, L., et al. 2010, ApJ, 723, 993, doi: [10.1088/0004-637X/723/2/993](https://doi.org/10.1088/0004-637X/723/2/993)
- Díaz-Santos, T., Armus, L., Charmandaris, V., et al. 2013, ApJ, 774, 68, doi: [10.1088/0004-637X/774/1/68](https://doi.org/10.1088/0004-637X/774/1/68)
- . 2014, ApJL, 788, L17, doi: [10.1088/2041-8205/788/1/L17](https://doi.org/10.1088/2041-8205/788/1/L17)
- . 2017, ApJ, 846, 32, doi: [10.3847/1538-4357/aa81d7](https://doi.org/10.3847/1538-4357/aa81d7)
- Dong, R., Greene, J. E., & Ho, L. C. 2012, ApJ, 761, 73, doi: [10.1088/0004-637X/761/1/73](https://doi.org/10.1088/0004-637X/761/1/73)
- Dorodnitsyn, A., & Kallman, T. 2017, ApJ, 842, 43, doi: [10.3847/1538-4357/aa7264](https://doi.org/10.3847/1538-4357/aa7264)
- Dorodnitsyn, A., Kallman, T., & Bisnovatyi-Kogan, G. S. 2012, ApJ, 747, 8, doi: [10.1088/0004-637X/747/1/8](https://doi.org/10.1088/0004-637X/747/1/8)
- Draine, B. T. 2003, ARA&A, 41, 241, doi: [10.1146/annurev.astro.41.011802.094840](https://doi.org/10.1146/annurev.astro.41.011802.094840)
- Draine, B. T., & Lee, H. M. 1984, ApJ, 285, 89, doi: [10.1086/162480](https://doi.org/10.1086/162480)

- Draine, B. T., & Li, A. 2007, ApJ, 657, 810, doi: [10.1086/511055](https://doi.org/10.1086/511055)
- Draine, B. T., & Salpeter, E. E. 1979, ApJ, 231, 438, doi: [10.1086/157206](https://doi.org/10.1086/157206)
- Draine, B. T., Aniano, G., Krause, O., et al. 2014, ApJ, 780, 172, doi: [10.1088/0004-637X/780/2/172](https://doi.org/10.1088/0004-637X/780/2/172)
- Efstathiou, A., Farrah, D., Afonso, J., et al. 2022, MNRAS, 512, 5183, doi: [10.1093/mnras/stab3642](https://doi.org/10.1093/mnras/stab3642)
- Elbaz, D., Daddi, E., Le Borgne, D., et al. 2007, A&A, 468, 33, doi: [10.1051/0004-6361:20077525](https://doi.org/10.1051/0004-6361:20077525)
- Ellison, S. L., Mendel, J. T., Patton, D. R., & Scudder, J. M. 2013, MNRAS, 435, 3627, doi: [10.1093/mnras/stt1562](https://doi.org/10.1093/mnras/stt1562)
- Ellison, S. L., Secrest, N. J., Mendel, J. T., Satyapal, S., & Simard, L. 2017, MNRAS, 470, L49, doi: [10.1093/mnrasl/slx076](https://doi.org/10.1093/mnrasl/slx076)
- Enoki, M., Inoue, K. T., Nagashima, M., & Sugiyama, N. 2004, ApJ, 615, 19, doi: [10.1086/424475](https://doi.org/10.1086/424475)
- Fabian, A. C., Vasudevan, R. V., & Gandhi, P. 2008, MNRAS, 385, L43, doi: [10.1111/j.1745-3933.2008.00430.x](https://doi.org/10.1111/j.1745-3933.2008.00430.x)
- Fabian, A. C., Vasudevan, R. V., Mushotzky, R. F., Winter, L. M., & Reynolds, C. S. 2009, MNRAS, 394, L89, doi: [10.1111/j.1745-3933.2009.00617.x](https://doi.org/10.1111/j.1745-3933.2009.00617.x)
- Farrah, D., Efstathiou, A., Afonso, J., et al. 2022, MNRAS, 513, 4770, doi: [10.1093/mnras/stac980](https://doi.org/10.1093/mnras/stac980)
- Faucher-Giguère, C.-A., & Quataert, E. 2012, MNRAS, 425, 605, doi: [10.1111/j.1365-2966.2012.21512.x](https://doi.org/10.1111/j.1365-2966.2012.21512.x)
- Feruglio, C., Fiore, F., Carniani, S., et al. 2015, A&A, 583, A99, doi: [10.1051/0004-6361/201526020](https://doi.org/10.1051/0004-6361/201526020)
- Finnerty, L., Larson, K., Soifer, B. T., et al. 2020, ApJ, 905, 16, doi: [10.3847/1538-4357/abc3bf](https://doi.org/10.3847/1538-4357/abc3bf)
- Fischer, T. C., Crenshaw, D. M., Kraemer, S. B., & Schmitt, H. R. 2013, ApJS, 209, 1, doi: [10.1088/0067-0049/209/1/1](https://doi.org/10.1088/0067-0049/209/1/1)
- Flewelling, H. A., Magnier, E. A., Chambers, K. C., et al. 2020, ApJS, 251, 7, doi: [10.3847/1538-4365/abb82d](https://doi.org/10.3847/1538-4365/abb82d)
- Fluetsch, A., Maiolino, R., Carniani, S., et al. 2019, MNRAS, 483, 4586, doi: [10.1093/mnras/sty3449](https://doi.org/10.1093/mnras/sty3449)
- . 2021, MNRAS, 505, 5753, doi: [10.1093/mnras/stab1666](https://doi.org/10.1093/mnras/stab1666)
- Fritz, J., Franceschini, A., & Hatziminaoglou, E. 2006, MNRAS, 366, 767, doi: [10.1111/j.1365-2966.2006.09866.x](https://doi.org/10.1111/j.1365-2966.2006.09866.x)
- Fujimoto, S., Brammer, G. B., Watson, D., et al. 2022, Nature, 604, 261, doi: [10.1038/s41586-022-04454-1](https://doi.org/10.1038/s41586-022-04454-1)
- Furui, S., Fukazawa, Y., Odaka, H., et al. 2016, ApJ, 818, 164, doi: [10.3847/0004-637X/818/2/164](https://doi.org/10.3847/0004-637X/818/2/164)
- Gabriel, C., Denby, M., Fyfe, D. J., et al. 2004, Astronomical Society of the Pacific Conference Series, Vol. 314, The XMM-Newton SAS - Distributed Development and Maintenance of a Large Science Analysis System: A Critical Analysis, ed. F. Ochsenbein, M. G. Allen, & D. Egret, 759
- Gallagher, S. C., Everett, J. E., Abado, M. M., & Keating, S. K. 2015, MNRAS, 451, 2991, doi: [10.1093/mnras/stv1126](https://doi.org/10.1093/mnras/stv1126)
- Gámez Rosas, V., Isbell, J. W., Jaffe, W., et al. 2022, Nature, 602, 403, doi: [10.1038/s41586-021-04311-7](https://doi.org/10.1038/s41586-021-04311-7)
- Gandhi, P., Horst, H., Smette, A., et al. 2009, A&A, 502, 457, doi: [10.1051/0004-6361/200811368](https://doi.org/10.1051/0004-6361/200811368)
- García-Bernete, I., Ramos Almeida, C., Landt, H., et al. 2017, MNRAS, 469, 110, doi: [10.1093/mnras/stx795](https://doi.org/10.1093/mnras/stx795)
- García-Bernete, I., Ramos Almeida, C., Acosta-Pulido, J. A., et al. 2016, MNRAS, 463, 3531, doi: [10.1093/mnras/stw2125](https://doi.org/10.1093/mnras/stw2125)
- García-Bernete, I., Ramos Almeida, C., Alonso-Herrero, A., et al. 2019, MNRAS, 486, 4917, doi: [10.1093/mnras/stz1003](https://doi.org/10.1093/mnras/stz1003)
- García-Bernete, I., González-Martín, O., Ramos Almeida, C., et al. 2022, A&A, 667, A140, doi: [10.1051/0004-6361/202244230](https://doi.org/10.1051/0004-6361/202244230)
- Garmire, G. P., Bautz, M. W., Ford, P. G., Nousek, J. A., & Ricker, Jr., G. R. 2003, in Proc. SPIE, Vol. 4851, X-Ray and Gamma-Ray Telescopes and Instruments for Astronomy., ed. J. E. Truemper & H. D. Tananbaum, 28–44, doi: [10.1117/12.461599](https://doi.org/10.1117/12.461599)
- Gaskell, C. M., Goosmann, R. W., Antonucci, R. R. J., & Whysong, D. H. 2004, ApJ, 616, 147, doi: [10.1086/423885](https://doi.org/10.1086/423885)
- Gehrels, N., Chincarini, G., Giommi, P., et al. 2004, ApJ, 611, 1005, doi: [10.1086/422091](https://doi.org/10.1086/422091)
- González-Alfonso, E., Fischer, J., Spoon, H. W. W., et al. 2017, ApJ, 836, 11, doi: [10.3847/1538-4357/836/1/11](https://doi.org/10.3847/1538-4357/836/1/11)
- Gordon, Y. A., Boyce, M. M., O'Dea, C. P., et al. 2021, ApJS, 255, 30, doi: [10.3847/1538-4365/ac05c0](https://doi.org/10.3847/1538-4365/ac05c0)
- Goulding, A. D., Greene, J. E., Bezanson, R., et al. 2018a, PASJ, 70, S37, doi: [10.1093/pasj/psx135](https://doi.org/10.1093/pasj/psx135)
- Goulding, A. D., Zakamska, N. L., Alexandroff, R. M., et al. 2018b, ApJ, 856, 4, doi: [10.3847/1538-4357/aab040](https://doi.org/10.3847/1538-4357/aab040)
- Graham, A. W., Driver, S. P., Petrosian, V., et al. 2005, AJ, 130, 1535, doi: [10.1086/444475](https://doi.org/10.1086/444475)
- Granato, G. L., Danese, L., & Franceschini, A. 1997, ApJ, 486, 147, doi: [10.1086/304502](https://doi.org/10.1086/304502)
- Greene, J. E., Strader, J., & Ho, L. C. 2020, ARA&A, 58, 257, doi: [10.1146/annurev-astro-032620-021835](https://doi.org/10.1146/annurev-astro-032620-021835)
- Griffin, M. J., Abergel, A., Abreu, A., et al. 2010, A&A, 518, L3, doi: [10.1051/0004-6361/201014519](https://doi.org/10.1051/0004-6361/201014519)

- Gruppioni, C., Berta, S., Spinoglio, L., et al. 2016, MNRAS, 458, 4297, doi: [10.1093/mnras/stw577](https://doi.org/10.1093/mnras/stw577)
- Gültekin, K., Richstone, D. O., Gebhardt, K., et al. 2009, ApJ, 698, 198, doi: [10.1088/0004-637X/698/1/198](https://doi.org/10.1088/0004-637X/698/1/198)
- Haan, S., Surace, J. A., Armus, L., et al. 2011, AJ, 141, 100, doi: [10.1088/0004-6256/141/3/100](https://doi.org/10.1088/0004-6256/141/3/100)
- Hainline, L. J., Blain, A. W., Smail, I., et al. 2011, ApJ, 740, 96, doi: [10.1088/0004-637X/740/2/96](https://doi.org/10.1088/0004-637X/740/2/96)
- Hamann, F., Zakamska, N. L., Ross, N., et al. 2017, MNRAS, 464, 3431, doi: [10.1093/mnras/stw2387](https://doi.org/10.1093/mnras/stw2387)
- Harrison, F. A., Craig, W. W., Christensen, F. E., et al. 2013, ApJ, 770, 103, doi: [10.1088/0004-637X/770/2/103](https://doi.org/10.1088/0004-637X/770/2/103)
- Helfand, D. J., White, R. L., & Becker, R. H. 2015, ApJ, 801, 26, doi: [10.1088/0004-637X/801/1/26](https://doi.org/10.1088/0004-637X/801/1/26)
- Helou, G., Soifer, B. T., & Rowan-Robinson, M. 1985, ApJL, 298, L7, doi: [10.1086/184556](https://doi.org/10.1086/184556)
- Hickox, R. C., & Alexander, D. M. 2018, ARA&A, 56, 625, doi: [10.1146/annurev-astro-081817-051803](https://doi.org/10.1146/annurev-astro-081817-051803)
- Hickox, R. C., Wardlow, J. L., Smail, I., et al. 2012, MNRAS, 421, 284, doi: [10.1111/j.1365-2966.2011.20303.x](https://doi.org/10.1111/j.1365-2966.2011.20303.x)
- Hitomi Collaboration, Aharonian, F., Akamatsu, H., et al. 2018, PASJ, 70, 13, doi: [10.1093/pasj/psx147](https://doi.org/10.1093/pasj/psx147)
- Hönig, S. F. 2019, ApJ, 884, 171, doi: [10.3847/1538-4357/ab4591](https://doi.org/10.3847/1538-4357/ab4591)
- Hönig, S. F., Beckert, T., Ohnaka, K., & Weigelt, G. 2006, A&A, 452, 459, doi: [10.1051/0004-6361:20054622](https://doi.org/10.1051/0004-6361:20054622)
- Hönig, S. F., & Kishimoto, M. 2010, A&A, 523, A27, doi: [10.1051/0004-6361/200912676](https://doi.org/10.1051/0004-6361/200912676)
- . 2011, A&A, 534, A121, doi: [10.1051/0004-6361/201117750](https://doi.org/10.1051/0004-6361/201117750)
- . 2017, ApJL, 838, L20, doi: [10.3847/2041-8213/aa6838](https://doi.org/10.3847/2041-8213/aa6838)
- Hönig, S. F., Kishimoto, M., Antonucci, R., et al. 2012, ApJ, 755, 149, doi: [10.1088/0004-637X/755/2/149](https://doi.org/10.1088/0004-637X/755/2/149)
- Hönig, S. F., Kishimoto, M., Tristram, K. R. W., et al. 2013, ApJ, 771, 87, doi: [10.1088/0004-637X/771/2/87](https://doi.org/10.1088/0004-637X/771/2/87)
- Hopkins, P. F., Hernquist, L., Cox, T. J., & Kereš, D. 2008, ApJS, 175, 356, doi: [10.1086/524362](https://doi.org/10.1086/524362)
- Hopkins, P. F., Somerville, R. S., Hernquist, L., et al. 2006, ApJ, 652, 864, doi: [10.1086/508503](https://doi.org/10.1086/508503)
- Hopkins, P. F., Strauss, M. A., Hall, P. B., et al. 2004, AJ, 128, 1112, doi: [10.1086/423291](https://doi.org/10.1086/423291)
- Hurley-Walker, N., Callingham, J. R., Hancock, P. J., et al. 2017, MNRAS, 464, 1146, doi: [10.1093/mnras/stw2337](https://doi.org/10.1093/mnras/stw2337)
- Hurley-Walker, N., Hancock, P. J., Franzen, T. M. O., et al. 2019, PASA, 36, e047, doi: [10.1017/pasa.2019.37](https://doi.org/10.1017/pasa.2019.37)
- Ichikawa, K., Ricci, C., Ueda, Y., et al. 2017, ApJ, 835, 74, doi: [10.3847/1538-4357/835/1/74](https://doi.org/10.3847/1538-4357/835/1/74)
- Ichikawa, K., Ueda, Y., Terashima, Y., et al. 2012, ApJ, 754, 45, doi: [10.1088/0004-637X/754/1/45](https://doi.org/10.1088/0004-637X/754/1/45)
- Ichikawa, K., Packham, C., Ramos Almeida, C., et al. 2015, ApJ, 803, 57, doi: [10.1088/0004-637X/803/2/57](https://doi.org/10.1088/0004-637X/803/2/57)
- Ichikawa, K., Ricci, C., Ueda, Y., et al. 2019, ApJ, 870, 31, doi: [10.3847/1538-4357/aaef8f](https://doi.org/10.3847/1538-4357/aaef8f)
- Ikeda, S., Awaki, H., & Terashima, Y. 2009, ApJ, 692, 608, doi: [10.1088/0004-637X/692/1/608](https://doi.org/10.1088/0004-637X/692/1/608)
- Imanishi, M., Dudley, C. C., Maiolino, R., et al. 2007, ApJS, 171, 72, doi: [10.1086/513715](https://doi.org/10.1086/513715)
- Imanishi, M., Dudley, C. C., & Maloney, P. R. 2006, ApJ, 637, 114, doi: [10.1086/498391](https://doi.org/10.1086/498391)
- Imanishi, M., Kawamuro, T., Kikuta, S., Nakano, S., & Saito, Y. 2020, ApJ, 891, 140, doi: [10.3847/1538-4357/ab733e](https://doi.org/10.3847/1538-4357/ab733e)
- Imanishi, M., Nakagawa, T., Ohyama, Y., et al. 2008, PASJ, 60, S489, doi: [10.1093/pasj/60.sp2.S489](https://doi.org/10.1093/pasj/60.sp2.S489)
- Imanishi, M., Nakagawa, T., Shirahata, M., Ohyama, Y., & Onaka, T. 2010, ApJ, 721, 1233, doi: [10.1088/0004-637X/721/2/1233](https://doi.org/10.1088/0004-637X/721/2/1233)
- Imanishi, M., & Saito, Y. 2014, ApJ, 780, 106, doi: [10.1088/0004-637X/780/1/106](https://doi.org/10.1088/0004-637X/780/1/106)
- Inaba, K., Ueda, Y., Yamada, S., et al. 2022, ApJ, 939, 88, doi: [10.3847/1538-4357/ac97ec](https://doi.org/10.3847/1538-4357/ac97ec)
- Inami, H., Armus, L., Charmandaris, V., et al. 2013, ApJ, 777, 156, doi: [10.1088/0004-637X/777/2/156](https://doi.org/10.1088/0004-637X/777/2/156)
- Inami, H., Armus, L., Matsuhara, H., et al. 2018, A&A, 617, A130, doi: [10.1051/0004-6361/201833053](https://doi.org/10.1051/0004-6361/201833053)
- Inayoshi, K., Ichikawa, K., & Haiman, Z. 2018, ApJL, 863, L36, doi: [10.3847/2041-8213/aad8ad](https://doi.org/10.3847/2041-8213/aad8ad)
- Inoue, A. K. 2011, MNRAS, 415, 2920, doi: [10.1111/j.1365-2966.2011.18906.x](https://doi.org/10.1111/j.1365-2966.2011.18906.x)
- Intema, H. T., Jagannathan, P., Mooley, K. P., & Frail, D. A. 2017, A&A, 598, A78, doi: [10.1051/0004-6361/201628536](https://doi.org/10.1051/0004-6361/201628536)
- Isbell, J. W., Meisenheimer, K., Pott, J. U., et al. 2022, A&A, 663, A35, doi: [10.1051/0004-6361/202243271](https://doi.org/10.1051/0004-6361/202243271)
- Ishibashi, W., Fabian, A. C., Ricci, C., & Celotti, A. 2018, MNRAS, 479, 3335, doi: [10.1093/mnras/sty1620](https://doi.org/10.1093/mnras/sty1620)
- Ishihara, D., Onaka, T., Kataza, H., et al. 2010, A&A, 514, A1, doi: [10.1051/0004-6361/200913811](https://doi.org/10.1051/0004-6361/200913811)
- Iwasawa, K., Sanders, D. B., Teng, S. H., et al. 2011, A&A, 529, A106, doi: [10.1051/0004-6361/201015264](https://doi.org/10.1051/0004-6361/201015264)
- Iwasawa, K., Ricci, C., Privon, G. C., et al. 2020, A&A, 640, A95, doi: [10.1051/0004-6361/202038513](https://doi.org/10.1051/0004-6361/202038513)
- Izumi, T., Kawakatu, N., & Kohno, K. 2016, ApJ, 827, 81, doi: [10.3847/0004-637X/827/1/81](https://doi.org/10.3847/0004-637X/827/1/81)
- Izumi, T., Wada, K., Fukushige, R., Hamamura, S., & Kohno, K. 2018, ApJ, 867, 48, doi: [10.3847/1538-4357/aae20b](https://doi.org/10.3847/1538-4357/aae20b)

- Jadhav, Y., Robinson, A., Almeyda, T., Curran, R., & Marconi, A. 2021, MNRAS, 507, 484, doi: [10.1093/mnras/stab2176](https://doi.org/10.1093/mnras/stab2176)
- Jahnke, K., & Macciò, A. V. 2011, ApJ, 734, 92, doi: [10.1088/0004-637X/734/2/92](https://doi.org/10.1088/0004-637X/734/2/92)
- Jansen, F., Lumb, D., Altieri, B., et al. 2001, A&A, 365, L1, doi: [10.1051/0004-6361:20000036](https://doi.org/10.1051/0004-6361:20000036)
- Jarrett, T. H., Cohen, M., Masci, F., et al. 2011, ApJ, 735, 112, doi: [10.1088/0004-637X/735/2/112](https://doi.org/10.1088/0004-637X/735/2/112)
- Jones, A. P., Tielens, A. G. G. M., Hollenbach, D. J., & McKee, C. F. 1994, ApJ, 433, 797, doi: [10.1086/174689](https://doi.org/10.1086/174689)
- Just, D. W., Brandt, W. N., Shemmer, O., et al. 2007, ApJ, 665, 1004, doi: [10.1086/519990](https://doi.org/10.1086/519990)
- Kakkad, D., Groves, B., Dopita, M., et al. 2018, A&A, 618, A6, doi: [10.1051/0004-6361/201832790](https://doi.org/10.1051/0004-6361/201832790)
- Kamizuka, T., Miyata, T., Sako, S., et al. 2020, in Society of Photo-Optical Instrumentation Engineers (SPIE) Conference Series, Vol. 11447, Society of Photo-Optical Instrumentation Engineers (SPIE) Conference Series, 114475X, doi: [10.1117/12.2560789](https://doi.org/10.1117/12.2560789)
- Kawaguchi, T., Yutani, N., & Wada, K. 2020, ApJ, 890, 125, doi: [10.3847/1538-4357/ab655a](https://doi.org/10.3847/1538-4357/ab655a)
- Kawamuro, T., Ricci, C., Izumi, T., et al. 2021, ApJS, 257, 64, doi: [10.3847/1538-4365/ac2891](https://doi.org/10.3847/1538-4365/ac2891)
- Kawamuro, T., Ricci, C., Imanishi, M., et al. 2022, ApJ, 938, 87, doi: [10.3847/1538-4357/ac8794](https://doi.org/10.3847/1538-4357/ac8794)
- Kelly, B. C. 2007, ApJ, 665, 1489, doi: [10.1086/519947](https://doi.org/10.1086/519947)
- Kennicutt, Robert C., J. 1998, ARA&A, 36, 189, doi: [10.1146/annurev.astro.36.1.189](https://doi.org/10.1146/annurev.astro.36.1.189)
- Kim, D. C., Veilleux, S., & Sanders, D. B. 2002, ApJS, 143, 277, doi: [10.1086/343843](https://doi.org/10.1086/343843)
- Klöckner, H. R., & Baan, W. A. 2004, A&A, 419, 887, doi: [10.1051/0004-6361:20040998](https://doi.org/10.1051/0004-6361:20040998)
- Kocevski, D. D., Brightman, M., Nandra, K., et al. 2015, ApJ, 814, 104, doi: [10.1088/0004-637X/814/2/104](https://doi.org/10.1088/0004-637X/814/2/104)
- Kormendy, J., & Ho, L. C. 2013, ARA&A, 51, 511, doi: [10.1146/annurev-astro-082708-101811](https://doi.org/10.1146/annurev-astro-082708-101811)
- Koss, M., Mushotzky, R., Treister, E., et al. 2012, ApJL, 746, L22, doi: [10.1088/2041-8205/746/2/L22](https://doi.org/10.1088/2041-8205/746/2/L22)
- Koss, M., Mushotzky, R., Veilleux, S., & Winter, L. 2010, ApJL, 716, L125, doi: [10.1088/2041-8205/716/2/L125](https://doi.org/10.1088/2041-8205/716/2/L125)
- Koss, M. J., Blecha, L., Bernhard, P., et al. 2018, Nature, 563, 214, doi: [10.1038/s41586-018-0652-7](https://doi.org/10.1038/s41586-018-0652-7)
- Krolik, J. H. 1999, ApJL, 515, L73, doi: [10.1086/311979](https://doi.org/10.1086/311979)
- . 2007, ApJ, 661, 52, doi: [10.1086/515432](https://doi.org/10.1086/515432)
- Krolik, J. H., & Begelman, M. C. 1988, ApJ, 329, 702, doi: [10.1086/166414](https://doi.org/10.1086/166414)
- Kron, R. G. 1980, ApJS, 43, 305, doi: [10.1086/190669](https://doi.org/10.1086/190669)
- Kroupa, P. 2001, MNRAS, 322, 231, doi: [10.1046/j.1365-8711.2001.04022.x](https://doi.org/10.1046/j.1365-8711.2001.04022.x)
- Laha, S., Guainazzi, M., Piconcelli, E., et al. 2018, ApJ, 868, 10, doi: [10.3847/1538-4357/aae390](https://doi.org/10.3847/1538-4357/aae390)
- Laha, S., Markowitz, A. G., Krumpe, M., et al. 2020, ApJ, 897, 66, doi: [10.3847/1538-4357/ab92ab](https://doi.org/10.3847/1538-4357/ab92ab)
- Lane, W. M., Cotton, W. D., van Velzen, S., et al. 2014, MNRAS, 440, 327, doi: [10.1093/mnras/stu256](https://doi.org/10.1093/mnras/stu256)
- Lansbury, G. B., Alexander, D. M., Aird, J., et al. 2017, ApJ, 846, 20, doi: [10.3847/1538-4357/aa8176](https://doi.org/10.3847/1538-4357/aa8176)
- Laor, A., Baldi, R. D., & Behar, E. 2019, MNRAS, 482, 5513, doi: [10.1093/mnras/sty3098](https://doi.org/10.1093/mnras/sty3098)
- Laurent, O., Mirabel, I. F., Charmandaris, V., et al. 2000, A&A, 359, 887. <https://arxiv.org/abs/astro-ph/0005376>
- Lee, J. C., Hwang, H. S., Lee, M. G., Kim, M., & Lee, J. H. 2012, ApJ, 756, 95, doi: [10.1088/0004-637X/756/1/95](https://doi.org/10.1088/0004-637X/756/1/95)
- Leroy, A. K., Evans, A. S., Momjian, E., et al. 2011, ApJL, 739, L25, doi: [10.1088/2041-8205/739/1/L25](https://doi.org/10.1088/2041-8205/739/1/L25)
- Liang, Y. C., Hammer, F., Flores, H., et al. 2004, A&A, 423, 867, doi: [10.1051/0004-6361:20035740](https://doi.org/10.1051/0004-6361:20035740)
- Linden, S. T., Song, Y., Evans, A. S., et al. 2019, ApJ, 881, 70, doi: [10.3847/1538-4357/ab2872](https://doi.org/10.3847/1538-4357/ab2872)
- Liu, J., Höning, S. F., Ricci, C., & Paltani, S. 2019, MNRAS, 490, 4344, doi: [10.1093/mnras/stz2908](https://doi.org/10.1093/mnras/stz2908)
- Liu, T., Wang, J.-X., Yang, H., Zhu, F.-F., & Zhou, Y.-Y. 2014, ApJ, 783, 106, doi: [10.1088/0004-637X/783/2/106](https://doi.org/10.1088/0004-637X/783/2/106)
- Liu, Y., & Li, X. 2014, ApJ, 787, 52, doi: [10.1088/0004-637X/787/1/52](https://doi.org/10.1088/0004-637X/787/1/52)
- Lo Faro, B., Buat, V., Roehlly, Y., et al. 2017, MNRAS, 472, 1372, doi: [10.1093/mnras/stx1901](https://doi.org/10.1093/mnras/stx1901)
- Lodato, G., & Bertin, G. 2003, A&A, 398, 517, doi: [10.1051/0004-6361:20021672](https://doi.org/10.1051/0004-6361:20021672)
- Longobardi, A., Arnaboldi, M., Gerhard, O., & Mihos, J. C. 2015, A&A, 579, L3, doi: [10.1051/0004-6361/201526282](https://doi.org/10.1051/0004-6361/201526282)
- Lonsdale, C. J., Lonsdale, C. J., Smith, H. E., & Diamond, P. J. 2003, ApJ, 592, 804, doi: [10.1086/375778](https://doi.org/10.1086/375778)
- Lonsdale, C. J., Cappallo, R. J., Morales, M. F., et al. 2009, IEEE Proceedings, 97, 1497, doi: [10.1109/JPROC.2009.2017564](https://doi.org/10.1109/JPROC.2009.2017564)
- López-Gonzaga, N., Burtscher, L., Tristram, K. R. W., Meisenheimer, K., & Schartmann, M. 2016, A&A, 591, A47, doi: [10.1051/0004-6361/201527590](https://doi.org/10.1051/0004-6361/201527590)
- López-Gonzaga, N., & Jaffe, W. 2016, A&A, 591, A128, doi: [10.1051/0004-6361/201527149](https://doi.org/10.1051/0004-6361/201527149)
- López-Gonzaga, N., Jaffe, W., Burtscher, L., Tristram, K. R. W., & Meisenheimer, K. 2014, A&A, 565, A71, doi: [10.1051/0004-6361/201323002](https://doi.org/10.1051/0004-6361/201323002)
- Lopez-Rodriguez, E., Packham, C., Jones, T. J., et al. 2017, MNRAS, 464, 1762, doi: [10.1093/mnras/stw2491](https://doi.org/10.1093/mnras/stw2491)
- Lopez-Rodriguez, E., Fuller, L., Alonso-Herrero, A., et al. 2018, ApJ, 859, 99, doi: [10.3847/1538-4357/aabd7b](https://doi.org/10.3847/1538-4357/aabd7b)

- Lu, N., Zhao, Y., Díaz-Santos, T., et al. 2017, *ApJS*, 230, 1, doi: [10.3847/1538-4365/aa6476](https://doi.org/10.3847/1538-4365/aa6476)
- Lusso, E., Comastri, A., Vignali, C., et al. 2010, *A&A*, 512, A34, doi: [10.1051/0004-6361/200913298](https://doi.org/10.1051/0004-6361/200913298)
- Lutz, D., Maiolino, R., Spoon, H. W. W., & Moorwood, A. F. M. 2004, *A&A*, 418, 465, doi: [10.1051/0004-6361:20035838](https://doi.org/10.1051/0004-6361:20035838)
- Lyu, J., & Rieke, G. H. 2018, *ApJ*, 866, 92, doi: [10.3847/1538-4357/aae075](https://doi.org/10.3847/1538-4357/aae075)
- . 2021, *ApJ*, 912, 126, doi: [10.3847/1538-4357/abee14](https://doi.org/10.3847/1538-4357/abee14)
- Lyu, J., Rieke, G. H., & Shi, Y. 2017, *ApJ*, 835, 257, doi: [10.3847/1538-4357/835/2/257](https://doi.org/10.3847/1538-4357/835/2/257)
- Madau, P., & Dickinson, M. 2014, *ARA&A*, 52, 415, doi: [10.1146/annurev-astro-081811-125615](https://doi.org/10.1146/annurev-astro-081811-125615)
- Magdis, G. E., Daddi, E., Béthermin, M., et al. 2012, *ApJ*, 760, 6, doi: [10.1088/0004-637X/760/1/6](https://doi.org/10.1088/0004-637X/760/1/6)
- Magnier, E. A., Chambers, K. C., Flewelling, H. A., et al. 2020a, *ApJS*, 251, 3, doi: [10.3847/1538-4365/abb829](https://doi.org/10.3847/1538-4365/abb829)
- Magnier, E. A., Sweeney, W. E., Chambers, K. C., et al. 2020b, *ApJS*, 251, 5, doi: [10.3847/1538-4365/abb82c](https://doi.org/10.3847/1538-4365/abb82c)
- Magnier, E. A., Schlaflay, E. F., Finkbeiner, D. P., et al. 2020c, *ApJS*, 251, 6, doi: [10.3847/1538-4365/abb82a](https://doi.org/10.3847/1538-4365/abb82a)
- Maiolino, R., Marconi, A., & Oliva, E. 2001, *A&A*, 365, 37, doi: [10.1051/0004-6361:20000012](https://doi.org/10.1051/0004-6361:20000012)
- Mannucci, F., Cresci, G., Maiolino, R., Marconi, A., & Gnerucci, A. 2010, *MNRAS*, 408, 2115, doi: [10.1111/j.1365-2966.2010.17291.x](https://doi.org/10.1111/j.1365-2966.2010.17291.x)
- Marconi, A., & Hunt, L. K. 2003, *ApJL*, 589, L21, doi: [10.1086/375804](https://doi.org/10.1086/375804)
- Martin, D. C., Fanson, J., Schiminovich, D., et al. 2005, *ApJL*, 619, L1, doi: [10.1086/426387](https://doi.org/10.1086/426387)
- Martocchia, S., Piconcelli, E., Zappacosta, L., et al. 2017, *A&A*, 608, A51, doi: [10.1051/0004-6361/201731314](https://doi.org/10.1051/0004-6361/201731314)
- Mateos, S., Alonso-Herrero, A., Carrera, F. J., et al. 2013, *MNRAS*, 434, 941, doi: [10.1093/mnras/stt953](https://doi.org/10.1093/mnras/stt953)
- . 2012, *MNRAS*, 426, 3271, doi: [10.1111/j.1365-2966.2012.21843.x](https://doi.org/10.1111/j.1365-2966.2012.21843.x)
- Mateos, S., Carrera, F. J., Alonso-Herrero, A., et al. 2015, *MNRAS*, 449, 1422, doi: [10.1093/mnras/stv299](https://doi.org/10.1093/mnras/stv299)
- Matsumoto, K., Nakagawa, T., Wada, K., et al. 2022, *ApJ*, 934, 25, doi: [10.3847/1538-4357/ac755f](https://doi.org/10.3847/1538-4357/ac755f)
- Mattila, S., Pérez-Torres, M., Efstathiou, A., et al. 2018, *Science*, 361, 482, doi: [10.1126/science.aao4669](https://doi.org/10.1126/science.aao4669)
- Mauch, T., Murphy, T., Buttery, H. J., et al. 2003, *MNRAS*, 342, 1117, doi: [10.1046/j.1365-8711.2003.06605.x](https://doi.org/10.1046/j.1365-8711.2003.06605.x)
- . 2008, VizieR Online Data Catalog, VIII/81A
- Mazzarella, J. M., Iwasawa, K., Vavilkin, T., et al. 2012, *AJ*, 144, 125, doi: [10.1088/0004-6256/144/5/125](https://doi.org/10.1088/0004-6256/144/5/125)
- Meier, D. S., Turner, J. L., Beck, S. C., et al. 2010, *AJ*, 140, 1294, doi: [10.1088/0004-6256/140/5/1294](https://doi.org/10.1088/0004-6256/140/5/1294)
- Meng, X.-M., Wu, H., Gu, Q.-S., Wang, J., & Cao, C. 2010, *ApJ*, 718, 928, doi: [10.1088/0004-637X/718/2/928](https://doi.org/10.1088/0004-637X/718/2/928)
- Mills, B. Y. 1981, *PASA*, 4, 156, doi: [10.1017/S1323358000016222](https://doi.org/10.1017/S1323358000016222)
- Mineo, S., Gilfanov, M., & Sunyaev, R. 2012, *MNRAS*, 419, 2095, doi: [10.1111/j.1365-2966.2011.19862.x](https://doi.org/10.1111/j.1365-2966.2011.19862.x)
- Mitsuda, K., Bautz, M., Inoue, H., et al. 2007, *PASJ*, 59, S1, doi: [10.1093/pasj/59.sp1.S1](https://doi.org/10.1093/pasj/59.sp1.S1)
- Miyaji, T., Herrera-Endoqui, M., Krumpe, M., et al. 2019, *ApJL*, 884, L10, doi: [10.3847/2041-8213/ab46bc](https://doi.org/10.3847/2041-8213/ab46bc)
- Mizukoshi, S., Minezaki, T., Tsunetsugu, S., et al. 2022, *MNRAS*, 516, 2876, doi: [10.1093/mnras/stac2307](https://doi.org/10.1093/mnras/stac2307)
- Mizumoto, M., Izumi, T., & Kohno, K. 2019, *ApJ*, 871, 156, doi: [10.3847/1538-4357/aaf814](https://doi.org/10.3847/1538-4357/aaf814)
- Mor, R., & Netzer, H. 2012, *MNRAS*, 420, 526, doi: [10.1111/j.1365-2966.2011.20060.x](https://doi.org/10.1111/j.1365-2966.2011.20060.x)
- Mor, R., Netzer, H., & Elitzur, M. 2009, *ApJ*, 705, 298, doi: [10.1088/0004-637X/705/1/298](https://doi.org/10.1088/0004-637X/705/1/298)
- Morganti, R., Veilleux, S., Oosterloo, T., Teng, S. H., & Rupke, D. 2016, *A&A*, 593, A30, doi: [10.1051/0004-6361/201628978](https://doi.org/10.1051/0004-6361/201628978)
- Morić, I., Smolčić, V., Kimball, A., et al. 2010, *ApJ*, 724, 779, doi: [10.1088/0004-637X/724/1/779](https://doi.org/10.1088/0004-637X/724/1/779)
- Morrissey, P., Conrow, T., Barlow, T. A., et al. 2007, *ApJS*, 173, 682, doi: [10.1086/520512](https://doi.org/10.1086/520512)
- Murakami, H., Baba, H., Barthel, P., et al. 2007, *PASJ*, 59, S369, doi: [10.1093/pasj/59.sp2.S369](https://doi.org/10.1093/pasj/59.sp2.S369)
- Murphy, E. J. 2013, *ApJ*, 777, 58, doi: [10.1088/0004-637X/777/1/58](https://doi.org/10.1088/0004-637X/777/1/58)
- Murphy, E. J., Stierwalt, S., Armus, L., Condon, J. J., & Evans, A. S. 2013, *ApJ*, 768, 2, doi: [10.1088/0004-637X/768/1/2](https://doi.org/10.1088/0004-637X/768/1/2)
- Narayanan, D., Dey, A., Hayward, C. C., et al. 2010, *MNRAS*, 407, 1701, doi: [10.1111/j.1365-2966.2010.16997.x](https://doi.org/10.1111/j.1365-2966.2010.16997.x)
- Nenkova, M., Sirocky, M. M., Ivezić, Ž., & Elitzur, M. 2008a, *ApJ*, 685, 147, doi: [10.1086/590482](https://doi.org/10.1086/590482)
- Nenkova, M., Sirocky, M. M., Nikutta, R., Ivezić, Ž., & Elitzur, M. 2008b, *ApJ*, 685, 160, doi: [10.1086/590483](https://doi.org/10.1086/590483)
- Nersesian, A., Xilouris, E. M., Bianchi, S., et al. 2019, *A&A*, 624, A80, doi: [10.1051/0004-6361/201935118](https://doi.org/10.1051/0004-6361/201935118)
- Netzer, H. 1987, *MNRAS*, 225, 55, doi: [10.1093/mnras/225.1.55](https://doi.org/10.1093/mnras/225.1.55)
- Netzer, H., Lutz, D., Schweitzer, M., et al. 2007, *ApJ*, 666, 806, doi: [10.1086/520716](https://doi.org/10.1086/520716)
- Niklas, S., Klein, U., & Wielebinski, R. 1997, *A&A*, 322, 19
- Noeske, K. G., Weiner, B. J., Faber, S. M., et al. 2007, *ApJL*, 660, L43, doi: [10.1086/517926](https://doi.org/10.1086/517926)

- Noll, S., Burgarella, D., Giovannoli, E., et al. 2009, A&A, 507, 1793, doi: [10.1051/0004-6361/200912497](https://doi.org/10.1051/0004-6361/200912497)
- Ogawa, S., Ueda, Y., Tanimoto, A., & Yamada, S. 2021, ApJ, 906, 84, doi: [10.3847/1538-4357/abccce](https://doi.org/10.3847/1538-4357/abccce)
- Ogawa, S., Ueda, Y., Yamada, S., Tanimoto, A., & Kawaguchi, T. 2019, ApJ, 875, 115, doi: [10.3847/1538-4357/ab0e08](https://doi.org/10.3847/1538-4357/ab0e08)
- Oh, K., Koss, M., Markwardt, C. B., et al. 2018, ApJS, 235, 4, doi: [10.3847/1538-4365/aaa7fd](https://doi.org/10.3847/1538-4365/aaa7fd)
- Ohyama, Y., Sakamoto, K., Aalto, S., & Gallagher, John S. I. 2019, ApJ, 871, 191, doi: [10.3847/1538-4357/aaf9a5](https://doi.org/10.3847/1538-4357/aaf9a5)
- Onken, C. A., Wolf, C., Bessell, M. S., et al. 2019, PASA, 36, e033, doi: [10.1017/pasa.2019.27](https://doi.org/10.1017/pasa.2019.27)
- Panessa, F., Baldi, R. D., Laor, A., et al. 2019, Nature Astronomy, 3, 387, doi: [10.1038/s41550-019-0765-4](https://doi.org/10.1038/s41550-019-0765-4)
- Paspalas, E. D., Xilouris, E. M., Nersesian, A., et al. 2021, A&A, 649, A137, doi: [10.1051/0004-6361/202038605](https://doi.org/10.1051/0004-6361/202038605)
- Pearson, W. J., Wang, L., Hurley, P. D., et al. 2018, A&A, 615, A146, doi: [10.1051/0004-6361/201832821](https://doi.org/10.1051/0004-6361/201832821)
- Petric, A. O., Armus, L., Howell, J., et al. 2011, ApJ, 730, 28, doi: [10.1088/0004-637X/730/1/28](https://doi.org/10.1088/0004-637X/730/1/28)
- Pfeifle, R. W., Satyapal, S., Secrest, N. J., et al. 2019, ApJ, 875, 117, doi: [10.3847/1538-4357/ab07bc](https://doi.org/10.3847/1538-4357/ab07bc)
- Pfeifle, R. W., Ricci, C., Boorman, P. G., et al. 2022, ApJS, 261, 3, doi: [10.3847/1538-4365/ac5b65](https://doi.org/10.3847/1538-4365/ac5b65)
- Pilbratt, G. L., Riedinger, J. R., Passvogel, T., et al. 2010, A&A, 518, L1, doi: [10.1051/0004-6361/201014759](https://doi.org/10.1051/0004-6361/201014759)
- Poglitsch, A., Waelkens, C., Geis, N., et al. 2010, A&A, 518, L2, doi: [10.1051/0004-6361/201014535](https://doi.org/10.1051/0004-6361/201014535)
- Polletta, M., Tajer, M., Maraschi, L., et al. 2007, ApJ, 663, 81, doi: [10.1086/518113](https://doi.org/10.1086/518113)
- Prevot, M. L., Lequeux, J., Maurice, E., Prevot, L., & Rocca-Volmerange, B. 1984, A&A, 132, 389
- Privon, G. C., Barnes, J. E., Evans, A. S., et al. 2013, ApJ, 771, 120, doi: [10.1088/0004-637X/771/2/120](https://doi.org/10.1088/0004-637X/771/2/120)
- Privon, G. C., Ricci, C., Aalto, S., et al. 2020, ApJ, 893, 149, doi: [10.3847/1538-4357/ab8015](https://doi.org/10.3847/1538-4357/ab8015)
- Puccetti, S., Comastri, A., Bauer, F. E., et al. 2016, A&A, 585, A157, doi: [10.1051/0004-6361/201527189](https://doi.org/10.1051/0004-6361/201527189)
- Raftery, A. E. 1995, Sociological Methodology, 25, 111, <http://www.jstor.org/stable/271063>
- Ramos Almeida, C., Pérez García, A. M., Acosta-Pulido, J. A., & Rodríguez Espinosa, J. M. 2007, AJ, 134, 2006, doi: [10.1086/522625](https://doi.org/10.1086/522625)
- Rani, B., Madejski, G. M., Mushotzky, R. F., Reynolds, C., & Hodgson, J. A. 2018, ApJL, 866, L13, doi: [10.3847/2041-8213/aae48f](https://doi.org/10.3847/2041-8213/aae48f)
- Reines, A. E., & Volonteri, M. 2015, ApJ, 813, 82, doi: [10.1088/0004-637X/813/2/82](https://doi.org/10.1088/0004-637X/813/2/82)
- Rémy-Ruyer, A., Madden, S. C., Galliano, F., et al. 2014, A&A, 563, A31, doi: [10.1051/0004-6361/201322803](https://doi.org/10.1051/0004-6361/201322803)
- Rengelink, R. B., Tang, Y., de Bruyn, A. G., et al. 1997, A&AS, 124, 259, doi: [10.1051/aas:1997358](https://doi.org/10.1051/aas:1997358)
- Revalska, M., Crenshaw, D. M., Kraemer, S. B., et al. 2018, ApJ, 856, 46, doi: [10.3847/1538-4357/aab107](https://doi.org/10.3847/1538-4357/aab107)
- Ricci, C., Bauer, F. E., Treister, E., et al. 2016, ApJ, 819, 4, doi: [10.3847/0004-637X/819/1/4](https://doi.org/10.3847/0004-637X/819/1/4)
- . 2017a, MNRAS, 468, 1273, doi: [10.1093/mnras/stx173](https://doi.org/10.1093/mnras/stx173)
- Ricci, C., Trakhtenbrot, B., Koss, M. J., et al. 2017b, ApJS, 233, 17, doi: [10.3847/1538-4365/aa96ad](https://doi.org/10.3847/1538-4365/aa96ad)
- Ricci, C., Assef, R. J., Stern, D., et al. 2017c, ApJ, 835, 105, doi: [10.3847/1538-4357/835/1/105](https://doi.org/10.3847/1538-4357/835/1/105)
- Ricci, C., Trakhtenbrot, B., Koss, M. J., et al. 2017d, Nature, 549, 488, doi: [10.1038/nature23906](https://doi.org/10.1038/nature23906)
- Ricci, C., Privon, G. C., Pfeifle, R. W., et al. 2021, MNRAS, 506, 5935, doi: [10.1093/mnras/stab2052](https://doi.org/10.1093/mnras/stab2052)
- Ricci, C., Ananna, T. T., Temple, M. J., et al. 2022, ApJ, 938, 67, doi: [10.3847/1538-4357/ac8e67](https://doi.org/10.3847/1538-4357/ac8e67)
- Rich, J. A., Kewley, L. J., & Dopita, M. A. 2015, ApJS, 221, 28, doi: [10.1088/0067-0049/221/2/28](https://doi.org/10.1088/0067-0049/221/2/28)
- Rieke, G. H., Wright, G. S., Böker, T., et al. 2015, PASP, 127, 584, doi: [10.1086/682252](https://doi.org/10.1086/682252)
- Rivers, E., Risaliti, G., Walton, D. J., et al. 2015, ApJ, 804, 107, doi: [10.1088/0004-637X/804/2/107](https://doi.org/10.1088/0004-637X/804/2/107)
- Robertson, J. G. 1991, Australian Journal of Physics, 44, 729, doi: [10.1071/PH910729](https://doi.org/10.1071/PH910729)
- Roseboom, I. G., Bunker, A., Sumiyoshi, M., et al. 2012, MNRAS, 426, 1782, doi: [10.1111/j.1365-2966.2012.21777.x](https://doi.org/10.1111/j.1365-2966.2012.21777.x)
- Rowan-Robinson, M. 1995, MNRAS, 272, 737, doi: [10.1093/mnras/272.4.737](https://doi.org/10.1093/mnras/272.4.737)
- Rupke, D. S. N., Gültekin, K., & Veilleux, S. 2017, ApJ, 850, 40, doi: [10.3847/1538-4357/aa94d1](https://doi.org/10.3847/1538-4357/aa94d1)
- Rupke, D. S. N., & Veilleux, S. 2013, ApJ, 768, 75, doi: [10.1088/0004-637X/768/1/75](https://doi.org/10.1088/0004-637X/768/1/75)
- Rupke, D. S. N., Veilleux, S., & Baker, A. J. 2008, ApJ, 674, 172, doi: [10.1086/522363](https://doi.org/10.1086/522363)
- Saintonge, A., Catinella, B., Cortese, L., et al. 2016, MNRAS, 462, 1749, doi: [10.1093/mnras/stw1715](https://doi.org/10.1093/mnras/stw1715)
- Salim, S., Boquien, M., & Lee, J. C. 2018, ApJ, 859, 11, doi: [10.3847/1538-4357/aabf3c](https://doi.org/10.3847/1538-4357/aabf3c)
- Salim, S., & Narayanan, D. 2020, ARA&A, 58, 529, doi: [10.1146/annurev-astro-032620-021933](https://doi.org/10.1146/annurev-astro-032620-021933)
- Salpeter, E. E. 1955, ApJ, 121, 161, doi: [10.1086/145971](https://doi.org/10.1086/145971)
- Salvato, M., Hasinger, G., Ilbert, O., et al. 2009, ApJ, 690, 1250, doi: [10.1088/0004-637X/690/2/1250](https://doi.org/10.1088/0004-637X/690/2/1250)
- Sanders, D. B., Mazzarella, J. M., Kim, D. C., Surace, J. A., & Soifer, B. T. 2003, AJ, 126, 1607, doi: [10.1086/376841](https://doi.org/10.1086/376841)

- Sanders, D. B., & Mirabel, I. F. 1996, ARA&A, 34, 749, doi: [10.1146/annurev.astro.34.1.749](https://doi.org/10.1146/annurev.astro.34.1.749)
- Santini, P., Maiolino, R., Magnelli, B., et al. 2014, A&A, 562, A30, doi: [10.1051/0004-6361/201322835](https://doi.org/10.1051/0004-6361/201322835)
- Satyapal, S., Ellison, S. L., McAlpine, W., et al. 2014, MNRAS, 441, 1297, doi: [10.1093/mnras/stu650](https://doi.org/10.1093/mnras/stu650)
- Satyapal, S., Secrest, N. J., Ricci, C., et al. 2017, ApJ, 848, 126, doi: [10.3847/1538-4357/aa88ca](https://doi.org/10.3847/1538-4357/aa88ca)
- Savage, B. D., & Sembach, K. R. 1996, ARA&A, 34, 279, doi: [10.1146/annurev.astro.34.1.279](https://doi.org/10.1146/annurev.astro.34.1.279)
- Schartmann, M., Krause, M., & Burkert, A. 2011, MNRAS, 415, 741, doi: [10.1111/j.1365-2966.2011.18751.x](https://doi.org/10.1111/j.1365-2966.2011.18751.x)
- Schartmann, M., Meisenheimer, K., Camenzind, M., Wolf, S., & Henning, T. 2005, A&A, 437, 861, doi: [10.1051/0004-6361:20042363](https://doi.org/10.1051/0004-6361:20042363)
- Schartmann, M., Wada, K., Prieto, M. A., Burkert, A., & Tristram, K. R. W. 2014, MNRAS, 445, 3878, doi: [10.1093/mnras/stu2020](https://doi.org/10.1093/mnras/stu2020)
- Schlafly, E. F., & Finkbeiner, D. P. 2011, ApJ, 737, 103, doi: [10.1088/0004-637X/737/2/103](https://doi.org/10.1088/0004-637X/737/2/103)
- Schlegel, D. J., Finkbeiner, D. P., & Davis, M. 1998, ApJ, 500, 525, doi: [10.1086/305772](https://doi.org/10.1086/305772)
- Schwarz, G. 1978, Annals of Statistics, 6, 461
- Scoville, N., Abraham, R. G., Aussel, H., et al. 2007, ApJS, 172, 38, doi: [10.1086/516580](https://doi.org/10.1086/516580)
- Seaquist, E., Yao, L., Dunne, L., & Cameron, H. 2004, MNRAS, 349, 1428, doi: [10.1111/j.1365-2966.2004.07612.x](https://doi.org/10.1111/j.1365-2966.2004.07612.x)
- Secrest, N. J., Dudik, R. P., Dorland, B. N., et al. 2015, ApJS, 221, 12, doi: [10.1088/0067-0049/221/1/12](https://doi.org/10.1088/0067-0049/221/1/12)
- Shangguan, J., Ho, L. C., Li, R., et al. 2019, ApJ, 870, 104, doi: [10.3847/1538-4357/aaf21a](https://doi.org/10.3847/1538-4357/aaf21a)
- Shankar, F., Salucci, P., Granato, G. L., De Zotti, G., & Danese, L. 2004, MNRAS, 354, 1020, doi: [10.1111/j.1365-2966.2004.08261.x](https://doi.org/10.1111/j.1365-2966.2004.08261.x)
- Shimwell, T. W., Tasse, C., Hardcastle, M. J., et al. 2019, A&A, 622, A1, doi: [10.1051/0004-6361/201833559](https://doi.org/10.1051/0004-6361/201833559)
- Skrutskie, M. F., Cutri, R. M., Stiening, R., et al. 2003, 2MASS All-Sky Point Source Catalog, IPAC, doi: [10.26131/IRSA2](https://doi.org/10.26131/IRSA2)
- . 2006, AJ, 131, 1163, doi: [10.1086/498708](https://doi.org/10.1086/498708)
- Smith, R. N., Tombesi, F., Veilleux, S., Lohfink, A. M., & Luminari, A. 2019, ApJ, 887, 69, doi: [10.3847/1538-4357/ab4ef8](https://doi.org/10.3847/1538-4357/ab4ef8)
- Soltan, A. 1982, MNRAS, 200, 115, doi: [10.1093/mnras/200.1.115](https://doi.org/10.1093/mnras/200.1.115)
- Speagle, J. S., Steinhardt, C. L., Capak, P. L., & Silverman, J. D. 2014, ApJS, 214, 15, doi: [10.1088/0004-6361/214/2/15](https://doi.org/10.1088/0004-6361/214/2/15)
- Spoon, H. W. W., Farrah, D., Lebouteiller, V., et al. 2013, ApJ, 775, 127, doi: [10.1088/0004-637X/775/2/127](https://doi.org/10.1088/0004-637X/775/2/127)
- Stalevski, M., Asmus, D., & Tristram, K. R. W. 2017, MNRAS, 472, 3854, doi: [10.1093/mnras/stx2227](https://doi.org/10.1093/mnras/stx2227)
- Stalevski, M., Fritz, J., Baes, M., Nakos, T., & Popović, L. Č. 2012, MNRAS, 420, 2756, doi: [10.1111/j.1365-2966.2011.19775.x](https://doi.org/10.1111/j.1365-2966.2011.19775.x)
- Stalevski, M., Ricci, C., Ueda, Y., et al. 2016, MNRAS, 458, 2288, doi: [10.1093/mnras/stw444](https://doi.org/10.1093/mnras/stw444)
- Stein, Y., Vollmer, B., Boch, T., et al. 2021, A&A, 655, A17, doi: [10.1051/0004-6361/202039659](https://doi.org/10.1051/0004-6361/202039659)
- Stern, D. 2015, ApJ, 807, 129, doi: [10.1088/0004-637X/807/2/129](https://doi.org/10.1088/0004-637X/807/2/129)
- Stern, D., Eisenhardt, P., Gorjian, V., et al. 2005, ApJ, 631, 163, doi: [10.1086/432523](https://doi.org/10.1086/432523)
- Stern, D., Assef, R. J., Benford, D. J., et al. 2012, ApJ, 753, 30, doi: [10.1088/0004-637X/753/1/30](https://doi.org/10.1088/0004-637X/753/1/30)
- Stern, D., Lansbury, G. B., Assef, R. J., et al. 2014, ApJ, 794, 102, doi: [10.1088/0004-637X/794/2/102](https://doi.org/10.1088/0004-637X/794/2/102)
- Stierwalt, S., Armus, L., Surace, J. A., et al. 2013, ApJS, 206, 1, doi: [10.1088/0067-0049/206/1/1](https://doi.org/10.1088/0067-0049/206/1/1)
- Swarup, G. 1991, in Astronomical Society of the Pacific Conference Series, Vol. 19, IAU Colloq. 131: Radio Interferometry. Theory, Techniques, and Applications, ed. T. J. Cornwell & R. A. Perley, 376–380
- Swinbank, A. M., Chapman, S. C., Smail, I., et al. 2006, MNRAS, 371, 465, doi: [10.1111/j.1365-2966.2006.10673.x](https://doi.org/10.1111/j.1365-2966.2006.10673.x)
- Tananbaum, H., Avni, Y., Branduardi, G., et al. 1979, ApJL, 234, L9, doi: [10.1086/183100](https://doi.org/10.1086/183100)
- Tanimoto, A., Ueda, Y., Kawamuro, T., et al. 2018, ApJ, 853, 146, doi: [10.3847/1538-4357/aaa47c](https://doi.org/10.3847/1538-4357/aaa47c)
- Tanimoto, A., Ueda, Y., Odaka, H., et al. 2019, ApJ, 877, 95, doi: [10.3847/1538-4357/ab1b20](https://doi.org/10.3847/1538-4357/ab1b20)
- . 2020, ApJ, 897, 2, doi: [10.3847/1538-4357/ab96bc](https://doi.org/10.3847/1538-4357/ab96bc)
- Tanimoto, A., Ueda, Y., Odaka, H., Yamada, S., & Ricci, C. 2022, ApJS, 260, 30, doi: [10.3847/1538-4365/ac5f59](https://doi.org/10.3847/1538-4365/ac5f59)
- Taylor, M. B. 2006, in Astronomical Society of the Pacific Conference Series, Vol. 351, Astronomical Data Analysis Software and Systems XV, ed. C. Gabriel, C. Arviset, D. Ponz, & S. Enrique, 666
- Teng, S. H., Brandt, W. N., Harrison, F. A., et al. 2014, ApJ, 785, 19, doi: [10.1088/0004-637X/785/1/19](https://doi.org/10.1088/0004-637X/785/1/19)
- Teng, S. H., Rigby, J. R., Stern, D., et al. 2015, ApJ, 814, 56, doi: [10.1088/0004-637X/814/1/56](https://doi.org/10.1088/0004-637X/814/1/56)
- Tingay, S. J., Goeke, R., Bowman, J. D., et al. 2013, PASA, 30, e007, doi: [10.1017/pasa.2012.007](https://doi.org/10.1017/pasa.2012.007)
- Toba, Y., Bae, H.-J., Nagao, T., et al. 2017a, ApJ, 850, 140, doi: [10.3847/1538-4357/aa918a](https://doi.org/10.3847/1538-4357/aa918a)
- Toba, Y., Komugi, S., Nagao, T., et al. 2017b, ApJ, 851, 98, doi: [10.3847/1538-4357/aa9d17](https://doi.org/10.3847/1538-4357/aa9d17)

- Toba, Y., Ueda, Y., Matsuoka, K., et al. 2019a, MNRAS, 484, 196, doi: [10.1093/mnras/sty3523](https://doi.org/10.1093/mnras/sty3523)
- Toba, Y., Nagao, T., Strauss, M. A., et al. 2015, PASJ, 67, 86, doi: [10.1093/pasj/psv057](https://doi.org/10.1093/pasj/psv057)
- Toba, Y., Yamashita, T., Nagao, T., et al. 2019b, ApJS, 243, 15, doi: [10.3847/1538-4365/ab238d](https://doi.org/10.3847/1538-4365/ab238d)
- Toba, Y., Yamada, S., Ueda, Y., et al. 2020a, ApJ, 888, 8, doi: [10.3847/1538-4357/ab5718](https://doi.org/10.3847/1538-4357/ab5718)
- Toba, Y., Goto, T., Oi, N., et al. 2020b, ApJ, 899, 35, doi: [10.3847/1538-4357/ab9cb7](https://doi.org/10.3847/1538-4357/ab9cb7)
- Toba, Y., Ueda, Y., Gandhi, P., et al. 2021a, ApJ, 912, 91, doi: [10.3847/1538-4357/abe94a](https://doi.org/10.3847/1538-4357/abe94a)
- Toba, Y., Brusa, M., Liu, T., et al. 2021b, A&A, 649, L11, doi: [10.1051/0004-6361/202140317](https://doi.org/10.1051/0004-6361/202140317)
- Toba, Y., Liu, T., Urrutia, T., et al. 2022a, A&A, 661, A15, doi: [10.1051/0004-6361/202141547](https://doi.org/10.1051/0004-6361/202141547)
- Toba, Y., Yamada, S., Matsubayashi, K., et al. 2022b, PASJ, 74, 1356, doi: [10.1093/pasj/psac073](https://doi.org/10.1093/pasj/psac073)
- Tombesi, F., Meléndez, M., Veilleux, S., et al. 2015, Nature, 519, 436, doi: [10.1038/nature14261](https://doi.org/10.1038/nature14261)
- Tomczak, A. R., Quadri, R. F., Tran, K.-V. H., et al. 2016, ApJ, 817, 118, doi: [10.3847/0004-637X/817/2/118](https://doi.org/10.3847/0004-637X/817/2/118)
- Torres-Albà, N., Iwasawa, K., Díaz-Santos, T., et al. 2018, A&A, 620, A140, doi: [10.1051/0004-6361/201834105](https://doi.org/10.1051/0004-6361/201834105)
- Trakhtenbrot, B., & Netzer, H. 2010, MNRAS, 406, L35, doi: [10.1111/j.1745-3933.2010.00876.x](https://doi.org/10.1111/j.1745-3933.2010.00876.x)
- Travascio, A., Zappacosta, L., Cantalupo, S., et al. 2020, A&A, 635, A157, doi: [10.1051/0004-6361/201936197](https://doi.org/10.1051/0004-6361/201936197)
- Tristram, K. R. W., & Schartmann, M. 2011, A&A, 531, A99, doi: [10.1051/0004-6361/201116867](https://doi.org/10.1051/0004-6361/201116867)
- Tristram, K. R. W., Raban, D., Meisenheimer, K., et al. 2009, A&A, 502, 67, doi: [10.1051/0004-6361/200811607](https://doi.org/10.1051/0004-6361/200811607)
- Tsai, C.-W., Eisenhardt, P. R. M., Jun, H. D., et al. 2018, ApJ, 868, 15, doi: [10.3847/1538-4357/aae698](https://doi.org/10.3847/1538-4357/aae698)
- Tully, R. B. 1988, *Nearby Galaxies Catalog*. Cambridge Univ. Press, Cambridge
- Turner, D. G. 2011, RMxAA, 47, 127, <https://arxiv.org/abs/1102.0347>
- U, V. 2022, Universe, 8, 392, doi: [10.3390/universe8080392](https://doi.org/10.3390/universe8080392)
- U, V., Sanders, D. B., Mazzarella, J. M., et al. 2012, ApJS, 203, 9, doi: [10.1088/0067-0049/203/1/9](https://doi.org/10.1088/0067-0049/203/1/9)
- U, V., Medling, A. M., Inami, H., et al. 2019, ApJ, 871, 166, doi: [10.3847/1538-4357/aaf1c2](https://doi.org/10.3847/1538-4357/aaf1c2)
- Ueda, Y., Akiyama, M., Hasinger, G., Miyaji, T., & Watson, M. G. 2014, ApJ, 786, 104, doi: [10.1088/0004-637X/786/2/104](https://doi.org/10.1088/0004-637X/786/2/104)
- Ueda, Y., Hatsukade, B., Kohno, K., et al. 2018, ApJ, 853, 24, doi: [10.3847/1538-4357/aa9f10](https://doi.org/10.3847/1538-4357/aa9f10)
- Uematsu, R., Ueda, Y., Tanimoto, A., et al. 2021, ApJ, 913, 17, doi: [10.3847/1538-4357/abf0a2](https://doi.org/10.3847/1538-4357/abf0a2)
- Vardoulaki, E., Charmandaris, V., Murphy, E. J., et al. 2015, A&A, 574, A4, doi: [10.1051/0004-6361/201424125](https://doi.org/10.1051/0004-6361/201424125)
- Vasudevan, R. V., & Fabian, A. C. 2007, MNRAS, 381, 1235, doi: [10.1111/j.1365-2966.2007.12328.x](https://doi.org/10.1111/j.1365-2966.2007.12328.x)
- Veilleux, S., Meléndez, M., Tripp, T. M., Hamann, F., & Rupke, D. S. N. 2016, ApJ, 825, 42, doi: [10.3847/0004-637X/825/1/42](https://doi.org/10.3847/0004-637X/825/1/42)
- Veilleux, S., Kim, D. C., Rupke, D. S. N., et al. 2009a, ApJ, 701, 587, doi: [10.1088/0004-637X/701/1/587](https://doi.org/10.1088/0004-637X/701/1/587)
- Veilleux, S., Rupke, D. S. N., Kim, D. C., et al. 2009b, ApJS, 182, 628, doi: [10.1088/0067-0049/182/2/628](https://doi.org/10.1088/0067-0049/182/2/628)
- Veilleux, S., Meléndez, M., Sturm, E., et al. 2013, ApJ, 776, 27, doi: [10.1088/0004-637X/776/1/27](https://doi.org/10.1088/0004-637X/776/1/27)
- Venanzi, M., Höning, S., & Williamson, D. 2020, ApJ, 900, 174, doi: [10.3847/1538-4357/aba89f](https://doi.org/10.3847/1538-4357/aba89f)
- Venturi, G., Nardini, E., Marconi, A., et al. 2018, A&A, 619, A74, doi: [10.1051/0004-6361/201833668](https://doi.org/10.1051/0004-6361/201833668)
- Vietri, G., Misawa, T., Piconcelli, E., et al. 2022, A&A, 668, A87, doi: [10.1051/0004-6361/202243285](https://doi.org/10.1051/0004-6361/202243285)
- Vika, M., Driver, S. P., Cameron, E., Kelvin, L., & Robotham, A. 2012, MNRAS, 419, 2264, doi: [10.1111/j.1365-2966.2011.19881.x](https://doi.org/10.1111/j.1365-2966.2011.19881.x)
- Vito, F., Brandt, W. N., Stern, D., et al. 2018, MNRAS, 474, 4528, doi: [10.1093/mnras/stx3120](https://doi.org/10.1093/mnras/stx3120)
- Wada, K. 2012, ApJ, 758, 66, doi: [10.1088/0004-637X/758/1/66](https://doi.org/10.1088/0004-637X/758/1/66)
- Wada, K., Fukushige, R., Izumi, T., & Tomisaka, K. 2018, ApJ, 852, 88, doi: [10.3847/1538-4357/aa9e53](https://doi.org/10.3847/1538-4357/aa9e53)
- Wada, K., Papadopoulos, P. P., & Spaans, M. 2009, ApJ, 702, 63, doi: [10.1088/0004-637X/702/1/63](https://doi.org/10.1088/0004-637X/702/1/63)
- Wada, K., Schartmann, M., & Meijerink, R. 2016, ApJL, 828, L19, doi: [10.3847/2041-8205/828/2/L19](https://doi.org/10.3847/2041-8205/828/2/L19)
- Waters, C. Z., Magnier, E. A., Price, P. A., et al. 2020, ApJS, 251, 4, doi: [10.3847/1538-4365/abb82b](https://doi.org/10.3847/1538-4365/abb82b)
- Wenger, M., Ochsenbein, F., Egret, D., et al. 2000, A&AS, 143, 9, doi: [10.1051/aas:2000332](https://doi.org/10.1051/aas:2000332)
- Weston, M. E., McIntosh, D. H., Brodwin, M., et al. 2017, MNRAS, 464, 3882, doi: [10.1093/mnras/stw2620](https://doi.org/10.1093/mnras/stw2620)
- Williamson, D., Höning, S., & Venanzi, M. 2019, ApJ, 876, 137, doi: [10.3847/1538-4357/ab17d5](https://doi.org/10.3847/1538-4357/ab17d5)
- . 2020, ApJ, 897, 26, doi: [10.3847/1538-4357/ab989e](https://doi.org/10.3847/1538-4357/ab989e)
- Willingale, R., Starling, R. L. C., Beardmore, A. P., Tanvir, N. R., & O'Brien, P. T. 2013, MNRAS, 431, 394, doi: [10.1093/mnras/stt175](https://doi.org/10.1093/mnras/stt175)
- Winter, L. M., Mushotzky, R. F., Reynolds, C. S., & Tueller, J. 2009, ApJ, 690, 1322, doi: [10.1088/0004-637X/690/2/1322](https://doi.org/10.1088/0004-637X/690/2/1322)
- Wolf, C., Onken, C. A., Luvaal, L. C., et al. 2018, PASA, 35, e010, doi: [10.1017/pasa.2018.5](https://doi.org/10.1017/pasa.2018.5)

- Woo, J.-H., Son, D., & Rakshit, S. 2020, ApJ, 901, 66, doi: [10.3847/1538-4357/abad97](https://doi.org/10.3847/1538-4357/abad97)
- Wright, E. L., Eisenhardt, P. R. M., Mainzer, A. K., et al. 2010, AJ, 140, 1868, doi: [10.1088/0004-6256/140/6/1868](https://doi.org/10.1088/0004-6256/140/6/1868)
- . 2019, AllWISE Source Catalog, IPAC, doi: [10.26131/IRSA1](https://doi.org/10.26131/IRSA1)
- Wright, G. S., Wright, D., Goodson, G. B., et al. 2015, PASP, 127, 595, doi: [10.1086/682253](https://doi.org/10.1086/682253)
- Wu, J., Jun, H. D., Assef, R. J., et al. 2018, ApJ, 852, 96, doi: [10.3847/1538-4357/aa9ff3](https://doi.org/10.3847/1538-4357/aa9ff3)
- Xie, Y., Ho, L. C., Zhuang, M.-Y., & Shangguan, J. 2021, ApJ, 910, 124, doi: [10.3847/1538-4357/abe404](https://doi.org/10.3847/1538-4357/abe404)
- Yamada, S., Ueda, Y., Oda, S., et al. 2018, ApJ, 858, 106, doi: [10.3847/1538-4357/aabacb](https://doi.org/10.3847/1538-4357/aabacb)
- Yamada, S., Ueda, Y., Tanimoto, A., et al. 2021, ApJS, 257, 61, doi: [10.3847/1538-4365/ac17f5](https://doi.org/10.3847/1538-4365/ac17f5)
- . 2019, ApJ, 876, 96, doi: [10.3847/1538-4357/ab14f0](https://doi.org/10.3847/1538-4357/ab14f0)
- . 2020, ApJ, 897, 107, doi: [10.3847/1538-4357/ab94b1](https://doi.org/10.3847/1538-4357/ab94b1)
- Yang, G., Boquien, M., Buat, V., et al. 2020a, MNRAS, 491, 740, doi: [10.1093/mnras/stz3001](https://doi.org/10.1093/mnras/stz3001)
- Yang, G., Boquien, M., Brandt, W. N., et al. 2022, ApJ, 927, 192, doi: [10.3847/1538-4357/ac4971](https://doi.org/10.3847/1538-4357/ac4971)
- Yang, X., Yao, S., Yang, J., et al. 2020b, ApJ, 904, 200, doi: [10.3847/1538-4357/abb775](https://doi.org/10.3847/1538-4357/abb775)
- Yoshida, M., Kawabata, K. S., & Ohyama, Y. 2011, PASJ, 63, 493, doi: [10.1093/pasj/63.sp2.S493](https://doi.org/10.1093/pasj/63.sp2.S493)
- Yoshii, Y., Aoki, T., Doi, M., et al. 2010, in Society of Photo-Optical Instrumentation Engineers (SPIE) Conference Series, Vol. 7733, Ground-based and Airborne Telescopes III, ed. L. M. Stepp, R. Gilmozzi, & H. J. Hall, 773308, doi: [10.1117/12.856680](https://doi.org/10.1117/12.856680)
- Yu, Q., & Tremaine, S. 2002, MNRAS, 335, 965, doi: [10.1046/j.1365-8711.2002.05532.x](https://doi.org/10.1046/j.1365-8711.2002.05532.x)
- Yuan, H. B., Liu, X. W., & Xiang, M. S. 2013, MNRAS, 430, 2188, doi: [10.1093/mnras/stt039](https://doi.org/10.1093/mnras/stt039)
- Yun, M. S., Reddy, N. A., & Condon, J. J. 2001, ApJ, 554, 803, doi: [10.1086/323145](https://doi.org/10.1086/323145)
- Yutani, N., Toba, Y., Baba, S., & Wada, K. 2022, ApJ, 936, 118, doi: [10.3847/1538-4357/ac87a2](https://doi.org/10.3847/1538-4357/ac87a2)
- Zakamska, N. L., Hamann, F., Pâris, I., et al. 2016, MNRAS, 459, 3144, doi: [10.1093/mnras/stw718](https://doi.org/10.1093/mnras/stw718)
- Zappacosta, L., Piconcelli, E., Duras, F., et al. 2018, A&A, 618, A28, doi: [10.1051/0004-6361/201732557](https://doi.org/10.1051/0004-6361/201732557)
- Zappacosta, L., Piconcelli, E., Giustini, M., et al. 2020, A&A, 635, L5, doi: [10.1051/0004-6361/201937292](https://doi.org/10.1051/0004-6361/201937292)
- Zhang, Z., Shi, Y., Rieke, G. H., et al. 2016, ApJL, 819, L27, doi: [10.3847/2041-8205/819/2/L27](https://doi.org/10.3847/2041-8205/819/2/L27)
- Zou, F., Brandt, W. N., Vito, F., et al. 2020, MNRAS, 499, 1823, doi: [10.1093/mnras/staa2930](https://doi.org/10.1093/mnras/staa2930)